論文 / 著書情報
Article / Book Information

題目(和文)	
Title(English)	Enhancement of Photocatalytic Performance for Environmental Remediation of Layered Bismuth Tungstate Through Doping and Compositing
著者(和文)	
Author(English)	Mirabbos Hojamberdiev
出典(和文)	学位:博士(工学), 学位授与機関:東京工業大学, 報告番号:乙第4182号, 授与年月日:2021年3月31日, 学位の種別:論文博士, 審査員:松下 伸広,中島 章,宮内 雅浩,生駒 俊之,北野 政明
Citation(English)	Degree:Doctor (Engineering), Conferring organization: Tokyo Institute of Technology, Report number:乙第4182号, Conferred date:2021/3/31, Degree Type:Thesis doctor, Examiner:,,,,
学位種別(和文)	博士論文
Type(English)	Doctoral Thesis

DOCTORAL DISSERTATION

Enhancement of Photocatalytic Performance for Environmental Remediation of Layered Bismuth Tungstate Through Doping and Compositing

BY

HOJAMBERDIEV Mirabbos

submitted for the Degree of

DOCTOR OF ENGINEERING

under the guidance of

Prof. NOBUHIRO MATSUSHITA

DEPARTMENT OF MATERIALS SCIENCE AND ENGINEERING
TOKYO INSTITUTE OF TECHNOLOGY

O-okayama, Meguro, Tokyo 152-8552

JAPAN
2019

Thesis title: Enhancement of Photocatalytic Performance for Environmental Remediation of Layered Bismuth Tungstate Through Doping and Compositing

Abstract:

Air and water pollution has been one of the challenging environmental issues in modern society. Since the Honda-Fujishima effect was first reported in 1972, a semiconductor-based photocatalysis has been regarded as one of the most green and economical processes for potential application in environmental remediation due to its use of abundant solar energy and environmentally friendliness. Bismuth-based semiconductors are regarded as a promising group of advanced photocatalytic materials due to their suitable band gap for visible light response, an increased mobility of photo-generated charge carriers because of well-dispersed Bi 6s orbital, non-toxicity, and easy tailoring of their morphologies. As one of the simplest members of the Aurivillius oxide family of layered perovskites, Bi_2WO_6 is structurally composed of alternating perovskite-like blocks (BO_6 octahedra) and fluorite-like Bi_2O_2 layers. Having an optical bang gap of 2.80 eV, Bi_2WO_6 exhibited a decent photocatalytic activity for the removal of various organic pollutants.

To utilize its full potential in environmental remediation, the present study aims at enhancing the photocatalytic performance of layered Bi_2WO_6 through cerium doping and compositing it with other semiconductors, such as $ZnWO_4$, BiOI, $CeVO_4$, and reduced graphene oxide. The synthesized $Bi_2WO_6/ZnWO_4$, Bi_2WO_6/BiOI/allophane, and $Bi_2WO_6/CeVO_4$/allophane composite photocatalysts exhibited an enhanced photocatalytic activity for the degradation of gaseous acetaldehyde under UV and visible light irradiation, respectively, in comparison with individual Bi_2WO_6. The enhancement in photocatalytic activity is attributed to larger specific surface area, greater number of easily accessible active sites, the extended light absorption range, multiple scattering of incident light, facilitated diffusion of reactants, *n–n* isotype junction, *p–n* heterojunction, and effective separation of photogenerated electron-hole pairs, respectively. The Bi_2WO_6/BiOI composite photocatalyst modified with reduced graphene oxide having unique physicochemical, optical, and electrical properties exhibited a remarkable improvement in the photocatalytic activity for the degradation of gaseous acetaldehyde (as a typical indoor air pollutant) and chloramphenicol in aqueous solution (pharmaceutical water pollutant) under visible light irradiation due to an easy capture of photoinduced electrons and formation of an additional *p–n* heterojunction. The cerium doping not only tuned the morphological structure, light absorption, surface property, and adsorption capacity but also influenced the photocatalytic activity of Bi_2WO_6 and Bi_2WO_6-BiOCl for the degradation of salicylic acid under visible light irradiation due to the synergistic effect of cerium and the formed *p–n* heterojunction. The developed photocatalytic materials are photostable, recyclable, environmentally friendly, inexpensive and efficient and can be applied for effective removal of various air and water pollutants.

Notations:

ICDD PDF	International Centre for Diffraction Data - Powder Diffraction File
IUPAC	International Union of Pure and Applied Chemistry
C_0	initial concentration at time t_0
C	concentration after light irradiation
t	time
k	first-order rate constant
BW	Bi_2WO_6
BI	BiOI
CV	$CeVO_4$
A	allophane
rGO	reduced graphene oxide
S_{BET}	specific surface area
V_t	total pore volume
α	absorption coefficient
hv	photon energy
A	a constant
E_g	band gap energy
AcH	acetaldehyde
CAP	chloramphenicol
mmol	millimole
e^-	electron
h^+	hole
•OH	hydroxyl radical
O_2^-•	superoxide anion radical
NHE	normal hydrogen electrode
FWHM	full width at half maximum
FFT	fast fourier transformation
R	absolute reflectance
k	molar absorption coefficient
s	scattering coefficient

CONTENTS

CHAPTER 1: Introduction and Background

1.1. Introduction

1.1.1. Heterogeneous photocatalysis for environmental remediation

An extensive range of pollutants has been released into the terrestrial, aquatic, and atmospheric environments due to rapid urbanization, industrialization and agricultural development. Particularly, the environmental pollution has accelerated a dramatic alteration in the aquatic and atmospheric compositions, leading to the global climate change and endangering the environment and human health [1]. The degradation of these pollutants can be done by various chemical, photochemical and biological processes; however, these processes need a long treatment time and generates solid wastes requiring further disposal [2]. Since the Honda-Fujishima effect was first reported in the early 1970's [3], the heterogeneous photocatalytic degradation of various organic pollutants in air and water has gained much attention because this advanced oxidation process has several advantages over the competing conventional air purification and water treatment processes, such as complete mineralization, no waste generation, inexpensive, and mild conditions (temperature and pressure). To date, an environmentally friendly advanced oxidation process has been successfully applied for efficient treatment of municipal and hospital wastewater, agricultural wastewater, and wastewater from various industries, including dairy, paper, textile, oil, distillery, pharmaceutical, and volatile organic compounds. Generally, such heterogeneous advanced oxidation processes are complex and have following steps to enable the heterogeneous reaction: (i) diffusion of reactants to the surface, (ii) adsorption of reactants onto the surface, (iii) photocatalytic reaction on the surface, (iv) desorption of reaction products from the surface, and (v) diffusion of products from the surface [4].

Figure 1 shows a schematic illustration of the basic principles of overall water splitting and photodegradation of organic pollutants on a heterogeneous photocatalyst. As shown in Figure 1, the photocatalytic reaction is generally initiated by the absorption of a photon with energy

equal to, or greater than the band gap of the semiconductor, and the generation of electrons (e^-) and holes (h^+).

$$\text{Photocatalyst} + h\nu \rightarrow \text{electrons } (e_{CB}^-) + \text{holes } (h_{VB}^+)$$

In photocatalytic water splitting, electrons in the valence band are excited upon irradiation and migrate to the conduction band, leaving holes in the valence band. The photogenerated electrons are involved in the water reduction reaction (H^+/H_2), while the photogenerated holes participate in the water oxidation reaction (H_2O/O_2), promoting an overall water splitting.

$$4H^+ + 4e^- \rightarrow 2H_2 \qquad E^0 = 0.00 \text{ eV}$$

$$2H_2O \rightarrow O_2 + 4H^+ + 4e^- \qquad E^0 = -1.23 \text{ eV}$$

In photodegradation of organic pollutants, the mechanism of heterogeneous photocatalysis is primarily described by the semiconductor capability to generate charge carriers upon light irradiation followed by the generation of radicals [5]. On one hand, the photogenerated electrons and holes can directly drive the reduction and oxidation degradation reactions of pollutants, respectively. On the other hand, upon light irradiation electrons in the valence band move to the conduction band and react with the surface-adsorbed oxygen molecules to form superoxide radicals ($O_2^{\bullet -}$). Meantime, the oxidation of H_2O and OH^- by photogenerated holes produces hydroxyl ions ($^\bullet OH$), an extremely powerful oxidant with the oxidation potential of 2.8 V versus normal hydrogen electrode. Further, the formed $O_2^{\bullet -}$ and $^\bullet OH$ ions are engaged in the photocatalytic degradation of organic pollutants adsorbed on the photocatalyst surface.

$$O_{2\ ads.} + e^- \rightarrow O_2^{\bullet -}$$

$$OH^- + h^+ \rightarrow {}^\bullet OH$$

$$O_2^{\bullet -} / {}^\bullet OH + \text{organic pollutants} \rightarrow \text{mineralization products}$$

When the photogenerated holes also reach the surface, they can react with the surface-adsorbed organic molecules by interfacial electron transfer, assuming that the adsorbed organic molecules have a redox potential appropriate for thermodynamically allowed reaction. Therefore, an adsorbed electron donor can be oxidized by transferring an electron to a

photogenerated hole on the surface, and an adsorbed acceptor can be reduced by accepting an electron from the surface [6].

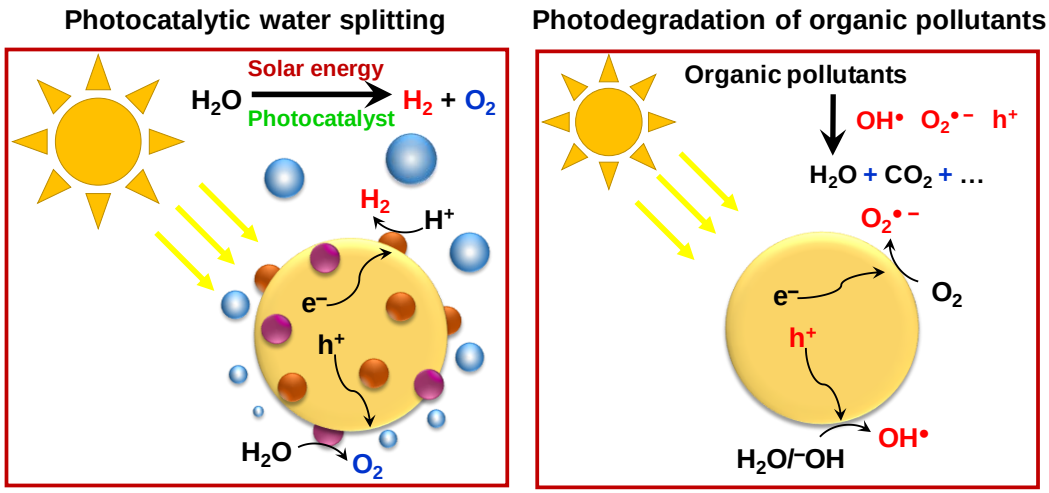

Figure 1. Basic principles of photocatalytic water splitting (*left*) and photodegradation of organic pollutants (*right*) over semiconductors.

Heterogeneous photocatalysis has been widely applied in different applications, including environmental (water and air purification, photocatalytic water splitting), structural (self-cleaning paints, tiles, glasses, ceramics, textile, etc.), healthcare (self-sanitizing coating, medical instruments, etc.), selective redox reactions (synthesis of organic compounds, the reduction of graphene oxide), cancer treatment (drug delivery, endoscopic instruments, etc.), etc. [7,8], because it fulfills the practical requirements, such as cost, efficiency, stability, safety, and utilization of visible light (Figure 2) [7].

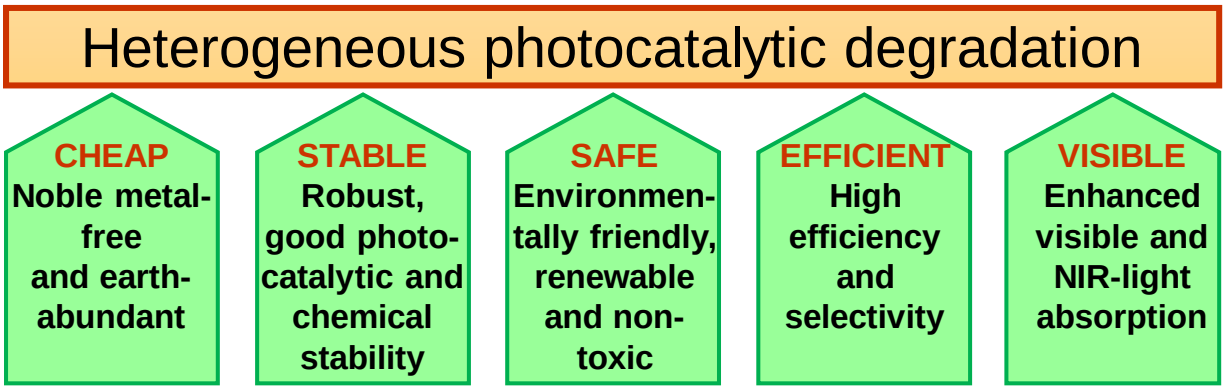

Figure 2. Practical requirements for the photocatalysts in environmental remediation [7].

In heterogeneous photocatalysis, the photocatalyst should promote reactions in the presence of light without being consumed in the overall reaction. Therefore, it is necessary to select a good photocatalyst promoting the heterogeneous photocatalytic reaction. In general, a good photocatalyst should be photoactive in the visible region, (ii) photostable during the photocatalytic reaction, (iii) biologically and chemically inert, (iv) inexpensive, and (v) non-toxic. The photocatalytic activity strongly depends on the particle morphology, size, dimension, specific surface area, hierarchical and hollow structures, etc. [9]. Heterogeneous photocatalysts can be classified into the following categories depending on dimension:

- Zero-dimensional (nanoparticles [9] and quantum dots [10]);
- One-dimensional (nanorods [11,12], nanoribbons [13], and nanotubes [14]);
- Two-dimensional (graphene-based nanocomposites [15,16]);
- Three-dimensional (3D carbon materials [15]).

The most widely used group of nanomaterials is the zero-dimensional group, particularly in the form of core-shell nanoparticles. Also, efficient separation and transfer of photogenerated charge carriers in a low dosage of photocatalyst can be achieved by developing ultrathin, hierarchical and hollow structures and immobilization on substrates with specific morphologies. The photodegradation of organic pollutants in gas and liquid phase systems can be done by heterogeneous photocatalysis (Figure 3) [7].

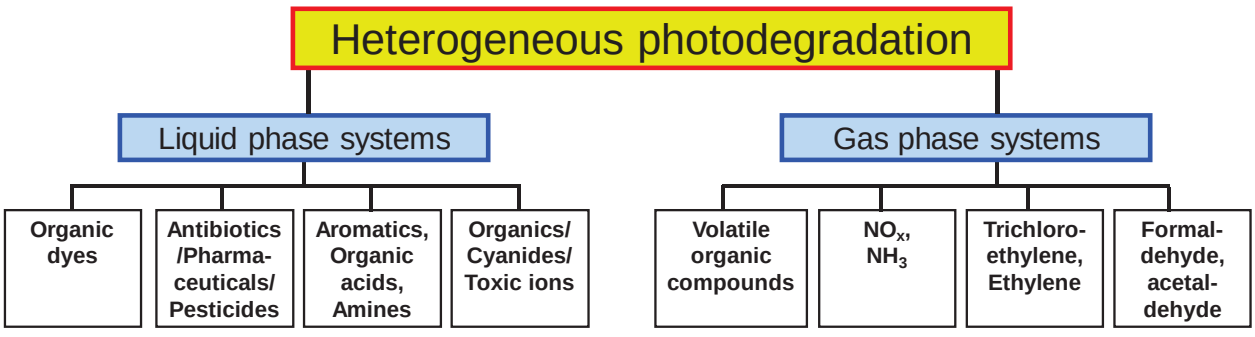

Figure 3. Heterogeneous photodegradation systems for various pollutants [7].

1.1.2. Layered compounds as photocatalysts for environmental remediation

As mentioned above, the photocatalytic activity of a photocatalyst is strongly dependent on its morphology, size and dimension, which promote the migration of photogenerated charge carriers to the surface. In comparison with zero-dimensional (0D), one-dimensional (1D), and three-dimensional (3D) materials, two-dimensional (2D) layered materials have advantages, namely larger specific surface area, greater number of active sites, good conductivity, superior electron mobility, expanded contact surface, increased charge transfer rate, good photocatalyst support [17]. Graphene has a 2D nanostructure comprised of a single layer of sp^2-bonded carbon atoms with honeycomb rings. Yu and co-workers [18] have studied the effect of graphene on the photocatalytic activity of CdS and found that the CdS-graphene composite could exhibit a 5-fold increased photocatalytic hydrogen production rate compared with pure CdS because of the improved crystallinity and specific surface area and the inhibited recombination of photogenerated charge carriers. As another carbon-based material, graphitic carbon nitride (g-C_3N_4) has high thermal stability, high chemical stability against acid, base and organic solvents, high photoreactivity and high electron transfer ability. Various g-C_3N_4-based heterojunction photocatalysts have exhibited an enhanced photocatalytic activity for the degradation of methylene blue, methyl orange, phenol, ciprofloxacin, toluene, brilliant red, formaldehyde, isoniazid, rhodamine B, acridine orange, 2,4-dichlorophenol, sulforhodamine B, fuchsin, bisphenol A, etc. [19]. As an example, the high photocatalytic activity was achieved for the degradation of methyl orange by Ag@AgBr/g-C_3N_4 due to the formation of the Z-scheme system [20]. Molybdenum disulphide (MoS_2) has a layered structure in which the layers, constituting an atomic plane of Mo sandwiched between two atomic planes of S in a trigonal prismatic arrangement, are connected by weak van der Waals forces. Since the valence band edge potentials for bulk MoS_2 and monolayer MoS_2 are estimated to be 1.40 eV and 1.78 eV, respectively, they are not oxidative enough to generate free radicals (e.g. •OH) and directly decompose pollutants. However, MoS_2 can serve as a cocatalyst to improve the photocatalytic

activity of the support photocatalyst [21]. Due to the excellent electronic conductivity of MoS_2, the TiO_2 nanofibers vertically coated with MoS_2 layer acted as a 'wire' to transfer photogenerated electrons from Ag_3PO_4 into the solution quickly, and the photocorrosion of Ag^+ was also inhibited, improving the photocatalytic activity $Ag_3PO_4/TiO_2@MoS_2$ for the degradation of dyes and antibiotics [22]. Layered double hydroxides (LDHs), generally called anionic clays, have emerged as one of the promising candidates for heterogenous photocatalysis for environmental remediation owing to their unique layered structure, compositional flexibility, low manufacturing cost and easy synthesis [23]. A highly efficient visible-light-driven hybrid nanocomposite, consisting of positively charged ZnCr-LDH nanosheets and negatively charged graphene nanosheets, exhibited superior photocatalytic activity for the degradation of rhodamine B due to efficient separation and transfer of photogenerated charge carriers [24].

Although two-dimensional (2D) materials have several advantages, single-layered materials are however thermodynamically unstable and self-agglomerated into larger particle to reduce surface energy during growth. Therefore, various photocatalysts have been synthesized with hierarchical structures (3D) assembled by single layers.

Layered perovskite oxides are a large family of promising photocatalysts due to their structural simplicity and flexibility, good stability and efficient photocatalytic performance. The general formulae of the well-known layered perovskite oxides are $(Bi_2O_2)(A_{n-1}B_nO_{3n+1})$ (Aurivillius phase), $A_{n+1}B_nO_{3n+1}$ or $A_2'A_{n-1}B_nO_{3n+1}$ (Ruddlesden–Popper phase) and $A'[A_{n-1}B_nO_{3n+1}]$ (Dion–Jacobson phase) for {100} series, $(A_nB_nO_{3n+2})$ for {110} series and $(A_{n+1}B_nO_{3n+3})$ for {111} series [25]. The representative examples of these layered structures are shown in Figure 4. In these structures, *n* represents the number of BO_6 octahedra that span a layer, which defines the thickness of the layer.

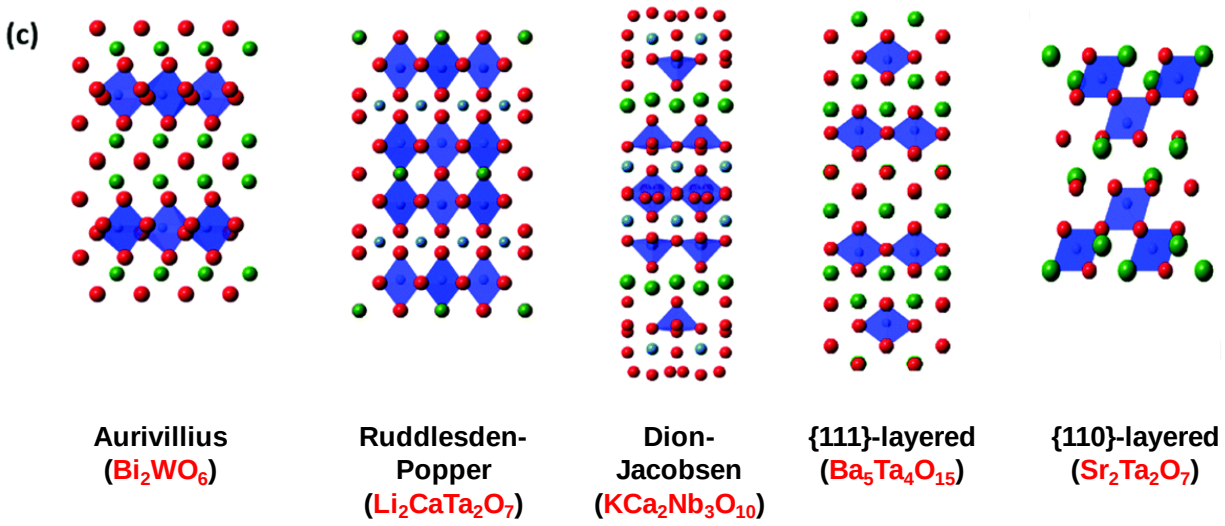

Figure 4. Crystal structures of the representatives of layered perovskite oxides [25].

The crystal structures of the Aurivillius phases are built by altering the layers of $[Bi_2O_2]^{2+}$ and pseudo-perovskite blocks (e.g., Bi_2WO_6, $BiMoO_6$). A series of Aurivillius layered perovskites, $Bi_{5-x}La_xTi_3FeO_{15}$ (x = 0 - 2), exhibited the photocatalytic activity towards the degradation of rhodamine B, which is comparable or higher than many of the single-phase and composite photocatalysts with Aurivillius and perovskite structures in the bulk or nanostructured form reported recently [26]. The crystal structures of the Ruddlesden–Popper phases result from the intergrowth of perovskite ABO_3 and A′O as the intermediate spacing layer (e.g., Sr_2SnO_4, $Li_2CaTa_2O_7$). A series of Ruddlesden−Popper-type hydrous layered perovskites, $A_2'ATa_2O_7$ (A′ = H or K, A = $La_{2/3}$ or Sr) were synthesized as novel photocatalyst for water splitting under UV light irradiation, and the addition of Ni cocatalyst to $H_2La_{2/3}Ta_2O_7$ via an ion-exchange reaction increased the photocatalytic activity [27]. In the crystal structures of the Dion–Jacobson phases, A′ (a univalent alkali cation) separates the perovskite-like blocks (e.g., $RbLnTa_2O_7$ (n = 2), $KCa_2Nb_3O_{10}$ (n = 3)). The $[Ca_2Ta_3O_{9.7}N_{0.2}]^-$ nanosheets prepared by exfoliating a Dion–Jacobson phase layered perovskite oxynitride ($CsCa_2Ta_3O_{9.7}N_{0.2}$) via proton exchange and two-step intercalation of ethylamine and tetrabutylammonium ions showed a photocatalytic activity for hydrogen evolution under visible light irradiation [28]. The

$A_nB_nO_{3n+2}$ and $A_{n+1}B_nO_{3n+3}$ structural series with different layered orientations have demonstrated a photocatalytic activity (e.g., $Sr_2Ta_2O_7$, $Sr_5Ta_4O_{15}$). Among various metal dopants for $La_2Ti_2O_7$, only Cr and Fe showed intense absorption in the visible light region (>400 nm), and only these photocatalysts produced H_2 photocatalytically in the presence of methanol under visible light irradiation [29]. Monomolecular-layer perovskite $Ba_5Ta_4O_{15}$ nanosheets synthesized by a hydrothermal method showed a high photocatalytic activity in the degradation of rhodamine B and gaseous formaldehyde because of efficient charge separation and delocalization of photogenerated electrons and holes [30].

1.1.3. Bismuth-based photocatalysts for environmental remediation

Bismuth-based semiconductors are an important class of visible-light-responsive photocatalysts and have received an increasing attention due to their appropriate band gap for visible-light absorption, high mobility of photogenerated charge carriers stemming from the well-dispersed Bi 6s orbital, layered structure, easily tailored morphology, and non-toxicity. In terms of environmental remediation, Bi_2E_3 (E = O, S, Se, Te), Bi$O$$X$ (X = Br, Cl, I), Bi_2MO_6 (M = Cr, Mo, W), Bi$M$$O_4$ (M = P, V, Nb, Ta), $BiFeO_3$, and other related compounds ($Bi_4Ti_3O_{12}$, $Bi_{12}TiO_{20}$, $Bi_2O_2CO_3$, Bi_3TiNbO_9, $Bi_{0.5}K_{0.5}TiO_3$, etc.) have exhibited good photocatalytic activity for degradation of organic water pollutants, oxidation of gaseous pollutants, and photoreduction of CO_2 [31]. However, Bi-based photocatalysts have a lower conduction band that is insufficient for the reduction of H^+ to H_2 (Figure 5) [32]. Most of these Bi-based compounds have a layered structure, where van der Waals and covalent interaction forces simultaneously exist between layers, giving higher stability and an efficient separation and transfer of charge carriers due to the ultrathin structure.

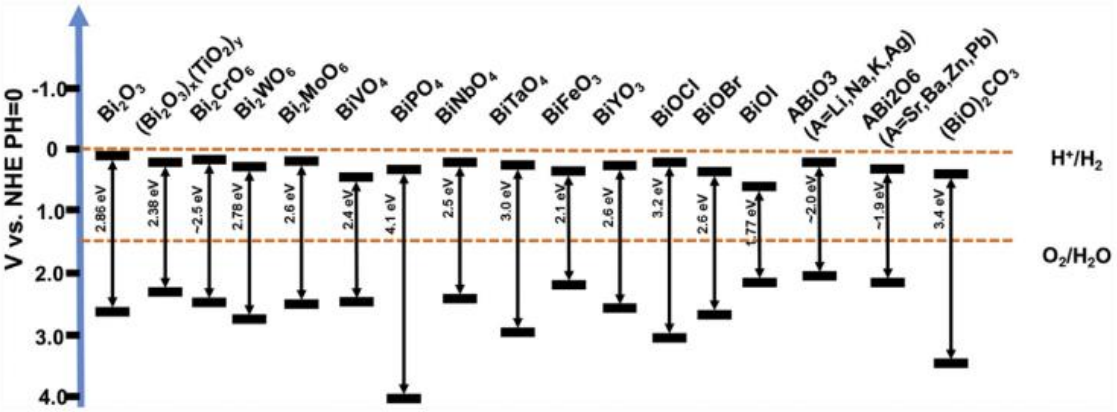

Figure 5. Band positions of bismuth-based photocatalysts [32].

As the simplest member of the Aurivillius family with general formula $Bi_2A_{n-1}B_nO_{3n+3}$ (A = Ca, Sr, Ba, Pb, Bi, Na, K and B = Ti, Nb, Ta, Mo, W, Fe) and layered structure, Bi_2WO_6 has an orthorhombic structure constructed by alternating $[Bi_2O_2]_n^{2n+}$ layers and perovskite-like $[WO_4]_n^{2n-}$ layers and attracted much attention due to its excellent physical and chemical properties [33]. Such layered structure generally favors the efficient separation of photogenerated charge carriers and improves the photocatalytic activity due to the formed internal fields between the slabs. Earlier, Kudo and Hijii [34] found that only Bi_2WO_6 could photocatalytically generate oxygen from water splitting under visible light irradiation among the layered oxide photocatalysts consisting of Bi^{3+} with $6s^2$ configuration and d^0 transition metal ions ($Bi_2W_2O_9$, Bi_2WO_6, Bi_3TiNbO_9) [34]. Later, the mineralization of both $CHCl_3$ and CH_3CHO to CO_2 by Bi_2WO_6 photocatalyst under visible light irradiation was reported by Tan et al. [35]. Since these pioneering works on Bi_2WO_6, several research groups have developed various strategies (morphology control, doping, heterostructure, etc.) to further improve the photocatalytic activity of Bi_2WO_6. Zhang and Zhu [36] successfully synthesized square Bi_2WO_6 nanoplates by a simple hydrothermal process via controlling the hydrothermal reaction temperature and time and found that the nanoplates with the (001) basal plane can exhibit three times higher photocatalytic activity for the degradation of rhodamine B under visible light irradiation compared with bulk sample prepared by solid-state reaction. Shang et al. [37] applied an electrospinning technique to fabricate Bi_2WO_6 nanofibers that showed higher

photocatalytic activity in the decomposition of acetaldehyde and aqueous ammonia under visible light irradiation than the sample prepared by solid-state reaction and nanoparticles. Zhang et al. [38] synthesized flower-like Bi_2WO_6 superstructures by a hydrothermal method without any template, which exhibited excellent visible-light-driven photocatalytic activity for the degradation of rhodamine B compared with P25-TiO_2. The Bi_2WO_6 nanocages were successfully prepared with colloidal carbon spheres as the template via a facile refluxing process in ethylene glycol and exhibited higher shape-associated photocatalytic activity (nearly 10 times higher) in the degradation of RhB under visible-light irradiation compared with the sample prepared by solid-state reaction and P25-TiO_2 [39]. Due to the electrophilic and oxytropic properties of boron, the adsorption capacity of Bi_2WO_6 was significantly enhanced by boron doping, and the separation and transfer of photogenerated electron-hole pairs were improved because boron can act as an electron trap, resulting in higher photocatalytic activity in degradation of rhodamine B compared with pure Bi_2WO_6 [40]. Although enormous efforts have been made to synthesize pure and doped Bi_2WO_6 nano/micro-structures with relatively high photocatalytic activity, there are still some drawbacks limiting their practical applications, such as short lifetime of photogenerated electron-hole pairs and a limited absorption of visible light. To further improve its photocatalytic activity, Bi_2WO_6 was combined with other semiconductors to create a heterojunction. As is well known, heterojunction is defined as the interface between two different semiconductors having unequal band structures. Typically, there are three types of heterojunctions: (i) straddling type, (ii) staggered type, and (iii) broken gap type (Figure 6). In *straddling type*, the energy band gap of semiconductor A is wider than that of semiconductor B, resulting in the accumulation of charge carriers on small-band-gap semiconductor. In *staggered type*, the valence band and conduction band of semiconductor A are higher and lower than those of semiconductor B, resulting in the spatial separation of charge carriers which prevents the recombination of electrons and holes. In *broken gap type,* the staggered gap becomes so wide that electron-hole migration is not possible [8].

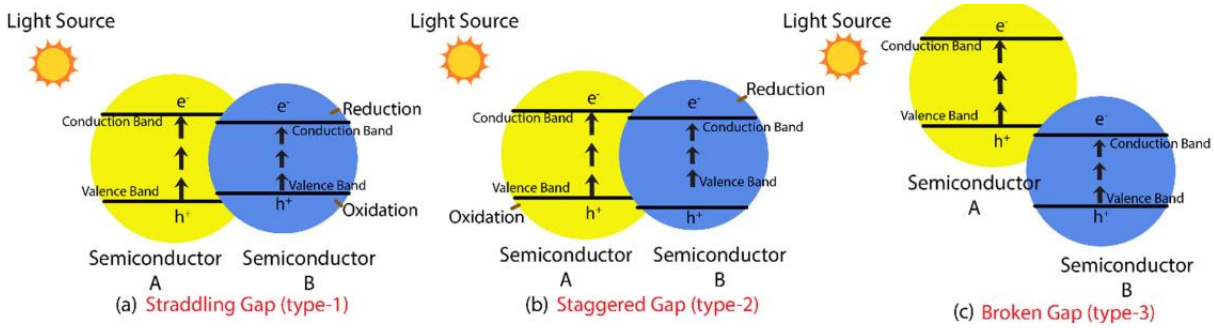

Figure 6. Types of conventional heterojunction [8].

In addition to conventional heterojunctions, p–n heterojunction, surface heterojunction, direct Z-scheme heterojunction and semiconductor/graphene heterojunctions have also been studied. The p–n heterojunction improves the photocatalytic activity by providing an additional electric field due to the combination of n-type and p-type semiconductors. Surface heterojunction involves creating different crystal facets on the exposed surface of semiconductor. Z-scheme heterojunction maximizes the redox potential of the heterojunction due to the presence of two different semiconductors without physical contact, where the migration of charge carriers takes place through the acceptor/donor pair. Semiconductor/graphene heterojunction is based on ultra-high electron conductivity of graphene, enhancing the electron flow [8]. Colón et al. [41] synthesized Bi_2WO_6-TiO_2 heterostructures by a hydrothermal method, which showed high photocatalytic activity for the degradation of rhodamine B under sun-like irradiation owing to the improved charge carrier separation. As a novel plasmonic visible-light-driven photocatalyst, the Bi_2WO_6/Ag_3PO_4–Ag Z-scheme heterojunction was prepared by ultrasound assisted *in situ* precipitation and the hydrothermal method and showed superior photocatalytic activity for the simultaneous degradation of auramine-O and methyl green under visible light because of the decreased recombination rate of photogenerated electron-hole pairs and the enhanced diffusion rate of electrons and holes across the heterojunction [42]. Bi_2WO_6 was modified with graphene to enhance its visible-light-induced photocatalytic activity for H_2/O_2 generation [43] and degradation of rhodamine B [44] because the chemical bonding formed between graphene and

Bi_2WO_6 facilitated the electron collection and transfer, inhibited the recombination of photogenerated charge carriers, and shifted the Fermi level. The immobilization of photocatalytic particles can reduce the scale of the reactor by eliminating the separation and washing unit. Recently, Raizada et al. [45] immobilized magnetically retrievable Bi_2WO_6/Fe_3O_4 nanocomposite particles on graphene sand composite and studied their photocatalytic activity for the mineralization of oxytetracycline and ampicillin under visible light irradiation, and it was found that the immobilized nanocomposite particles can be photostable and recyclable for at least ten photocatalytic runs.

1.2. Background and scheme of research

1.2.1. Present status and future trend

Bi-based materials are promising visible-light-active photocatalysts with applications in photocatalytic environmental remediation and energy conversion. More specifically, these photocatalysts can be used for the visible-light-induced photocatalytic degradation of organic pollutants, H_2 generation from water splitting, and CO_2 reduction. Although significant progress has been achieved so far, the bulk Bi-based photocatalysts have shown an unsatisfactory photocatalytical activity under visible light irradiation. In this context, a number of strategies, such as changing the composition, controlling the morphology, constructing the heterojunction, and modifying the surface are necessary to improve the photocatalytic activity (Figure 7). This can be achieved by applying various approaches, namely, cation/anion doping, stoichiometry controlling, synthesis of solid solutions, low-dimensional nanostructures, and hierarchical and porous architectures, creation of conventional heterojunctions and direct Z-scheme junctions, and surface modification. Also, it is expected that the combination of different nanomaterials and layered nanostructures with Bi-based photocatalysts can improve the photocatalytic activity due to the improvement of light absorption, separation and transfer of photogenerated charge carriers, and band gap engineering. Therefore, it is necessary to understand the roles of dopant, altered morphology and particle size, the formed heterojunction, and the modified surface in improving the photocatalytic activity of Bi-based photocatalysts and the mechanisms involved in the adsorption and photodegradation processes of organic molecules.

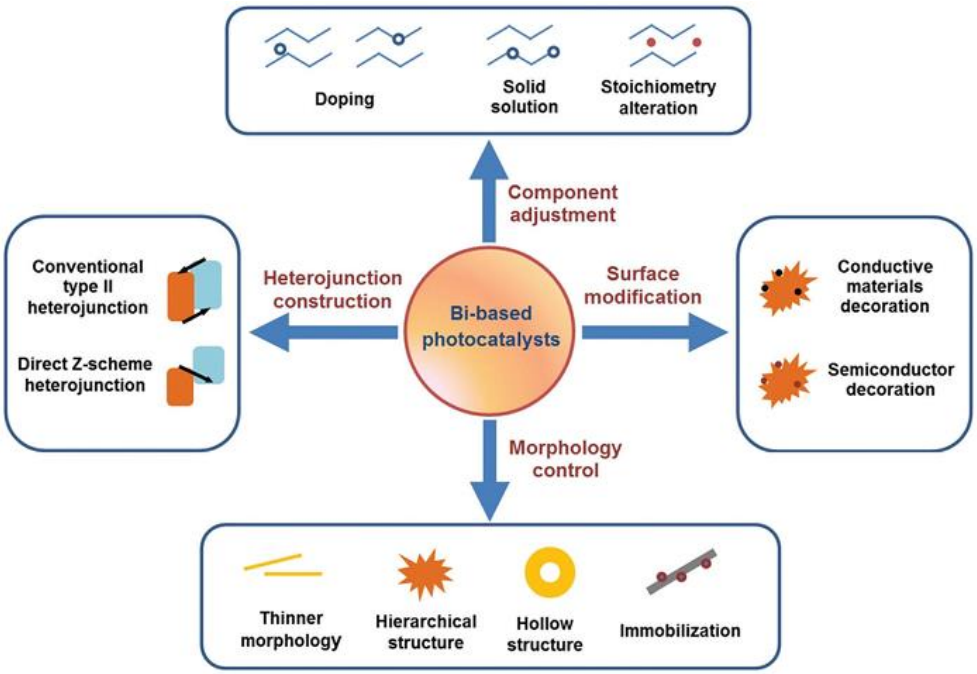

Figure 7. Strategies for enhancing the photocatalytic activity of Bi-based photocatalysts [32].

The following aspects of the research area of Bi-based photocatalysts can be studied in the future to explore the full potential in practical applications:

- **Theoretical modeling** is necessary for predicting the electronic property and photocatalytic activity, and the interactions at the surfaces and interfaces at the atomic and molecular levels.
- **In situ and operando techniques** are essential for the characterization of molecular structure-activity relationship and understanding the photocatalytic mechanisms.
- **Low-dimensional nanostructures** are a promising class of nanomaterials that show an enhanced photocatalytic activity compared with their bulk counterparts due to their unique structural, optical, and physico-chemical properties.
- **Extension of applications** of Bi-based photocatalysts to solar water reduction, reduction of CO_2 and NO, and indoor air purification. The poor reducing ability of these compounds due to a less negative conduction band minimum can be improved by constructing a direct Z-scheme heterojunction by coupling with other semiconductors with more negative conduction band minimum.

- **Immobilization of photocatalyst nanoparticles** on stable supports in order to recover the photocatalyst particles after the reaction and to reduce the scale of the reactor by eliminating the separation and washing units in the continuous reactor type.

The heterogeneous photocatalysis is one of the promising technologies for water and air purification at ambient temperature and pressure, utilizing atmospheric oxygen as oxidant. The heterogeneous photocatalysis can be applied for the degradation of various contaminants, including organic dyes, pharmaceuticals, detergents, pesticides, herbicides, viruses, bacteria, etc. However, there are only a few commercial implementations made for the pretreatment process and stand-alone purification system. Therefore, the design of visible-light-active low-dimensional nanostructures of Bi-based photocatalysts can provide cost-effective and sustainable alternative to the conventional wastewater treatment process.

1.2.2. Needs and approach for research

Considering the present status and future trend in designing the Bi-based photocatalytic systems, the following needs and approaches are identified:

- **Compositing with other semiconductors**: Improvement of photocatalytic activity via simply compositing Bi_2WO_6 with other semiconductors, $ZnWO_4$, BiOI, BiOCl, and $CeVO_4$, with suitable band structure and visible light absorption. These composite photocatalysts can be synthesized by hydrothermal and mechanical mixing.
- **Immobilizing in clay support**: Improvement of photocatalytic activity via involving allophane, as a clay-based support, with high adsorption ability for ionic and polar pollutants and high specific surface area. Allophane-containing composite photocatalysts can be synthesized by hydrothermal and mechanical mixing.
- **Cation doping**: Improvement of photocatalytic activity of Bi_2WO_6 via cerium doping and compositing with BiOCl. Ce-doped Bi_2WO_6 and Bi_2WO_6-BiOCl can be synthesized by a hydrothermal method using ethylene glycol and dilute HCl as solvent and $Ce(NO_3)_3 \cdot 6H_2O$.
- **Involving carbon material**: Improvement of photocatalytic activity of Bi_2WO_6 via compositing with BiOI and reduced graphene oxide (conjugated π-structured

carbon material) with good electrical conductivity. Reduced graphene oxide-modified Bi_2WO_6/BiOI can be synthesized by hydrothermal method.

1.2.3. Objectives of the present research

The main objectives of this study are:

- To investigate the role of other semiconductors, $ZnWO_4$, BiOI, BiOCl, and $CeVO_4$, on improving the photocatalytic activity of Bi_2WO_6.
- To study the effect of an allophane support on photocatalytic activity and recovery of Bi_2WO_6, BiOI, and Bi_2WO_6/BiOI.
- To explore the influence of cerium doping on morphology, physico-chemical properties and photocatalytic activity of Bi_2WO_6.
- To gain insights into improving the photocatalytic activity of a Bi_2WO_6/BiOI composite by modifying with reduced graphene oxide.
- To understand the mechanistic pathways for the degradation of organic pollutants, such as acetaldehyde, salicylic acid, and chloramphenicol, over the developed samples under visible light irradiation.

1.2.4. Scheme of the present research

The scheme of this study is presented below.

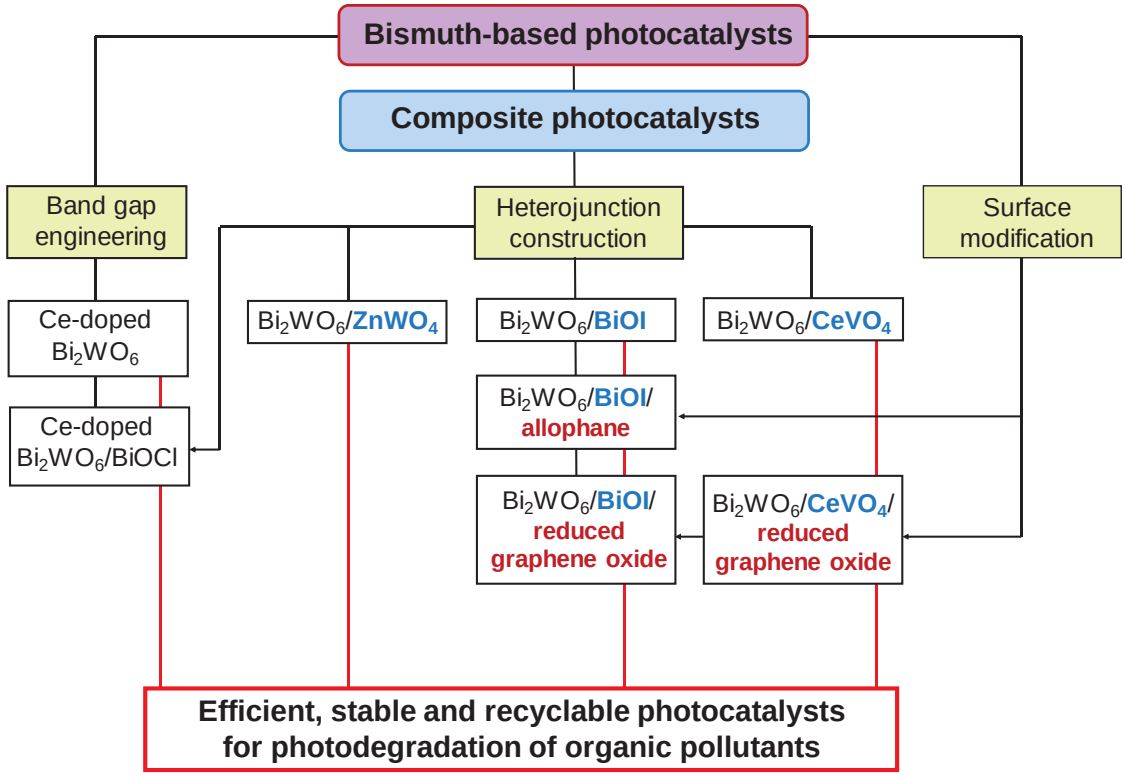

1.2.5. Brief description of the chapters

CHAPTER 1 introduces past achievements, the state of the art, and future perspectives in heterogeneous photocatalysis and its application in environmental remediation, particularly in photocatalytic air and water purification. The layered compounds, bismuth-based photocatalysts, and composite photocatalysts and their application in environmental remediation are discussed. The scheme of research and objectives of the present work are presented.

CHAPTER 2 describes the influence of pH and Bi_2WO_6 content on the formation of the $ZnWO_4/Bi_2WO_6$ composite photocatalyst synthesized by a one-step hydrothermal method and the effect of Bi_2WO_6 content on the performance for the photocatalytic degradation of gaseous acetaldehyde under UV light irradiation and the mechanistic pathways for the degradation of acetaldehyde.

CHAPTER 3 emphasizes the involvement of $CeVO_4$ in improving the photocatalytic activity of the Bi_2WO_6/allophane composite for the degradation of gaseous acetaldehyde under visible light irradiation. Specifically, the photocatalytic activities of the $Bi_2WO_6/CeVO_4$/allophane composites prepared by mechanical mixing and hydrothermal synthesis are studied as a function of the $CeVO_4$ amount, and the mechanistic pathways for the degradation of acetaldehyde over the composites and recyclability are explored.

CHAPTER 4 presents the effect of different Bi_2WO_6:BiOI molar ratios on the physico-chemical properties, adsorption capacity and photocatalytic activity for gaseous acetaldehyde of the Bi_2WO_6/BiOI/allophane composites prepared by mechanical mixing and hydrothermal synthesis. Moreover, the mechanistic pathways for the degradation of gaseous acetaldehyde and recyclability of the prepared composite photocatalysts are also studied.

CHAPTER 5 underlines the important role of cerium doping on tuning the morphological structure, light absorption, and photocatalytic activity of Bi_2WO_6 and Bi_2WO_6-BiOCl synthesized by a hydrothermal method using ethylene glycol and dilute HCl as solvent, respectively. The photocatalytic activities of the prepared samples are evaluated for the degradation of salicylic acid under visible light irradiation. The adsorption affinities and preferential sites of salicylic acid molecules on the prepared samples are studied using

molecular dynamics simulations. The mechanistic pathways and recyclability of the prepared composite photocatalysts are explored.

CHAPTER 6 highlights the modification of the Bi_2WO_6/BiOI composite photocatalyst with reduced graphene oxide in a varying content for enhancing the photocatalytic performance towards the degradation of colorless organic pollutants under visible light irradiation. The adsorption affinities and preferential sites of acetaldehyde and chloramphenicol molecules on the prepared samples are studied using molecular dynamics simulations. The mechanistic pathways and recyclability of the prepared composite photocatalysts are explored.

CHAPTER 7 outlines the general conclusions of the research, the application of research findings, and future prospective of this research area.

1.3. References

[1] A.L. Power, R.K. Tennant, R.T. Jones, Y. Tang, J. Du, A.T. Worsley, J. Love, Monitoring Impacts of Urbanisation and Industrialisation on Air Quality in the Anthropocene Using Urban Pond Sediments, *Front. Earth Sci.* 6 (2018) 131. DOI: 10.3389/feart.2018.00131

[2] Hussain Al-Ekabi, Nick Serpone, Kinetics studies in heterogeneous photocatalysis. I. Photocatalytic degradation of chlorinated phenols in aerated aqueous solutions over titania supported on a glass matrix, *J. Phys. Chem.* 92 (1988) 5726–5731.

[3] A. Fujishima, K. Honda, Electrochemical Photolysis of Water at a Semiconductor Electrode, *Nature* 238 (1972) 37–38.

[4] J.C.R. Turner, An introduction to the theory of catalytic reactors. In: J.R. Anderson, M. Boudart, (Eds.), Catalysis Science and Technology, vol. 1. Springer-Verlag, Berlin, Germany, 1981, pp. 43–86.

[5] A. Trapalis, N. Todorova, T. Giannakopoulou, N. Boukos, T. Speliotis, D. Dimotikali, J. Yu, TiO_2/graphene composite photocatalysts for NO_x removal: a comparison of surfactant-stabilized graphene and reduced graphene oxide, *Appl. Catal. B* 180 (2016) 637–647.

[6] M.A. Fox, M.T. Dulay, Heterogeneous Photocatalysis, *Chem. Rev.* 93 (1993) 341–357.

[7] X. Li, J. Xie, C. Jiang, J. Yu, P. Zhang, Review on design and evaluation of environmental photocatalysts. *Front. Environ. Sci. Eng. 12* (2018), 14. DOI: 10.1007/s11783-018-1076-1

[8] S.N. Ahmed, W. Haider, Heterogeneous photocatalysis and its potential applications in water and wastewater treatment: a review. *Nanotechnology* 29 (2018) 342001.

[9] M. Maisano, M.V. Dozzi, E. Selli, Searching for facet-dependent photoactivity of shape-controlled anatase TiO_2, *J. Photochem. Photobiol. C* 28 (2016) 29–43.

[10] A. Mclaren, T. Valdes-Solis, G. Li, S.C. Tsang, Shape and size effects of ZnO nanocrystals on photocatalytic activity, *J. Amer. Chem. Soc.* 131 (2009) 12540–12541.

[11] J. Ge, M. Lan, W. Liu, Q. Jia, L. Guo, B. Zhou, X. Meng, G. Niu, P. Wang, Graphene quantum dots as efficient, metal-free, visible-light-active photocatalysts, *Sci. Chn. Mater.* 59 (2016) 12–19.

[12] C. Liu, J. Tang, H.M. Chen, B. Liu, P. Yang, A fully integrated nanosystem of semiconductor nanowires for direct solar water splitting, *Nano Lett.* 13 (2013) 2989–2992.

[13] P. Basnet, G.K. Larsen, R.P. Jadeja, Y.C. Hung, Y. Zhao, α-Fe_2O_3 nanocolumns and nanorods fabricated by electron beam evaporation for visible light photocatalytic and antimicrobial applications, *ACS Appl. Mater. Interfaces* 5 (2013) 2085–2095.

[14] J. Jin, T. He, Facile synthesis of Bi_2S_3 nanoribbons for photocatalytic reduction of CO_2 into CH_3OH, *Appl. Surf. Sci.* 394 (2017) 364–370.

[15] J. Podporska-Carroll, E. Panaitescu, B. Quilty, L. Wang, L. Menon, S.C. Pillai, Antimicrobial properties of highly efficient photocatalytic TiO_2 nanotubes. *Appl. Catal. B* 176 (2015) 70–75.

[16] S. Kumar, A. Kumar, A. Bahuguna, V. Sharma, V. Krishnan, Two-dimensional carbon-based nanocomposites for photocatalytic energy generation and environmental remediation applications, *Beilstein J. Nanotechnol.* 8 (2017) 1571–1600.

[17] J. Low, S. Cao, J. Yu, S. Wageh, Two-dimensional layered composite photocatalysts, *Chem. Commun.* 50 (2014) 10768–10777.

[18] J. Yu, Y. Yu, P. Zhou, W. Xiao, B. Cheng, Morphology-dependent photocatalytic H_2-production activity of CdS, *Appl. Catal. B* 156–157 (2014) 184–191.

[19] W.-J. Ong, L.-L. Tan, Y. Hau Ng, S.-T. Yong, S.-P. Chai, Graphitic Carbon Nitride (g-C_3N_4)-Based Photocatalysts for Artificial Photosynthesis and Environmental

Remediation: Are We a Step Closer To Achieving Sustainability? *Chem. Rev.* 116 (2016) 7159–7329.

[20] Y. Yang, W. Guo, Y. Guo, Y. Zhao, X. Yuan, Y. Guo, Fabrication of Z-scheme plasmonic photocatalyst Ag@AgBr/g-C_3N_4 with enhanced visible-light photocatalytic activity, *J. Hazard. Mater.* 271 (2014) 150–159.

[21] Z. Li, X. Meng, Z. Zhang, Recent development on MoS_2-based photocatalysis: A review, *J. Photochem. Photobiol. C* 35 (2018) 39–55.

[22] N. Shao, J. Wang, D. Wang, P. Corvini, Preparation of three-dimensional $Ag_3PO_4/TiO_2@MoS_2$ for enhanced visible-light photocatalytic activity and anti-photocorrosion, *Appl. Catal. B* 203 (2017) 964–978.

[23] L. Mohapatra, K. Parida, A review on the recent progress, challenges and perspective of layered double hydroxides as promising photocatalysts, *J. Mater. Chem. A* 4 (2016) 10744–10766.

[24] M. Lan, G. Fan, L. Yang, F. Li, Significantly Enhanced Visible-Light-Induced Photocatalytic Performance of Hybrid Zn–Cr Layered Double Hydroxide/Graphene Nanocomposite and the Mechanism Study, *Ind. Eng. Chem. Res.* 53 (2014) 12943–12952.

[25] G. Zhang, G. Liu, L. Wang, J.T.S. Irvine, Inorganic perovskite photocatalysts for solar energy utilization, *Chem. Soc. Rev.* 45 (2016) 5951–5984.

[26] G. Naresh, T.K. Mandal, Excellent Sun-Light-Driven Photocatalytic Activity by Aurivillius Layered Perovskites, $Bi_{5-x}La_xTi_3FeO_{15}$ (x = 1, 2), *ACS Appl. Mater. Interfaces* 6 (2014) 21000–21010.

[27] K.-i. Shimizu, S. Itoh, T. Hatamachi, T. Kodama, M. Sato, K. Toda, Photocatalytic Water Splitting on Ni-Intercalated Ruddlesden-Popper Tantalate $H_2La_{2/3}Ta_2O_7$, *Chem. Mater.* 17 (2005) 5161–5166.

[28] S. Ida, Y. Okamoto, M. Matsuka, H. Hagiwara, T. Ishihara, Preparation of Tantalum-Based Oxynitride Nanosheets by Exfoliation of a Layered Oxynitride, $CsCa_2Ta_3O_{10-x}N_y$, and Their Photocatalytic Activity, *J. Am. Chem. Soc.* 134 (2012) 15773–15782.

[29] D.W. Hwang, H.G. Kim, J.S. Lee, J. Kim, W. Li, S.H. Oh, Photocatalytic Hydrogen Production from Water over M-Doped $La_2Ti_2O_7$ (M = Cr, Fe) under Visible Light Irradiation (λ > 420 nm), *J. Phys. Chem. B* 109 (2005) 2093–2102.

[30] T.-G. Xu, C. Zhang, X. Shao, K. Wu, Y. Zhu, Monomolecular-Layer $Ba_5Ta_4O_{15}$ Nanosheets: Synthesis and Investigation of Photocatalytic Properties, *Adv. Funct. Mater.* 16 (2006) 1599–1607.

[31] R. He, D. Xu, B. Cheng, J. Yu, W. Ho, Review on nanoscale Bi-based photocatalysts, *Nanoscale Horiz.* 3 (2018) 464–504.

[32] W. Fang, W. Shangguan, A review on bismuth-based composite oxides for photocatalytic hydrogen generation, *Int. J. Hydrogen Energy* 44 (2019) 895–912.

[33] N. Zhang, R. Ciriminna, M. Pagliaro, Y.-J. Xu, Nanochemistry-derived Bi_2WO_6 nanostructures: towards production of sustainable chemicals and fuels induced by visible light, Chem. *Soc. Rev.* 43 (2014) 5276–5287.

[34] K. Akihiko, H. Satoshi, H_2 or O_2 Evolution from Aqueous Solutions on Layered Oxide Photocatalysts Consisting of Bi^{3+} with $6s^2$ Configuration and d^0 Transition Metal Ions, *Chem. Lett.* 28 (1999) 1103–1104.

[35] J. Tang, Z. Zou, J. Ye, Photocatalytic decomposition of organic contaminants by Bi_2WO_6 under visible light irradiation, *Catal. Lett.* 92 (2004) 53–56.

[36] C. Zhang, Y. Zhu, Synthesis of Square Bi_2WO_6 Nanoplates as High-Activity Visible-Light-Driven Photocatalysts, *Chem. Mater.* 17 (2005) 3537–3545.

[37] M. Shang, W. Wang, J. Ren, S. Sun, L. Wang, L. Zhang, A practical visible-light-driven Bi_2WO_6 nanofibrous mat prepared by electrospinning, *J. Mater. Chem.* 19 (2009) 6213–6218.

[38] L. Zhang, W. Wang, Z. Chen, L. Zhou, H. Xu, W. Zhu, Fabrication of flower-like Bi_2WO_6 superstructures as high performance visible-light driven photocatalysts, *J. Mater. Chem.* 17 (2007) 2526–2532.

[39] M. Shang, W. Wang, H. Xu, New Bi_2WO_6 Nanocages with High Visible-Light-Driven Photocatalytic Activities Prepared in Refluxing EG, *Cryst. Growth Des.* 9 (2009) 991–996.

[40] Y. Fu, C. Chang, P. Chen, X. Chu, L. Zhu, Enhanced photocatalytic performance of boron doped Bi_2WO_6 nanosheets under simulated solar light irradiation, *J. Hazard. Mater.* 254–255 (2013) 185–192.

[41] G. Colón, S. Murcia López, M.C. Hidalgo, J.A. Navío, Sunlight highly photoactive Bi_2WO_6–TiO_2 heterostructuresfor rhodamine B degradation, *Chem. Commun.* 46 (2010) 4809–4811.

[42] M. Amiri, K. Dashtian, M. Ghaedi, S. Moslehb, R. Jannesar, Bi_2WO_6/Ag_3PO_4–Ag Z-scheme heterojunction as a new plasmonic visible-light-driven photocatalyst: performance evaluation and mechanism study, *New J. Chem.* 43 (2019) 1275–1284.

[43] Z. Sun, J. Guo, S. Zhu, L. Mao, J. Ma, D. Zhang, A high-performance Bi_2WO_6–graphene photocatalyst for visible light-induced H_2 and O_2 generation, *Nanoscale* 6 (2014) 2186–2193.

[44] E. Gao, W. Wang, M. Shang, J. Xu, Synthesis and enhanced photocatalytic performance of graphene-Bi_2WO_6 composite, *Phys. Chem. Chem. Phys.* 13 (2011) 2887–2893.

[45] P. Raizada, J. Kumari, P. Shandilya, R. Dhiman, V.P. Singh, P. Singh, Magnetically retrievable Bi_2WO_6/Fe_3O_4 immobilized on graphene sand composite for investigation of photocatalytic mineralization of oxytetracycline and ampicillin, *Process Safety Environ. Protec.* 106 (2017) 104–116.

CHAPTER 2: One-step hydrothermal synthesis and photocatalytic performance of $ZnWO_4/Bi_2WO_6$ composite photocatalysts for efficient degradation of acetaldehyde under UV light irradiation

2.1. Introduction

Semiconductors exhibit several properties that are strongly sensitive to their structures, and are considered to be important materials for environmental applications, such as air purification, water disinfection, hazardous waste remediation, and water purification [1,2]. Among them, metal tungstates-based semiconductors have been intensively investigated as potential candidates for photocatalytic processes. As a member of the metal tungstate family, zinc tungstate ($ZnWO_4$) crystallizes in the monoclinic wolframite structure and has a high application potential in various fields as an X-ray, γ-scintillator, microwave system, solid-state laser host, gas and humidity sensors, acoustic and optical fibers, and magnetic material, due to characteristics, such as high chemical stability, high average refractive index, high X-ray absorption coefficient, high light yield, short decay time, and long afterglow to luminescence[3,4].There have been a number of recent reports concerning improvement of the optical properties of $ZnWO_4$ by the introduction of rare earth ions [5–8]; excitation of the tungstate group may effectively transfer energy to the rare earth element and become potential phosphors.

The molecular and electronic versatility, reactivity, and stability of $ZnWO_4$ have also made it a candidate environmental material for the photodegradation of organic water pollutants and water splitting [9–12]. The difference in the photocatalytic activities of $ZnWO_4$ with different morphologies, including nanorods [9], porous films [11], and nanoparticles [13], is mainly due to differences in crystallinity and specific surface area. Moreover, the photocatalytic activity of $ZnWO_4$ could also be influenced by the crystal growth orientation [14], nanorods aspect ratio [15], OH^- defects [16], ion doping [17–19], and the porous structure [11]. However, $ZnWO_4$ with a wide band gap of 3.75 eV [20] exhibits low photocatalytic activity, but the effective combination of photon absorption, bulk diffusion, and surface transfer of photoinduced charge-carriers could lead to enhancement of its photocatalytic activity.

Bismuth tungstate (Bi_2WO_6) is one of the simplest members of the Aurivillius oxide family of layered perovskites with the general formula $Bi_2A_{n-1}B_nO_{3n+3}$ (*A* = Ca, Sr, Ba, Pb, Na, K; *B* = Ti, Nb, Ta, Mo, W, Fe; and *n* = number of perovskite-like layers $(A_{n-1}B_nO_{3n+1})^{2-}$), which are structurally composed of alternating perovskite-like and fluorite-like blocks. Bi_2WO_6 exhibits several important physical properties, such as ferroelectric piezoelectricity, pyroelectricity, catalytic behavior, oxide anion conductivity, nonlinear dielectric susceptibility, and luminescence. Bi_2WO_6, which has a band gap of 2.80 eV, has excellent photocatalytic activity for O_2 evolution and for the mineralization of $CHCl_3$ and CH_3CHO into CO_2 under visible light irradiation [21,22].

Recently, composite photocatalyst have received much attention due to enhanced photocatalytic activity that results from the formation of heterojunction structures. The combination of two semiconductors in contact that have different redox energy levels of their corresponding conduction and valence bands can be considered to be one of the most promising methods to improve charge separation, increase the lifetime of charge carriers, and enhance the efficiency of the interfacial charge transfer to the adsorbed substrate [23]. To date, there has been much effort to enhance the photodegradation efficiency of Bi_2WO_6 by coupling with other semiconductors, such as TiO_2 [24], ZnO [25], Bi_2O_3 [26], Co_2O_3 [27], Bi_2S_3 [28], graphene [29], g-C_3N_4 [30], BiOI [31], and $CeVO_4$ [32]. Very recently, the $Bi_2WO_6/ZnWO_4$ composite photocatalyst, which is composed of Bi_2WO_6 nanoparticles grown on primary $ZnWO_4$ nanorods, was obtained by a simple hydrothermal method [33]. Although promising results have been obtained with this composite nanocatalyst, the efficiency is limited due to the rapid recombination of photogenerated charge carriers and the back reaction of intermediate chemical species [34]. Nanostructured powders do not support internal space charges; therefore, the photogenerated electrons and holes are not efficiently separated [35]. Another composite photocatalyst was also synthesized using a two-step hydrothermal method and the photocatalytic activity was evaluated for the degradation of Rhodamine B under UV light irradiation [36].

We propose a one-step strategy for the preparation of the $ZnWO_4/Bi_2WO_6$ composite photocatalyst by hydrothermal processing, and the photocatalytic activity of the resultant composite photocatalyst is evaluated for the degradation of acetaldehyde (AcH) under UV light

irradiation. The $ZnWO_4/Bi_2WO_6$ ratio in the composite photocatalyst was also varied to determine the optimal composition of the photocatalyst for higher photocatalytic efficiency under UV light irradiation.

2.2. Experimental

2.2.1. Synthesis

The $ZnWO_4/Bi_2WO_6$ composite photocatalyst was prepared using a one-step hydrothermal method. The experimental procedures were as follows: first, 2.5 mmol of $Zn(NO_3)_2 \cdot 6H_2O$ (Wako Pure Chemical Industries, Ltd.) was dissolved in 15 mL of deionized water (Millipore Milli-Q Plus purification system, 18.2 M Ω·cm), 2.5 mmol of $Bi(NO_3)_3 \cdot 5H_2O$ (Wako Pure Chemical Industries, Ltd.) was dissolved in 15 mL of diluted nitric acid, and 2.5 mmol of Na_2WO_4 (Wako Pure Chemical Industries, Ltd.) was dissolved in 15 mL of deionized water. 15 mL of bismuth nitrate solution with different mole percentages (0-30 mol%) was introduced into the zinc nitrate solution, and then 15 mL of sodium tungstate solution was added under vigorous stirring. The pH of the suspension was adjusted by the addition of aqueous ammonia (Wako Pure Chemical Industries, Ltd.) to determine the optimal synthesis conditions. After being well homogenized for 30 min, the white-colored suspension obtained was transferred into a 40 mL Teflon-lined stainless steel autoclave. The autoclave was sealed and maintained at 160°C for 12 h. After hydrothermal treatment, the autoclave was allowed to cool to room temperature. The resulting precipitate was collected by centrifugation, washed with deionized water several times and dried at 80°C for 8 h.

2.2.2. Characterization

The crystalline phases formed in the as-synthesized composite photocatalyst samples were identified by X-ray powder diffraction (XRD) using an RINT-2100 diffractometer (Rigaku) with monochromated Cu Kα radiation (λ = 1.5405 Å) at 40 kV and 40 mA. The XRD patterns of the samples were measured at a scanning rate of $2° \cdot min^{-1}$ in the 2θ range of 10-70°. The crystalline phases present in the as-synthesized composite photocatalysts were also confirmed using a T64000 Raman spectroscopy (Horiba Jobin Yvon S.A.S.) with an Ar laser (514.5 nm) operated at 50 mW. The morphologies and particle sizes of the as-synthesized composite photocatalysts were examined using an S-4500 ultra-high-resolution scanning electron microscope (SEM) (Hitachi), operated at an accelerating voltage of 15 kV. The SEM was also

equipped with an X-ray energy dispersive spectroscopy (EDS) attachment for elemental analysis. Transmission electron microscopy (TEM) observations were performed on powder samples using a JEM-2010UHR electron microscope (JEOL), operated at an accelerating voltage of 200 kV to distinguish the crystal structures and particle sizes. For TEM observation, a powder sample was dispersed in ethanol under ultrasonication, and a small amount of the suspension was dropped on the holey carbon grid. The UV-vis diffuse reflectance spectra of the composite photocatalysts were recorded at room temperature with a Lambda 950 UV/vis/NIR spectrophotometer (Perkin-Elmer) in the wavelength range of 200-600 nm, using $BaSO_4$ as a reference.

2.2.3. Photocatalytic activity test

Acetaldehyde (AcH), which is a typical indoor air pollutant, was selected as a probe molecule to evaluate the photocatalytic activity of the as-synthesized composite photocatalyst under UV light irradiation. The photodegradation of AcH was conducted in a batch-type reactor over the as-synthesized composite photocatalyst at room temperature (25°C). The photocatalyst (50 mg) was placed in the 500 mL Pyrex® glass reaction vessel. Pure air (Taiyo Nippon Sanso Corp.) was blown through the reaction vessel at room temperature to remove any air contaminants. A certain amount of AcH was then introduced into the reaction vessel using a 2 mL Pressure-Lok® glass syringe until the concentration of AcH in the reactor reached about 250 ppm. After equilibration of adsorption onto the composite photocatalyst in the dark for 24 h, the reactor was placed under an FL10BLB black-light lamps (Toshiba) with a wavelength range of 290-420 nm with a peak at 352 nm. UV light was emitted with an irradiance of ca. 0.4 $mW \cdot cm^{-2}$, which was measured with a UV 340 UV light meter (Lutron Electronic Enterprise Co., Ltd.). The decrease and increase in the respective concentrations of AcH and CO_2 were monitored using a GC-2014 gas chromatograph (Shimadzu) equipped with a 2 m Porapak-Q column, methanizer and a flame ionization detector, with N_2 employed as the carrier gas.

2.3. Results and Discussion

2.3.1. Effect of the pH of synthesis solution

The hydrothermal method is mainly based on low-temperature solution processes where the pH of the synthesis solution (or suspension) is one of the key factors that influences the

precipitation of a desired phase. Therefore, preliminary experiments were first performed with various hydrothermal conditions (different pH) for synthesis of the $ZnWO_4/Bi_2WO_6$ composite photocatalyst.

The effect of the synthesis solution pH on the formation of the $ZnWO_4/Bi_2WO_6$ composite photocatalyst was studied using XRD. Figure 2.1 shows the XRD patterns of powders hydrothermally synthesized at 160°C for 12 h with 10 mol% Bi^{3+} at pH = 3-9. When the pH of the synthesis suspension was adjusted to 3, the as-synthesized powders predominantly consisted of two crystalline phases: $ZnWO_4$ (ICDD PDF# 15-0774) with the monoclinic wolframite structure and WO_3 (ICDD PDF# 33-1387) with the hexagonal structure, which is an undesirable phase in the composite photocatalyst. As the pH of synthesis suspension was increased to 5, the WO_3 phase completely disappeared, while the orthorhombic Bi_2WO_6 (ICDD PDF# 39-0256) phase began to form, which indicated that a synthesis suspension pH of 3 was more favorable for the formation of the WO_3 phase rather than the Bi_2WO_6 phase. All reflections in the XRD pattern of the powders that were hydrothermally synthesized at pH = 7 could be readily assigned to the $ZnWO_4$ and Bi_2WO_6 phases. No XRD reflections corresponding to impurity phases were detected in these composite photocatalysts. Further increase in the pH of the synthesis suspension to 9 led to the simultaneous precipitation of $ZnWO_4$ and Bi_2WO_6 as major phases, with the inclusion of another undesired phase, ZnO (ICDD PDF# 65-3411). Comparison of all the XRD data for the products hydrothermally synthesized at different pH indicated that the only pH = 7 was favorable for the formation of both the $ZnWO_4$ and Bi_2WO_6 phases without any impurity phases under the current experimental conditions.

Figure 2.2 shows the microstructural features of powders hydrothermally synthesized at 160°C for 12 h with 10 mol% Bi^{3+} at pH = 3-9. The powders hydrothermally synthesized at pH = 3 have large irregular particles mixed with submicron rod- and plate-like particles. The

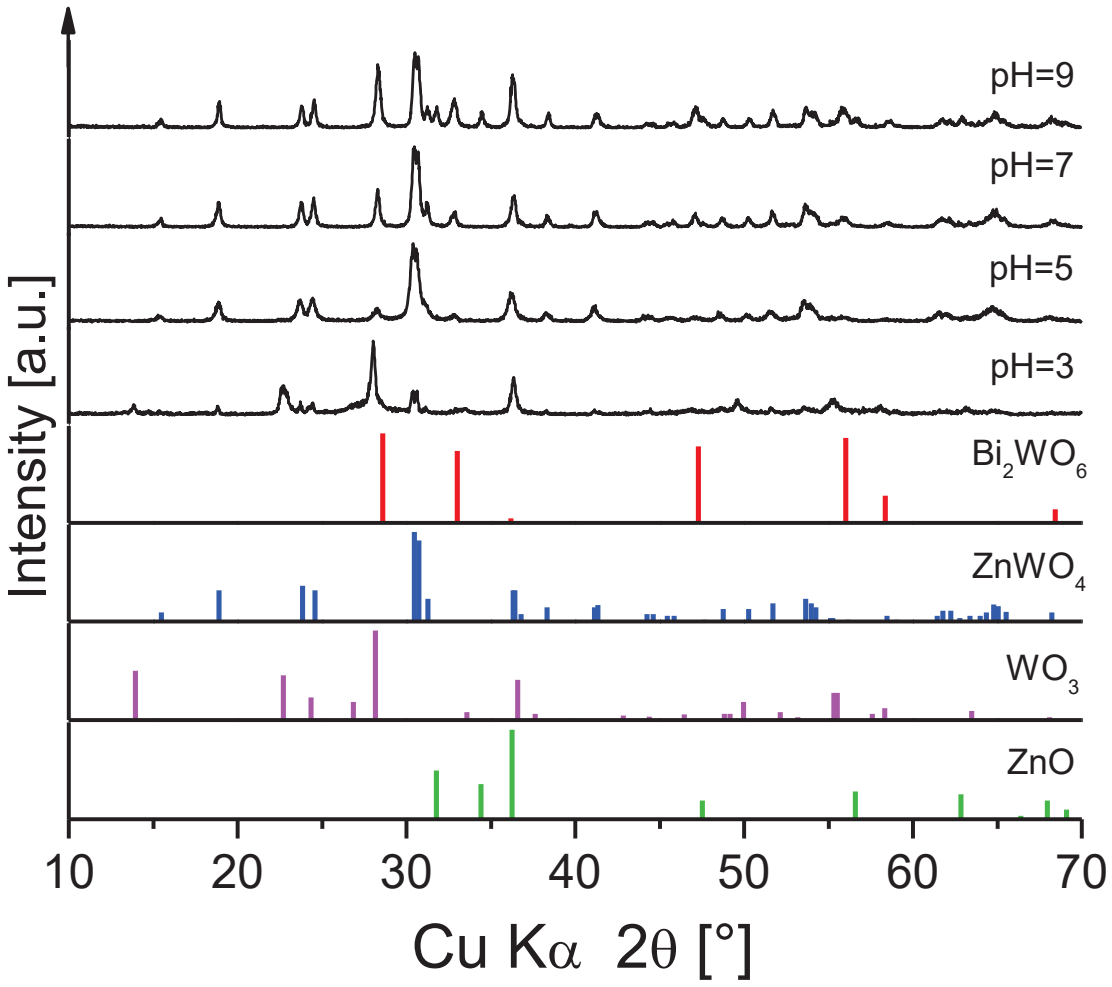

Figure 2.1. XRD patterns of the $ZnWO_4/Bi_2WO_6$ composite photocatalysts hydrothermally synthesized with 10 mol% Bi^{3+} at 160°C for 12 h with various pH of synthesizing suspensions.

EDS results (not shown here) suggest that the large irregular particles are $ZnWO_4$, whereas the rod- and plate-like particles are representative of the WO_3 phase. The powders hydrothermally synthesized at pH = 5 are mostly agglomerated quasi-spheres constructed from the aggregation of $ZnWO_4$ nanorods. A few plate-like particles are also visible, which indicates the presence of the Bi_2WO_6 phase. These results are consistent with the XRD data shown in Figure 2.1. The hydrothermal synthesis at pH = 7 has a pronounced effect on the morphology of the resultant powders; the majority of particles shown in Figure 2.2 are submicron-sized $ZnWO_4$ rod-like particles, and the number of plate-like Bi_2WO_6 particles has also increased with the increase in the pH. With further increase of the synthesis suspension pH to 9, the sizes of the rod- and plate-like particles are decreased, along with the formation of small irregular particles of ZnO. The SEM results demonstrate that the morphology of the composite photocatalyst can easily be tailored by adjustment of the pH. We have also investigated the effect of the synthesis

suspension pH on the morphologies of $ZnWO_4$ [37], $YVO_4:Eu^{3+}$ [38,39], and PbI_2 [40] under hydrothermal conditions.

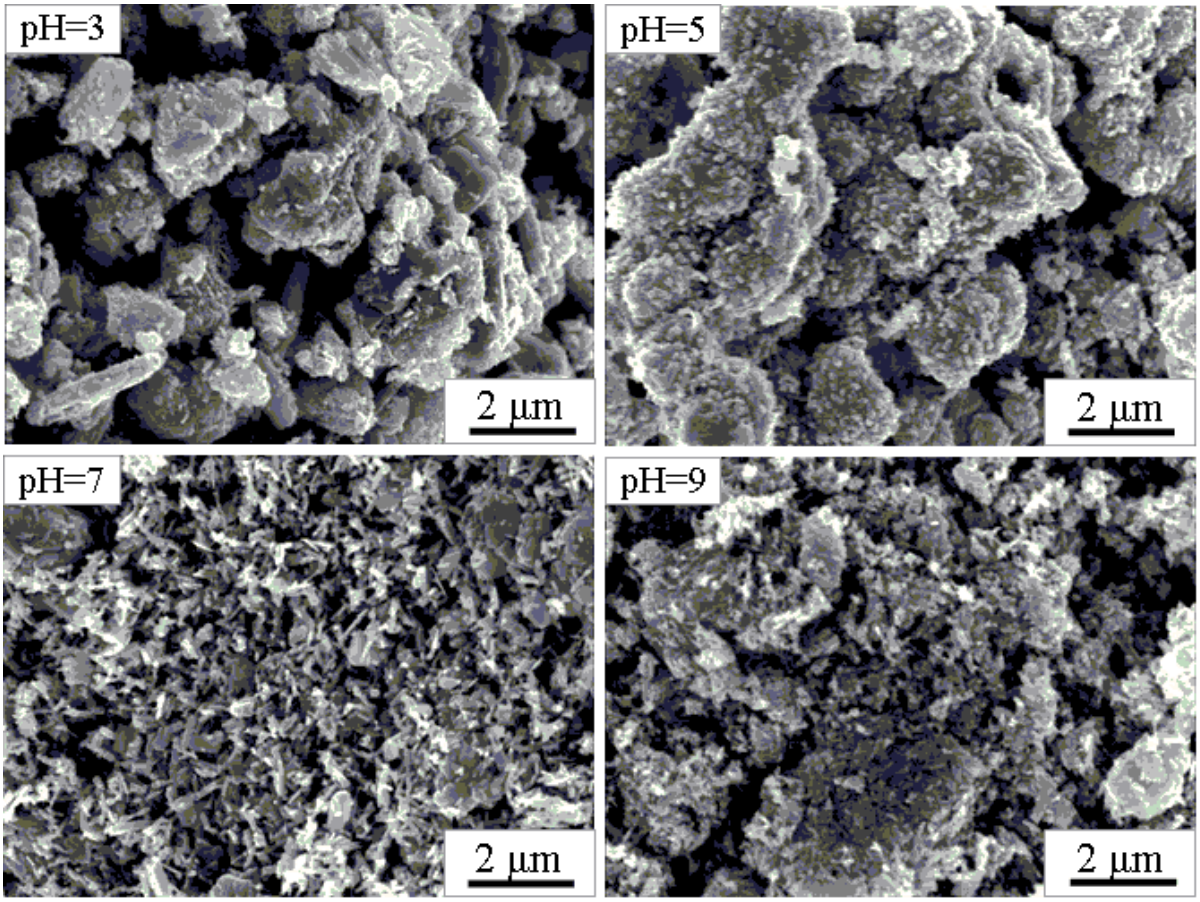

Figure 2.2. SEM micrographs of the $ZnWO_4/Bi_2WO_6$ composite photocatalysts hydrothermally synthesized with 10 mol% Bi^{3+} at 160°C for 12 h with various pH of synthesizing suspension.

2.3.2. Effect of Bi^{3+} ion concentration

The Bi^{3+} ion concentration was varied from 0 to 30 mol% in the synthesis suspension to obtain various mole fractions of Bi_2WO_6 in the composite photocatalyst and investigate the contribution of Bi_2WO_6 to the degradation of AcH under UV light irradiation. Figure 2.3 shows the XRD patterns of composite photocatalyst hydrothermally synthesized at 160°C for 12 h with various Bi^{3+} ion concentrations at pH = 7. As expected, the sample hydrothermally synthesized without Bi^{3+} ions contains only the $ZnWO_4$ phase. In contrast, the introduction of 5-30 mol% Bi^{3+}

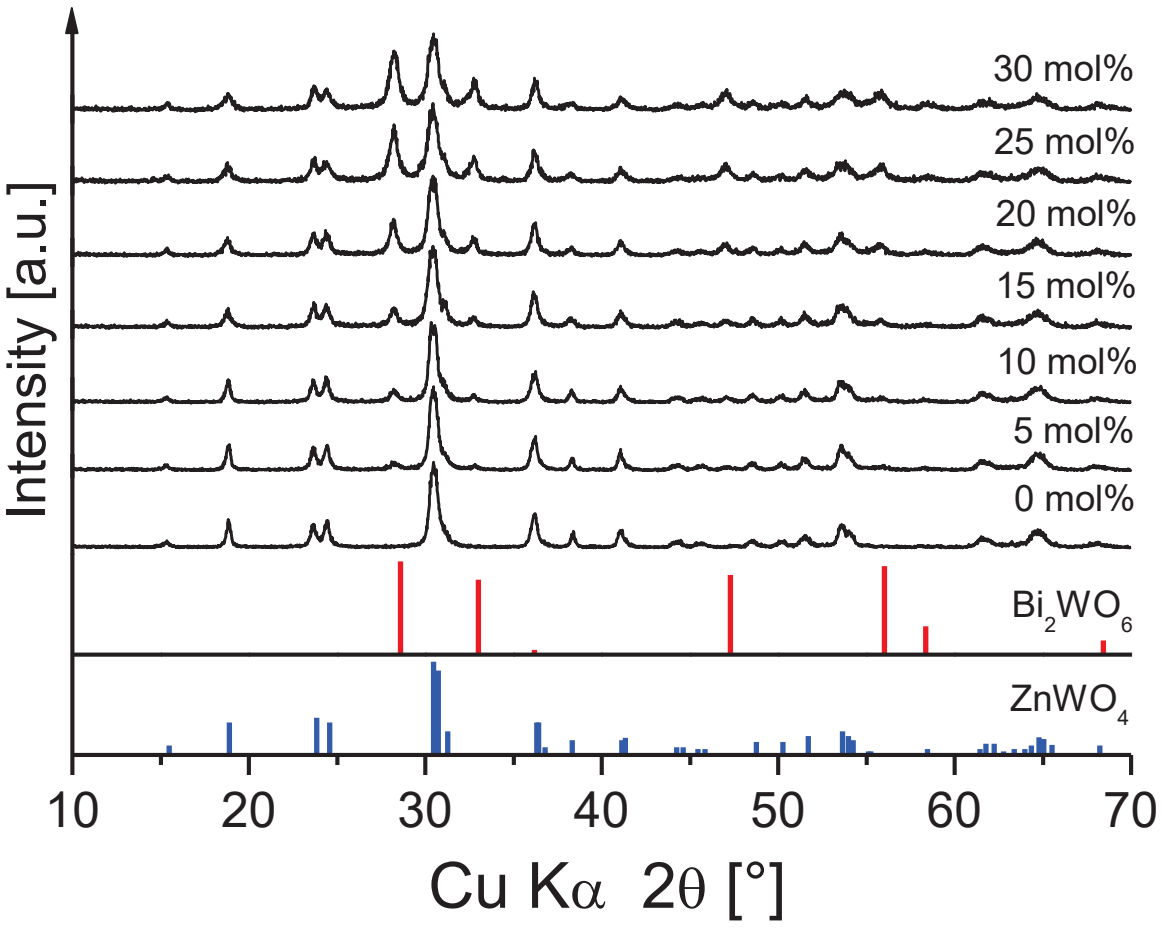

Figure 2.3. XRD patterns of the $ZnWO_4/Bi_2WO_6$ composite photocatalysts hydrothermally synthesized at 160°C for 12 h with various Bi^{3+} ion concentrations at pH = 7.

into the synthesis suspension resulted in composite photocatalysts composed of both the $ZnWO_4$ and Bi_2WO_6 phases. No XRD reflections belonging to secondary phases were evident, even in the composite photocatalyst synthesized with the highest Bi^{3+} ion concentration (30 mol%). The intensity of the reflections corresponding to the Bi_2WO_6 phase gradually increased with the Bi^{3+} ion concentration. It should be noted that no peak shift was observed in the XRD patterns for both phases, which provides evidence that the current experimental conditions were not adequate for an ion doping process. This was also confirmed by comparison of the calculated lattice parameters for the phases present in the samples. Furthermore, the $ZnWO_4$ and Bi_2WO_6 phases in the composite photocatalyst were quantitatively analyzed by the Rietveld method using the obtained XRD patterns. The percentage of Bi_2WO_6 phase in the composite photocatalyst increases with the increase in the Bi^{3+} ion concentration as follows: 0% (0 mol%) < 6% (5 mol%) < 9% (10 mol%) < 12% (15 mol%) < 22% (20 mol%) < 29% (25

mol%) < 34% (30 mol%). The $ZnWO_4$ phase still prevails as the predominant fraction in the composite photocatalyst. Thus, the direct relationship between the Bi^{3+} ion concentration added and the mole fraction of Bi_2WO_6 phase present in the composite photocatalyst was verified.

Figure 2.4 shows the SEM micrographs of samples hydrothermally synthesized at 160°C for 12 h with various Bi^{3+} ion concentrations at pH = 7. The pure $ZnWO_4$ powders without Bi^{3+} have larger irregular particles formed by the aggregation of nano- and submicron-sized particles. With the addition of 5 mol% Bi^{3+} to the synthesis system, the $ZnWO_4/Bi_2WO_6$ composite photocatalyst was obtained with irregular morphology, and the particle size was significantly diminished in comparison to that of pure $ZnWO_4$. The morphologies of the $ZnWO_4/Bi_2WO_6$ composite photocatalysts obtained with 10-30 mol% Bi^{3+}, shown in Figure 2.4, are principally comprised of three types of distinctive particles: large micrometer-sized quasi-spheres, and nanometer-sized rice- and plate-like particles. These particles become larger and more distinct with the increase in Bi^{3+} from 10 to 30 mol%, which suggests that the incorporation of Bi^{3+} ions is essential for alteration of the overall morphology of the composite photocatalyst.

To discriminate the particles and gain insight into the crystal structures, TEM analysis was conducted on the $ZnWO_4/Bi_2WO_6$ composite photocatalyst that was hydrothermally synthesized at 160°C for 12 h with 30 mol% Bi^{3+} at pH = 7. Figure 2.5 shows the TEM micrographs (a, c, d), EDS spectra (b), selected area electron diffraction (SAED) patterns (insets), and HRTEM micrographs (e, f) of the $ZnWO_4/Bi_2WO_6$ composite photocatalyst. The TEM image of the composite photocatalyst in Figure 2.5a indicates the coexistence of three different particles in the composite photocatalyst, which is consistent with the SEM observations. The elemental analysis results of these three different particles using EDS are shown in Figure 2.5b. The quasi-spherical particles (0.8-1.3 μm) correspond to the $ZnWO_4$ phase and the rice (400-600 nm long and 80-150 nm wide) - and plate (300-500 nm diameters)-like particles to the Bi_2WO_6 phase. Figures 2.5c and d show that a number of rice- and plate-like Bi_2WO_6 particles are attached to the surface of the quasi-spherical $ZnWO_4$ particles, and the rice-like Bi_2WO_6 particles are constructed with a significant amount of tiny nanorods. Separately located particles were most probably detached from the composite photocatalyst by strong utrasonication used during the TEM sample preparation.

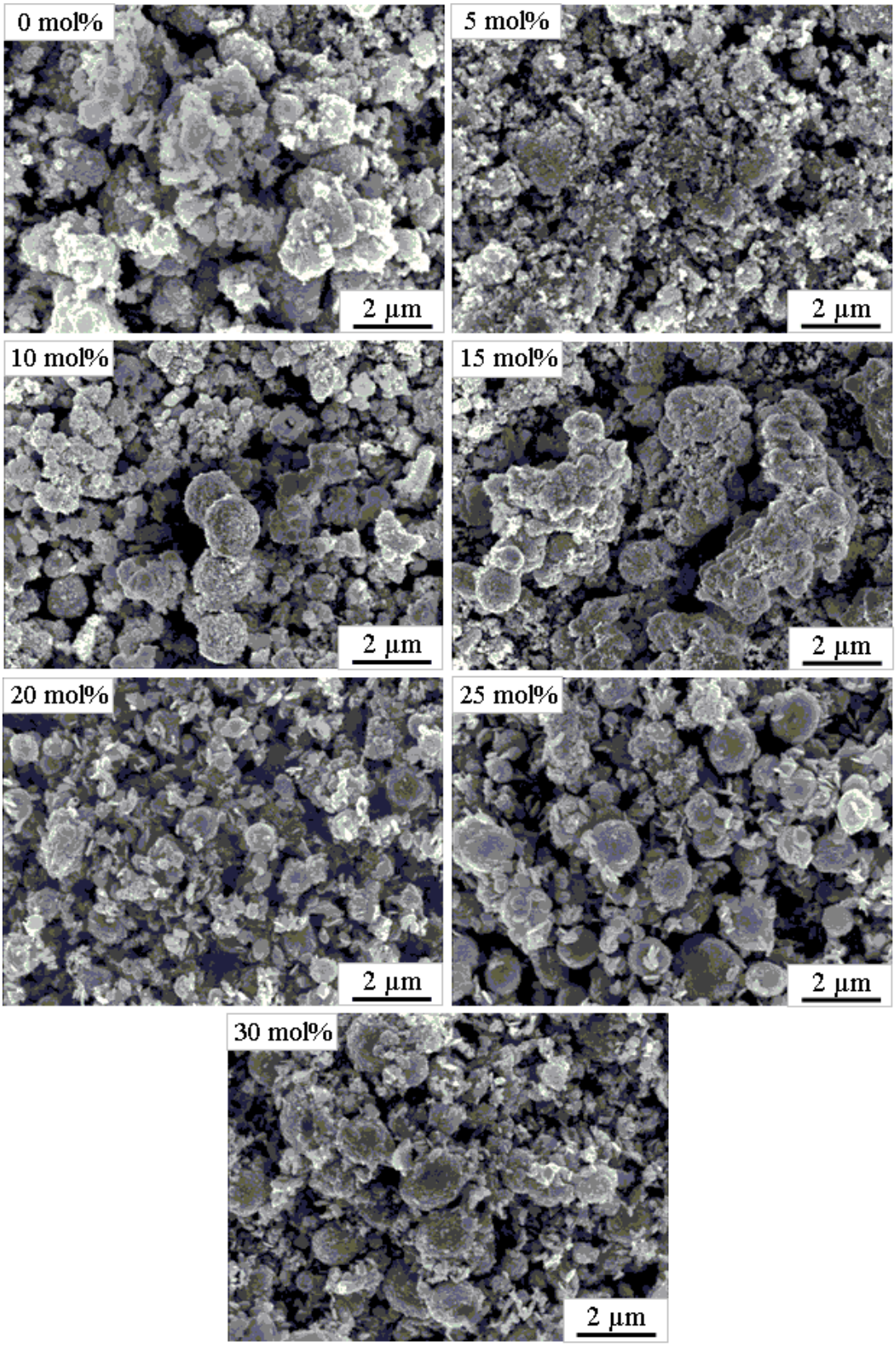

Figure 2.4. SEM micrographs of the $ZnWO_4/Bi_2WO_6$ composite photocatalysts hydrothermally synthesized at 160°C for 12 h with various Bi^{3+} ion concentrations at pH = 7.

The ring-like SAED patterns shown in the insets of Figures 2.5c and d reveal the overall polycrystallinity of the quasi-spherical $ZnWO_4$ particles and the rice-like Bi_2WO_6 particles. The HRTEM images shown in Figures 2.5e and f confirm uniform lattice fringes with an interval of 0.362 nm that correspond to the *d* spacing between adjacent (110) crystallographic planes of monoclinic $ZnWO_4$, while the lattice fringes of d = 0.320 are consistent with the (131) crystallographic planes of orthorhombic Bi_2WO_6. The SEM and TEM observations indicate that the as-synthesized composite photocatalyst has a contacting junction structure between $ZnWO_4$ and Bi_2WO_6 crystals.

Although time-dependent experiments were not performed in this study, based on previous reports, we briefly present the formation processes for the $ZnWO_4/Bi_2WO_6$ composite photocatalyst, without a strong intention to provide an exact mechanism. It is supposed that in the competitive precipitation process, the formation of tiny crystalline nuclei of $ZnWO_4$ in the supersaturated medium occurs first. While the crystal growth process of $ZnWO_4$ probably occurs at the expense of smaller crystals, according to the Gibbs-Thompson theory, tiny crystalline nuclei of Bi_2WO_6 begin to form from Bi^{3+} and remaining $[WO_4]^{2-}$ ions. Under hydrothermal treatment, $ZnWO_4$ and Bi_2WO_6 nanorods form from tiny nuclei, due to their anisotropic nature, and are further self-assembled into quasi-spheres and rice- and plate-like particles, respectively, by an oriented attachment process, of which the driving force is a reduction of the surface energy of crystal planes [41,42]. Consequently, a number of rice- and plate-like particles of Bi_2WO_6 are attached to the surface of quasi-spherical particles of $ZnWO_4$, where a moderate junction structure is formed.

Figure 2.6 shows the Raman spectra of $ZnWO_4/Bi_2WO_6$ composite photocatalysts hydrothermally synthesized at 160°C for 12 h with various Bi^{3+} ion concentrations at pH = 7, including that for pure Bi_2WO_6. The space groups of $ZnWO_4$ and Bi_2WO_6 are $P2/c = C_{2h}^4$ and $Pca2_1 = C_{2v}^5$, respectively. Group theory analysis for wolframite-type $ZnWO_4$ predicts 36 lattice modes, of which 18 even vibrations ($8A_g+10B_g$) are Raman active [43]. The Raman peaks at approximately 126, 148, 166, 191, 198, 270, 277, 316, 343, 356, 408, 516, 550, 680, 710 and 787 cm^{-1} are assignable to the internal vibrations of the WO_6 octahedra of $ZnWO_4$.

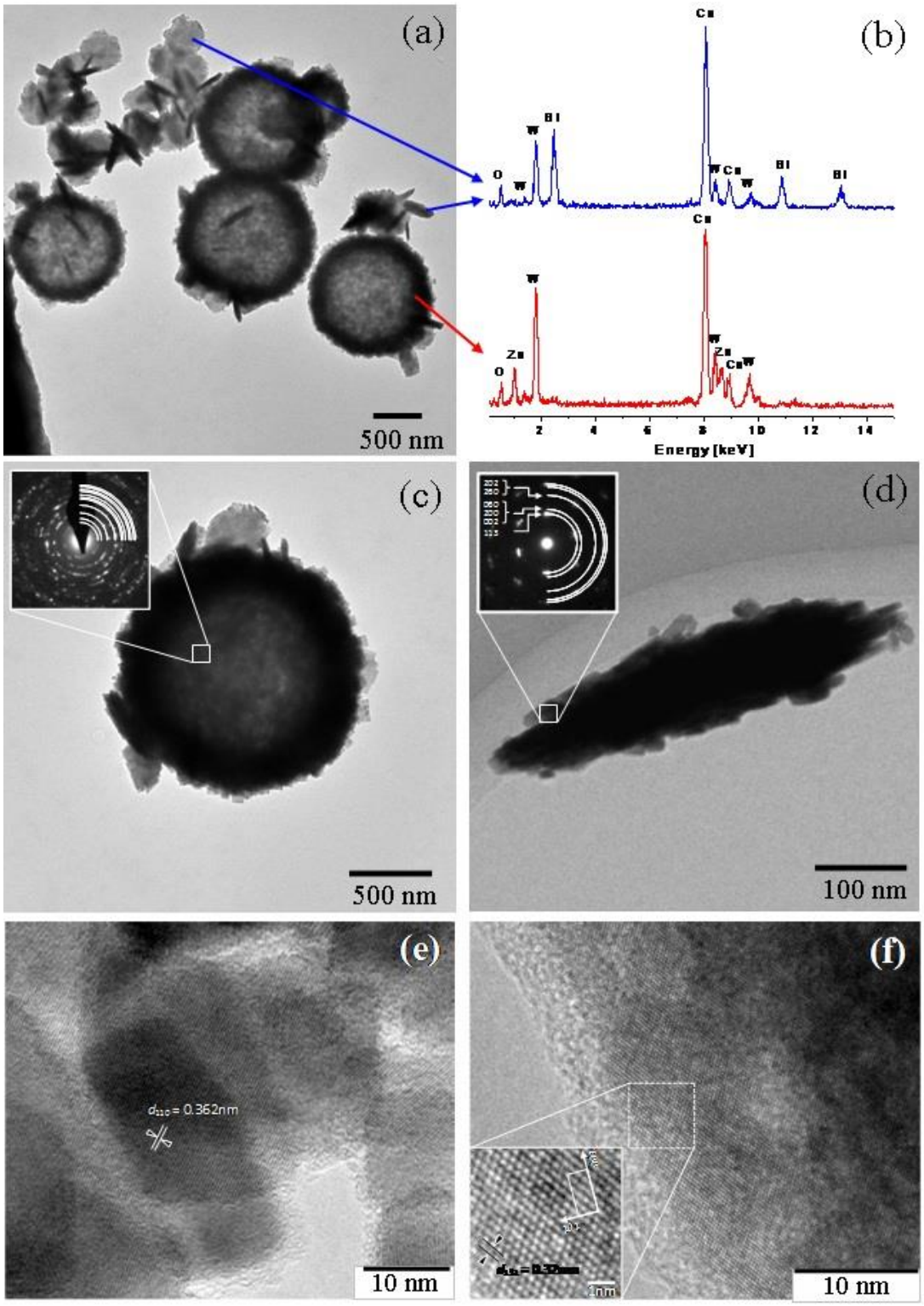

Figure 2.5. TEM micrographs (a, c, d), EDS spectra (b), SAED patterns (insets), and HRTEM micrographs (e, f) of the $ZnWO_4/Bi_2WO_6$ composite photocatalyst hydrothermally synthesized at 160°C for 12 h with 30 mol% Bi^{3+} at pH = 7.

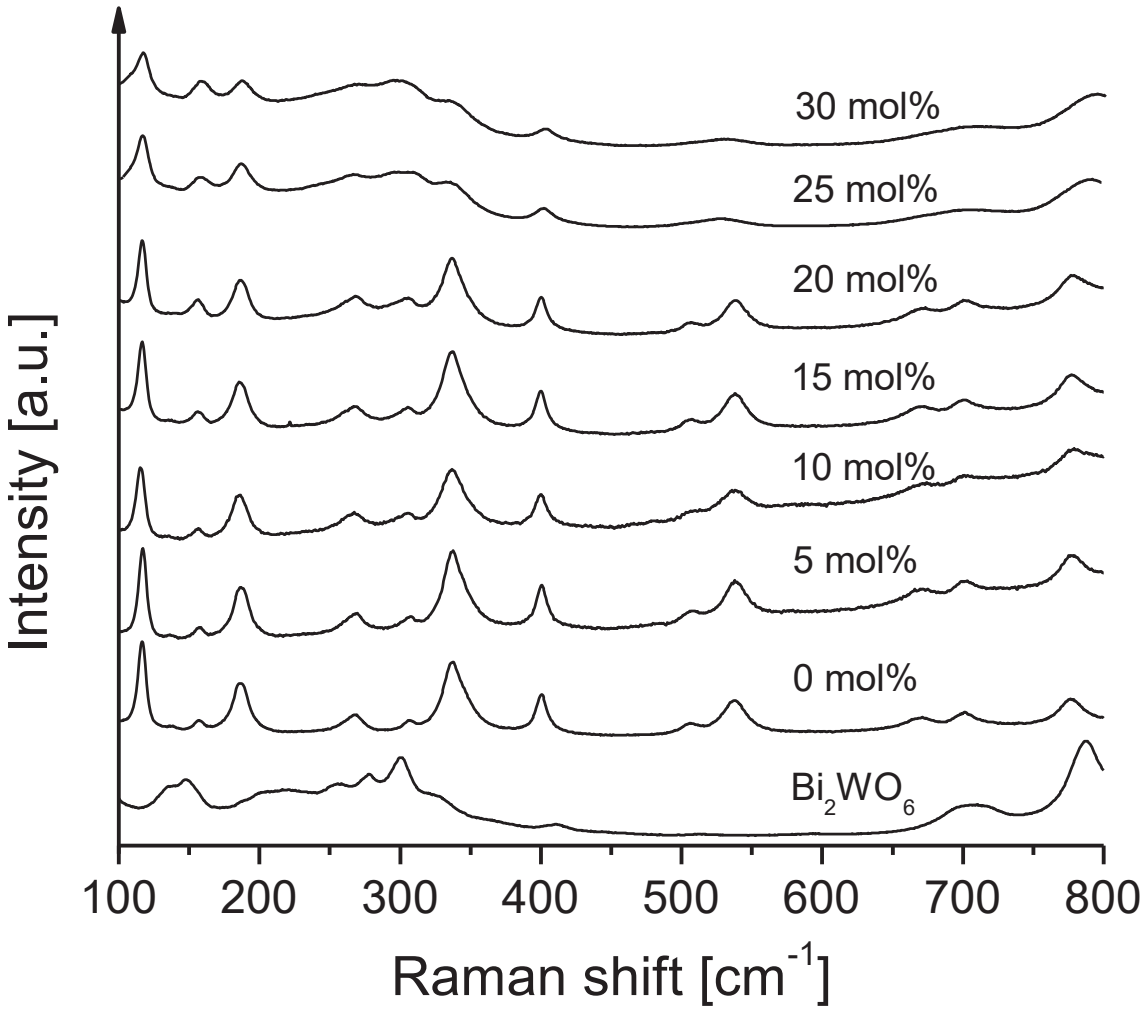

Figure 2.6. Raman spectra of the $ZnWO_4/Bi_2WO_6$ composite photocatalysts hydrothermally synthesized at 160°C for 12 h with various Bi^{3+} ion concentrations and pH = 7.

Note that two Raman peaks at 93 and 908 cm^{-1} are not shown here. The Raman spectrum of pure Bi_2WO_6 with the orthorhombic *Pbca*(61) space group shown in Figure 2.6 is similar to that of the orthorhombic $Pca2_1$ space group [44]; therefore, it is considered that the Raman peaks of the *Pbca*(61) phase can be assigned to those modes of the $Pca2_1$ phase. The number of optic modes for the $Pca2_1$ phase is $26A_1 + 27A_2 + 26B_1 + 26B_2$. The A_2 modes are Raman active and the A_1, B_1, and B_2 modes are both IR and Raman active [45]. From the Raman spectra of composite photocatalyst and Bi_2WO_6, the Raman peaks at 788 and 703 cm^{-1} can be assigned to the symmetric and asymmetric stretching modes of WO_6 octahedra that involve motions of the apical and equatorial oxygen atoms perpendicular to and within layers, respectively. The Raman peaks at 412, 300, 278, 256, 215 and 187 cm^{-1} can be attributed to

the bending modes of the WO_6 octahedra and the stretching and bending modes of BiO_6 polyhedra. The Raman peaks at 140 and 147 cm^{-1} may be assigned to the translations of the tungsten and bismuth ions [44].

As the Bi^{3+} ion concentration in the synthesis suspension increases, the intensity of the Raman modes corresponding to the monoclinic $ZnWO_4$ phase is decreased. In addition, all the Raman spectra we carefully examined and no considerable shift of the Raman peaks of the $ZnWO_4$ and Bi_2WO_6 phases was confirmed. The overall intensities of the Raman spectra for the composite photocatalysts were significantly enhanced. The enhancement in the intensities of the Raman spectra was primarily postulated by Chen et al. [46] on the basis of two theories: electromagnetic, which relies upon the excitation of localized surface plasmons, and chemical, which rationalizes the effect through the formation of charge-transfer complexes.

2.3.3. UV–vis diffuse reflectance spectra

Figure 2.7 shows the UV–vis diffuse reflectance spectra of $ZnWO_4/Bi_2WO_6$ composite photocatalysts hydrothermally synthesized at 160°C for 12 h with various Bi^{3+} ion concentrations and pH = 7. The light absorbance of pure $ZnWO_4$ lies in the UV region with an absorption edge of about 355 nm, and the band gap is estimated to be about 3.8 eV. With the introduction of Bi^{3+} ions in the synthesis suspension, $ZnWO_4$ becomes associated with Bi_2WO_6 in the composite photocatalyst. Therefore, compared with pure $ZnWO_4$, a gradual increase in the Bi_2WO_6 content in the composite photocatalyst results in a monotonic shift of the absorption edge from about 355 nm to longer wavelength up to about 450 nm due to the intrinsic transitions of both semiconductors. This also supports the formation of a junction structure between $ZnWO_4$ and Bi_2WO_6 in the composite photocatalyst. The band gaps of the $ZnWO_4/Bi_2WO_6$ composite photocatalyst range from about 3.08 to about 2.90 eV, in accordance with the Bi_2WO_6 content. Therefore, considering the absorption edge of the composite photocatalyst, it seems reasonable that the as-synthesized composite photocatalyst can be excited under UV light irradiation, which would result in higher photocatalytic activity.

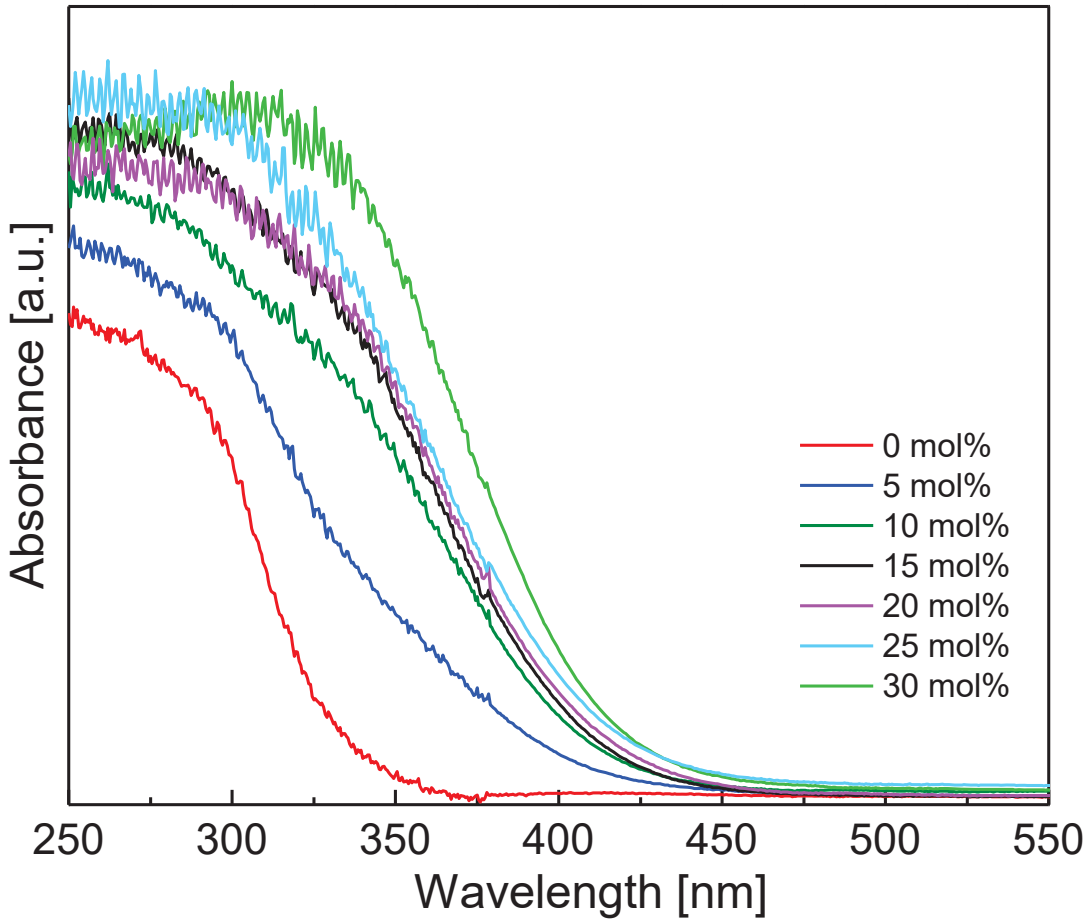

Figure 2.7. UV-vis diffuse reflectance spectra of the $ZnWO_4/Bi_2WO_6$ composite photocatalysts hydrothermally synthesized at 160°C for 12 h with various Bi^{3+} ion concentrations at pH = 7.

2.3.4. Photocatalytic activity

The photocatalytic activity of the as-synthesized composite photocatalysts for the photodegradation of AcH under UV light irradiation was evaluated and compared with pure $ZnWO_4$, Bi_2WO_6, and a mechanical mixture of $ZnWO_4/Bi_2WO_6$. AcH is known as a key indoor air pollutant and is also largely formed as an intermediate during the photocatalytic oxidation of other organic compounds [47]. The generation of CO_2 from the photocatalytic oxidation of AcH occurs according to the following reaction:

$$2CH_3CHO + 5O_2 \xrightarrow[hv]{photocatalyst} 4CO_2 + 4H_2O.$$

Figure 2.8 shows the photodegradation of AcH over various samples as a function of time, in which C_0 and C are the concentrations of AcH after 24 h adsorption equilibrium in the dark at time t_0 and after a period of UV light irradiation t, respectively. A blank test with 250 ppm

AcH in the absence of a photocatalyst was also run under UV light irradiation, where the concentration of AcH decreases negligibly over time, which indicates the stability of AcH under UV light irradiation. The same experimental conditions were applied for all samples. The incorporation of Bi_2WO_6 in $ZnWO_4$ was observed to enhance the photocatalytic activity compared to that of pure $ZnWO_4$. Nevertheless, only the composite photocatalyst with 30 mol% Bi^{3+}exhibited complete conversion (100%) of AcH into CO_2 after 6 h of UV light irradiation, whereas the mechanically mixed counterpart ($ZnWO_4$/30 mol% Bi_2WO_6 composite photocatalyst) had a slightly lower conversion (94%) of AcH into CO_2.

Mechanical mixing tends to cause the formation of crystal lattice defects that serve as electron-hole recombination centers for the composite photocatalyst. However, it is expected that a one-step synthesis of the composite photocatalyst would enable better contact between the two semiconductors, which would facilitate charge transfer from one particle to another. The overall conversion of AcH into CO_2 for the as-synthesized samples was calculated using the formula:

$$\text{Conversion (\%)} = ([CO_2]/2[CH_3CHO]) \times 100$$

The following results were obtained: 36.2% ($ZnWO_4$) < 44.0% (Bi_2WO_6) < 52.8% (5 mol%) < 60.8% (10 mol%) < 71.2% (15 mol%) < 79.8% (20 mol%) < 86.2% (25 mol%) < 94.0% (mechanical mixture of $ZnWO_4$/30 mol% Bi_2WO_6) < 100% (30 mol%). In addition, apparent first-order rate constants (k) for the degradation of AcH were calculated using the Langmuir-Hinshelwood kinetic model:

$$-\ln(C/C_0) = kt$$

where C_0 and C are the concentrations of AcH after 24 h adsorption equilibrium in the dark at time t_0 and after a period of UV light irradiation t, respectively. A good linear relationship was observed for the $\ln(C/C_0)$ vs. time (t) plot over the first 4 h; therefore, the apparent rate constant (k) was calculated by fitting this portion of the linear plot. The calculated apparent rate constant increases in the following order: 0.0583 min^{-1} ($ZnWO_4$) < 0.0820 min^{-1} (5 mol%) < 0.0930 min^{-1} (10 mol%) < 0.1030 min^{-1} (15 mol%) < 0.1132 min^{-1} (20 mol%) < 0.1230 min^{-1} (Bi_2WO_6) < 0.1298 min^{-1} (25 mol%) < 0.1573 min^{-1} (mechanical mixture of $ZnWO_4$/30 mol% Bi_2WO_6) < 0.1840 min^{-1} (30 mol%). The apparent rate constant increases with the Bi_2WO_6 content in the composite photocatalyst. The highest apparent rate constant was observed for the

sample synthesized with 30 mol% Bi^{3+}, which is attributed to successful charge transfer achieved from one semiconductor to another. Compared with the previously reported results for the same composite system prepared by a simple hydrothermal method [33], the addition of 30 mol% Bi^{3+} was much higher, and the photocatalytic activity was monotonically increased with the Bi_2WO_6 content. The main reason for this difference may be related to the partial coverage of the surface of the quasi-spherical $ZnWO_4$ particles, as shown in Figure 2.5, which allows light absorption to occur in the $ZnWO_4$ particles. It has been widely reported that if a core particle is thickly covered by a shell, then interfacial transfer may be impeded or no light absorption in the core may occur, which would lead to lower photocatalytic activity [34,48].

It is evident that an increase in the Bi_2WO_6 content leads to higher photocatalytic activity of the composite photocatalyst, even though some of the Bi_2WO_6 particles are not attached to the surface of the quasi-spherical $ZnWO_4$ particles. This is because the layered structure of Bi_2WO_6 is favorable for charge transfer, which retards the recombination of photogenerated holes and electrons [49,50], and the higher specific surface area also provides more active reaction sites for the photocatalytic reaction to occur on the surface of the photocatalyst [51]. In addition, the valence band of the Bi_2WO_6 photocatalyst consists of O 2p and Bi 6p hybrid orbitals, and the bottom of the conduction band is formed by the W 5d orbitals with a small contribution from the Bi 6p. The hybridization of the Bi 6s and O 2p levels also causes the valence band to become largely dispersed, which favors the mobility of photoinduced holes in the valence band, which is beneficial for the photocatalytic oxidation reactions [52].

To clearly explain the enhancement in the photocatalytic activity of the $ZnWO_4/Bi_2WO_6$ composite photocatalysts in terms of *n*-*n* isotype junction, further investigation is required. $ZnWO_4$ and Bi_2WO_6 are *n*-type semiconductors; therefore, it is supposed that during UV light irradiation of the *n*-*n* isotype junction, the electrons from the $ZnWO_4$ region diffuse into the Bi_2WO_6 region, which creates an accumulation of negative charges in the Bi_2WO_6 region and an accumulation of positive charges in the $ZnWO_4$ region in the vicinity of the junction. This is expected to provide an internal electrostatic field directed from the $ZnWO_4$ region to the Bi_2WO_6 region, which creates an energy barrier for the electron transfer from $ZnWO_4$ to Bi_2WO_6 [53,54].

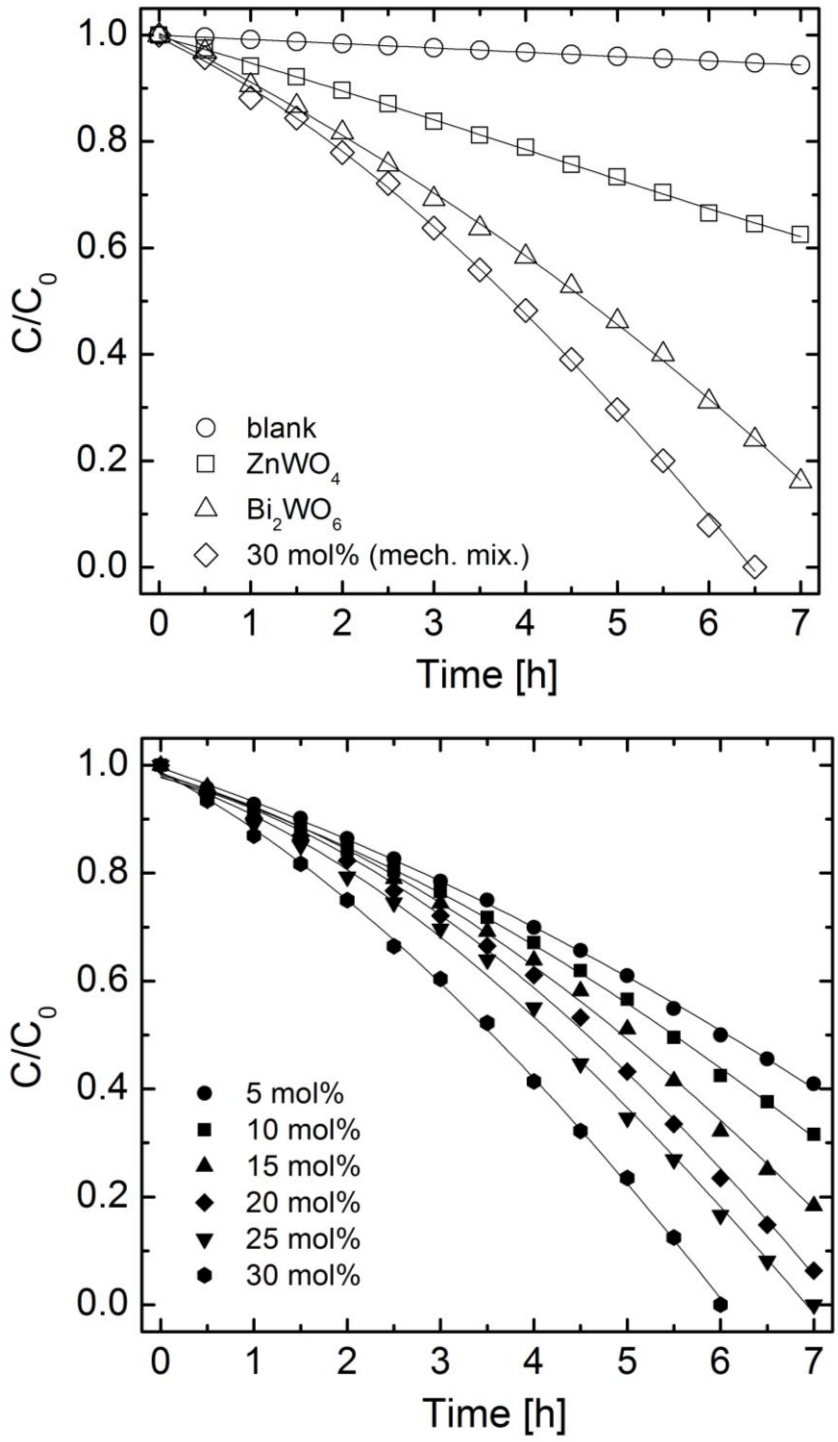

Figure 2.8. Photocatalytic oxidative decomposition of AcH (250 ppm) without a photocatalyst (blank), over $ZnWO_4$, Bi_2WO_6, a mechanical mixture of $ZnWO_4/Bi_2WO_6$ (30 mol%), and the as-synthesized $ZnWO_4/Bi_2WO_6$ composite photocatalyst samples (50 mg) under UV light irradiation (0.4 $mW \cdot cm^{-2}$). C_0 and C are the concentrations of AcH at time t_0 and t, respectively.

Moreover, another mechanism may be attributed to the state of tungsten present in both semiconductors. W^{6+} is generally a strong oxidizing agent that is readily reduced to W^{5+}. The band structure diagram presented in Ref. [55] features a donor level that arises from the $5d^1$ configuration of W^{5+}, between the valence (O^{2-}) and conduction (W^{6+}) bands. Therefore, it is considered that both W^{6+} and W^{5+} are present in the composite photocatalyst synthesized in this study. Thus, by reaching a saturation level of W^{6+}-to-W^{5+} conversion, the presence of oxygen can further re-oxidize W^{5+} to W^{6+} [56], which could also contribute to the photocatalytic enhancement of the composite photocatalyst.

2.4. Conclusions

The effect of Bi_2WO_6 content in the $ZnWO_4/Bi_2WO_6$ composite photocatalyst on the performance for the photocatalytic degradation of AcH under UV light irradiation was investigated in this study. A gradual increase in the Bi_2WO_6 content of the composite photocatalyst resulted in a monotonic shift of the absorption edge from about 355 nm to longer wavelength up to about 450 nm. The composite photocatalyst synthesized with 30 mol% Bi^{3+} exhibited higher photocatalytic activity for the conversion of AcH into CO_2 under UV light irradiation compared with that for individual $ZnWO_4$ and Bi_2WO_6, and that for a mechanically mixed $ZnWO_4/Bi_2WO_6$ composite photocatalyst. The enhancement of the photocatalytic activity can be attributed to *n-n* isotype junctions formed between the two semiconductors and to the charge separation of each semiconductor, because the $ZnWO_4$ and Bi_2WO_6 particles in the composite photocatalyst are either joined or separate.

2.5. References

[1] M.R. Hoffmann, S.T. Martin, W. Choi, D.W. Bahneman, Environmental applications of semiconductor photocatalysis, *Chem. Rev.* 95 (1995) 69–96.

[2] A. Fujishima, T.N. Rao, D.A. Tryk, Titanium dioxide photocatalysis, *J. Photochem. Photobiol. C* 1 (2000) 1–21.

[3] T. Oi, K. Takagi, T. Fukazawa, Scintillation study of $ZnWO_4$ single crystals, *Appl. Phys. Lett.* 36 (1980) 278–279.

[4] P.J. Born, D.S. Robertson, P.W. Smith, G. Hames, J. Reed, J. Telfor, The preparation and scintillation properties of zinc tungstate single crystals, *J. Lumin.* 24–25 (1981) 131–134.

[5] F.-S. Wen, X. Zhao, H. Huo, J.-S. Chen, E. Shu-Lin, J.-H. Zhang, Hydrothermal synthesis and photoluminescent properties of $ZnWO_4$ and Eu^{3+}-doped $ZnWO_4$, *Mater. Lett.* 55 (2002) 152–157.

[6] F. Yang, C. Tu, J. Li, G. Jia, H. Wang, Y. Wei, Z. You, Z. Zhu, Y. Wang, X. Lu, Growth and optical property of $ZnWO_4$: Er^{3+} crystal, *J. Lumin.* 126 (2007) 623–628.

[7] H.Y. He, Preparation and luminescence property of Sm-doped $ZnWO_4$ powders and films with wet chemical methods, *Phys. Status Solidi B* 246 (2009) 177–182.

[8] F. Yang, C. Tu, H. Wang, Y. Wei, Z. You, G. Jia, J. Li, Z. Zhu, X. Lu, Y. Wang, Growth and spectroscopy of Dy^{3+} doped in $ZnWO_4$ crystal, *Opt. Mater.* 29 (2007) 1861–1865.

[9] H. Fu, J. Lin, L. Zhang, Y. Zhu, Photocatalytic activities of a novel $ZnWO_4$ catalyst prepared by a hydrothermal process, *Appl. Catal. A* 306 (2006) 58–67.

[10] X. Zhao, Y. Zhu, Synergetic degradation of Rhodamine B at a porous $ZnWO_4$ film electrode by combined electro-oxidation and photocatalysis, *Environ. Sci. Technol.* 40 (2006) 3367–3372.

[11] X. Zhao, W. Yao, Y. Wu, S. Zhang, H. Yang, Y. Zhu, Fabrication and photoelectrochemical properties of porous $ZnWO_4$ film, *J. Solid State Chem.* 179 (2006) 2562–2570.

[12] M. Hojamberdiev, G. Zhu, Y. Xu, Template-free synthesis of $ZnWO_4$ powders via hydrothermal process in a wide pH range, *Mater. Res. Bull.* 45 (2010) 1934–1940.

[13] G. Huang, C. Zhang, Y. Zhu, $ZnWO_4$ photocatalyst with high activity for degradation of organic contaminants, *J. Alloys Compd.* 432 (2007) 269–276.

[14] R. Shi, Y. Wang, D. Li, J. Xu, Y. Zhu, Synthesis of $ZnWO_4$ nanorods with [100] orientation and enhanced photocatalytic properties, *Appl. Catal. B* 100 (2010) 173–178.

[15] D. Li, R. Shi, C. Pan, Y. Zhu, H. Zhao, Influence of $ZnWO_4$ nanorod aspect ratio on the photocatalytic activity, *CrystEngComm* 13 (2011) 4695–4700.

[16] J. Lin, J. Lin, Y. Zhu, Controlled synthesis of the $ZnWO_4$ nanostructure and effects on the photocatalytic performance, *Inorg. Chem.* 46 (2007) 8372–8378.

[17] G. Huang, Y. Zhu, Enhanced photocatalytic activity of $ZnWO_4$ catalyst via fluorine doping, *J. Phys. Chem. C* 111 (2007) 11952–11958.

[18] G. Huang, S. Zhang, T. Xu, Y. Zhu, Fluorination of $ZnWO_4$ photocatalyst and influence on the degradation mechanism for 4-Chlorophenol, *Environ. Sci. Technol.* 42 (2008) 8516–8521.

[19] X.C. Song, Y.F. Zheng, E. Yang, G. Liu, Y. Zhang, H.F. Chen, Y.Y. Zhang, Photocatalytic activities of Cd-doped $ZnWO_4$ nanorods prepared by a hydrothermal process, *J. Hazard. Mater.* 179 (2010) 1122–1127.

[20] M. Bonanni, L. Spanhel, M. Lerch, E. Füglein, G. Müller, F. Jermann, Conversion of colloidal ZnO−WO_3 heteroaggregates into strongly blue luminescing $ZnWO_4$ xerogels and films, *Chem. Mater.* 10 (1998) 304–310.

[21] A. Kudo, S. Hijii, H_2 or O_2 Evolution from aqueous solutions on layered oxide photocatalysts consisting of Bi^{3+} with $6s^2$ configuration and d^0 transition metal ions, *Chem. Lett.* 28 (1999) 1103–1104.

[22] J. Tang, Z. Zou, J. Ye, Photocatalytic decomposition of organic contaminants by Bi_2WO_6 under visible light irradiation, *Catal. Lett.* 92 (2004) 53–56.

[23] Y. Bessekhouad, D. Robert, J.V. Weber, Bi_2S_3/TiO_2 and CdS/TiO_2 heterojunctions as an available configuration for photocatalytic degradation of organic pollutant, *J. Photochem. Photobiol. A* 163 (2004) 569–580.

[24] M. Shang, W. Wang, L. Zhang, S. Sun, L. Wang, L. Zhou, 3D Bi_2WO_6/TiO_2 hierarchical heterostructure: controllable synthesis and enhanced visible photocatalytic degradation performances, *J. Phys. Chem. C* 113 (2009) 14727–14731.

[25] C.-L. Yu, K. Yang, J.C. Yu, F.-F. Cao, X. Li, X.-C. Zhou, Hydrothermal synthesis and photocatalytic performance of Bi_2WO_6/ZnO heterojunction photocatalysts, *J. Inorg. Mater.* 26 (2011) 1157–1163.

[26] M. Ge, Y. Li, L. Liu, Z. Zhou, W. Chen, Bi_2O_3−Bi_2WO_6 composite microspheres: Hydrothermal synthesis and photocatalytic performances, *J. Phys. Chem. C* 115 (2011) 5220–5225.

[27] Q. Xiao, J. Zhang, C. Xiao, X. Tan, Photocatalytic degradation of methylene blue over Co_3O_4/Bi_2WO_6 composite under visible light irradiation, *Catal. Commun.* 9 (2008) 1247–1253.

[28] Z. Zhang, W. Wang, L. Wang, S. Sun, Enhancement of visible-light photocatalysis by coupling with narrow-band-gap semiconductor: A case study on Bi_2S_3/Bi_2WO_6, *ACS Appl. Mater. Interfaces* 4 (2012) 593–597.

[29] E. Gao, W. Wang, M. Shang, J. Xu, Synthesis and enhanced photocatalytic performance of graphene-Bi_2WO_6 composite, *Phys. Chem. Chem. Phys.* 13 (2011) 2887–2893.

[30] L. Ge, C. Han, J. Liu, Novel visible light-induced g-C_3N_4/Bi_2WO_6 composite photocatalysts for efficient degradation of methyl orange, *Appl. Catal. B* 108–109 (2011) 100–107.

[31] M. Hojamberdiev, Z.C. Kadirova, Y. Makinose, G. Zhu, N. Matsushita, J. Rodríguez, S. Aldabe Bilmes, M. Hasegawa, K. Okada, Influence of BiOI content on the photocatalytic activity of Bi_2WO_6/BiOI/allophane composites and molecular modeling studies of acetaldehyde adsorption, *J. Taiwan Inst. Chem. Eng.* 81 (2017) 258–264.

[32] M. Hojamberdiev, Z.C. Kadirova, Y. Makinose, G. Zhu, S. Emin, N. Matsushita, M. Hasegawa, K. Okada, Involving $CeVO_4$ in improving the photocatalytic activity of a Bi_2WO_6/allophane composite for the degradation of gaseous acetaldehyde under visible light, *Colloid. Surf. A* 529 (2017) 600–612.

[33] D. He, L. Wang, D. Xu, J. Zhai, D. Wang, T. Xie, Investigation of photocatalytic activities over $Bi_2WO_6/ZnWO_4$ composite under UV light and its photoinduced charge transfer properties, *ACS Appl. Mater. Interfaces* 3 (2011) 3167–3171.

[34] K. Domen, Characterization of photoexcitation processes on solid surfaces, In: Surface Photochemistry, Edited by M. Anpo. J. Wiley & Sons, Chichester, 1996, pp. 1–18.

[35] W.J. Albery, P.N. Bartlett, The transport and kinetics of photogenerated carriers in colloidal semiconductor electrode particles, *J. Electrochem. Soc.* 131 (1984) 315–325.

[36] X. Yan, T. Ohno, K. Nishijima, R. Abe, B. Ohtani, Is methylene blue an appropriate substrate for a photocatalytic activity test? A study with visible-light responsive titania, *Chem. Phys. Lett.* 429 (2006) 606–610.

[37] M. Hojamberdiev, G. Zhu, Y. Xu, Template-free synthesis of $ZnWO_4$ powders via hydrothermal process in a wide pH range, *Mater. Res. Bull.* 45 (2010) 1934–1940.

[38] J. Wang, M. Hojamberdiev, Y. Xu, J. Peng, Nonionic surfactant-assisted hydrothermal synthesis of $YVO_4:Eu^{3+}$ powders in a wide pH range and their luminescent properties, *Mater. Chem. Phys.* 25 (2010) 82–86.

[39] J. Wang, Y. Xu, M. Hojamberdiev, J. Peng, G. Zhu, Na_2EDTA–assisted hydrothermal synthesis and luminescent properties of $YVO_4:Eu^{3+}$ with different morphologies in a wide pH range, *Mater. Sci. Eng. B* 156 (2009) 42–47.

[40] G. Zhu, M. Hojamberdiev, P. Liu, J. Peng, J. Zhou, X. Bian, X. Huang, The effects of synthesis parameters on the formation of PbI_2 particles under DTAB-assisted hydrothermal process, *Mater. Chem. Phys.* 131 (2011) 64–71.

[41] C. Pacholski, A. Kornowski, H. Weller, Self-assembly of ZnO: From nanodots to nanorods, *Angew. Chem. Int. Ed.* 41 (2002) 1188–1191.

[42] E.J.H. Lee, C. Ribeiro, E. Longo, E.R. Leite, Oriented attachment: An effective mechanism in the formation of anisotropic nanocrystals, *J. Phys. Chem. B* 109 (2005) 20842–20846.

[43] D. Errandonea, F.J. Manjón, N. Garro, P. Rodríguez-Hernández, S. Radescu, A. Mujica, A. Muñoz, C.Y. Tu, Combined Raman scattering and *ab initio* investigation of pressure-induced structural phase transitions in the scintillator $ZnWO_4$, *Phys. Rev. B* 78 (2008) 054116.

[44] M. Maczka, W. Paraguassu, A.G. Souza Filho, P.T.C. Freire, J. Mendes Filho, J. Hanuza, Phonon-instability-driven phase transitions in ferroelectric $Bi_2WO_6:Eu^{3+}$: High-pressure Raman and photoluminescence studies, *Phys. Rev. B* 77 (2008) 094137.

[45] M. Maczka, J. Hanuza, W. Paraguassu, A.G. Souza Filho, P.T.C. Freire, J. Mendes Filho, Phonons in ferroelectric Bi_2WO_6: Raman and infrared spectra and lattice dynamics, *Appl. Phys. Lett.* 92 (2008) 112911.

[46] C. Chen, Y. Zheng, Y. Zhan, X. Lin, Q. Zheng, K. Wei, Enhanced Raman scattering and photocatalytic activity of Ag/ZnO heterojunction nanocrystals, *Dalton Trans.* 40 (2011) 9566–9570.

[47] J. Tang, Z. Zou, J. Ye, Efficient photocatalytic decomposition of organic contaminants over $CaBi_2O_4$ under visible-light irradiation, *Angew. Chem. Int. Ed.* 43 (2004) 4463–4466.

[48] L. Li, G.S. Rohrer, P.A. Salvador, Heterostructured ceramic powders for photocatalytic hydrogen production: Nanostructured TiO_2 shells surrounding microcrystalline (Ba,Sr)TiO_3 cores, *J. Am. Ceram. Soc.* 95 (2012) 1414–1420.

[49] J.-Y. Kim, I. Chung, J.-H. Choy, G.-S. Park, Macromolecular nanoplatelet of Aurivillius-type layered perovskite oxide, $Bi_4Ti_3O_{12}$, *Chem. Mater.* 13 (2001) 2759–2761.

[50] Y. Tsunoda, W. Sugimoto, Y. Sugahara, Intercalation behavior of *n*-Alkylamines into a protonated form of a layered perovskite derived from Aurivillius phase $Bi_2SrTa_2O_9$, *Chem. Mater.* 15 (2003) 632–635.

[51] F. Amano, K. Nogami, M. Tanaka, B. Ohtani, Correlation between surface area and photocatalytic activity for acetaldehyde decomposition over bismuth tungstate particles with a hierarchical structure, *Langmuir* 26 (2010) 7174–7180.

[52] M. Oshikiri, M. Boero, J. Ye, Z. Zou, G. Kido, Electronic structures of promising photocatalysts $InMO_4$ (M=V, Nb, Ta) and $BiVO_4$ for water decomposition in the visible wavelength region, *J. Chem. Phys.* 117 (2002) 7313–7318.

[53] S. Liu, J. Wu, X. Liu, R. Jiang, TiO_2/V–TiO_2 composite photocatalysts with an n–n heterojunction semiconductor structure, *J. Mol. Catal. A* 332 (2010) 84–92.

[54] R.A. Smith, Semiconductors, Second edition, Cambridge University Press, London, 1978.

[55] D.E. Macphee, D. Rosenberg, M.G. Skellern, R.P. Wells, J.A. Duffy, K.S. Killham, A tungsten oxide-based photoelectrocatalyst for degradation of environmental contaminants, *J. Solid State Electrochem.* 15 (2011) 99–103.

[56] K.K. Akurati, A. Vital, J.-P. Dellemann, K. Michalow, T. Graule, D. Ferri, A. Baiker, Flame-made WO_3/TiO_2 nanoparticles: Relation between surface acidity, structure and photocatalytic activity, *Appl. Catal. B* 79 (2008) 53–62.

CHAPTER 3: Involving $CeVO_4$ in improving the photocatalytic activity of a Bi_2WO_6/allophane composite for the degradation of gaseous acetaldehyde under visible light irradiation

3.1. Introduction

Bi_2WO_6 is a visible-light-responsive photocatalyst studied for the degradation of organic pollutants [1,2]. Various techniques have been developed to synthesize Bi_2WO_6-based photocatalysts, such as solid-state [3], microwave-solvothermal [4,5], sonochemical [6], sol-gel [7], and hydrothermal [8] methods. However, Bi_2WO_6 can only respond to visible light of wavelengths shorter than 450 nm, which accounts for only a small part of the solar spectrum. The rapid recombination of photoinduced electron-hole pairs also greatly decreases the photocatalytic activity of Bi_2WO_6, hindering its large-scale application. Two main approaches have been employed to extend the wavelength range of visible-light absorption and to promote the separation of photoinduced charge carriers in Bi_2WO_6: (i) cation and anion doping of Bi_2WO_6 (such as Sm, Ce, N, and F) [9–11] and (ii) heterostructure formation between Bi_2WO_6 and semiconductors (namely, $BiVO_4$ [12], $BiPO_4$ [13], and $ZnWO_4$ [14]) or metals [15].

Recent investigations have reported that the photocatalytic performance of Bi_2WO_6 can be enhanced by the use of various carbon-based materials because of the enhanced visible light absorption of the carbon component, an improved mass transfer due to absorption in the porous support, and strong interfacial electronic effects between carbon nanostructures and Bi_2WO_6. The use of porous carbon-based materials also allows to recover easily and reuse of photocatalyst powders. For instance, Bi_2WO_6 was composited with g-C_3N_4 for both the degradation of Rhodamine B and hydrogen generation from water under visible light irradiation [16], reduced graphene oxide for photocatalytic selective reduction of 4-NP to 4-AP and Cr(VI), photocatalytic selective oxidation of benzyl alcohol to benzaldehyde, and photocatalytic degradation of bisphenol A [17], graphene for enhancing the photocatalytic water splitting [18], and acidic carbon additives (biomass-derived activated carbon, carbon nanotubes, and carbon spheres) for boosting the visible-light photoactivity of Bi_2WO_6 for the photooxidation of Rhodamine B (RhB) [19]. Heteropoly acids (HPA) were immobilized on Bi_2WO_6 to decrease the recombination of photogenerated electrons and holes, to improve the light efficiency and

photocatalytic efficiency for the denitrification of simulated oil [20]. Also, Bi_2WO_6 photocatalyst was sensitized by copper (II) meso-tetra (4-carboxyphenyl) porphyrin (Cu-TCPP) to increase its visible-light harvesting and to facilitate the separation of photo-generated electron-hole pairs [21].

Also, various cationic and anionic clay materials have been studied to develop efficient Bi_2WO_6-clay photocatalytic composite materials for environmental remediation and energy conversion because of their special layered structures, large specific surface areas, and remarkable adsorption capacities [22]. Guo et al. [23] improved the photocatalytic activity of Bi_2WO_6 for the degradation of 4BS dye in aqueous solution under visible-light irradiation by combining it with rectorite, an interstratified layered silicate mineral with a regular (1:1) stacking of dioctahedral mica-like layers and dioctahedral smectite-like layers. The average lifetime of the photogenerated charge carriers was increased from 3.06 μs to 18.8 μs by constructing Bi_2WO_6 quantum dots (QDs)—intercalated montmorillonite (MMT) nanostructures that can significantly inhibit electron-hole recombination and improve the photocatalytic performance of Bi_2WO_6 in both solar water oxidation and environmental purification [24].

Although acetaldehyde (CH_3CHO), as a common indoor air pollutant, is included in Group II of the WHO guidelines for indoor air quality [25], it is still toxic when applied externally for prolonged periods, an irritant, and a probable carcinogen [26]. The main sources of acetaldehyde in homes include building materials, laminate, linoleum, wooden varnished, cork/pine flooring, automotive exhaust and tobacco smoke. It is also found in plastic water-based and matt emulsion paints, in wood ceilings, and wooden, particle-board, plywood, pine wood, and chipboard furniture [27,28].

We previously reported the effect of allophane on the photocatalytic activity of Bi_2WO_6 for efficient photodegradation of gaseous acetaldehyde under visible-light irradiation because allophane has a strong ability to adsorb ionic or polar pollutants from the gaseous phase and aqueous solutions due to its amphoteric ion-exchange activity and high specific surface area [29].

In this study, to further enhance its photocatalytic performance, the Bi_2WO_6- allophane was composited with $CeVO_4$, an important semiconducting derivative of vanadium oxide, due to its

suitable band structure, smaller band-gap, and simultaneous presence of Ce^{3+} and Ce^{4+}, allowing $CeVO_4$ to act as an electron scavenger during photocatalytic reactions. Particularly, the effect of the Bi_2WO_6:$CeVO_4$ mass ratio on photocatalytic performance of the as-synthesized composites for the degradation of acetaldehyde under visible-light irradiation was studied along with that of the mechanically mixed composite. Although the enhanced photocatalytic performance of Bi_2WO_6-based photocatalysts was previously reported for the degradation of various organic pollutants, including dyes [30,31], phenol [32], and pathogens [33], the present work is the first study demonstrating the design of a Bi_2WO_6/$CeVO_4$/allophane composite for the effective photodegradation of gaseous acetaldehyde under visible-light irradiation.

3.2. Experimental

3.2.1. Synthesis of Bi_2WO_6

Bi_2WO_6 powder was synthesized by a hydrothermal method as follows: First, 5 mmol of $Bi(NO_3)_3 \cdot 5H_2O$ (99.9%, Wako Pure Chemical Industries Ltd.) was dissolved in 15 mL of ethylene glycol (99.0%, Wako Pure Chemical Industries Ltd.), and 2.5 mmol of Na_2WO_4 (Strem Chemicals, Inc.) was dissolved in 15 mL of deionized water (Millipore Milli-Q Plus purification system, 18.2 MΩ·cm). Then, the two solutions were mixed together under vigorous stirring at room temperature for 30 min, and the pH of the suspension was measured to be approximately 1. After stirring for another 30 min, the suspension was transferred into a 40 mL Teflon-lined stainless steel autoclave and maintained at 180°C for 12 h. After the hydrothermal synthesis, the autoclave was cooled down to room temperature naturally, and the resulting precipitate was collected by centrifugation, washed with deionized water several times and dried at 80°C for 12 h.

3.2.2. Synthesis of allophane

Allophane powder was also synthesized by a hydrothermal method as follows: First, $2Na_2O \cdot SiO_2 \cdot nH_2O$ (63.0%, Wako Pure Chemical Industries Ltd.) and $AlCl_3 \cdot 6H_2O$ (98.0%, Wako Pure Chemical Industries Ltd.) were separately dissolved in deionized water to obtain a 0.1 $mol \cdot L^{-1}$ aqueous solution from each. Then, the two solutions were mixed together under vigorous stirring at room temperature to a total volume of 30 mL (Al/Si = 1). The pH of the suspension was measured to be approximately 3.5. After stirring for 2 h, the suspension was transferred into a 40 mL Teflon-lined stainless steel autoclave and maintained at 90°C for 90

h. After the hydrothermal synthesis, the autoclave was cooled to room temperature naturally, and the resulting precipitate was collected by centrifugation, washed with deionized water several times and dried at 80°C for 12 h.

3.2.3. Synthesis of the Bi_2WO_6/$CeVO_4$/allophane composite

The Bi_2WO_6/$CeVO_4$/allophane (BW/CV/A) composite was synthesized by a hydrothermal method used previously for the synthesis of Bi_2WO_6/allophane composite [29]. The experimental details are as follows: First, $Ce(NO_3)_3 \cdot 6H_2O$ (98.0%, Wako Pure Chemical Industries Ltd.) and Na_3VO_4 (75.0%, Wako Pure Chemical Industries Ltd.) in a stoichiometric ratio were dissolved in 20 mL of deionized water. Meanwhile, 0.3489 g of the as-synthesized Bi_2WO_6 (0.5 mmol) powder and 0.3489 g of the allophane powder were separately dispersed in 10 mL of deionized water under ultrasonication. To obtain the Bi_2WO_6/$CeVO_4$/allophane composite, the aqueous solutions of $Ce(NO_3)_3 \cdot 6H_2O$ and Na_3VO_4 were mixed together with the aqueous suspensions of Bi_2WO_6 and allophane powders under vigorous stirring at room temperature for 30 min. The pH of the suspension was adjusted to 7 by adding 28% aqueous ammonia (Wako Pure Chemical Industries Ltd.). After stirring for 30 min, the formed suspension was transferred into a 40 mL Teflon-lined stainless steel autoclave and maintained at 180°C for 12 h. After the hydrothermal synthesis, the autoclave was cooled to room temperature naturally, and the resulting precipitate was collected by centrifugation, washed with deionized water several times and dried at 80°C for 8 h. To investigate the effect of the amount of $CeVO_4$ on the photocatalytic activity of the BW/CV/A composite, the molar ratio of Bi_2WO_6:$CeVO_4$ was varied while keeping the amounts of Bi_2WO_6 and allophane powders constant. The compositions of the prepared composites are listed in Table 3.1.

3.2.4. Characterization

The crystalline phases formed were identified by X-ray powder diffraction (XRD) using an RINT-2100 diffractometer (Rigaku) with monochromatic Cu Kα radiation (λ = 1.5405 Å) at 40 kV and 40 mA. The powdered samples were scanned at a rate of $2° \cdot min^{-1}$ over the 2θ range of 10–70°. The formation of crystalline phases was also confirmed by a T64000 Raman spectrometer (Horiba Jobin Yvon S.A.S.) with an Ar laser (514.5 nm) operated at 50 mW. Particle morphology and size were examined using an S-4500 ultra-high-resolution scanning electron microscope (Hitachi) operated at an accelerating voltage of 15 kV. Transmission

Table 3.1. Compositions, porous properties and adsorption and photodegradation of gaseous acetaldehyde over the prepared samples.

Sample name	Composition	S_{BET}, $m^2 \cdot g^{-1}$	V_t, $mL \cdot g^{-1}$	Pore size, nm	AcH adsorption in the dark		AcH photodegaradation		
					$\mu mol \cdot g^{-1}$	%	7 h, %	4 h, %	k, min^{-1}
BW	Bi_2WO_6	21	0.1126	14.1	13.9	30.9	74.7	64.9	0.118
CV	$CeVO_4$	85	0.1726	4.05	14.9	33.1	55.3	50.9	0.08
A	Allophane	263	0.7895	7.98	17.5	38.9	2.4*	0	–
BW1/CV05/A	Bi_2WO_6:$CeVO_4$ = 1:0.5	182	0.4107	10.4	9.0	20	100	77.6	0.255
BW1/CV1/A	Bi_2WO_6:$CeVO_4$ = 1:1	154	0.3468	13.1	10.0	22.2	100	100	0.356
BW1/CV2/A	Bi_2WO_6:$CeVO_4$ = 1:2	120	0.2094	15.8	11.0	24.4	81.8	61.6	0.176
BW1/CV3/A	Bi_2WO_6:$CeVO_4$ = 1:3	110	0.1541	16.5	13.4	29.8	87.6	62.7	0.171
BW1/CV1/A (mechanically mixed)	Bi_2WO_6:$CeVO_4$ = 1:1 (mech.mix.)	125	0.1709	17.4	9.5	21.1	100	69.3	0.159

*Ref. [25]

electron microscopy (TEM) was performed using a JEM-2010UHR (JEOL) operated at an accelerating voltage of 200 kV to distinguish the crystal structures and crystal sizes in the prepared composites. For TEM observation, the powdered sample was dispersed in cyclohexane under sonication, and a small amount of the suspension was dropped onto a holey carbon grid. Ultraviolet-visible (UV-vis) diffuse reflectance spectra of the samples were recorded over the wavelength range of 200-600 nm on a Lambda 950 UV/VIS/NIR spectrophotometer (Perkin-Elmer) equipped with an integrating sphere, and $BaSO_4$ was used as a reference. The porous properties of the resulting samples were investigated by determining their nitrogen adsorption-desorption isotherms at 77 K using an Autosorb-3B instrument (Quantachrome Instruments). The samples were preheated at 150°C for 4 h under vacuum before the measurements. The specific surface area (S_{BET}) was calculated by the Brunauer, Emmett, and Teller (BET) method from the linear portion of the adsorption isotherm. The pore size distribution (PSD) was calculated by the Barrett, Joyner and Halenda (BJH) method from the desorption branch of the isotherm. The surface chemical states of the elements were evaluated by X-ray photoelectron spectroscopy (XPS, JPS-9010 MC, JEOL) using non-monochromated Mg Kα radiation (1253.6 eV).

3.2.5. Adsorption and photocatalytic activity tests

As a typical indoor air pollutant, acetaldehyde (AcH) was chosen as a probe molecule for evaluating the adsorption and photocatalytic performance of the as-synthesized samples under visible light irradiation. The photodegradation of AcH in a batch-type reactor over the as-synthesized samples was conducted at room temperature. The photocatalyst sample (50 mg) was placed in a reaction vessel made of Pyrex® glass with a volume of 500 mL, and the lid, inlet, and outlet were firmly sealed. Pure air (Taiyo Nippon Sanso Corp.) was blown through the reaction vessel at room temperature to remove any air contaminants. Then, a certain amount of AcH was introduced into the reaction vessel using a 2-mL Pressure-Lok® glass syringe until the concentration of AcH in the reaction vessel reached 200 ppm. After adsorption equilibration in the dark for 24 h, the reaction vessel was placed under an FL10 W white fluorescent daylight lamp (>400 nm, Toshiba) that emitted visible light with an irradiance of ~8000 lux, as measured with an LX-101A light meter (Lutron Electronic Enterprise Co., Ltd.). To eliminate UV light from the light source, an SC42 cutoff filter (<420 nm, Fujifilm) was used. The decrease in AcH

concentration and the increase in CO_2 concentration were monitored using a GC-2014 gas chromatograph (Shimadzu), equipped with a 2-m Porapak-Q column, methanizer and a flame ionization detector, using N_2 as the carrier gas.

3.3. Results and Discussion

3.3.1. Characterization of the prepared samples

The XRD patterns and SEM images of individual Bi_2WO_6, $CeVO_4$ and allophane are shown in Figure 3.1. The SEM image in Figure 3.1a shows the hierarchical flower-like microstructure of Bi_2WO_6 composed of many ultrathin nanosheets with an average size of 2 μm and some defects on their surfaces. The diffraction lines in the XRD pattern can be assigned to orthorhombic Bi_2WO_6 with a space group of *Pbca* (61) (ICDD PDF# 39–0256) [34]. The broad diffraction peaks suggest that the hierarchical flower-like microstructures of Bi_2WO_6 are constructed by nanosheets. The mean crystallite size of the Bi_2WO_6 particles calculated from the full width at half maximum (FWHM) of the most intense diffraction peak *131* at $2\theta = 28.31°$ using the Scherrer equation was determined to be approximately 10 nm. In Figure 3.1b, the $CeVO_4$ nanocrystals having an average size of 10–20 nm [35] and cube-like morphologies are well-crystallized and slightly agglomerated. All the diffraction lines in the XRD pattern of $CeVO_4$ are in good agreement with the standard ICDD PDF# 12–0757 for tetragonal $CeVO_4$ with a space group of $I4_1/amd$ [36]. The mean crystallite size of the $CeVO_4$ nanocrystals was estimated from the FWHM of the most intense diffraction peak *200* at $2\theta = 24.24°$ to be approximately 18 nm. As shown in Figure 3.1c, allophane ($1{-}2SiO_2{\cdot}Al_2O_3{\cdot}5{-}6H_2O$) has an amorphous microstructure with a particle size of 1−3 μm, and the two halo peaks at $2\theta = 27°$ and 40° correspond to the (002) and (040) planes of allophane (ICDD PDF# 38−0449), respectively [37].

TEM results are illustrated in Figure 3.2, showing clear differences in the crystal size and crystallinity of Bi_2WO_6, $CeVO_4$, and allophane. The fast Fourier transform (FFT) patterns confirm the amorphous structure of allophone and the single-crystalline natures of the Bi_2WO_6 nanosheets and $CeVO_4$ nanocrystals (insets of Figures 3.2b, d, and f). The typical TEM images shown in Figures 3.2a and c shows that the as-synthesized Bi_2WO_6 and $CeVO_4$ particles are composed of many ultrathin nanosheets and nanocubes, respectively. The HR-TEM image in Figure 3.2b indicates that the continuous lattice fringes with interplanar spacing of 4.1 Å

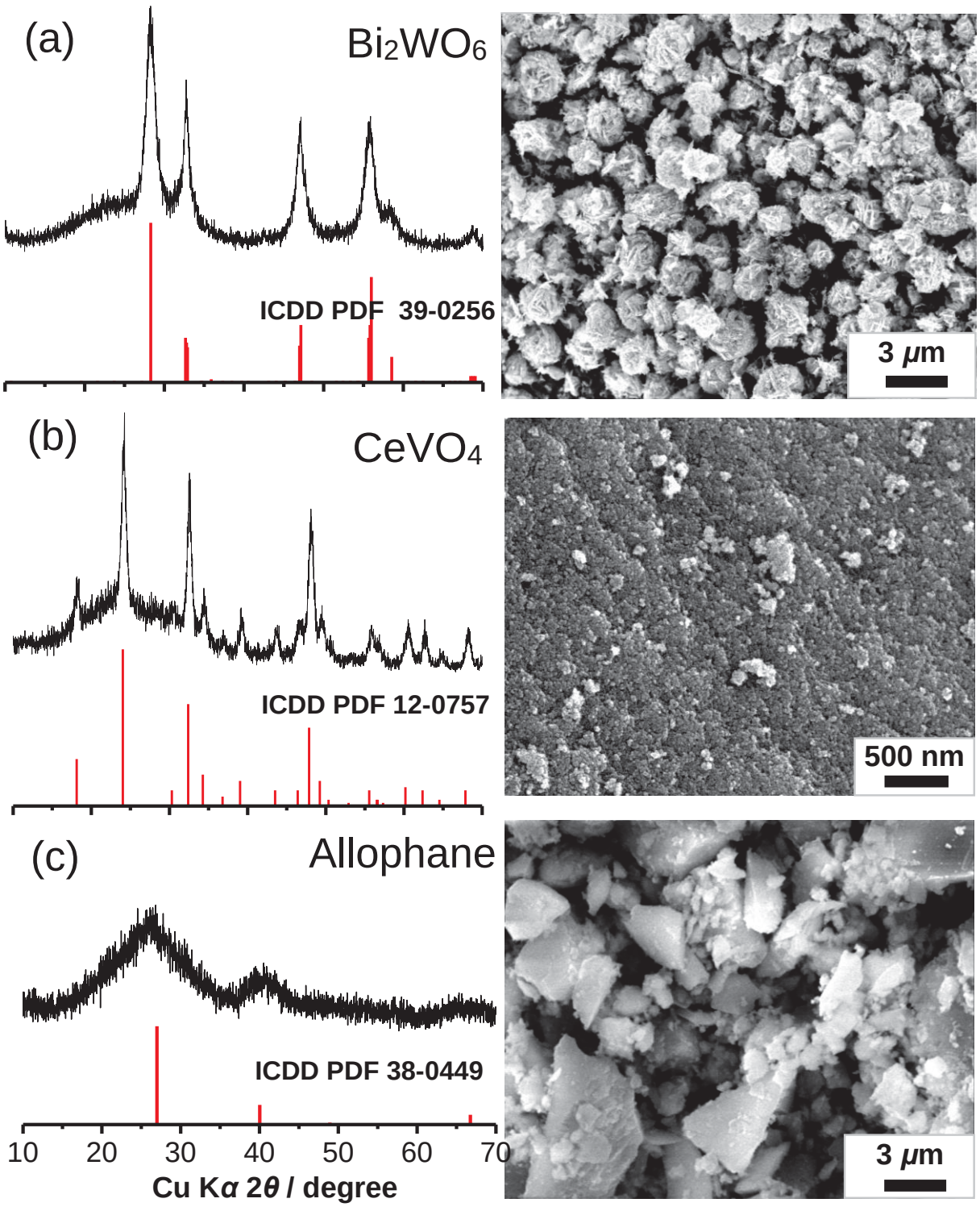

Figure 3.1. XRD patterns and SEM images of (a) Bi_2WO_6, (b) $CeVO_4$, and (c) allophane.

correspond to the (040) lattice planes of orthorhombic Bi_2WO_6. The six sides of the Bi_2WO_6 nanosheets may be surrounded by the {100}, {141} and {101} planes. Figures 3.2c and d clearly show uniform cube-like nanocrystals of $CeVO_4$ with regular facets and sharp edges, which were estimated to measure approximately 30 nm in width, suggesting that each

nanocrystal of $CeVO_4$ has a single-crystalline nature. Figure 3.2d shows highly regular fringes with an interlayer distance of approximately 3.7 Å, corresponding to the separation between the (020) lattice planes. The side surfaces are bounded by the {220} and {020} planes of $CeVO_4$ [35]. The low- and high-magnification TEM images distinctly show hollow allophane spherules with an outer diameter of approximately 5 nm and small pores measuring 0.3–0.5 nm on the surface [37]. Clearly, the allophane spherules are highly aggregated into globular clusters with an average size of 100–300 nm. According to the SEM results, these globular clusters can further agglomerate to form large, chunky aggregates measuring 1–3 μm.

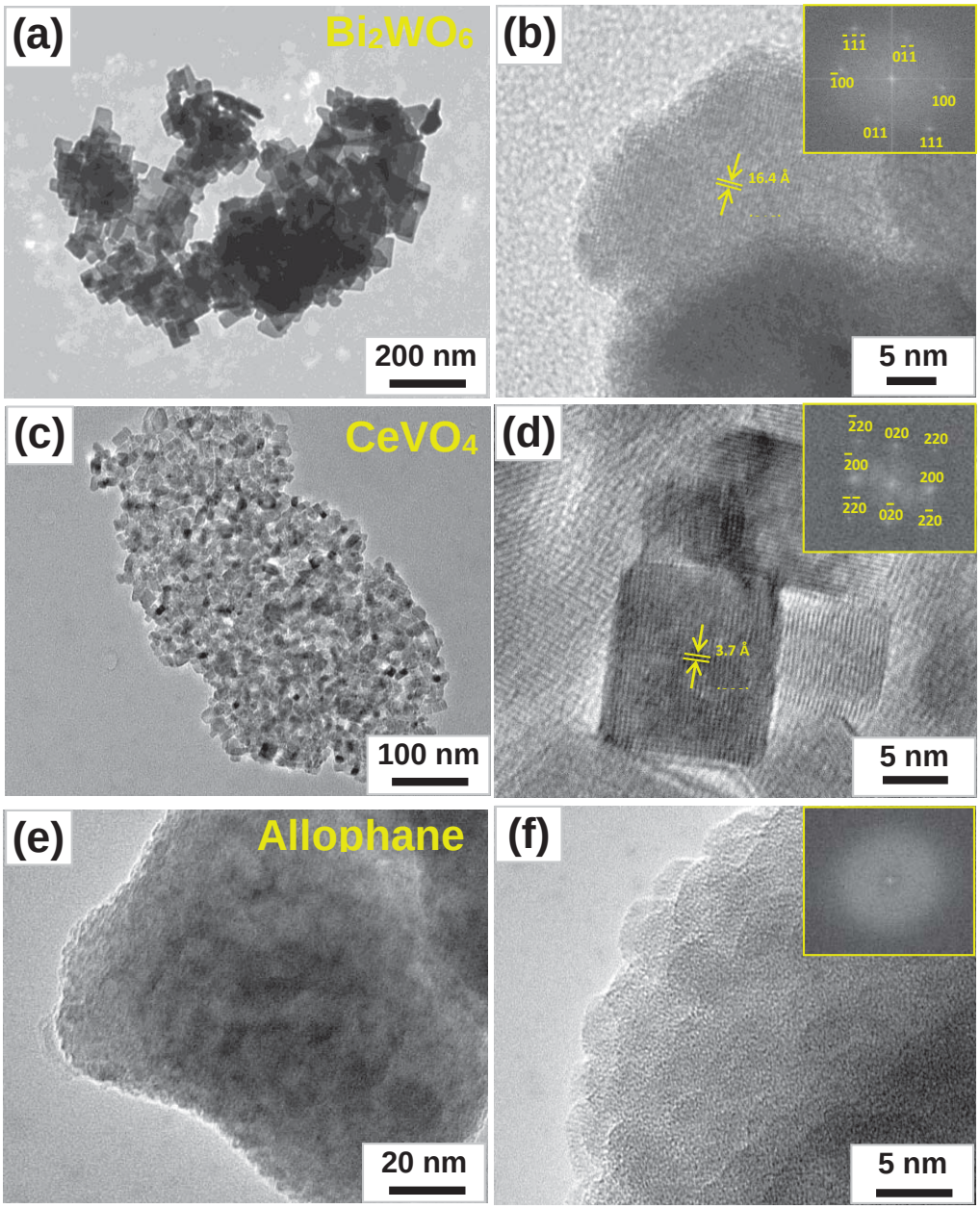

Figure 3.2. TEM and HR-TEM images and FFT patterns (*inset*) of (a,b) Bi_2WO_6, (c,d) $CeVO_4$, and (e,f) allophane.

The XRD patterns of the mechanically mixed and hydrothermally synthesized Bi_2WO_6/$CeVO_4$/allophane (hereafter denoted as BW/CV/A) composites are shown in Figure 3.3. All the diffraction peaks in the XRD patterns of the BW/CV/A composites can be assigned to orthorhombic Bi_2WO_6 with a space group of *Pbca* (61) (ICDD PDF# 39–0256) and tetragonal $CeVO_4$ with a space group of $I4_1/amd$ (ICDD PDF# 12–0757). No traces of other crystalline phases were detected in the XRD patterns of the BW/CV/A composites. Because the intensities of the diffraction peaks of the Bi_2WO_6 and $CeVO_4$ crystalline phases are high, it is difficult to distinguish the two main halo peaks of amorphous allophane (ICDD PDF# 38-0449) at $2\theta = 27°$ and 40°, corresponding to the (002) and (040) planes [29]. It should be noted that the BW/CV/A composites exhibit broad diffraction peaks similar to those of the individual components mentioned above and the mechanically mixed composite. The FWHM values of the *131* diffraction peak of Bi_2WO_6 in the Bi_2WO_6 and BW/CV/A composites are slightly different. The high-intensity diffraction peaks of $CeVO_4$ were observed only for the composites with the highest amount of $CeVO_4$ nanocrystals. This finding can be explained by the formation of small $CeVO_4$ nanocrystals and the crystallization of the $CeVO_4$ phase [38].

Figure 3.4 shows the SEM images of the mechanically mixed and hydrothermally synthesized BW/CV/A composites. Some flakes and small spherules of allophane and $CeVO_4$ nanocrystals were attached to the surfaces of the hierarchical flower-like particles of Bi_2WO_6. The attached particles are uniformly distributed and are in close contact with each other, and the hierarchical flower-like Bi_2WO_6 particles can be regarded as a support assembled by nanosheets for the allophane particles and $CeVO_4$ nanocrystals in the BW/CV/A composites (Figure 3.5). The magnified SEM images reveal that allophane, $CeVO_4$, and Bi_2WO_6 also exist as nanocrystals within the three-dimensional structure of the BW/CV/A composite. This explains the broad diffraction peaks in the XRD patterns and the lack of well-marked crystalline morphology observed for the hydrothermally synthesized BW/CV/A composites; however, some hierarchical flower-like Bi_2WO_6 particles were also observed in the composites (Figure 3.3). With an increasing amount of $CeVO_4$ in the composite, the hierarchical flower-like structure of Bi_2WO_6 gradually ceased to be visible because the $CeVO_4$ nanocrystals completely covered the surface. Compared with the hydrothermally synthesized composites, the mechanically mixed BW/CV/A composite has a slightly different morphology of

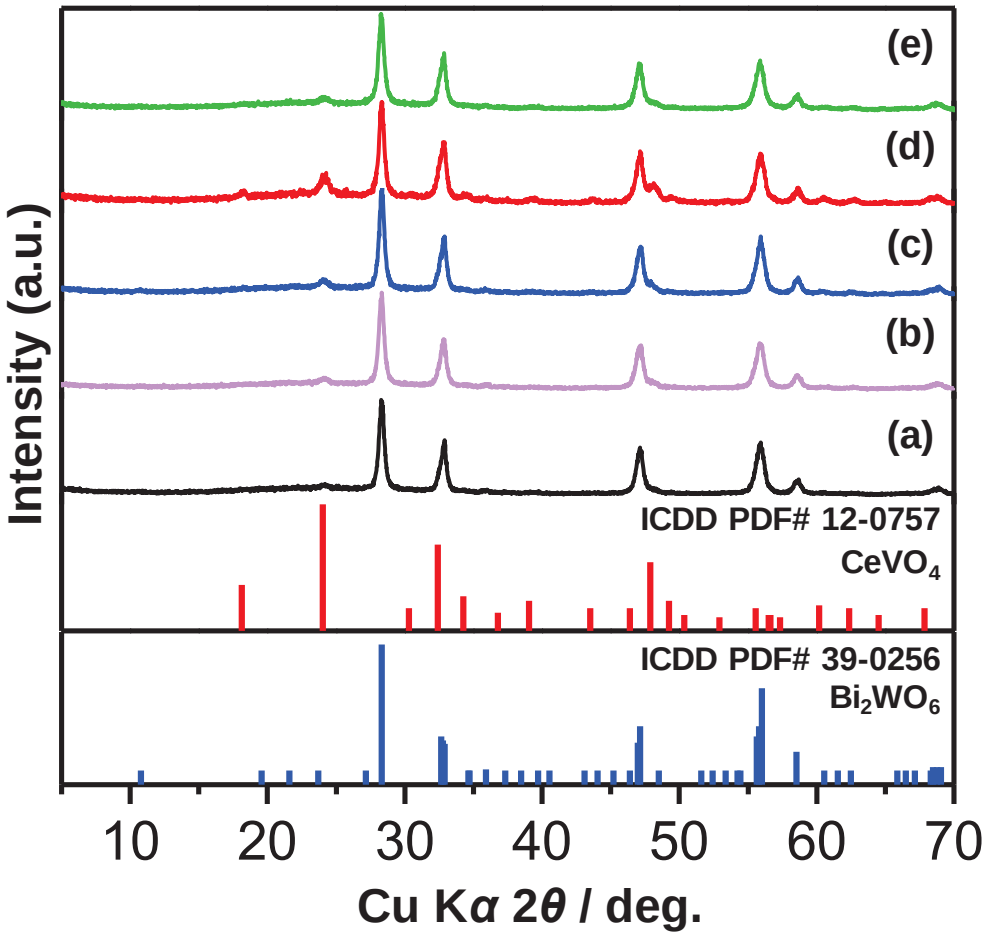

Figure 3.3. XRD patterns of the Bi_2WO_6/$CeVO_4$/allophane composite photocatalysts synthesized with different ratios of Bi_2WO_6:$CeVO_4$: (a) 1:0.5, (b) 1:1, (c) 1:2, (d) 1:3, and (e) 1:1 (mech. mix.).

homogenously distributed particles of allophane, Bi_2WO_6, and $CeVO_4$. The co-existence and change in morphology of agglomerated and un-agglomerated particles can be substantiated by comparing the SEM images before and after mechanical mixing (Figure 3.1). Although the hierarchical flower-like microstructures of Bi_2WO_6 were partially damaged by mechanical mixing and the $CeVO_4$ nanocrystals were separated from allophane and Bi_2WO_6, most of the Bi_2WO_6 particles remained in close contact with the $CeVO_4$ nanocrystals and allophane particles. In addition, the Bi_2WO_6/allophane and $CeVO_4$/allophane composites were also observed by SEM for comparison. As shown in Figure 3.4f, the as-synthesized Bi_2WO_6/allophane composite has two different morphologies: (i) homogenously distributed sphere-like Bi_2WO_6 particles with the diameter of less than 1 μm and (ii) large chunk-like allophane particles. Some sphere-like Bi_2WO_6 particles are attached onto the surface of

allophane particles. Figure 3.4g confirms that large chunk-like allophane particles are covered with the $CeVO_4$ nanocrystals.

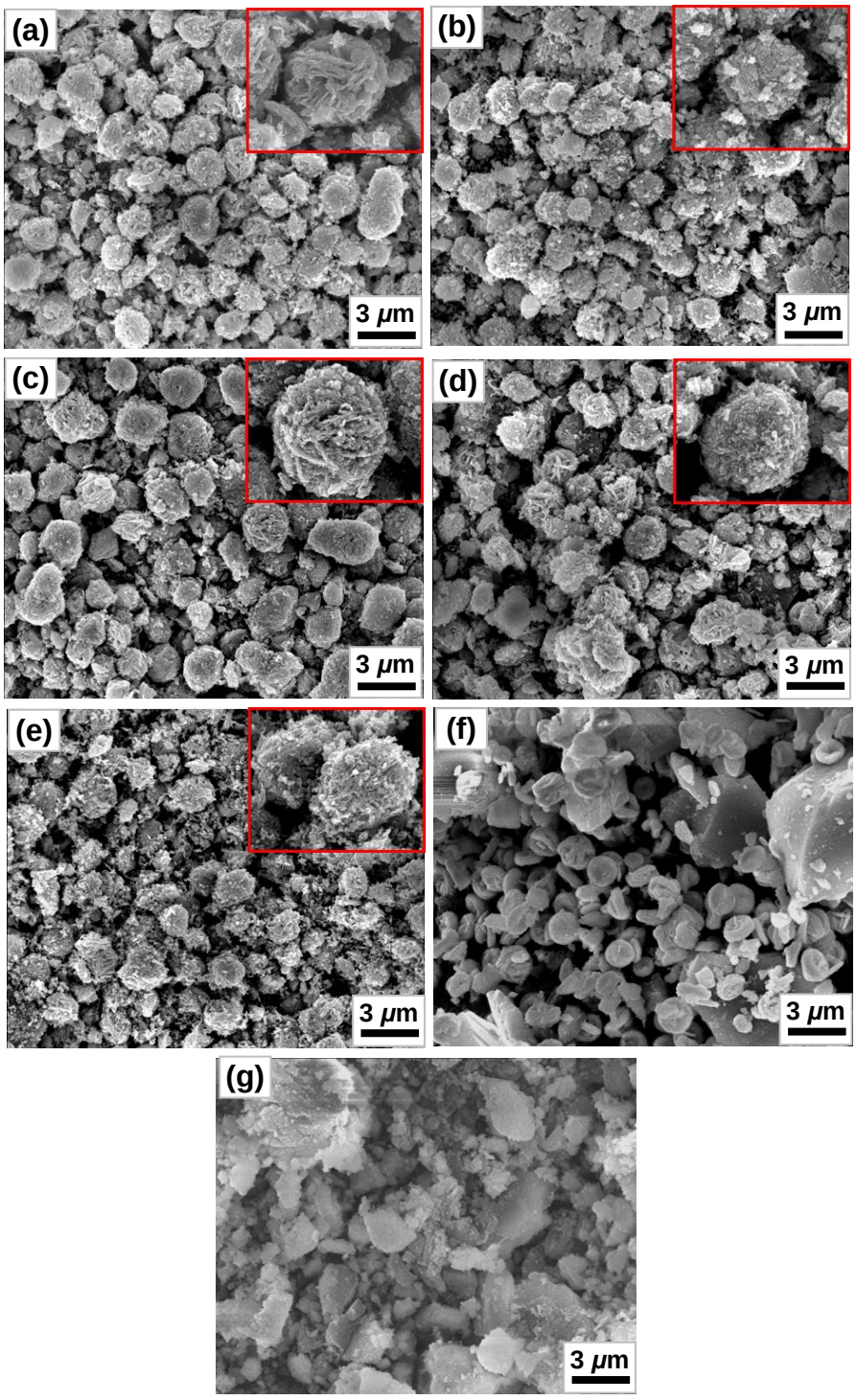

Figure 3.4. SEM images of the $Bi_2WO_6/CeVO_4$/allophane composite photocatalysts synthesized with different ratios of Bi_2WO_6:$CeVO_4$: (a) 1:0.5, (b) 1:1, (c) 1:2, (d) 1:3, (e) 1:1 (mech. mix.), and (g) 0:1.

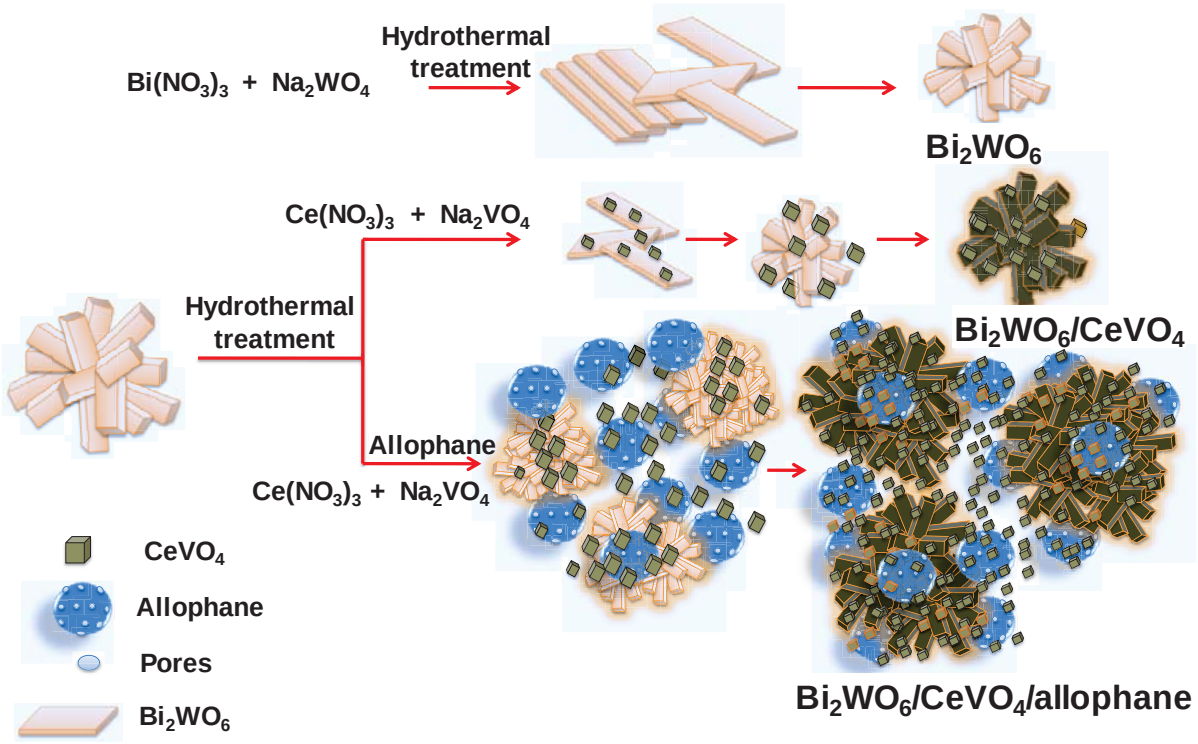

Figure 3.5. Formation of the $Bi_2WO_6/CeVO_4$/allophane composite photocatalyst.

Figure 3.6 shows the Raman spectra of the mechanically mixed and hydrothermally synthesized BW/CV/A composites. Because allophane is amorphous, according to XRD, only the Raman spectra of Bi_2WO_6 and $CeVO_4$ can be observed in the composites. The Raman spectrum of Bi_2WO_6 [29] is characterized by a number of optical modes, such as $26A_1 + 27A_2 + 26B_1 + 26B_2$. The A_2 modes are Raman active, and the A_1, B_1, and B_2 modes are both IR and Raman active. The Raman peaks at 786 and 706 cm^{-1} are assigned to the symmetric and asymmetric stretching modes of the WO_6 octahedra involving the motions of the apical and equatorial oxygen atoms perpendicular to and within the layers, respectively. The Raman peaks at 411, 298, 276, 253, 218, and 173 cm^{-1} are attributed to the bending modes of the WO_6 octahedra and the stretching and bending modes of the BiO_6 polyhedra. The Raman peaks at 140 and 147 cm^{-1} may be associated with the translations of the tungsten and bismuth ions [39].

Tetragonal $CeVO_4$ with a space group of $I4_1/amd$ and point group of D_{4h} has two molecular formulae per unit cell with Raman active modes of A_{1g}, B_{1g}, and E_g. The main Raman bands of $CeVO_4$ can be observed at 254, 368, 459, 779, 790, and 853 cm^{-1}. The Raman peak at 853 cm^{-1} (ν_1) is assigned to the A_{1g} symmetric stretching mode of VO_4^{3-}, whereas the Raman peaks

observed at 790 and 779 cm^{-1} are attributed to the E_g and B_{1g} antisymmetric stretching modes of the vanadates (v_3), respectively. The Raman peaks observed at 459 and 368 cm^{-1} are associated with the B_{1g} and A_{1g} deformations (v_4 and v_2), respectively. Similar to the XRD data of $CeVO_4$, the hydrothermally synthesized composites also showed low-intensity Raman peaks for $CeVO_4$, indicating crystallinity similar to that of the mechanically mixed composite. The B_{2g} bending mode of the VO_4^{3-} tetrahedra can be identified at 254 cm^{-1} [40]. No impurity phase of CeO_2 was detected because pure CeO_2 exhibits an intense Raman band at 460 cm^{-1} and less intense Raman bands at 239, 590, and 1174 cm^{-1} [41], and none of these peaks were observed in the Raman spectra.

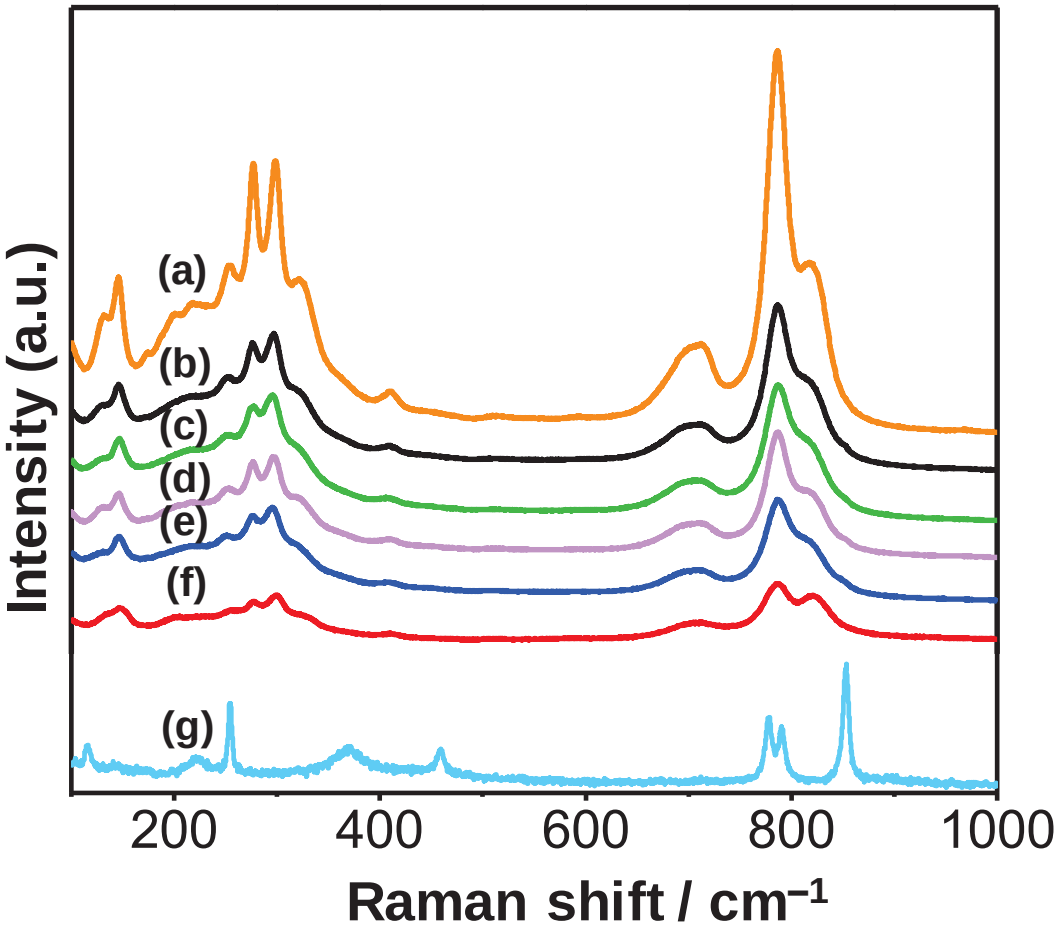

Figure 3.6. Raman spectra of the $Bi_2WO_6/CeVO_4$/allophane composite photocatalysts synthesized with different ratios of Bi_2WO_6:$CeVO_4$: (a) 1:0, (b) 1:0.5, (c) 1:1 (mech. mix.), (d) 1:1, (e) 1:2, (f) 1:3, and (g) 0:1.

When $CeVO_4$ is introduced into Bi_2WO_6 and allophane, the intensities of the Raman bands of $CeVO_4$ dramatically decrease. Only the symmetric (A_{1g}) stretching mode of VO_4^{3-} is shifted

towards lower frequency (821 cm^{-1}), overlapping with the Raman bands of Bi_2WO_6, whereas the intensities of all characteristic Raman bands of Bi_2WO_6 are decreased. These changes might be related to the formation of a BW/CV/A composite that is partly amorphous. The mode-assignable Raman peaks were not clearly observed for allophane, possibly due to the defects in the structure [42]. The results of the Raman spectroscopy analysis confirmed the formation of the BW/CV/A composites.

The nitrogen gas adsorption-desorption isotherms of individual Bi_2WO_6, $CeVO_4$, and allophane and the BW1/CV1/A composites are plotted in Figure 3.7, and the calculated specific surface area (S_{BET}) and total pore volume (V_t) values are listed in Table 3.1. The allophane, $CeVO_4$, and BW1/CV1/A show higher nitrogen gas adsorption and a single hysteresis loop with a type IV isotherm in the IUPAC classification and a steep increase at P/P_0 = 0.7−0.8 due to capillary condensation in the mesopores. According to the IUPAC classification, the nitrogen gas adsorption-desorption isotherms of Bi_2WO_6 is type II, describing the adsorption of nitrogen gas on a non-porous or macroporous adsorbent with strong adsorbate-adsorbent interactions. The BW1/CV05/A composite shows the largest total pore volume (V_t = 0.4107 $mL \cdot g^{-1}$) among the prepared composite samples. The allophane powder possesses a higher specific surface area (S_{BET} = 263 $m^2 \cdot g^{-1}$) in comparison to the Bi_2WO_6 (S_{BET} = 21 $m^2 \cdot g^{-1}$) and $CeVO_4$ (S_{BET} = 85 $m^2 \cdot g^{-1}$) powders. The slight difference between the S_{BET} and V_t values of the mechanically mixed and hydrothermally synthesized BW1/CV1/A composites may be attributed to the collapse of the pores and microstructures during the mechanical mixing. It should be noted that the S_{BET} value of the hydrothermally synthesized BW1/CV1/A composite is much lower than the theoretically expected value. Interestingly, the S_{BET} values of the hydrothermally synthesized composites decreased from 182 to 110 $m^2 \cdot g^{-1}$ and the V_t values decreased from 0.4107 to 0.1541 $mL \cdot g^{-1}$, whereas the average pore size increased from 10.4 to 16.5 nm with increasing the amount of the $CeVO_4$ nanocrystals in the composite, owing to the coverage of the surfaces of the Bi_2WO_6 spheres and allophane particles by a higher number of formed $CeVO_4$ nanocrystals. Comparing the nitrogen gas adsorption-desorption isotherms of allophane and hydrothermally synthesized BW1/CV1/A composite reveals that the porous structure of allophane remained intact during the hydrothermal synthesis of the $CeVO_4$ nanocrystals in the

composite. Thus, a large specific surface area and a moderate amount of mesopores should greatly improve the photocatalytic performance of the BW/CV/A composites.

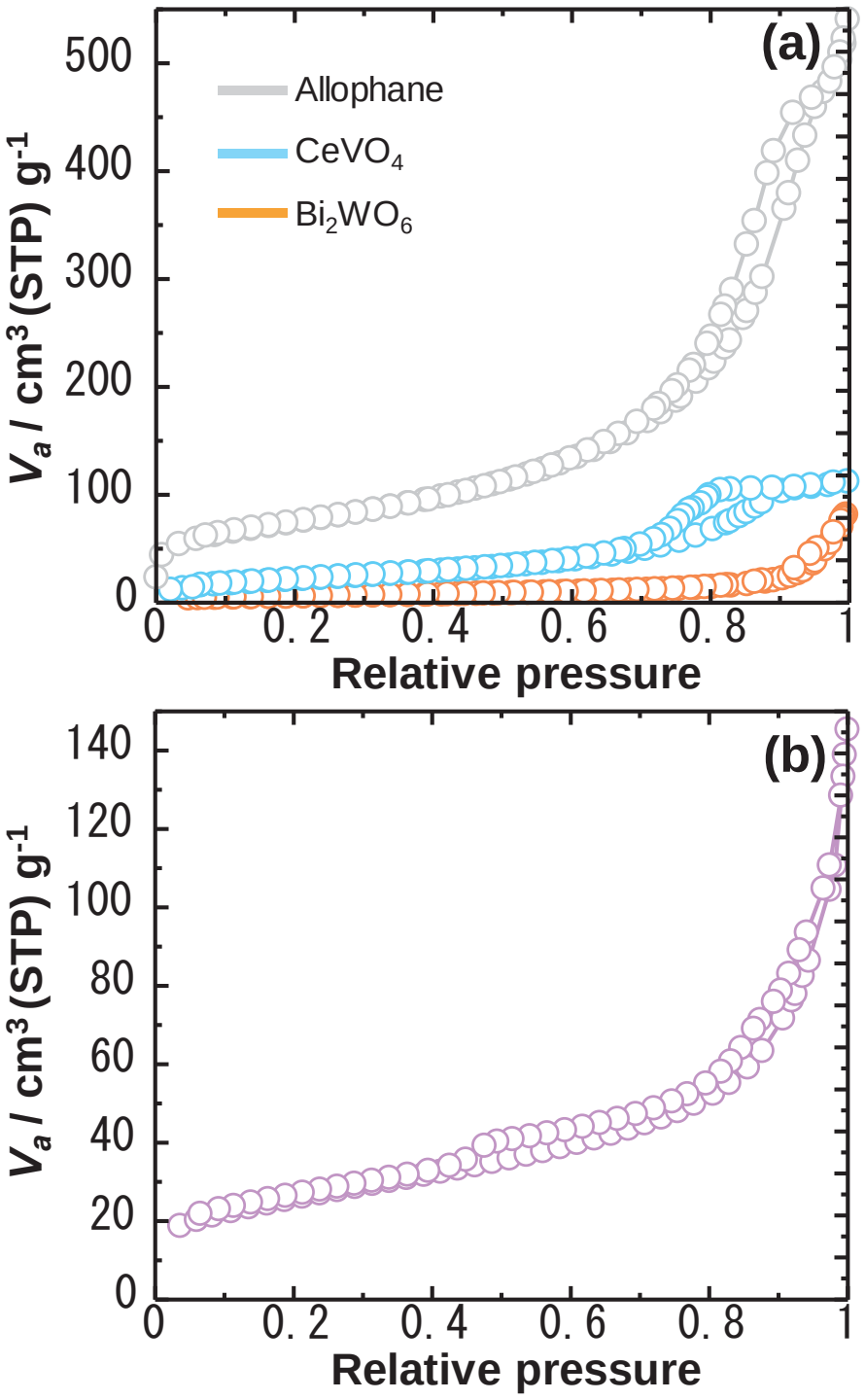

Figure 3.7. N_2 adsorption-desorption isotherms of (a) Bi_2WO_6, $CeVO_4$, and allophane and (b) the Bi_2WO_6/$CeVO_4$/allophane composite photocatalyst synthesized with a Bi_2WO_6:$CeVO_4$ ratio of 1:1.

Figure 3.8a shows the UV-vis diffuse reflectance spectra of the mechanically mixed and hydrothermally synthesized BW/CV/A composites. The absorption edge of the Bi_2WO_6/allophane powder was found to be approximately 450 nm, indicating that it is less responsive to visible light. The Bi_2WO_6/allophane powder has a milky-white color and partially absorbs wavelengths of visible light starting at approximately 325 nm. The $CeVO_4$/allophane nanocrystals are black; thus, they can easily absorb visible light starting at approximately 580 nm. In contrast, the BW/CV/A composites start to absorb light at approximately 400 nm. The optical band-gaps of the prepared composites were estimated by the following equation:

$$\alpha h\nu = A\left(h\nu - E_g\right)^{n/2} \quad (1)$$

where α, $h\nu$, E_g, and A are the absorption coefficient, the photon energy, the optical band-gap, and a constant, respectively, and the n value of Bi_2WO_6 is 1. The calculated optical band-gap of the Bi_2WO_6/allophane powder is 2.5 eV, which is slightly lower than that for the previously reported Bi_2WO_6 samples (E_g = 2.7 eV) [1]. Interestingly, the conflicting band-gap values of 2.0–2.1 [43,44] or 3.25 eV [45] for $CeVO_4$/allophane have been reported. However, the $CeVO_4$ nanocrystals synthesized hydrothermally in this study have an optical band-gap of approximately 0.8 eV. The combined optical band-gap with a blue shift from $CeVO_4$ and a red shift from Bi_2WO_6 was estimated to be in the range of 1.2–1.5 eV for the hydrothermally synthesized BW1/CV0.5/A, BW1/CV1/A, BW1/CV2/A, and BW1/CV3/A composites and the mechanically mixed BW1/CV1/A composite. The maximum shifts in the optical band-gap were observed for the mechanically mixed BW1/CV1/A and hydrothermally synthesized BW1/CV3/A composites due to the small particle sizes observed with increasing $CeVO_4$ content, leading to a blue shift in the absorption edge and an enhancement of the light absorption in the visible region (Figure 3.8b). The light absorbance of the prepared composites is mainly associated with their color deepening from milky white (Bi_2WO_6/allophane) to gray-yellow (BW/CV/A) and finally black ($CeVO_4$/allophane) (Figure 3.8a). Additionally, the intensity of the background absorption increases with the amount of $CeVO_4$ nanocrystals, presumably due to the increased density of defects in the composites. Considering these various factors, an enhancement in visible-light absorbance does not always result in an improvement in photocatalytic activity. Although the light absorbance of the BW1/CV1/A composite shows

only an intermediate enhancement, the band edge undergoes a red shift that is expected to significantly improve the photocatalytic activity of the composite possibly due to the generation of surface oxygen vacancies [46].

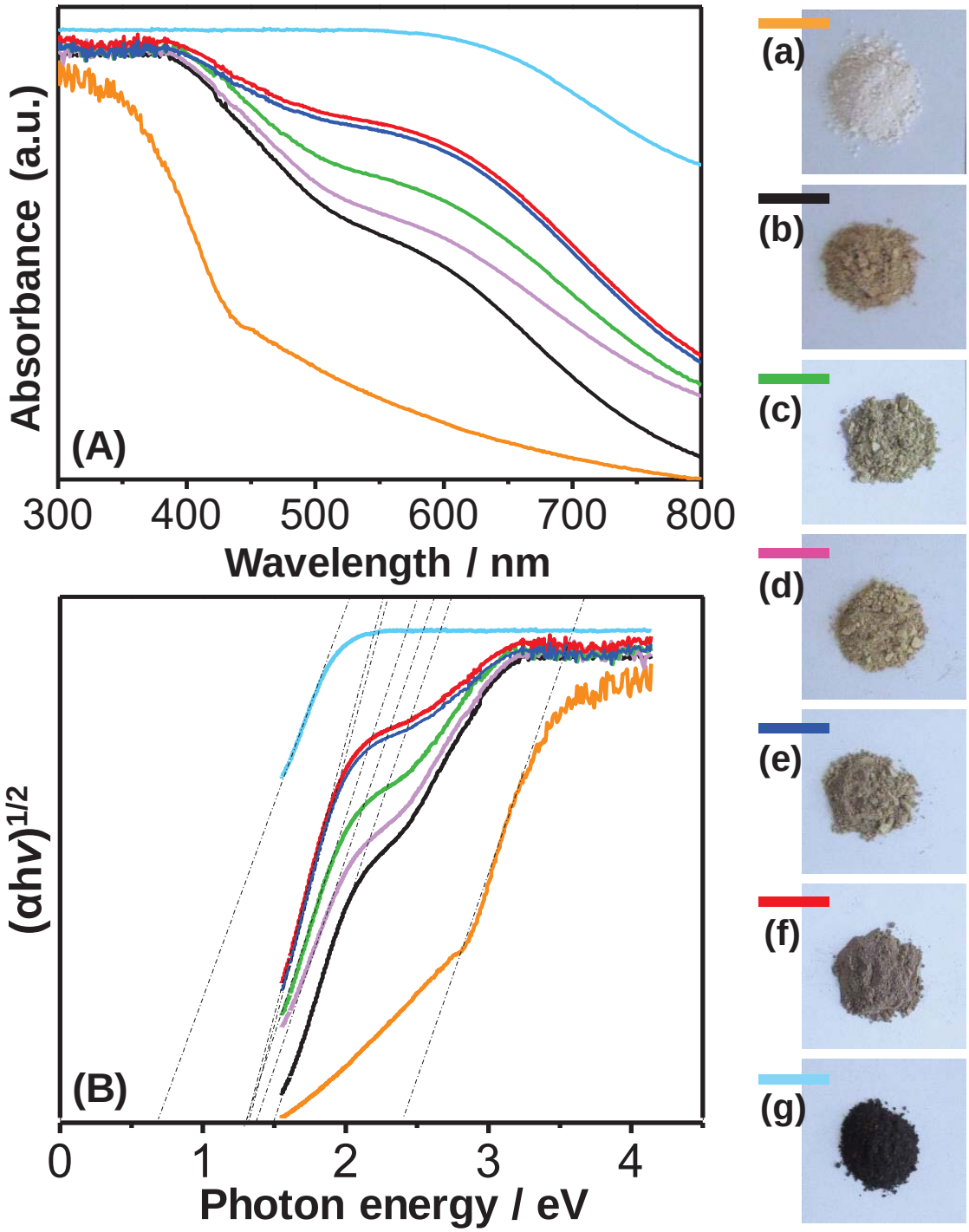

Figure 3.8. (A) UV-vis diffuse reflectance spectra and (B) plots of $(\alpha h\nu)^{1/2}$ versus energy ($h\nu$) of the $Bi_2WO_6/CeVO_4$/allophane composite photocatalysts synthesized with different ratios of Bi_2WO_6:$CeVO_4$: (a) 1:0, (b) 1:0.5, (c) 1:1 (mech. mix.), (d) 1:1, (e) 1:2, (f) 1:3, and (g) 0:1.

Figure 3.9 shows the Bi 4f, W 4f, Ce 3d, V 2p, and O 1s XPS spectra of the BW1/CV1/A composite. The XPS peaks centered at 164.8 and 159.5 eV are assigned to the binding energies of Bi $4f_{5/2}$ and Bi $4f_{7/2}$, respectively, whereas the XPS peaks centered at 37.8 and 35.6 eV are ascribed to the binding energies of W $4f_{5/2}$ and W $4f_{7/2}$, respectively [47]. The Ce 3d XPS spectrum shows two characteristic peaks at 886.1 and 904.1 eV assignable to Ce^{3+}, whereas the Ce 3d XPS peaks centered at 881.4 and 900.2 eV are ascribed to the presence of Ce^{4+}. The Ce 3d XPS spectrum corroborates the presence of a mixed valence state (Ce^{3+} and Ce^{4+}) for the hydrothermally synthesized $CeVO_4$ nanocrystals. The binding energy of V $2p_{3/2}$ is determined to be 516.8 eV, indicating that vanadium mainly exists as V^{5+} in the $CeVO_4$ nanocrystals. Similarly, the O 1s XPS spectrum shows the peaks corresponding to the $CeVO_4$ and Bi_2WO_6 phases. The photoelectrons from the O 1s core level display a relatively wide and asymmetric peak, with the highest point centered at 530.8 eV, and no other peaks characteristic of the metal oxidation states of these metals were detected [40].

3.3.2. Adsorption capacity and photocatalytic activity of the prepared samples

The adsorption and photocatalytic activity of the mechanically mixed and hydrothermally synthesized BW/CV/A composites were evaluated for the adsorption and photodegradation of gaseous acetaldehyde (CH_3CHO), a typical indoor air contaminant, in the dark and under visible-light irradiation, respectively. The adsorption and photodegradation results are shown in Figures 3.10 and 3.11 and Table 3.1. As shown in Figure 3.10(A), the concentration of the injected gaseous acetaldehyde gradually decreased for all samples due to the adsorption process in the dark.

Interestingly, the adsorption of acetaldehyde increased with increasing the content of $CeVO_4$ nanocrystals with respect to the Bi_2WO_6 amount in the following order: 20% for 1:0.5 < 22.2% for 1:1 < 24.4 for 1:2 < 29.8% for 1:3 (Table 3.1). Although the specific surface areas of the composites gradually decreased with increasing the content of $CeVO_4$ nanocrystals (Figures 3.11(A) and (B)), an increase in the adsorption of acetaldehyde is presumably associated with the interaction of $CeVO_4$ nanocrystals with acetaldehyde molecules. In particular, the Bi_2WO_6/allophane and $CeVO_4$/allophane composites showed higher adsorption capacities for gaseous acetaldehyde, which were similar to the capacity of the BW1/CV3/A composite containing an access amount of the $CeVO_4$ nanocrystals (Figure 3.10(A). The

adsorption results demonstrated that hollow allophane spherules and $CeVO_4$ nanocrystals are mainly responsible for the higher adsorption of gaseous acetaldehyde over the prepared composites.

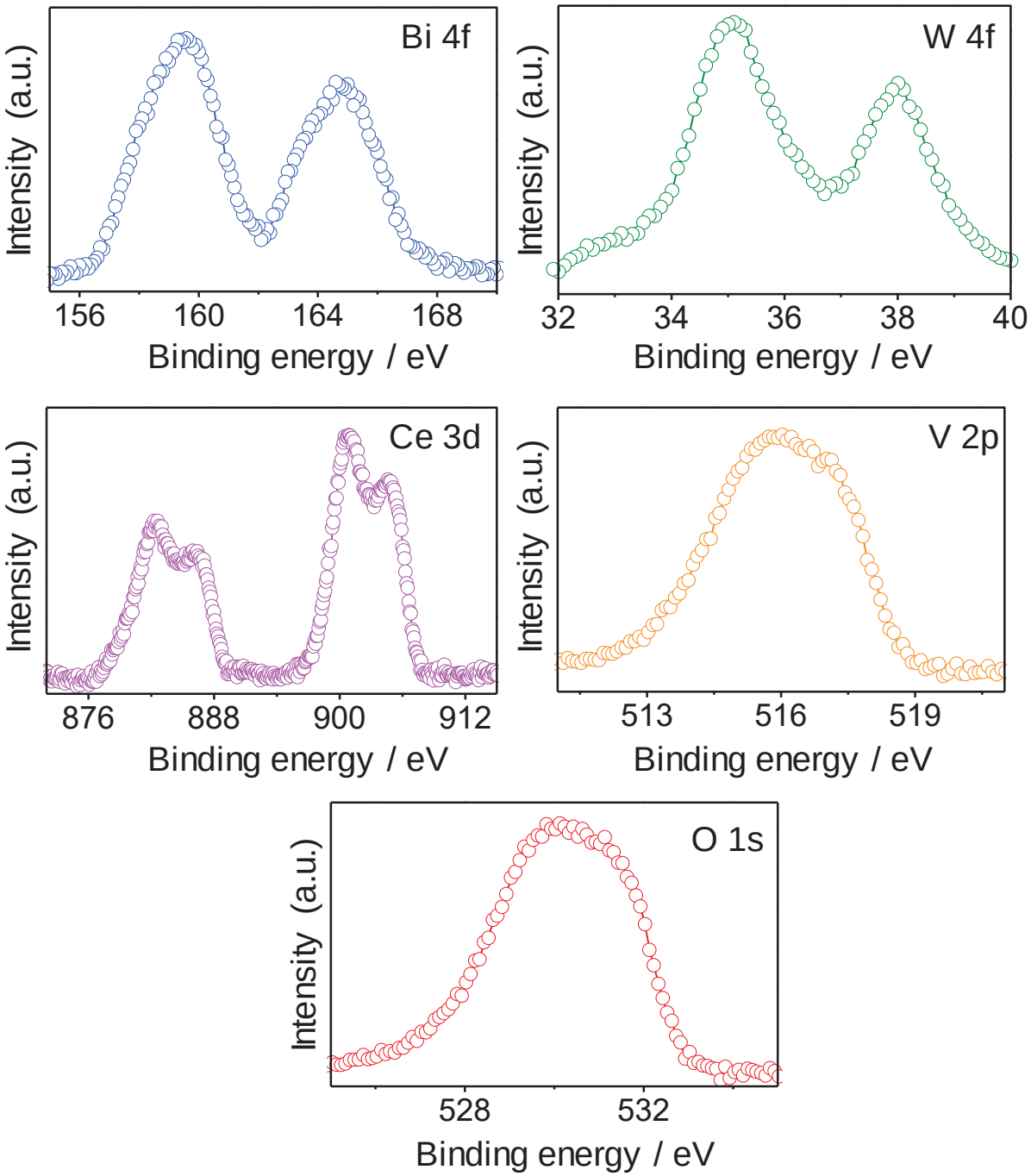

Figure 3.9. Bi 4f, W 4f, Ce 3d, V 2p, and O 1s XPS core-level spectra of the $Bi_2WO_6/CeVO_4$/allophane composite photocatalyst synthesized with a Bi_2WO_6:$CeVO_4$ ratio of 1:1.

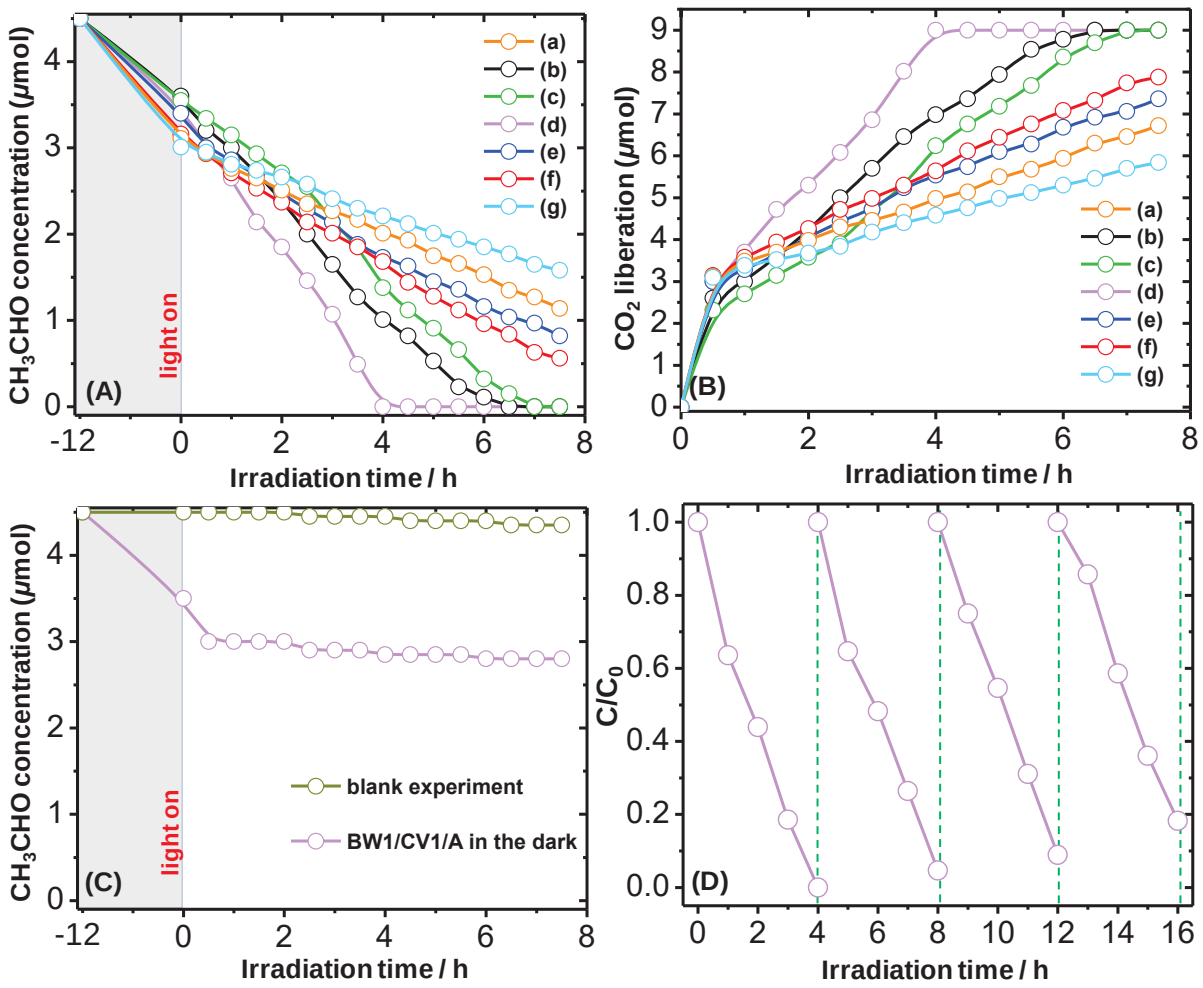

Figure 3.10. (A) Photocatalytic activity for the degradation of gaseous acetaldehyde and (B) CO_2 liberation of the Bi_2WO_6/$CeVO_4$/allophane composites synthesized with different ratios of Bi_2WO_6:$CeVO_4$: (a) 1:0, (b) 1:0.5, (c) 1:1 (mech. mix.), (d) 1:1, (e) 1:2, (f) 1:3, and (g) 0:1. (C) Blank test performed in the absence of photocatalyst under visible light irradiation and degradation of acetaldehyde over the hydrothermally synthesized BW1/CV1/A composite in the dark. (D) Photocatalytic activity for the degradation of gaseous acetaldehyde over the hydrothermally synthesized BW1/CV1/A composite for four cycles.

As shown in Figure 3.10(A) and Table 3.1, the concentration of gaseous acetaldehyde began declining after visible-light irradiation. However, the blank test without photocatalyst under visible-light irradiation and the degradation test in the dark showed no significant change in the concentration of acetaldehyde (Figure 3.10(C)), implying that the presence of photocatalyst and visible light is essential for the photo degradation of acetaldehyde. The

hydrothermally synthesized BW1/CV1/A composite showed higher photocatalytic activity for the degradation of acetaldehyde, as estimated based on the liberation of CO_2, as a final product during the photocatalytic reaction (Figure 3.10(B)) [48]. As shown in Figure 3.10(A), the BW1/CV1/A composite completely mineralized gaseous acetaldehyde within 4 h of the photocatalytic reaction, whereas the hydrothermally synthesized Bi_2WO_6/allophane and $CeVO_4$/allophane composites and the mechanically mixed BW1/CV1/A composite only mineralized gaseous acetaldehyde up to 65, 51, and 69%, respectively. The complete mineralization of gaseous acetaldehyde was achieved only by using the hydrothermally synthesized BW1/CV1/A and BW1/CV05/A composites and the mechanically mixed BW1/CV1/A composite after 7 h of the photocatalytic reaction. The highest photocatalytic activity was observed for the hydrothermally synthesized BW1/CV1/A composite, and a further increase in the content of $CeVO_4$ nanocrystals did not improve the photocatalytic activity of the BW/CV/A composites up to 7 h (100% for BW1/CV0.5/A = 100% for BW1/CV1/A > 81.8% for BW1/CV2/A < 87.6% for BW1/CV3/A). The apparent rate constant of acetaldehyde photodegradation over the prepared composites shows a slight relationship with the specific surface area and reaches a maximum value of 0.356 min^{-1} for BW1/CV1/A with the specific surface area of 154 $m^2 \cdot g^{-1}$ (Figure 3.11(C)). To investigate the recyclability and stability of the prepared composite, the hydrothermally synthesized BW1/CV1/A was tested for four recycling reactions, and the result is shown in Figure 3.10 (D). As shown, the photocatalytic performance of the BW1/CV1/A composite was stable for four cycles with a slight decrease due to the loss of photocatalyst particles during separation after each cycle, suggesting that the prepared BW1/CV1/A composite possesses excellent stability.

The possible mechanism governing the enhancement of the photocatalytic performance of the Bi_2WO_6/$CeVO_4$/allophane composite are based on the band structures of Bi_2WO_6 and $CeVO_4$, the formed *p-n* heterojunction, the co-existence of Ce^{3+} and Ce^{4+} in $CeVO_4$, and the presence of allophane. The valence and conduction bands of Bi_2WO_6 and $CeVO_4$ were estimated according to the previous reports (Figure 3.12) [49–51] Bi_2WO_6 shows a photo-absorption in the wavelength range from UV- to visible-light region shorter than 460 nm, corresponding to the band-gap of 2.8 eV.$CeVO_4$ with a narrow band-gap of 2.0-3.25 eV exhibits a broad absorption in the whole UV-vis region. The UV-absorption of $CeVO_4$ comes from the

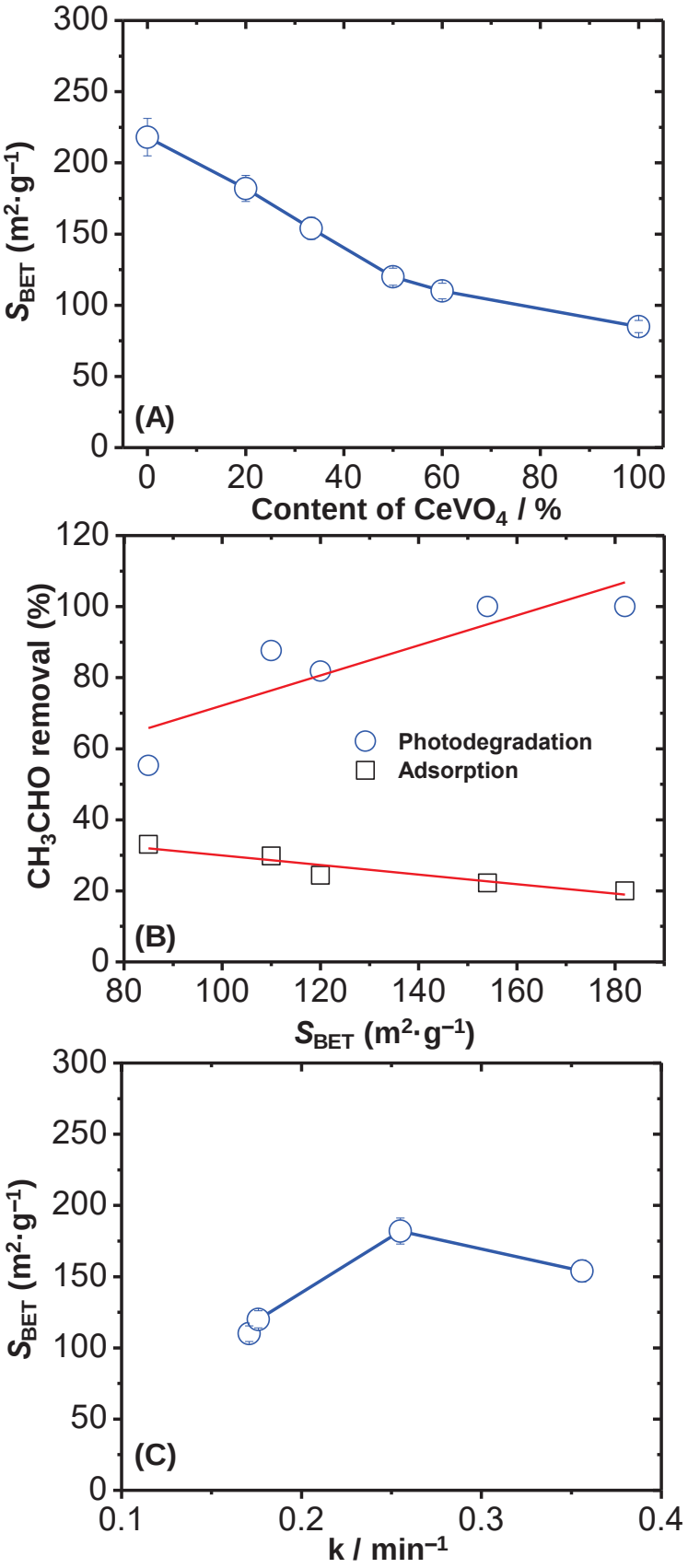

Figure 3.11. Relationship between the specific surface areas (S_{BET}) and (A) the content of $CeVO_4$ nanocrystals, (B) the apparent rate constant, and (C) the removal of acetaldehyde of the prepared composites.

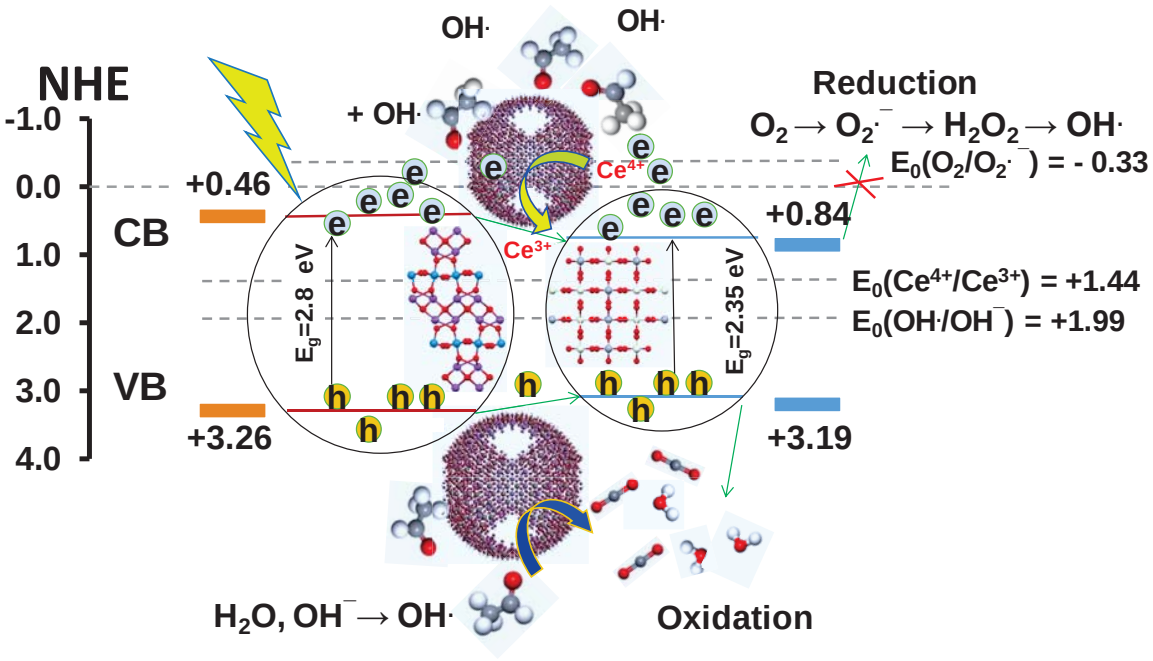

Figure 3.12. Schematic representation of the possible mechanisms of acetaldehyde photodegradation over the $Bi_2WO_6/CeVO_4$/allophane composite under visible-light irradiation.

direct transition from O_2 (2p) and V (3d) to Ce^{+3} (4f), and the visible-light absorption is resulted from the indirect transition between Ce^{3+} (3d) electrons [51]. $CeVO_4$ is a *p*-type semiconductor with a narrow band-gap of 2.2 eV, which can promote the separation and migration of photo-generated charge carriers [52]. The calculated electronic structure of $CeVO_4$ in comparison with the experimental data showed that the Ce orbitals have a considerable impact on the position of the valence and conduction band edges [50]. The electronic structure of BW/CV/A composite near the Fermi level originates largely from the molecular orbitals of the tungstate and vanadate ions [51]. However, the presence of 4f levels between the valence and conduction bands differentiates the electronic structure of $CeVO_4$ and allows lower energy electronic excitations as well as responsible for the dark color of $CeVO_4$ as shown in Figure 3.8.

The BW/CV/A composite can be excited by visible-light irradiation and can generate hole (h^+) and electron (e^-) pairs at the surface of $CeVO_4$ and Bi_2WO_6 if photon energy (hv) matches or exceeds the band-gap energies of those semiconductors. As shown in Figure 3.12, the holes at the valence band of Bi_2WO_6 (3.26 eV) can sequentially migrate to the lower valence band of $CeVO_4$ (3.19 eV) and directly react with acetaldehyde molecules. As the valence bands of

$CeVO_4$ and Bi_2WO_6 are more positive than the standard redox potential $E^{00} = (OH^-/\bullet OH)$ (1.99 V *vs.* NHE), the holes at the valence band of $CeVO_4$ can react with hydroxide ion (OH^-) or water (H_2O) to produce hydroxyl radical (•OH).

$$BW/CV/A + h\nu \rightarrow BW/CV/A + (e^- + h^+) \quad (2)$$

$$(AcH)_{ads} + h^+ \rightarrow (AcH)_{ads}^+ \rightarrow (Intermediate)_{ads} \rightarrow CO_2 + H_2O \quad (3)$$

The degradation path ultimately leads to the formation of the final product - carbon dioxide; however, the intermediate products (e.g., acetic acid) could not be detected by gas chromatography possibly due to their rapid adsorption on the surface of allophane in the BW/CV/A composite during the photocatalytic reaction. The electrons cannot be trapped by molecular oxygen to form superoxide anion radical ($O_2^-\bullet$) and later hydroxyl radicals because the relative conduction band potentials of Bi_2WO_6 (0.43 eV) and $CeVO_4$ (0.84 eV) [49,50] are more positive than the standard redox potential $E^0 = (O_2/O_2^-\bullet)$ (-0.33V *vs.* NHE) and H^+/H_2 reduction potential. However, the formation of a $Bi_2WO_6/CeVO_4$ *p-n* heterojunction is expected to accelerate the separation of photogenerated electron-hole pairs at the surface of Bi_2WO_6 and $CeVO_4$, and the recombination of the photogenerated charge carriers will be greatly reduced. $CeVO_4$ can act as a sensitizer to absorb a greater number of photons from visible light (>500 nm) and the electrons in the valence band of $CeVO_4$ can be excited up to a higher potential edge. The reformed conduction band edge potential becomes more active, and the electrons can react with oxygen to produce $O_2^-\bullet$ that directly attacks acetaldehyde molecules [53,54].

$$(BW/CV/A)(e_{CB}^-) + O_{2(ads)} \neq (BW/CV/A) + O_2^-{}_{(ads.)} \text{ (electron trapping by } O_2 \text{ adsorption)} \quad (4)$$

$$(BW/CV/A)\ (e_{CB}^- + h^+_{VB}) \neq (BW/CV/A) \text{ (charge recombination)} \quad (5)$$

$$CH_3CHO + O_2^-\bullet \rightarrow \text{degradation products} \quad (6)$$

The main contribution of allophane to the enhanced photocatalytic activity is related to its strong affinity to water and acetaldehyde molecules. The competitively adsorbed water molecules on the surfaces of allophane and $Bi_2WO_6/CeVO_4$ can be transformed into the hydroxyl radicals (•OH) by reaction with the photogenerated holes (h^+) or superoxide radicals ($O_2^-\bullet$) at the photocatalyst surface, and the acetaldehyde adsorbed on the surfaces of allophane and photocatalyst is subsequently decomposed into CO_2 by $Bi_2WO_6/CeVO_4$ [14,54].

In addition, the Ce^{3+}/Ce^{4+} pair can act as an electron scavenger and superoxide radical ($O_2^-\bullet$) generator because the photogenerated electrons can be trapped by Ce^{4+}, reducing Ce^{4+} to

Ce^{3+}. Then, Ce^{3+} can be re-oxidized to Ce^{4+} by the adsorbed oxygen in this system. Meanwhile, O_2 adsorbed on the surface of the photocatalyst can react with Ce^{3+} and e^- to generate O_2^-•.

$$Ce^{4+} + e^- \rightarrow Ce^{3+} \quad (7)$$

$$Ce^{3+} + O_2 \rightarrow Ce^{4+} + O_2^-\bullet \quad (8)$$

Therefore, the existence of the Ce^{3+}/Ce^{4+} pair not only can efficiently separate the photogenerated electrons and holes but also facilitates the generation of O_2^-• for the degradation of acetaldehyde molecules. However, excess $CeVO_4$ nanocrystals may cover the active sites of the hierarchical flower-like Bi_2WO_6 particles and act as recombination centers, reducing the separation efficiency of the photogenerated charge carriers. Therefore, the photocatalytic activities of the composites prepared with excess amounts of $CeVO_4$ nanocrystals decreased. Moreover, an optimum amount of the $CeVO_4$ nanocrystals was found in the hydrothermally synthesized BW1/CV1/A composite that showed the highest efficiency of charge separation compared with the mechanically mixed BW1/CV1/A composite [14]. The obtained results therefore suggest that the hydrothermally synthesized $Bi_2WO_6/CeVO_4$/allophane composite can be applied in environmental remediation, particularly for the photodegradation of acetaldehyde under visible-light irradiation.

3.4. Conclusions

In summary, $Bi_2WO_6/CeVO_4$/allophane composites (BW/CV/A) with different amounts of $CeVO_4$ nanocrystals were prepared by mechanical mixing and hydrothermal synthesis. The adsorption capacities and photocatalytic activities of the prepared composites were evaluated for the adsorption and photodegradation of gaseous acetaldehyde in the dark and under visible-light irradiation, respectively. The adsorption of acetaldehyde was strongly dependent on the specific surface area of the composites, and the hydrothermally synthesized BW1/CV1/A (Bi_2WO_6:$CeVO_4$ = 1:1 mass ratio) composite showed the maximum adsorption capacity for acetaldehyde. Additionally, the hydrothermally synthesized BW1/CV1/A composite exhibited higher photocatalytic activity than the mechanically mixed BW1/CV1/A composite and completely mineralized acetaldehyde within 4 h of the photocatalytic reaction. The enhanced photocatalytic activity of the Bi_2WO_6/allophane composite is related to the extended light absorption range of Bi_2WO_6 in the presence of the $CeVO_4$ nanocrystals; the unique structure of the composite prepared with allophane and $CeVO_4$ nanocrystals, which improved the transport

of the reactant and the final product molecules; and the effective separation of photogenerated electron-hole pairs.

3.5. References

[1] Y. Lu, K. Zhao, Y. Zhao, S. Zhu, X. Yuan, M. Huo, Y. Zhang, Y. Qiu, Bi_2WO_6/TiO_2/Pt nanojunction system: A UV–vis light responsive photocatalyst with high photocatalytic performance, *Colloids Surf. A* 481 (2015) 252–260.

[2] J. Zhu, S. Liu, Q. Yang, P. Xu, J. Ge, X. Guo, Fabrication of flower-like Ag@AgCl/Bi_2WO_6 photocatalyst and its mechanism of photocatalytic degradation, *Colloids Surf. A* 489 (2016) 275–281.

[3] D. Peng, Z. Zou, F. Long, J. He, T. Zhang, Solid state synthesis of nonstoichiometric Bi_2WO_6/Bi_2O_3 composites as visible-light photocatalyst, *Ionics* 22 (2016) 2347–2353.

[4] L. Pan, X. Liu, Z. Sun, C.Q. Sun, Nanophotocatalysts *via* microwave-assisted solution-phase synthesis for efficient photocatalysis, *J. Mater. Chem. A* 1 (2013) 8299–8326.

[5] L. Wu, J. Bi, Z. Li, X. Wang, X. Fu, Rapid preparation of Bi_2WO_6 photocatalyst with nanosheet morphology via microwave-assisted solvothermal synthesis, *Catal. Today* 131 (2008) 15–20.

[6] L. Zhou, W. Wang, L. Zhang, Ultrasonic-assisted synthesis of visible-light-induced Bi_2MO_6 (*M* = W, Mo) photocatalysts, *J. Mol. Catal. A* 268 (2007) 195–200.

[7] X. Xu, Y. Ge, H. Wang, B. Li, L. Yu, Y. Liang, K. Chen, F. Wang, Sol–gel synthesis and enhanced photocatalytic activity of doped bismuth tungsten oxide composite, *Mater. Res. Bull.* 73 (2016) 385–393.

[8] C. Yang, Y. Huang, F. Li, T. Li, One-step synthesis of Bi_2WO_6/TiO_2 heterojunctions with enhanced photocatalytic and superhydrophobic property via hydrothermal method, *J. Mater. Sci.* 51 (2016) 1032–1042.

[9] G. Zhu, J. Liang, M. Hojamberdiev, S. Aldabe Bilmes, X. Wei, P. Liu, J. Zhou, Ethylenediamine (EDA)-assisted hydrothermal synthesis of nitrogen-doped Bi_2WO_6 powders, *Mater. Lett.* 122 (2014) 216–219.

[10] F. Wang, W. Li, S. Gu, H. Li, X. Wu, X. Liu, Samarium and Nitrogen Co-Doped Bi_2WO_6 Photocatalysts: Synergistic Effect of Sm^{3+}/Sm^{2+} Redox Centers and N-Doped Level for Enhancing Visible-Light Photocatalytic Activity, *Chem. Eur. J.* 22 (2016) 12859–12867.

[11] H. Huang, K. Liu, K. Chen, Y. Zhang, Y. Zhang, S. Wang, Ce and F Comodification on the Crystal Structure and Enhanced Photocatalytic Activity of Bi_2WO_6 Photocatalyst under Visible Light Irradiation, *J. Phys. Chem. C* 118 (2014) 14379–14387.

[12] P. Ju, P. Wang, B. Li, H. Fan, S. Ai, D. Zhang, Y. Wang, A novel calcined $Bi_2WO_6/BiVO_4$ heterojunction photocatalyst with highly enhanced photocatalytic activity, *Chem. Eng. J.* 236 (2014) 430–437.

[13] Y. Zhu, Y. Wang, Q. Ling, Y. Zhu, Enhancement of full-spectrum photocatalytic activity over $BiPO_4/Bi_2WO_6$ composites, *Appl. Catal. B* 200 (2017) 222–229.

[14] M. Hojamberdiev, K.-i. Katsumata, K. Morita, S. Aldabe Bilmes, N. Matsushita, K. Okada, One-step hydrothermal synthesis and photocatalytic performance of $ZnWO_4/Bi_2WO_6$ composite photocatalyst for efficient degradation of acetaldehyde under UV light irradiation, *Appl. Catal. A* 457 (2013) 12–20.

[15] S.K. Cho, H.S. Park, H.C. Lee, K.M. Nam, A.J. Bard, Metal Doping of $BiVO_4$ by Composite Electrodeposition with Improved Photoelectrochemical Water Oxidation, *J. Phys. Chem. C* 117 (2013) 23048–23056.

[16] X. Xiao, J. Wei, Y. Yang, R. Xiong, C. Pan, J. Shi, Photoreactivity and Mechanism of *g*-C_3N_4 and Ag Co-Modified Bi_2WO_6 Microsphere under Visible Light Irradiation, *ACS Sustainable Chem. Eng.* 4 (2016) 3017–3023.

[17] J. Yang, X. Wang, X. Zhao, J. Dai, S. Mo, Synthesis of Uniform Bi_2WO_6-Reduced Graphene Oxide Nanocomposites with Significantly Enhanced Photocatalytic Reduction Activity, *J. Phys. Chem. C* 119 (2015) 3068−3078.

[18] Z. Sun, J. Guo, S. Zhu, L. Mao, J. Ma, D. Zhang, A high-performance Bi_2WO_6–graphene photocatalyst for visible light-induced H_2 and O_2 Generation, *Nanoscale* 6 (2014) 2186–2193.

[19] R.J. Carmona, L.F. Velasco, M.C. Hidalgo, J.A. Navío, C.O. Ania, Boosting the visible-light photoactivity of Bi_2WO_6 using acidic carbon additives, *Appl. Cat. A* 505 (2015) 467–477.

[20] Y. Chen, C. Xing, S.-l. Ji, H.-b. Liang, Preparation of HPA/Bi_2WO_6 and its photocatalytic properties for denitrification, *J. Fuel Chem. Technol.* 42 (2014) 978–985.

[21] Z. Zhang, H. Liu, J. Xu, N. Zhang, Enhancing the visible light absorption and charge separation of Bi_2WO_6 by hybridizing a CuTCPP sensitizer, *Photochem. Photobiol. Sci.* 16 (2017) 1194–1200.

[22] J. Liu, G. Zhang, Recent advances in synthesis and applications of clay-based photocatalysts: a review, *Phys. Chem. Chem. Phys.* 16 (2014) 8178–8192.

[23] Y. Guo, G. Zhang, H. Gan, Synthesis, characterization and visible light photocatalytic properties of Bi_2WO_6/rectorite composites, *J. Colloid Interface Sci.* 369 (2012) 323–329.

[24] S. Sun, W. Wang, D. Jiang, L. Zhang, X. Li, Y. Zheng, Q. An, Bi_2WO_6 quantum dot-intercalated ultrathin montmorillonite nanostructure and its enhanced photocatalytic performance, *Nano Res.* 7 (2014) 1497–1506.

[25] WHO guidelines for indoor air quality: selected pollutants, World Health Organization, Regional Office for Europe, Copenhagen, Denmark, 2010, p. 454,

[26] http://www.epa.gov/chemfact/s_acetal.txt

[27] D.A. Missia, E. Demetriou, N. Michael, E.I. Tolis, J.G. Bartzis, Indoor exposure from building materials: A field study, *Atmos. Environ.* 44 (2010) 4388–4395.

[28] T. Noguchi, A. Fujishima, P. Sawunyama, K. Hashimoto, Photocatalytic degradation of gaseous formaldehyde using TiO_2 film, *Environ. Sci. Technol.* 32 (1998) 3831–3833.

[29] M. Hojamberdiev, K.-i. Katsumata, N. Matsushita, K. Okada, Preparation of Bi_2WO_6– and BiOI–allophane composites for efficient photodegradation of gaseous acetaldehyde under visible light, *Appl. Clay Sci.* 101 (2014) 38–43.

[30] S. Issarapanacheewin, K. Wetchakun, S. Phanichphant, W. Kangwansupamonkon, N. Wetchakun, Efficient photocatalytic degradation of Rhodamine B by a novel CeO_2/Bi_2WO_6 composite film, *Catal. Today* 278 (2016) 280–290.

[31] Y.-H.B. Liao, J.X. Wang, J.-S. Lin, W.-H. Chung, W.-Y. Lin, C.-C. Chen, Synthesis, photocatalytic activities and degradation mechanism of Bi_2WO_6 toward crystal violet dye, *Catal. Today* 174 (2011) 148–159.

[32] M. Niu, R. Zhu, F. Tian, K. Song, G. Cao, F. Ouyang, The effects of precursors and loading of carbon on the photocatalytic activity of C–$BiVO_4$ for the degradation of high concentrations of phenol under visible light irradiation, *Catal. Today* 258 (2015) 585–594.

[33] A.Y. Booshehri, M.I. Polo-Lopez, M. Castro-Alférez, P. He, R. Xu, W. Rong, S. Malato, P. Fernández-Ibáñez, Assessment of solar photocatalysis using Ag/$BiVO_4$ at pilot solar Compound Parabolic Collector for inactivation of pathogens in well water and secondary effluents, *Catal. Today* 281 (2017) 124–134.

[34] C. Jaramillo-Páez, J.A. Navío, M.C. Hidalgo, A. Bouziani, M. El Azzouzi, Mixed α-Fe_2O_3/Bi_2WO_6 oxides for photo-assisted hetero-Fenton degradation of Methyl Orange and Phenol, *J. Photochem. Photobiol. A* 332 (2017) 521–533.

[35] Y. Shen, Y. Huang, S. Zheng, X. Guo, Z.-X. Chen, L. Peng, W. Ding, Nanocrystals of $CeVO_4$ Doped by Metallic Heteroions, *Inorg. Chem.* 50 (2011) 6189–6194.

[36] J. Ren, Y.Z. Wu, H. Zou, Y. Dai, D.W. Sha, M. Chen, J.J. Wang, J.M. Pan, X.H. Yan, Synthesis of a novel $CeVO_4$/graphitic C_3N_4 composite with enhanced visible-light photocatalytic property, *Mater. Lett.* 183 (2016) 219–222.

[37] Y. Ono, K.-i. Katsumata, Enhanced photocatalytic activity of titanium dioxide/allophane mixed powder by acid treatment, *Appl. Clay Sci.* 90 (2014) 61–66.

[38] X. Weng, Q. Yang, L. Wang, L. Xu, X. Sun, J. Liu, General synthesis and self-assembly of lanthanide orthovanadate nanorod arrays, *CrystEngComm* 15 (2013) 10230–10237.

[39] M. Mączka, A.F. Fuentes, L. Kępiński, M.R. Diaz-Guillen, J. Hanuza, Synthesis and electrical, optical and phonon properties of nanosized Aurivillius phase Bi_2WO_6, *Mater. Chem. Phys.* 120 (2010) 289–295.

[40] Q.Q. Liu, C.Y. Fan, H. Tang, T.D. Ma, J.Y. Shen, One-step synthesis of recycled 3D $CeVO_4$/*r*GO composite aerogels for efficient degradation of organic dyes, *RSC Adv.* 6 (2016) 85779–85786.

[41] F. Luo, C.-J. Jia, R. Liu, L.-D. Sun, C.-H. Yan, Nanorods-assembled $CeVO_4$ hollow spheres as active catalyst for oxidative dehydrogenation of propane, *Mater. Res. Bull.* 48 (2013) 1122–1127.

[42] B. Creton, D. Bougeard, K.S. Smirnov, J. Guilment, O. Poncelet, Structural Model and Computer Modeling Study of Allophane, *J. Phys. Chem. C* 112 (2008) 358–364.

[43] P.A. Deshpande, G. Madras, Photocatalytic degradation of dyes over combustion-synthesized $Ce_{1-x}Fe_xVO_4$, *Chem. Eng. J.* 158 (2010) 571–577.

[44] M. Mosleh, A. Mahinpour, Sonochemical synthesis and characterization of cerium vanadate nanoparticles and investigation of its photocatalyst application, *J. Mater. Sci.: Mater. Electron.* 27 (2016) 8930–8934.

[45] H.J. Huang, W.L. She, L.W. Yang, Mechanism of $CeVO_4/TiO_2$ Photocatalytic Degradation of VOCs under Visible Light Irradiation: Electrochemical, Photoluminescence and Active Oxygen Species Study, *Appl. Mech. Mater.* 217–219 (2012) 853–856.

[46] Y. Lv, W. Yao, R. Zong, Y. Zhu, Fabrication of Wide–Range–Visible Photocatalyst Bi_2WO_{6-x} nanoplates via Surface Oxygen Vacancies, *Sci. Rep.* 6 (2016) 9 pages, doi:10.1038/srep19347

[47] R. Tang, H. Su, Y. Sun, X. Zhang, L. Li, C. Liu, B. Wang, S. Zeng, D. Sun, Facile Fabrication of Bi_2WO_6/Ag_2S Heterostructure with Enhanced Visible-Light-Driven Photocatalytic Performances, *Nanoscale Res. Lett.* 11 (2016) 126 (12 pages).

[48] B. Neppolian, S. Mine, Y. Horiuchi, C.L. Bianchi, M. Matsuoka, D.D. Dionysiou, M. Anpo, Efficient photocatalytic degradation of organics present in gas and liquid phases using Pt-TiO_2/Zeolite (H-ZSM), *Chemosphere* 153 (2016) 237–243.

[49] Z. Zhang, W. Wang, L. Wang, S. Sun, Enhancement of Visible-Light Photocatalysis by Coupling with Narrow-Band-Gap Semiconductor: A Case Study on Bi_2S_3/Bi_2WO_6, *ACS Appl. Mater. Interfaces* 4 (2012) 593–597.

[50] M. Liu, Z.-L. Lv, Y. Cheng, G.-F. Ji, M. Gong, Structural, elastic and electronic properties of $CeVO_4$ via first-principles calculations, *Comp. Mater. Sci.* 79 (2013) 811–816.

[51] M.R. Dolgos, A.M. Paraskos, M.W. Stoltzfus, S.C. Yarnell, P.M. Woodward, The electronic structures of vanadate salts: Cation substitution as a tool for band gap manipulation, *J. Solid State Chem.* 182 (2009) 1964–1971.

[52] C.T.G. Petit, R. Lan, P.I. Cowin, J.T.S. Irvine, S. Tao, Structure, conductivity and redox reversibility of Ca-doped cerium metavanadate, *J. Mater. Chem.* 21 (2011) 8854–8861.

[53] Y. Xiang, P. Ju, Y. Wang, Y. Sun, J. Yu, Chemical etching preparation of the Bi_2WO_6/BiOI p–n heterojunction with enhanced photocatalytic antifouling activity under visible light irradiation, *Chem. Eng. J.* 288 (2016) 264–275.

[54] K.-i. Katsumata, X. Hou, M. Sakai, A. Nakajima, A. Fujishima, N. Matsushita, K.J.D. MacKenzie, K. Okada, Visible-light-driven photodegradation of acetaldehyde gas catalyzed by aluminosilicate nanotubes and Cu(II)-grafted TiO_2 composites, *Appl. Catal. B* 138–139 (2013) 243–252.

CHAPTER 4: Influence of BiOI content on the photocatalytic activity of Bi_2WO_6/BiOI/allophane composites and molecular modeling studies of acetaldehyde adsorption

4.1. Introduction

In modern urban life, indoor air quality has become an important health issue, particularly for those people who spend a large portion of their lives at home, offices, shopping centers, schools, day care centers, retirement homes, public buildings, health care facilities and other special buildings [1]. Indoor air quality can be affected by hazardous chemical substances emitted from buildings, construction and decoration materials, indoor equipment or even human activities [2]. In the World Health Organization (WHO) guidelines for indoor air quality [3], chemical pollutants are divided into two categories based on the existence of indoor sources, the availability of toxicological and epidemiological data, and whether indoor levels exceed those of health concern and/or the lowest observed adverse effect level. Group 1 includes benzene, carbon monoxide, formaldehyde, naphthalene, nitrogen dioxide, particulate matter ($PM_{2.5}$ and PM_{10}), polycyclic aromatic hydrocarbons (benzo-[*a*]-pyrene), radon, trichloroethylene and tetrachloroethylene, for which the guidelines for indoor air quality must be followed. In Group 2, acetaldehyde, asbestos, biocides, pesticides, flame retardants, glycol ethers, hexane, nitric oxide, ozone, phthalates, styrene, toluene, and xylenes are included as indoor air pollutants of potential interest. Exposure to the pollutants listed in Group 1 has critical consequences, including leukemia, genotoxicity, ischemic heart disease, respiratory tract lesions, respiratory infection, lung cancer, and renal disease. Although acetaldehyde (AcH), as a major indoor volatile organic compound, is included in Group 2, it is still toxic when applied externally for prolonged periods, an irritant, and a probable carcinogen [4]. The main sources of acetaldehyde in houses include building materials, laminate, linoleum, wooden varnished, cork/pine flooring, automotive exhaust and tobacco smoke. It is also found in plastic water-based and matt emulsion paints, wood ceilings, and wooden, particle-board, plywood, pine wood, and chipboard furniture [5,6].

Since the Honda-Fujishima effect was first reported in 1972 [7], semiconductor-based photocatalysis has been regarded as one of the promising strategies for water splitting and the

removal of organic compounds in contaminated water and air by the generation of hydroxyl radicals. The degradation of gaseous AcH over TiO_2 was initially studied by Sopyan et al. [8] under UV light irradiation, who found that AcH oxidation can be mediated not only by photogenerated holes but also by adsorbed oxygen, superoxide radicals and/or hydrogen peroxide. Visible light makes up 43% of solar energy while UV light only constitutes about 3–5% [9] of it, and the fraction of UV light available is low in indoor and inside-vehicle applications. Later, various visible light-active photocatalysts, e.g., $CuBi_2O_4/WO_3$ [10], $CaFe_2O_4/WO_3$ [11], $RbBi_2Nb_5O_{16}$ and $RbBiNb_2O_7$ [12], CuO/WO_3 and Pt/WO_3 [13], Pd/WO_3 [14], $NaBiO_3$-loaded WO_3 [15], Rh-doped $SrTiO_3$ [16], etc., were examined for the degradation of AcH. The photocatalytic activity for the oxidative photodegradation of AcH by visible light-responsive Pt/WO_3 was greatly enhanced by hybridizing it with siliceous mordenite (MOR), a zeolite adsorbent with a hydrophobic surface [17]. Katsumata et al. [18] demonstrated the synergistic effect of g-C_3N_4 and WO_3 on the photodegradation of AcH though the improvement of photogenerated carrier separation.

Bismuth-based semiconductors are regarded as a promising group of advanced photocatalytic materials due to their suitable band gap for visible light response, an increased mobility of photogenerated charge carriers because of well-dispersed Bi 6s orbital, non-toxicity, and easy tailoring of their morphologies. A wide variety of bismuth-based semiconductors (Bi_2O_3, Bi_2MO_6 (M = Cr, Mo, and W), $BiVO_4$, $BiOX$ (X = Cl, Br and I), $BiPO_4$, $(BiO)_2CO_3$, and pentavalent bismuthates) have been studied for the degradation of organic pollutants in wastewater (e.g., dye pollutants), oxidation of gaseous pollutants (e.g., NO), and photo reduction of CO_2, and photocatalytic water splitting to generate H_2 and O_2.

As one of the simplest members of the Aurivillius oxide family of layered perovskites, Bi_2WO_6 is structurally composed of alternating perovskite-like blocks (BO_6 octahedra) and fluorite-like Bi_2O_2 layers (Figure 4.1) [19]. Having an optical band gap of 2.80 eV, Bi_2WO_6 exhibited a high level of photocatalytic activity for the mineralization of acetaldehyde and acetic acid [20,21]. Furthermore, coupling of this semiconductor with other semiconductors [22,23] or metals [24,25] to form a junction structure was found to enhance its photocatalytic activity by improving charge separation, increasing the lifetime of charge carriers, and enhancing the efficiency of interfacial charge transfer.

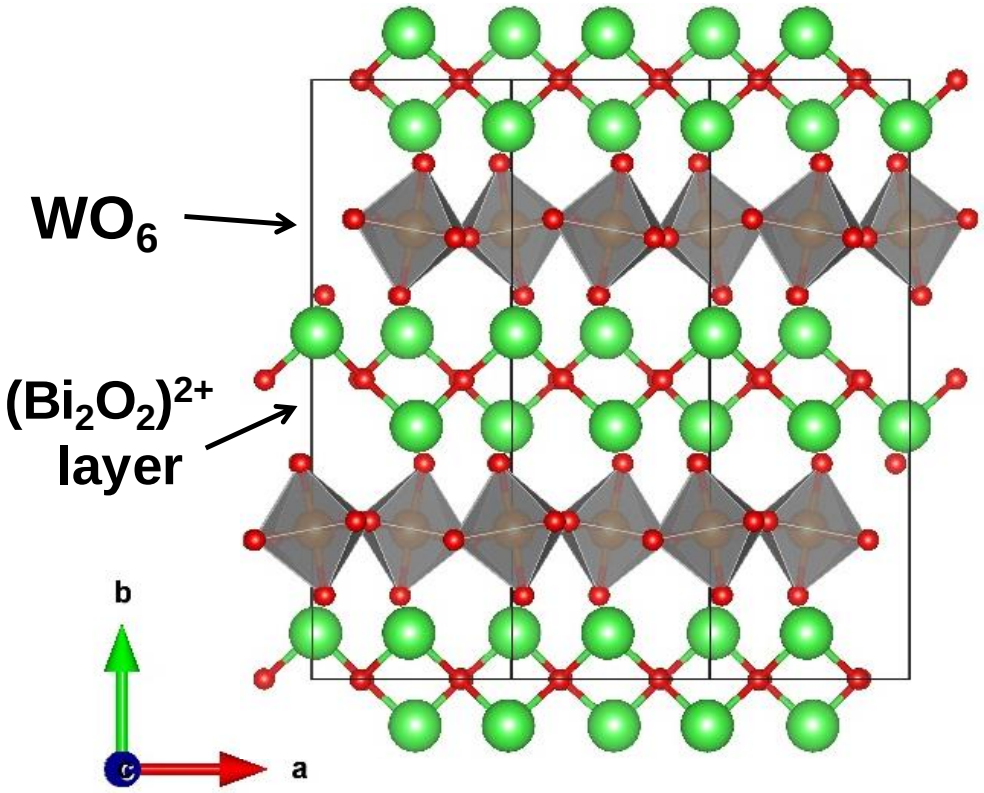

Figure 4.1. An idealized crystal structure of Bi_2WO_6.

Generally, the photocatalytic activities of photocatalysts are influenced by physicochemical variables such as particle size, crystallinity, specific surface area, pore volume, and pore size. Various porous materials such as silica gels, zeolites, activated carbons, and clay minerals with high specific surface areas and suitable pore volumes were reported to improve photocatalytic activities and separation of the photocatalyst powders after the reaction. Since allophane ($1–2SiO_2 \cdot Al_2O_3 \cdot 5–6H_2O$) with a 3.5–5.0 nm sized hollow spherical structure can adsorb ionic or polar pollutants due to its amphoteric ion-exchange activity and high surface area [26–28], combining it with Bi_2WO_6 and BiOI resulted in the improved photodegradation of gaseous acetaldehyde under visible light [29].

Herein, we demonstrate the synthesis of a Bi_2WO_6/BiOI/allophane (BW/BI/A) composite and the influence of the BiOI content on visible-light-induced photodegradation of gaseous acetaldehyde by the composite. The findings suggest that the synergistic effects of Bi_2WO_6/BiOI and photocatalyst/allophane can enhance the photocatalytic activity of the synthesized composite, whereas controlling the amount of BiOI is paramount in determining

the maximum efficiency of the BW/BI/A composite. Integrating Bi_2WO_6/BiOI on allophane makes the composite mechanically robust and easy to handle in the reaction systems.

4.2. Experimental

4.2.1. Synthesis

$Bi(NO_3)_3 \cdot 5H_2O$ (99.9%), KI (99.5%), ethylene glycol (99.0%), and aqueous ammonia (28%) were obtained from Wako Pure Chemical Industries, Ltd. Deionized water (Millipore Milli-Q Plus purification system, 18.2 MΩ·cm) was used throughout the experiments. Bi_2WO_6 and allophane powders were synthesized according to a previously reported experimental procedure [23]. The Bi_2WO_6/BiOI/allophane (BW/BI/A) composite was processed by a hydrothermal method. The experimental details are as follows: first, 0.5 mmol of $Bi(NO_3)_3 \cdot 5H_2O$ was dissolved in 10 mL of ethylene glycol and 0.5 mmol of KI was dissolved in 10 mL of deionized water. Then, 0.3489 g of the as-synthesized Bi_2WO_6 powder (0.5 mmol) and 0.3489 g of allophane powder (BW/A = 1:1 mass ratio) were dispersed into 10 mL of deionized water. To obtain the BW/BI/A composite, the two precursor solutions were mixed together with 10 mL of the aqueous suspension of Bi_2WO_6 and allophane under vigorous stirring at room temperature for 30 min. The pH of the suspension was adjusted to 7 by introducing aqueous ammonia. After stirring for 30 min, the orange-red-colored suspension was transferred into a 40 mL Teflon-lined stainless steel autoclave. The autoclave was sealed and maintained at 180°C for 12 h. After the hydrothermal synthesis, the autoclave was cooled down to room temperature naturally. The resulting precipitate was collected by centrifugation, washed with deionized water several times and dried at 80°C for 8 h. To study the influence of the amount of BiOI, the molar ratio of Bi_2WO_6:BiOI (BW:BI) was varied while keeping the amount of Bi_2WO_6 and allophane unchanged. The compositions and porous properties of the composites are listed in Table 4.1.

4.2.2. Characterization

The crystalline phases were identified by X-ray powder diffraction (XRD) using an RINT-2100 diffractometer (Rigaku) with monochromated Cu Kα radiation (λ = 1.5405 Å) at 40 kV and 40 mA. The powder samples were scanned at a scanning rate of $2° \cdot min^{-1}$ in the 2θ range of 10–70°. The formation of crystalline phases was also confirmed by a T64000 Raman

Table 4.1. The compositions and porous properties of samples.

Sample name	Composition	S_{BET}, $m^2 \cdot g^{-1}$	V_p, $mL \cdot g^{-1}$	Pore size, nm	k, min^{-1}
BW	Bi_2WO_6	21.3	0.1126	14.1	-0.10982
BI	BiOI	23.1	0.1592	25.8	-0.27800
A	Allophane	263.0	0.7895	7.98	–
Bi_2WO_6/BiOI/Allophane composite	Molar ratio of Bi_2WO_6:BiOI				
BW/0.5BI/A	1:0.5	174	0.3805	9.7	-0.67214
BW/1BI/A	1:1	106	0.2047	12.5	-0.44300
BW/2BI/A	1:2	96	0.1895	15.2	-0.23418
BW/3BI/A	1:3	84	0.1713	17.8	-0.22209
BW/1BI/A (mechanically mixed)	1:1 (mech.mix.)	81	0.1549	20.1	-0.33833

spectrometer (Horiba Jobin Yvon S.A.S.) with an Ar laser (514.5 nm) operated at 50 mW. The particle morphologies and sizes were examined using an S-4500 ultra-high-resolution scanning electron microscope (Hitachi) operated at an accelerating voltage of 15 kV. Transmission electron microscopy (TEM) was performed on powder samples using a JEM-2010UHR (JEOL) operated at an accelerating voltage of 200 kV to distinguish the crystal structures and particle sizes in the composites. For the TEM observations, the powder sample was dispersed in cyclohexane by sonication, and a small amount of the suspension was dropped onto the holey carbon grid. The UV-vis diffuse reflectance spectra of the samples were recorded in the wavelength range of 200–600 nm on a Lambda 950 UV/VIS/NIR spectrophotometer (Perkin-Elmer) equipped with an integrating sphere, and $BaSO_4$ was used as a reference. The optical band gaps of the prepared composites were estimated by the following equation:

$$\alpha h\nu = A\left(h\nu - E_g\right)^{n/2} \quad (1)$$

where α, hν, E_g, and A are the absorption coefficient, the photon energy, the optical band gap, and a constant, respectively. The n value is 1, which determines the transition state of the semiconductor. The porous properties of the samples were investigated by determining their nitrogen gas adsorption-desorption isotherms at 77 K using an Autosorb-3B instrument (Quantachrome Instruments). The samples were preheated at 150°C for 4 h under vacuum before the measurement. The specific surface area (S_{BET}) was calculated by the Brunauer, Emmett and Teller (BET) method from the linear portion of the adsorption isotherm. The pore size distribution (PSD) was calculated by the Barrett, Joyner and Halenda (BJH) method from the desorption branch of the isotherm. The surface chemical states of the elements were evaluated by X-ray photoelectron spectroscopy (XPS, JPS-9010 MC, JEOL) using Mg Kα radiation (1253.6 eV).

4.2.3. Adsorption and photocatalytic activity tests

Acetaldehyde (AcH) was selected as a probe molecule for evaluating the adsorption and photocatalytic performance of the samples under visible-light irradiation. The photodegradation of AcH in a batch-type reactor over the samples was conducted at room temperature. The photocatalyst sample (50 mg) was placed in a 500 mL reaction vessel made of Pyrex® glass, and the lid, inlet, and outlet were firmly sealed. Pure air (Taiyo Nippon Sanso Corp.) was blown through the reaction vessel at room temperature to remove any air contaminants. Then, a certain amount of AcH was introduced into the reaction vessel using a 2-mL Pressure-Lok® glass syringe until the concentration of AcH in the reaction vessel reached 200 ppm. After adsorption equilibration in the dark for 24 h, the reaction vessel was placed under an FL10 W white fluorescent daylight lamp (>400 nm, Toshiba) that emitted visible light with an irradiance of ~8000 lux, as measured with an LX-101A light meter (Lutron Electronic Enterprise Co., Ltd.). To eliminate UV from the light source, an SC42 cutoff filter (<420 nm, Fujifilm) was used. The decrease in AcH concentration and the increase in CO_2 concentration were monitored using a GC-2014 gas chromatograph (Shimadzu) equipped with a 2-m Porapak-Q column, a methanizer and a flame ionization detector, using N_2 as the carrier gas.

4.3. Results and Discussion

4.3.1. Characterization of the prepared samples

Figure 4.2 shows the XRD patterns and SEM images of the as-synthesized Bi_2WO_6, BiOI, and allophane. The diffraction peaks can be indexed to orthorhombic-phase Bi_2WO_6 with a space group of *Pbca*, tetragonal-phase BiOI with a space group of *P*4/*nmm*, and allophane and agree well with the International Centre for Diffraction Data Powder Diffraction File (ICDD PDF) data for Bi_2WO_6 (ICDD PDF# 39–0256), BiOI (ICDD PDF# 10–0445) and allophane (ICDD PDF# 38–0449) reported previously. Note that no diffraction peaks assignable to impurity phases are observed in the XRD patterns. The sharp and intense diffraction peaks of BiOI powders indicate their relatively high crystallinity compared to the Bi_2WO_6 and allophane powders. Since allophane is X-ray amorphous, its XRD pattern has two halo peaks at $2\theta = 27°$ and 40° corresponding to the (002) and (040) planes. The mean crystallite sizes of the Bi_2WO_6 and BiOI powders calculated from the full width at half maximum (FWHM) of the most intense diffraction peaks *131* and *102* at $2\theta = 28.31°$ and 29.64° using the Scherrer equation are found to be approximately 10 and 18 nm, respectively.

The SEM and TEM images shown in Figures 4.2 and 4.3 demonstrate that the as-synthesized Bi_2WO_6 particles have a flower-like morphology, assembled by ultrathin nanosheets, with an average size of 1.5 μm. Similarly, the as-synthesized BiOI sample also contains aggregated flower-like spheroids that are more densely constructed by ultrathin nanosheets with an average size of 1–1.5 μm. The allophane spherules (3–4 nm) are highly aggregated, forming the globular clusters with an average size of 100–300 nm that further agglomerate to produce large chunky aggregates with the sizes of 1–3 μm. Figure 4.3 shows the TEM images of individual Bi_2WO_6, BiOI, and allophane samples. The TEM images in Figures 4.3a and c show that the Bi_2WO_6 and BiOI particles are assembled by ultrathin and elongated nanosheets, respectively. In Figure 4.3b, the HR-TEM image indicates that the continuous lattice fringes with an interplanar spacing of 4.1 Å correspond to the (040) lattice planes of orthorhombic Bi_2WO_6. The six sides of the Bi_2WO_6 nanosheets may be surrounded by the {100}, {141}, and {101} planes [30]. The HR-TEM image of the BiOI nanosheet in Figure 4.3d exhibits highly regular lattice fringes with an interlayer distance of approximately 2.8 Å, agreeing well with the $(1\bar{1}0)$ lattice plane of tetragonal BiOI. The mainly exposed facet of the BiOI nanosheets was estimated to be the {001} plane. The measured angle in the FFT pattern is approximately 45°, which is consistent with the theoretically calculated angle between the

(110) and (200) planes. The low- and high-magnification TEM images in Figures 4.3e and f clearly show hollow allophane spherules with an outer diameter of approximately 5 nm and small pores measuring 0.3–0.5 nm on the surface. The allophane spherules are highly aggregated into globular clusters with an average size of 100–300 nm. According to the SEM results, these globular clusters can further agglomerate to form large, chunky aggregates measuring 1–3 μm [30]. The fast Fourier transform (FFT) patterns confirm the amorphous structure of the allophone and the single-crystalline natures of the Bi_2WO_6 and BiOI nanosheets (insets of Figures 4.3b, d, and f).

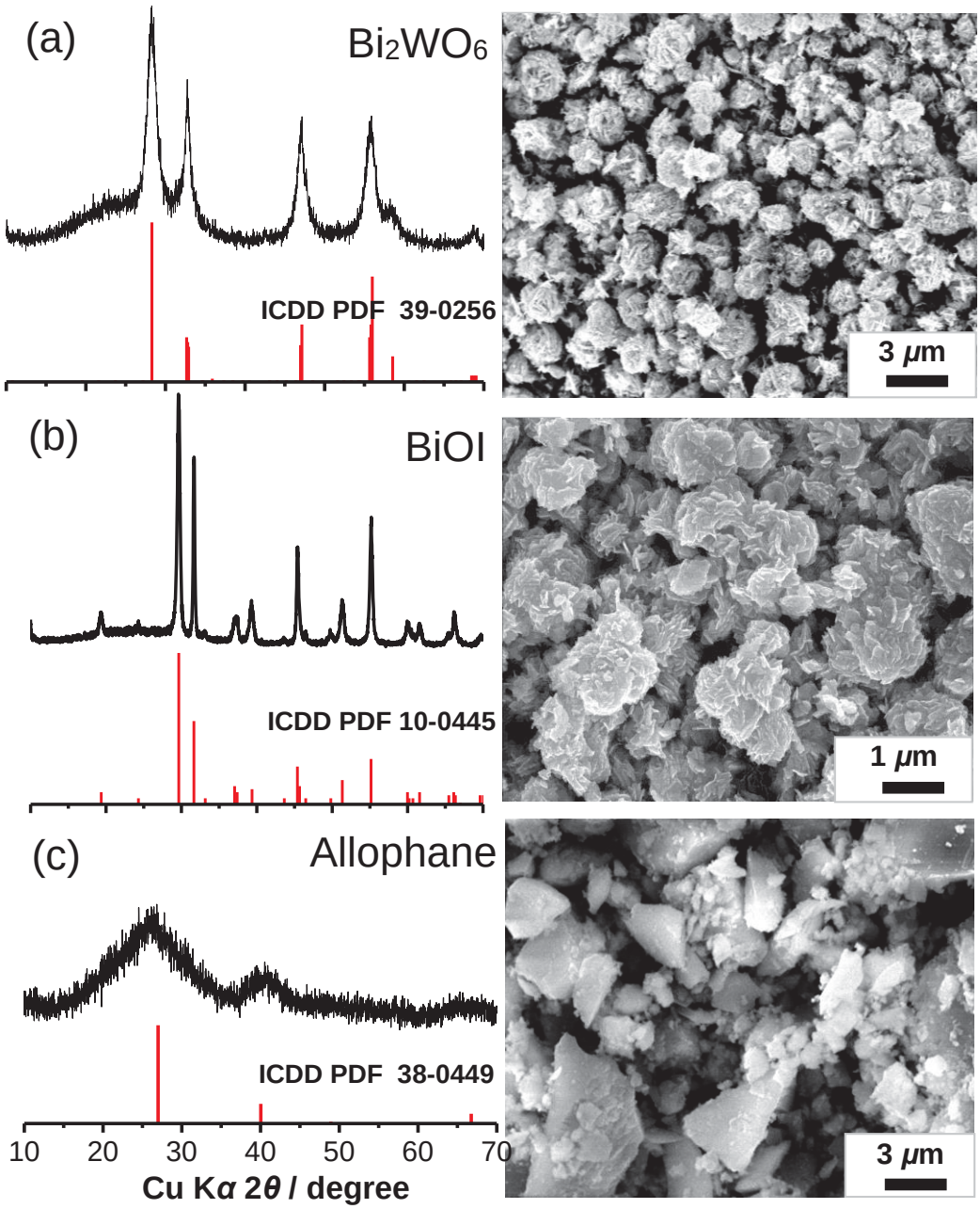

Figure 4.2. XRD patterns and SEM images of (a) Bi_2WO_6, (b) BiOI, and (c) allophane.

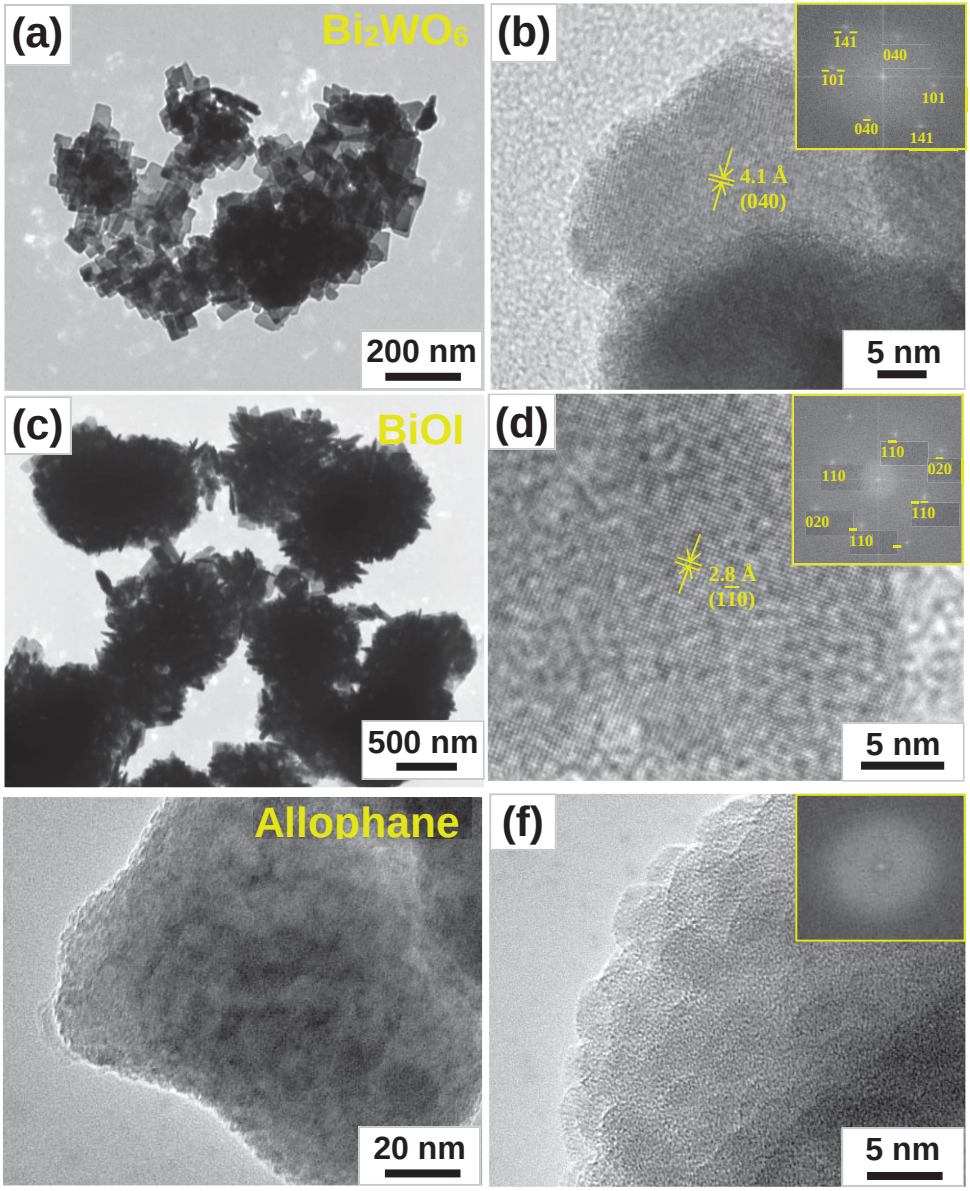

Figure 4.3. TEM and HR-TEM images and FFT patterns (*inset*) of (a,b) Bi_2WO_6, (c,d) BiOI, and (e,f) allophane.

The XRD patterns of the mechanically mixed and the hydrothermally synthesized BW/BI/A composites are shown in Figure 4.4. All the diffraction peaks in the XRD patterns of the BW/BI/A composites can be readily assigned to orthorhombic-phase Bi_2WO_6 with a space group of *Pbca* and tetragonal-phase BiOI with a space group of *P*4/*nmm* without any traces of other crystalline phases. No diffraction peaks related to BiOI are observed in the XRD pattern of the BW/0.5BI/A composite, possibly due to it having a lesser amount of BiOI than Bi_2WO_6. Further, the broad diffraction peaks of BiOI appear in the XRD patterns of the BW/BI/A

composites because of its smaller crystal size and become more intensive in composites with higher BiOI contents.

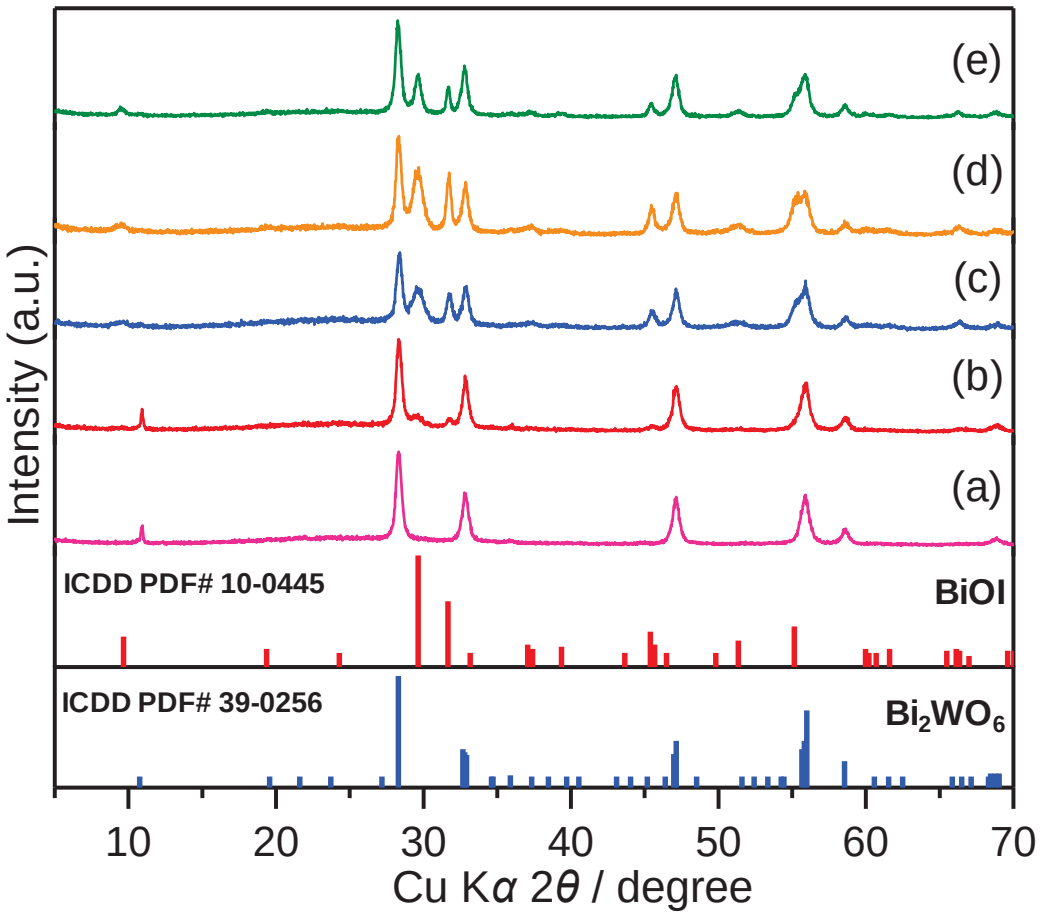

Figure 4.4. XRD patterns of the Bi_2WO_6/ BiOI/allophane composite photocatalysts synthesized with different ratios of Bi_2WO_6: BiOI: (a)1:0.5, (b)1:1, (c)1:2, (d) 1:3, and (e)1:1 (mech.mix.).

The SEM images of the BW/BI/A composites are depicted in Figure 4.5. As shown, the Bi_2WO_6 and BiOI particles are in close contact and uniformly distributed throughout the BW/BI/A composite. Only the BW/0.5BI/A composite retains three-dimensional flower-like structures of the Bi_2WO_6 particles (Figure 4.5a). With increasing contents of BiOI, the overall morphology of the composite changed because BiOI nanoparticles gradually occupied the surfaces of the nanosheets that constructed the flower-like structures, eventually covering the surfaces of the Bi_2WO_6 particles. Some Bi_2WO_6 nanosheets were detached from the flower-like structures and formed a composite with BiOI and allophane nanoparticles separately. A similar tendency was previously observed for Bi_2WO_6-allophane and BiOI-allophane composites [29].

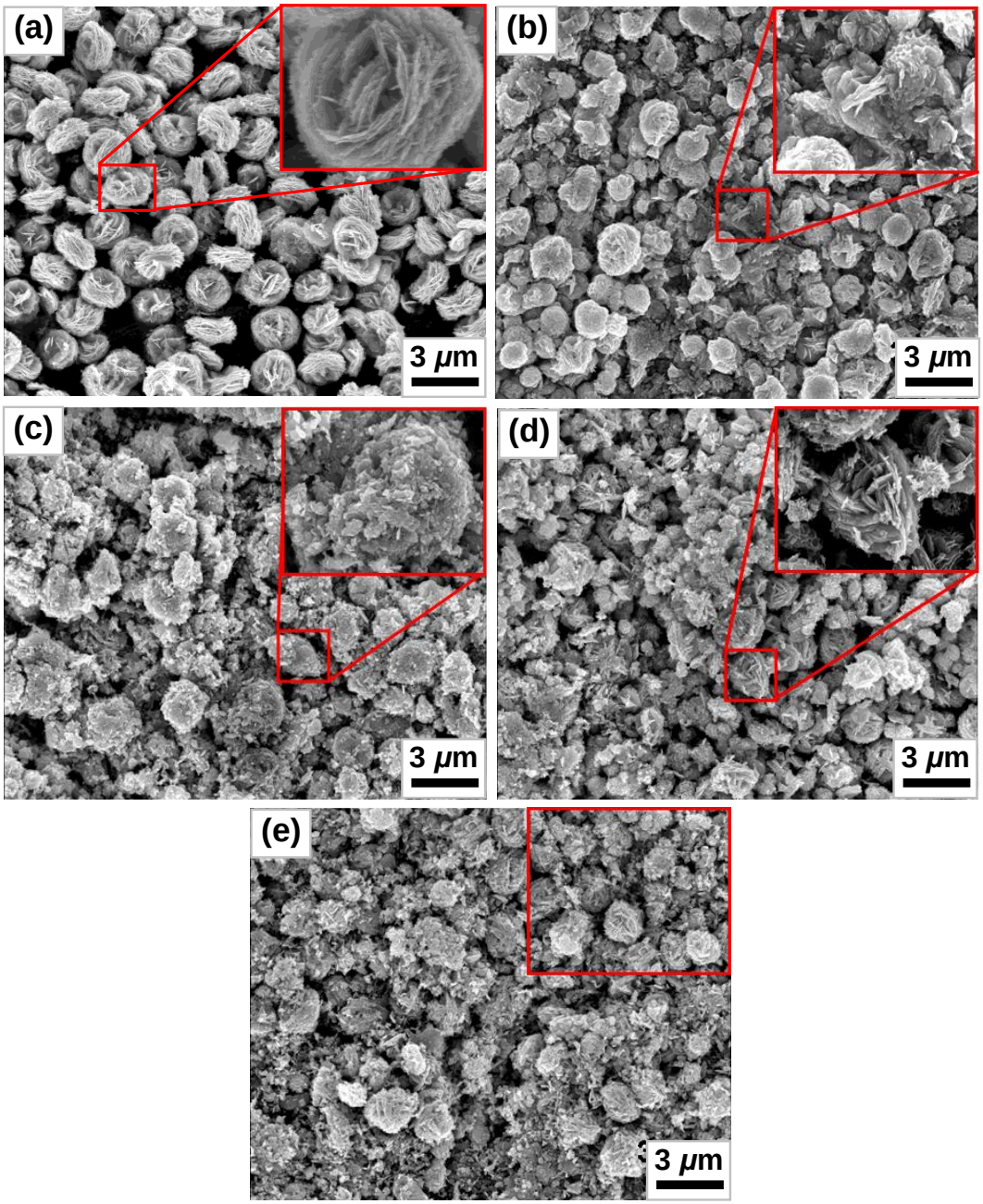

Figure 4.5. SEM images of the Bi_2WO_6/ BiOI/allophane composite photocatalysts synthesized with different ratios of Bi_2WO_6: BiOI: (a)1:0.5, (b)1:1, (c)1:2, (d) 1:3, and (e)1:1 (mech.mix.).

Figure 4.6 shows the Raman spectra of Bi_2WO_6, BiOI, and the BW/BI/A composites. The absence of Raman peaks for allophane is related to its quadratic functions in its character table for SiO_2 and Al_2O_3. Therefore, the Raman spectra of Bi_2WO_6 and BiOI can only be observed in the BW/BI/A composites. The Raman peaks at 786 and 706 cm^{-1} can be assigned to the symmetric and asymmetric stretching modes of the WO_6 octahedra involving the motions of the apical and equatorial oxygen atoms perpendicular to and within the layers, respectively. The

Raman peaks at 411, 298, 276, 253, 218, and 173 cm^{-1} can be attributed to the bending modes of the WO_6 octahedra and the stretching and bending modes of the BiO_6 polyhedra. The Raman peaks at 140 and 147 cm^{-1} may be assigned to the translations of the tungsten and bismuth ions [29,31]. The Raman peaks observed at 145 cm^{-1} in the BiOI-containing samples correspond to the E_g internal Bi–I stretching mode. When increasing amounts of BiOI were composited with the Bi_2WO_6 and allophane, the intensity of the Raman peaks of Bi_2WO_6 gradually decreased, implying that the surfaces of the Bi_2WO_6 particles became covered by BiOI and allophane particles.

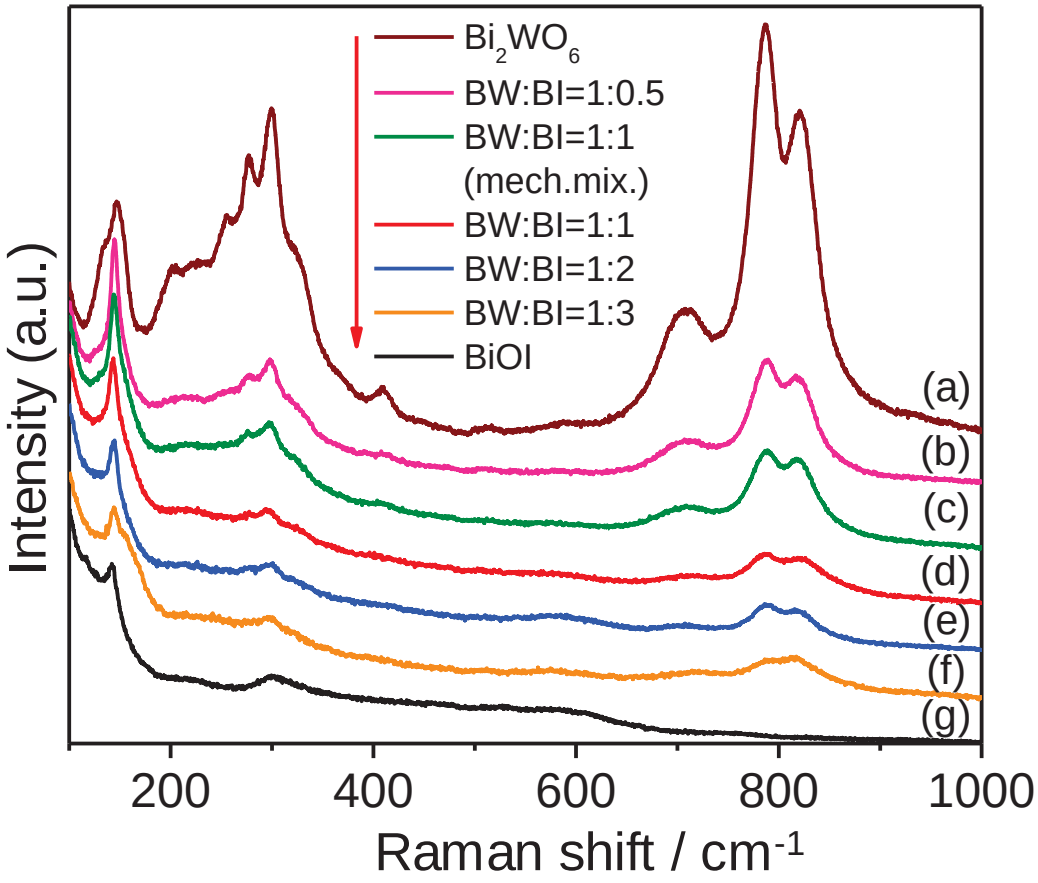

Figure 4.6. Raman spectra of Bi_2WO_6/ BiOI/allophane composite synthesized with different ratios of Bi_2WO_6: BiOI: (a)1:0, (b)1:0.5, (c)1:1(mech.mix.), (d) 1:1, (e)1:2, (f) 1:3, and (g) 0:1.

The nitrogen gas adsorption-desorption isotherms of Bi_2WO_6, BiOI, and allophane and the hydrothermally synthesized BW/0.5BI/A composite are plotted in Figure 4.7, and the calculated specific surface areas (S_{BET}) and total pore volumes (V_t) of Bi_2WO_6, BiOI, allophane, and the mechanically mixed and hydrothermally synthesized BW/BI/A composites are given in Table

4.1. Compared with Bi_2WO_6, BiOI, and the BW/BI/A composites, the allophane shows higher nitrogen gas adsorption because of its higher specific surface area (S_{BET} = 263 $m^2 \cdot g^{-1}$) in comparison to that of Bi_2WO_6 (S_{BET} = 21.3 $m^2 \cdot g^{-1}$), BiOI (S_{BET} = 23.1 $m^2 \cdot g^{-1}$), and the BW/BI/A composites (S_{BET} = 81–174 $m^2 \cdot g^{-1}$). The isotherms of the allophane and BW/0.5BI/A composite exhibit a single hysteresis loop with a type IV isotherm in the IUPAC classification due to capillary condensation in the mesopores [30]. According to the IUPAC classification, the nitrogen gas adsorption-desorption isotherms of Bi_2WO_6 and BiOI are type II, indicating the adsorption of nitrogen gas on a non-porous or macroporous adsorbent with strong adsorbate-adsorbent interactions. With increasing the BiOI content in the composite, the S_{BET} of the hydrothermally synthesized composites decreased from 174 to 84 $m^2 \cdot g^{-1}$ and the V_t decreased from 0.3805 to 0.1713 $mL \cdot g^{-1}$, while the average pore size increased from 9.7 to 17.8 nm due to the coverage of the surfaces of the Bi_2WO_6 and allophane particles by a large number of BiOI crystals. Therefore, it is essential to control the BiOI content to simultaneously achieve high adsorption capacity and high photocatalytic performance of the BW/BI/A composite.

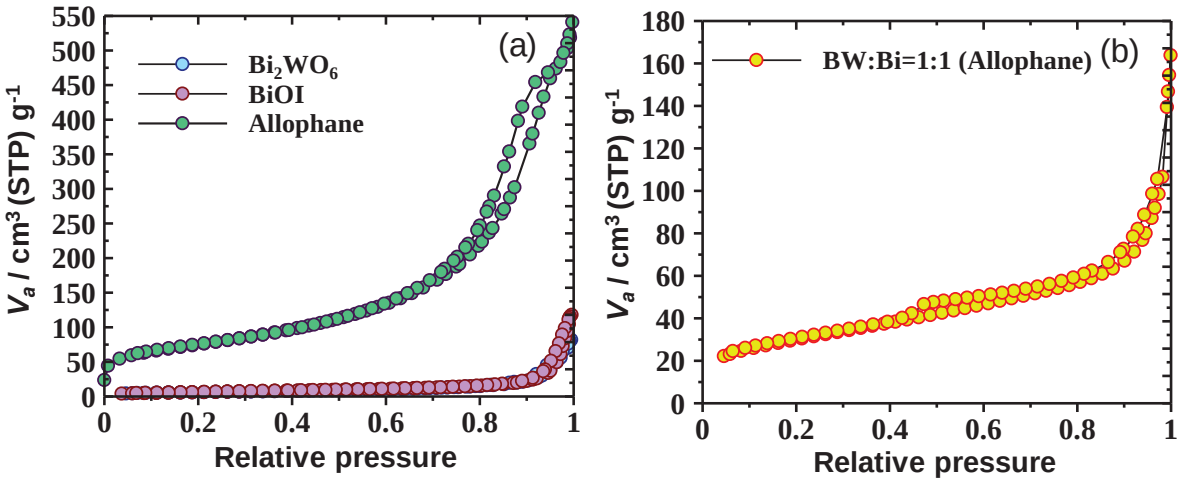

Figure 4.7. N_2 adsorption-desorption isotherms of (a) Bi_2WO_6, BiOI, and allophane and (b) the Bi_2WO_6/BiOI/allophane composite photocatalyst synthesized with a Bi_2WO_6:BiOI ratio of 1:0.5.

The Bi 4f, W 4f, O 1s, and I 3d XPS core-level spectra of the BW/0.5BI/A composite are shown in Figure 4.8. In Figure 4.8a, the XPS peaks centered at 163.2 and 157.8 eV can be assigned to the binding energies of Bi $4f_{7/2}$ and Bi $4f_{5/2}$, respectively, indicating that the bismuth has an oxidation state of +3. The XPS peaks centered at 36.4 and 33.5 eV can be ascribed to

the binding energies of W $4f_{5/2}$ and W $4f_{7/2}$, respectively, confirming that the tungsten has an oxidation state of +6 (Figure 4.8b) [32,33]. The O 1s XPS core-level spectrum can be fitted with two chemical states at binding energies of 530.2 eV and 531.8 eV, respectively (Figure 4.8c). The XPS peak at 530.2 eV is characteristic of oxygen bonded to bismuth in BiOI and Bi_2WO_6, and the other XPS peak at 531.8 eV is mainly attributed to the contribution of chemisorbed or dissociated oxygen species [34,35]. The XPS peaks at 629.9 and 618.3 eV (Figure 4.8d) are attributed to the binding energies of I $3d_{3/2}$ and I $3d_{5/2}$ [36], respectively.

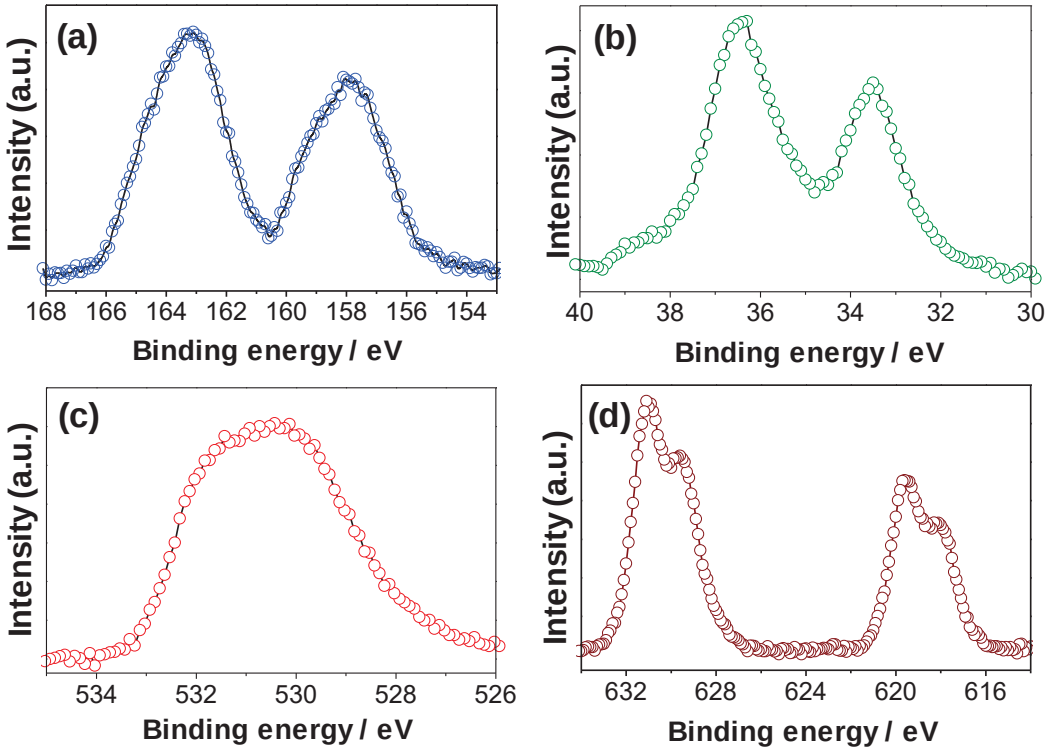

Figure 4.8. (a) Bi 4f, (b) W 4f, (c) O 1s, and (d) I 3d XPS core-level spectra of the Bi_2WO_6/BiOI/allophane composite photocatalyst synthesized with a Bi_2WO_6:BiOI ratio of 1:0.5.

The UV-vis diffuse reflectance spectra of Bi_2WO_6/allophane, BiOI/allophane, and the BW/BI/A composites are shown in Figure 4.9. The Bi_2WO_6/allophane and BiOI/allophane composites have absorption edges at approximately 450 and 660 nm, respectively. The estimated optical band gaps of the Bi_2WO_6/allophane and BiOI/allophane composites are 2.76 and 1.87 eV, respectively. This indicates that BiOI is more responsive to visible light compared with Bi_2WO_6. The color of the BW/BI/A composite powder is orange and gradually darkens

with increasing BiOI content. The BW/BI/A composites absorb visible light in the wavelength range of 640–650 nm, implying that the prepared composites can be used for visible light-induced photocatalytic reactions.

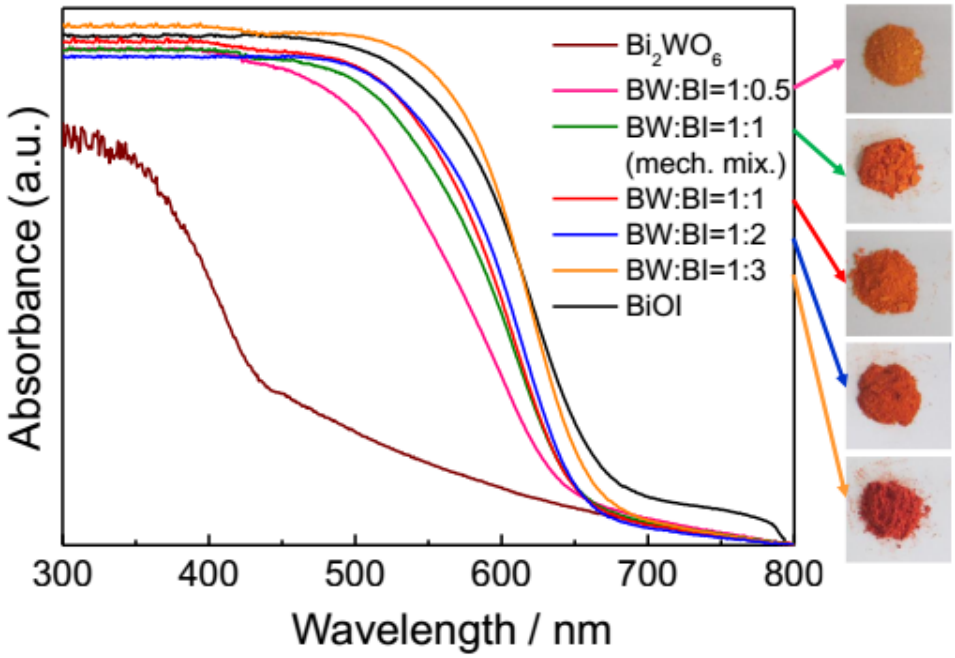

Figure 4.9. UV-vis diffuse reflectance spectra of Bi_2WO_6/ BiOI/allophane composites synthesized with different ratios of Bi_2WO_6:BiOI.

4.3.2. Adsorption capacity and photocatalytic activity of the prepared samples

The adsorption and photocatalytic activity of Bi_2WO_6/allophane, BiOI/allophane, and the BW/BI/A composites were evaluated for the adsorption and photodegradation of gaseous acetaldehyde (CH_3CHO), an indoor air contaminant, in the dark and under visible light irradiation ($\lambda \geq 420$ nm), and the results are shown in Figure 4.10 and Table 4.1. The concentration of the injected gaseous acetaldehyde gradually decreased for all the samples due to adsorption in the dark, which was allowed to occur for 12 h (Figure 4.10a). As shown in Figure 4.10d, the adsorption of gaseous acetaldehyde monotonously decreased as the molar ratio of Bi_2WO_6:BiOI increased and the specific surface area decreased: 37.7% for 1:0.5 (S_{BET} = 174 $m^2 \cdot g^{-1}$) > 31.1% for 1:1 (S_{BET} = 106 $m^2 \cdot g^{-1}$) > 22.2% for 1:1 (mech. mix.) (S_{BET} = 81 $m^2 \cdot g^{-1}$) > 19.6% for 1:2 (S_{BET} = 96 $m^2 \cdot g^{-1}$) > 17.8% for 1:3 (S_{BET} = 84 $m^2 \cdot g^{-1}$). This indicates that the adsorption of gaseous acetaldehyde was strongly dependent on the specific surface area of the BW/BI/A composite, which stemmed from the incorporation of allophane into it. The

concentration of gaseous acetaldehyde gradually decreased upon visible light irradiation and, after 4 h of visible light irradiation, achieved photodegradation efficiencies in the following order: 100% for 1:0.5 > 85.1% for 1:1 > 77.1% for 1:1 (mech. mix.) > 62.2% for 1:2 > 57.8% for 1:3 (Figure 10d). The Bi_2WO_6/allophane and BiOI/allophane composites showed 69.5 and 39.6% photodegradation efficiency, respectively. The photodegradation efficiency of acetaldehyde over the prepared samples was estimated based on the amount of CO_2 liberated during the photocatalytic reaction (Figure 4.10b). The control test performed without a photocatalyst either under visible light irradiation or in the dark showed no pronounced change in the concentration of acetaldehyde, implying that the presence of the photocatalyst and visible light was essential for the photodegradation of acetaldehyde over the prepared composites. The relationship between ln (C_0/C) and visible light irradiation-time is linear, suggesting that the photodegradation follows first-order kinetics. The calculated rate constants (k values) of the prepared composites are listed in Table 4.1. Among the samples, the BW/0.5BI/A composite showed the highest k value of -0.67214 min^{-1} with the best photocatalytic activity for the degradation of acetaldehyde. The k values gradually decreased with increases in the Bi_2WO_6:BiOI ratio in the composite because the surfaces of the Bi_2WO_6 and allophane particles became more covered by BiOI crystals. The Bi_2WO_6/allophane and BiOI/allophane composites had low k values of -0.10982 and -0.27800 min^{-1}, respectively. Interestingly, the hydrothermally synthesized BW/1BI/A composite exhibited a higher rate constant of -0.44300 min^{-1} compared with the mechanically mixed BW/BI/A composite (k = -0.33833 min^{-1}) because the porous structure of the allophane in the former was less damaged. Recyclability, chemical stability, and high photocatalytic activity are critical issues for the long-term use of composite photocatalysts. To determine the recyclability and stability of the prepared composite, the hydrothermally synthesized BW/0.5BI/A composite was exposed to four subsequent photocatalytic reactions under identical experimental conditions, and the results are plotted in Figure 4.10c. The BW/0.5BI/A composite photocatalyst maintains a high photocatalytic activity after four cycles, with a slight decrease due to the loss of photocatalyst particles during the separation after each cycle, suggesting that the prepared BW/0.5BI/A composite possesses excellent stability.

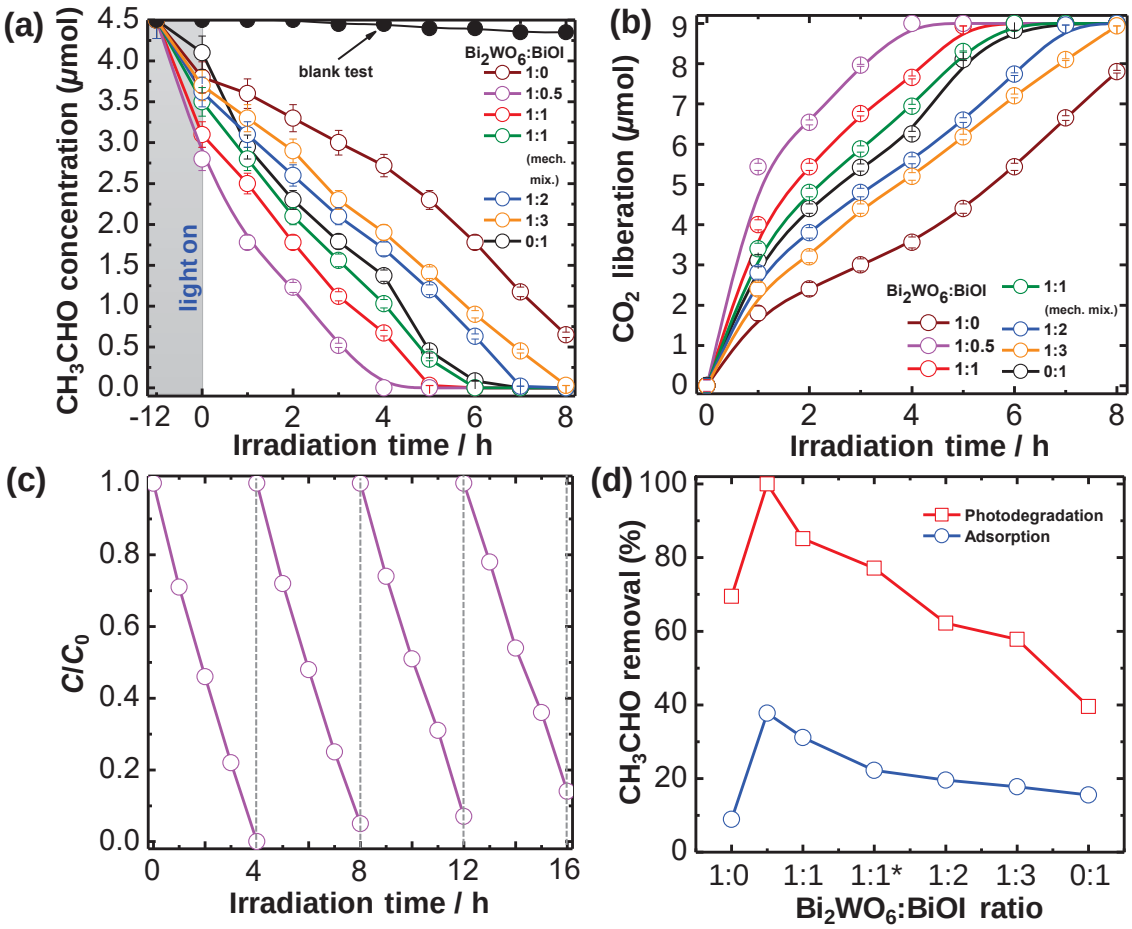

Figure 4.10. (a) Photocatalytic activity for the degradation of gaseous acetaldehyde and (b) CO_2 liberation of the Bi_2WO_6/ BiOI/allophane composites synthesized with different ratios of Bi_2WO_6: BiOI. (c) Photocatalytic activity for the degradation of gaseous acetaldehyde over the hydrothermally synthesized BW/0.5BI/A composite for four cycles. (d) Removal of gaseous acetaldehyde by adsorption and photodegradation as a function of Bi_2WO_6: BiOI molar ratio (* - mechanically mixed composite).

A possible mechanism for the enhanced visible light photocatalytic activity of BW/BI/A composite is schematically illustrated in Figure 4.11a. The relatively high efficiency of the BW/0.5BI/A composite for the photodegradation of gaseous acetaldehyde results from the formation of a *p–n* heterojunction and the presence of allophane. When *n*-type Bi_2WO_6 and *p*-type BiOI are in contact, a *p–n* heterojunction is formed, leading to the diffusion of electrons from Bi_2WO_6 to BiOI until the Fermi levels of BiOI and Bi_2WO_6 become equal. Hence, the conduction band edge of BiOI becomes higher than that of Bi_2WO_6, while the valence band edge of Bi_2WO_6 is positioned lower than that of BiOI, creating an internal electric field at the

interface of the *p–n* heterojunction at equilibrium. When the BW/BI/A composite is irradiated, the electrons in the valence band are excited to a higher potential edge of the conduction band, and the electrons from the conduction band of BiOI transfer to the more positive conduction band of Bi_2WO_6. Meanwhile, the holes in the valence band of Bi_2WO_6 migrate to the lower valence band of BiOI. The electrons in the conduction band will react with oxygen to produce $O_2^{-}\cdot$, which directly attacks acetaldehyde molecules, whereas the holes in the valence band react with acetaldehyde. This accelerated separation of photogenerated electrons and holes reduces their recombination rate and improves the photocatalytic activity [37,38]. Additionally, the enhanced photocatalytic activity of the BW/0.5BI/A composite is also affected by the presence of allophane because of its strong affinities to both water and acetaldehyde and its large specific surface area. The competitively adsorbed water molecules on the surfaces of the allophane and Bi_2WO_6/BiOI particles can be transformed into hydroxyl radicals (OH·) by reacting with the photogenerated holes (h^+) or superoxide radicals ($O_2^{-}\bullet$), and the acetaldehyde molecules adsorbed onto the surfaces of the allophane and Bi_2WO_6/BiOI particles are subsequently degraded into CO_2 [23,29,38].

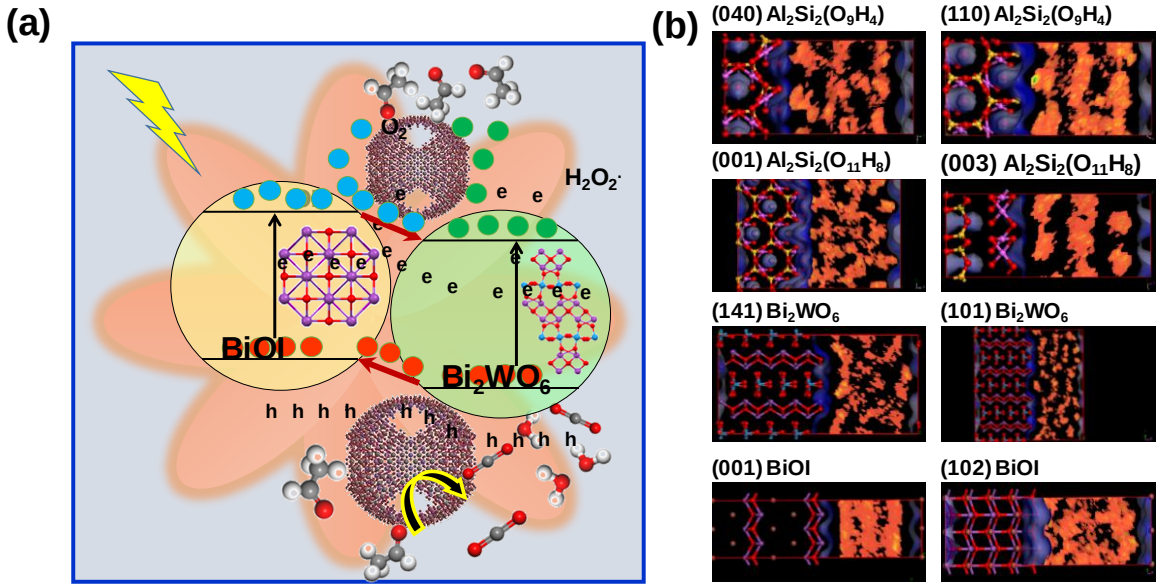

Figure 4.11. (a) Schematic representation of the adsorption and photodegradation of acetaldehyde over the BW/BI/A composite. (b) Visualization of the adsorption of acetaldehyde molecules onto different cleavage surfaces of allophane, Bi_2WO_6, and BiOI: *violet* – bismuth; *blue* – tungsten; *red* – oxygen; *brown* – iodine; *yellow* – silicon; *magenta* – aluminum. Isosurface: *blue*– Connolly surface.

4.3.3. Molecular modeling of adsorption of acetaldehyde molecules on the prepared samples

Calculations of the adsorption of AcH onto various cleavage planes of allophane, Bi_2WO_6, and BiOI surfaces were theoretically carried out to validate the adsorption of the BW/BI/A composite (Figure 4.11b). Since adsorption, as the first step of mineralization, plays an important role in improving the photocatalytic activity of a material, the main objective of this study was to find the most efficient interactions between AcH and each of the components present in the BW/BI/A composite. To determine the most likely adsorption configuration of AcH molecules on the surface of component, the Adsorption Locator module and Sorption module in Accelrys Materials Studio were used [39].

Two general types of calculations have been performed for the adsorption of AcH: static calculations of the total energy of the system and CPMD simulations of species adsorbed on the surface in microcanonical (NVE) ensembles. The Adsorption Locator identifies possible adsorption configurations by carrying out Monte Carlo searches of the substrate-adsorbate system as the temperature slowly decreases. The simulated annealing procedures in Adsorption Locator were performed with the Universal and COMPASS forcefield in the temperature range of 300–500 K. The top-layer atoms of the crystal plane (~0.5 nm) were selected for the interaction with AcH molecules, and the maximum adsorption distance value was 1.5 nm with a fixed energy window of 10 kcal·mol^{-1} for sampling configurations which differ from the lowest configuration in that maximum amount. Several tests were performed: one is with loading a single AcH molecule and others are with loading several AcH molecules (5, 10) on each surface.

The Sorption module shows the distribution of intermolecular energy for each sorbate component and calculates the isosteric heat of the AcH molecules, which is defined as the partial molar enthalpy of the AcH in the reservoir minus that in the framework (Table 4.2). The density of AcH on the components' planes at 10 kPa and 298 K is visualized using a solvent-accessible Connolly surface (Figure 4.11b). Accelrys Sorption module was used to simulate a pure AcH adsorbed in a sorbent framework in a series of fixed pressure (grand canonical ensemble) calculations performed over a series of fugacities (10-1000 kPa). In the MD model,

we found that the AcH equilibrium concentration in isotherm is compatible with experimental data.

Table 4.2. Energy parameters of cleavage planes calculated by Adsorption Locator module using COMPASS forcefield.

Structure	Plane	Total energy, kJ·mol^{-1}	Adsorption energy, kJ·mol^{-1}	Defor-mation energy, kJ·mol^{-1}	Total energy, kJ·mol^{-1}	Adsorption energy, kJ·mol^{-1}	Defor-mation energy, kJ·mol^{-1}
	Deprotonated				Protonated		
$Al_2Si_2(O_{11}H_8)$	(0 0 1)	-860	-826	43.6	–	–	–
	(0 0 3)	-562	-529	12.8	–	–	–
	(1 0 0)	-384	-350	4.6	-223	-190	-2
	(1 1 0)	-365	-332	3.5	-233	-199	0
	(2 1 0)	-249	-215	-1.1	-192	-159	-2
	(0 4 0)	-244	-211	0.7	–	–	–
	(3 0 0)	-229	-196	0.7	-197	-164	-1
$Al_2Si_2(O_9H_4)$	(0 4 0)	-195	-161	-1.8	–	–	–
	(1 1 0)	-181	-148	-1.7	-99	-66	-3
	(3 0 0)	-177	-144	-2.6	-147	-149	-2
	(1 0 0)	-166	-133	-2.9	-116	-83	-3
	(2 0 0)	-160	-127	-1.9	-105	-72	-3
	(2 1 0)	-140	-107	-1.2	-84	-51	-3
	(0 0 1)	-87	-54	-3.3	–	–	–
	(0 0 2)	-77	-44	-3.5	–	–	–

Bulk Bi_2WO_6 and BiOI structures were modeled using experimental lattice constants and atomic positions from the crystallographic structural database [40,41]. The respective surface cells were created at the principal cleavage planes, as reported in the literature, and at the most predominant planes as obtained from the TEM and XRD analyses. The stability of the allophane planes was determined on the basis of approximation that the allophane structure consists of different halloysite-7 Å and halloysite-10 Å planes [42,43]. During the structural optimization,

only the top-layer of the surface cells was allowed to relax, while the fractional coordinates of the rest of the atoms were frozen.

The input structure of the AcH molecule was optimized on the component surface, and the calculated parameters are listed in Tables 4.2 and 4.3. The bonds formed between the atom(s) available on the top-layer of the component surface with the hydrogen and oxygen atoms of the AcH molecule were estimated using an analysis of the close contact distances of less than 3.5 Å (Figure 4.11b). Different adsorption configurations of the AcH molecule over the component surfaces were investigated, and the most stable configuration and the adsorption energies for AcH over the component surfaces were calculated. The adsorption energy is equal to the energy, in $kJ \cdot mol^{-1}$, released (or required) when the relaxed AcH molecules (adsorbate) are adsorbed on the substrate. This is equal to the sum of the rigid adsorption energy and the deformation energy for the adsorbate components. The negative adsorption energies imply more exothermic adsorption and stronger mineral-adsorbate interaction. The interaction energies for water molecules being adsorbed onto the component surfaces (only for the surfaces most active for AcH adsorption) were also calculated. The interaction energy for AcH-component adsorption is stronger (more negative) compared with that for water-component adsorption, suggesting that the AcH molecules will replace water molecules on the component surface.

In this study, the single-crystal surfaces of these components were selected according to the experimental data. Based on the TEM results and previous reports [30,44], the most stable surfaces selected for this study were (110), (110), (200), and (001) for BiOI and (040), (101), (141), and (100) for Bi_2WO_6. Recent studies on different surfaces showed that adsorption can also occur on more exposed surfaces [45,46]. Therefore, the surfaces (102) and (131), obtained from intense XRD peaks, were used as stable surfaces for BiOI and Bi_2WO_6, respectively. However, ambiguity remains in selecting the most stable surface of allophane. According to previous report [43], allophane of the second-type has a Si/Al ratio close to 1 and a halloysite-like structure that contains condensed silicate units. To ascertain the most stable surface for allophane, the surface energies of different halloysite planes were calculated (Table 4.2). Due to the formation of hydroxyls on the allophane surface, the surfaces with deprotonated and protonated oxygen atoms were modeled. Based on this analysis, the (001) surface of Halloysite 10 Å $Al_2Si_2(O_{11}H_8)$ and the (040) surface of Halloysite-7 Å $Al_2Si_2(O_9H_4)$ were chosen as the

most stable surfaces since they have the highest adsorption energies and the highest deformation energies that are released when the adsorbed AcH molecules are relaxed on the substrate surface. The protonation of the cleavage surface was shown to decrease adsorption due to electrostatic effects.

Table 4.3. Calculated energy parameters of the Bi_2WO_6 and BiOI cleavage planes.

Structure	Plane	Total energy, kJ·mol^{-1}	Adsorption energy, kJ·mol^{-1}	Deformation energy, kJ·mol^{-1}	AA isosteric heat at 298 K, kJ·mol^{-1}
	Adsorption Locator module				Sorption module
Bi_2WO_6	(1 4 1)	-26.59	-28.09	0.0117	32.82
	(1 0 1)	-26.25	-27.76	0.0109	33.95
	(3 3 1)	-26.13	-27.63	0.0105	30.69
	(2 0 2)	-26.00	-27.51	0.0188	32.20
	(1 0 2)	-25.58	-27.09	0.0067	17.75
	(1 3 3)	-23.61	-25.12	0.0063	34.75
	(1 0 0)	-23.40	-24.91	0.0067	33.37
	(1 3 1)	-23.24	-24.74	0.0054	29.68
	(0 4 0)	-12.10	-13.61	0.0025	35.59
BiOI	(0 0 1)	-22.90	-24.45	0.0121	31.53
	(1 0 2)	-19.30	-20.85	0.0134	36.84
	(2 0 0)	-18.76	-20.31	0.0033	38.64
	(0 1 0)	-18.71	-20.22	0.0021	34.88
	(1-1 0)	-16.12	-17.63	0.0029	35.76
	(1 1 0)	-16.12	-17.63	0.0029	35.71
	(2 1 2)	-14.53	-16.08	0.0063	37.18

The modeling results of the cleavage surfaces of Bi_2WO_6 and BiOI are given in Table 4.3. The calculation results are compatible with the TEM and XRD results, as shown in Figure 4.12, indicating that the two most stable adsorption surfaces observed are (141) and (101) for Bi_2WO_6

and (001) and (102) for BiOI. As indicated in the XRD pattern of Bi_2WO_6, the most exposed surface, (131), is a less stable adsorption surface, which can be explained by the influence of crystalline disorder in the flower-like structures. AcH, like other organic aldehydes, is adsorbed on the substrate surfaces through the interactions between the atoms of the aldehyde ($O_{Carbonyl}$, $H_{Carbonyl}$) and methyl (H_{Met}) groups with the atoms on the substrate surfaces. The analysis of several close contacts found in the most stable configurations of AcH over Bi_2WO_6 and BiOI surfaces reveals a possible hydrogen-bonding configuration with a typical hydrogen bond length. Figure 4.12 shows the most stable adsorption configurations with close contacts for AcH on the Bi_2WO_6 and BiOI surfaces.

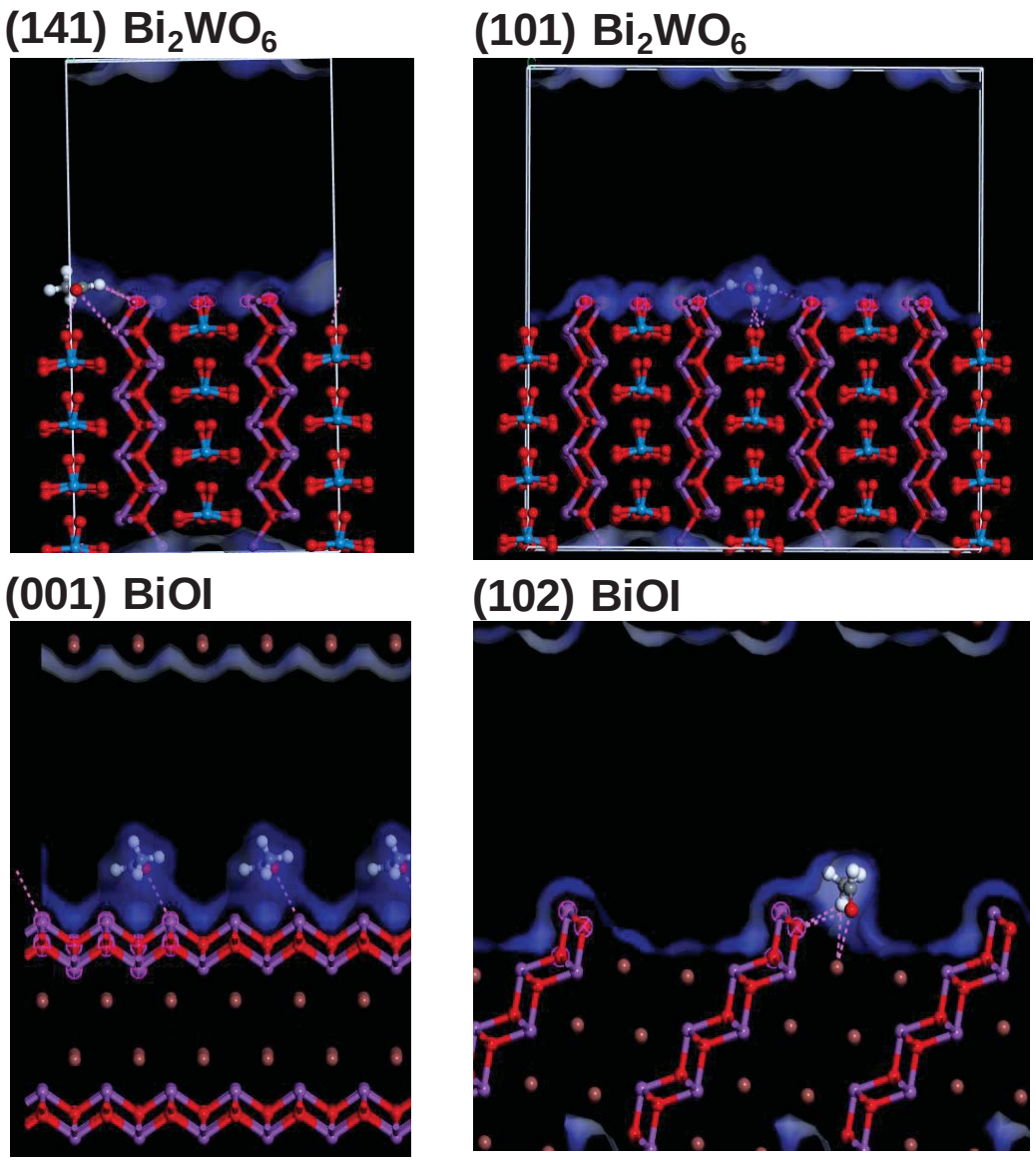

Figure 4.12. Acetaldehyde molecules - adsorbed structure models of Bi_2WO_6 and BiOI: *white* – hydrogen, *violet* – bismuth, *blue* – tungsten, *red* – oxygen, *gray* – carbon, and *brown* – iodine.

Over Bi_2WO_6 surfaces, it was found that acetaldehyde prefers to bind over the (1 4 1) and (1 0 1) surfaces to surface atoms such as ($O_{Carbonyl}$… Bi – 3.1 Å, $O_{Carbonyl}$… O_6W – 3.2 Å, $H_{Carbonyl}$… OBi – 3.1-3.3 Å, H_{Met}…H-O-W – 2.9-3.2 Å, H_{Met}…O-Bi – 3.2 Å). Over the BiOI surfaces, acetaldehyde prefers to bind over the (0 0 1) and (1 0 2) surfaces such that it binds to the surface atoms ($O_{Carbonyl}$… Bi – 3.2 Å, $H_{Carbonyl}$… I – 3.5 Å, H_{Met}…O-Bi – 3.2 Å). Among the three components of the BW/BI/A composite, the acetaldehyde molecule binds stronger on the (1 4 1) surface of Bi_2WO_6 than on the (0 0 1) surface of BiOI, while the adsorption occurs over the most stable and exposed surface of BiOI, as indicated by the XRD and TEM results. The results of the molecular dynamics simulations also confirmed that with increasing BiOI content, the adsorption and photocatalytic activity of the BW/BI/A composites gradually decrease. The BW/0.5BI/A composite has a high adsorption ability, excellent photocatalytic performance and good stability owing to its large specific surface area, greater number of easily accessible active sites, facilitated diffusion of reactants, multiple scattering of incident light, and *p–n* heterojunction, which suggest that it can be used in environmental remediation in the future.

4.4. Conclusions

In summary, the Bi_2WO_6/BiOI/allophane (BW/BI/A) composites with different molar ratios of Bi_2WO_6: BiOI were prepared by either mechanical mixing or a hydrothermal synthesis. With increasing BiOI content, the overall morphology of the BW/BI/A composite was altered because the BiOI nanoparticles gradually occupied more of the surfaces of the nanosheets that formed the flower-like structures and eventually covered the surfaces of the Bi_2WO_6 particles. The BW/BI/A composites absorb visible light in the wavelength range of 640–650 nm, implying that the prepared composites can be used for visible-light-induced photocatalytic reactions. The specific surface area, adsorption capacity, and photocatalytic activity of the BW/BI/A composite gradually decreased as the BiOI content increased. The molecular dynamics simulation showed that, among the three components of the BW/BI/A composite, acetaldehyde binds more strongly on the (1 4 1) surface of Bi_2WO_6 than on the (0 0 1) surface of BiOI, while adsorption occurs over the most stable and exposed surface of BiOI. Allophane contributed substantially to the adsorption of the BW/BI/A composite due to its strong affinity to water and acetaldehyde and its large specific surface area. The BW/0.5BI/A composite

exhibited high adsorption capacity, excellent photocatalytic performance and stability owing to its large specific surface area, greater number of easily accessible active sites, facilitated diffusion of reactants, multiple scattering of incident light, and *p–n* heterojunction, which suggest that it can be used in environmental remediation in the future.

4.5. References

[1] EPA Indoor Air Quality (IAQ). http://www.epa.gov/iaq/index.html

[2] CCOHS Indoor Air Quality – General. http://www.ccohs.ca/oshanswers/chemicals/iaq_intro.html

[3] WHO guidelines for indoor air quality: selected pollutants, World Health Organization, Regional Office for Europe, Copenhagen, Denmark, 2010, p. 454,

[4] EPA Acetaldehyde. http://www.epa.gov/chemfact/s_acetal.txt

[5] D.A. Missia, E. Demetriou, M. Michael, E.I. Tolis, J.G. Bartzis, Indoor exposure from building materials: A field study, *Atmos. Environ.* 44 (2010) 4388–4395.

[6] T. Noguchi, A. Fujishima, P. Sawunyama, K. Hashimoto, Photocatalytic degradation of gaseous formaldehyde using TiO_2 film, *Environ. Sci. Technol.* 32 (1998) 3831–3833.

[7] A. Fujishima, K. Honda, Electrochemical photolysis of water at a semiconductor electrode, *Nature* 238 (1972) 37–38.

[8] I. Sopyan, M. Watanabe, S. Murasawa, K. Hashimoto, A. Fujishima, An efficient TiO_2 thin-film photocatalyst: photocatalytic properties in gas-phase acetaldehyde degradation, *J. Photochem. Photobiol. A* 98 (1996) 79–86.

[9] D. Chatterjee, S. Dasgupta, Visible light induced photocatalytic degradation of organic pollutants, *J. Photochem. Photobiol. C* 6 (2005)186–192.

[10] T. Arai, M. Yanagida, Y. Konishi, Y. Iwasaki, H. Sugihara, K. Sayama, Efficient Complete Oxidation of Acetaldehyde into CO_2 over $CuBi_2O_4/WO_3$ Composite Photocatalyst under Visible and UV Light Irradiation, *J. Phys. Chem. C* 111 (2007) 7574–7577.

[11] Z. Liu, Z.G. Zhao, M. Miyauchi, Efficient Visible Light Active $CaFe_2O_4/WO_3$ Based Composite Photocatalysts: Effect of Interfacial Modification, *J. Phys. Chem. C* 113 (2009) 17132–17137.

[12] T. Kako, J. Ye, Photocatalytic Decomposition of Acetaldehyde over Rubidium Bismuth Niobates under Visible Light Irradiation, *Mater. Trans.* 46 (2005) 2694–2698.

[13] H. Widiyandari, A. Purwanto, R. Balgis, T. Ogi, K. Okuyama, CuO/WO_3 and Pt/WO_3 nanocatalysts for efficient pollutant degradation using visible light irradiation, *Chem. Eng. J.* 180 (2012) 323–329.

[14] T. Arai, M. Horiguchi, M. Yanagida, T. Gunji, H. Sugihara, K. Sayama, Complete oxidation of acetaldehyde and toluene over a Pd/WO_3 photocatalyst under fluorescent- or visible-light irradiation, *Chem. Commun.* 0 (2008) 5565–5567.

[15] T. Kako, X. Meng, J. Ye, Solid-base loaded WO_3 photocatalyst for decomposition of harmful organics under visible light irradiation, *APL Mater.* 3 (2015) 104411.

[16] Y. Yamaguchi, C. Terashima, H. Sakai, A. Fujishima, A. Kudo, K. Nakata, Photocatalytic Degradation of Gaseous Acetaldehyde over Rh-doped $SrTiO_3$ under Visible Light Irradiation, *Chem. Lett.* 45 (2016) 42–44.

[17] M. Takeuchi, H. Yamagawa, M. Matsuoka, M. Anpo, Photocatalytic oxidation of acetaldehyde by hybrid Pt/WO_3-MOR photocatalysts under visible or sunlight irradiation, *Res. Chem. Intermed.* 40 (2014) 23–31.

[18] K.I. Katsumata, R. Motoyoshi, N. Matsushita, K. Okada, Preparation of graphitic carbon nitride ($g\text{-}C_3N_4$)/WO_3 composites and enhanced visible-light-driven photodegradation of acetaldehyde gas, *J. Hazard. Mater.* 260 (2013) 475–482.

[19] B. Aurivillius, The structure of Bi_2NbO_5F and isomorphous compounds, *Ark Kemi* 5 (1952) 39–47.

[20] F. Amano, K. Nogami, R. Abe, B. Ohtani, Facile Hydrothermal Preparation and Photocatalytic Activity of Bismuth Tungstate Polycrystalline Flake-ball Particles, *Chem. Lett.* 36 (2007) 1314–1315.

[21] F. Amano, K. Nogami, R. Abe, B. Ohtani, Preparation and Characterization of Bismuth Tungstate Polycrystalline Flake-Ball Particles for Photocatalytic Reactions, *J. Phys. Chem. C* 112 (2008) 9320–9326.

[22] M. Hojamberdiev, K.I. Katsumata, K. Morita, S. Aldabe Bilmes, N. Matsushita, K. Okada, One-step hydrothermal synthesis and photocatalytic performance of $ZnWO_4/Bi_2WO_6$ composite photocatalysts for efficient degradation of acetaldehyde under UV light irradiation, *Appl. Catal. A* 457 (2013) 12–20.

[23] M. Hojamberdiev, Z.C. Kadirova, Y. Makinose, G. Zhu, S. Emin, N. Matsushita, M. Hasegawa, K. Okada, Involving $CeVO_4$ in improving the photocatalytic activity of a Bi_2WO_6/allophane composite for the degradation of gaseous acetaldehyde under visible light, *Colloids Surf. A* 529 (2017) 600–612.

[24] Y. Liu, G. Zhu, J. Gao, M. Hojamberdiev, R. Zhu, X. Wei, Q. Guo, P. Liu, Enhanced photocatalytic activity of $Bi_4Ti_3O_{12}$ nanosheets by Fe^{3+}-doping and the addition of Au nanoparticles: Photodegradation of phenol and bisphenol A, *Appl. Catal. B* 200 (2017) 72–82.

[25] L. Jin, G. Zhu, M. Hojamberdiev, X. Luo, C. Tan, J. Peng, X. Wei, J. Li, P. Liu, A Plasmonic Ag–AgBr/$Bi_2O_2CO_3$ Composite Photocatalyst with Enhanced Visible-Light Photocatalytic Activity, *Ind. Eng. Chem. Res.* 53 (2014) 13718–13727.

[26] K. Wada, A structural scheme of soil allophane, *Am. Mineral.* 52 (1967) 690–708.

[27] Y. Kitagawa, The "unit particle" of allophane, *Am. Mineral.* 56 (1971) 465–475.

[28] K. Okada, H. Morikawa, S. Iwai, Y. Ohira, J. Ossaka, A structure model of allophane, *Clay Sci.* 4 (1975) 291–303.

[29] M. Hojamberdiev, K.I. Katsumata, N. Matsushita, K. Okada, Preparation of Bi_2WO_6– and BiOI–allophane composites for efficient photodegradation of gaseous acetaldehyde under visible light, *Appl. Clay Sci.* 101 (2014) 38–43.

[30] M. Hojamberdiev, Z.C. Kadirova, Y. Makinose, G. Zhu, S. Emin, N. Matsushita, M. Hasegawa, K. Okada, Involving $CeVO_4$ in improving the photocatalytic activity of a Bi_2WO_6/allophane composite for the degradation of gaseous acetaldehyde under visible light, *Colloids Surf. A* 529 (2017) 600–612.

[31] M. Mączka, A.F. Fuentes, L. Kępiński, M.R. Diaz-Guillen, J. Hanuza, Synthesis and electrical, optical and phonon properties of nanosized Aurivillius phase Bi_2WO_6, *Mater. Chem. Phys.* 120 (2010) 289–295.

[32] R. Tang, H. Su, Y. Sun, X. Zhang, L. Li, C. Liu, B. Wang, S. Zeng, D. Sun, Facile fabrication of Bi_2WO_6/Ag_2S heterostructure with enhanced visible-light-driven photocatalytic performances, *Nanoscale Res. Lett.* 11 (2016) 126–138.

[33] K. Kawashima, M. Hojamberdiev, H. Wagata, E. Zahedi, K. Yubuta, K. Domen, K. Teshima, Two-step synthesis and visible-light-driven photocatalytic water oxidation activity of *A*W(O,N)$_3$ (*A* = Sr, La, Pr, Nd and Eu) perovskites, *J. Catal.* 344 (2016) 29–37.

[34] J. Di, J. Xia, M. Ji, B. Wang, S. Yin, H. Xu, Z. Chen, H. Li, Carbon quantum dots induced ultrasmall BiOI nanosheets with assembled hollow structures for broad spectrum photocatalytic activity and mechanism insight, *Langmuir* 32 (2016) 2075–2084.

[35] M. Hojamberdiev, M.F. Bekheet, J.N. Hart, J.J.M. Vequizo, A. Yamakata, K. Yubuta, A. Gurlo, M. Hasegawa, K. Domen, K. Teshima, Elucidating the impact of *A*-site cation change on photocatalytic H_2 and O_2 evolution activities of perovskite-type *Ln*TaON$_2$ (*Ln* = La and Pr), *Phys. Chem. Chem. Phys.* 19 (2017) 22210–22220.

[36] Y. Liu, G. Zhu, J. Gao, R. Zhu, M. Hojamberdiev, C. Wang, X. Wei, P. Liu, A novel synergy of Er^{3+}/Fe^{3+} co-doped porous Bi_5O_7I microspheres with enhanced photocatalytic activity under visible-light irradiation, *Appl. Catal. B* 205 (2017) 421–432.

[37] Y. Xiang, P. Ju, Y. Wang, Y. Sun, D. Zhang, J. Yu, Chemical etching preparation of the Bi_2WO_6/BiOI *p–n* heterojunction with enhanced photocatalytic antifouling activity under visible light irradiation, *Chem. Eng. J.* 288 (2016) 264–275.

[38] K.I. Katsumata, X. Hou, M. Sakai, A. Nakajima, A. Fujishima, N. Matsushita, K.J.D. MacKenzie, K. Okada, Visible-light-driven photodegradation of acetaldehyde gas catalyzed by aluminosilicate nanotubes and Cu(II)-grafted TiO_2 composites, *Appl. Catal. B* 138–139 (2013) 243–252.

[39] R.L.C. Akkermans, N.A. Spenley, S.H. Robertson, Monte Carlo methods in Materials Studio, *Mol. Simul.* 39 (2013) 1153–1164.

[40] E. Keller, V. Krämer, A Strong Deviation from Vegard's Rule: X-Ray Powder Investigations of the Three Quasi-Binary Phase Systems BiO*X*–BiO*Y* (X, Y = Cl, Br, I), *Z. Naturforsch. B* 60 (2005) 1255–1263.

[41] K.S. Knight, The crystal structure of russellite; a re-determination using neutron powder diffraction of synthetic Bi_2WO_6, *Mineral. Mag.* 56 (1992) 399–409.

[42] M. Mehmel, Über die Struktur von Halloysit und Metahalloysit, *Z. Krist. – Cryst. Mater.* 90 (1935) 35–43.

[43] B. Creton, D. Bougeard, K.S. Smirnov, J. Guilment, O. Poncelet, Structural Model and Computer Modeling Study of Allophane, *J. Phys. Chem. C* 112 (2008) 358–364.

[44] X.Q. Hu, C. Lin, L.X. Tang, X.W. Liu, Structure Sensitivity of H_2O Adsorption on Graphene-Supported Bi_2WO_6, *Appl. Mech. Mater.* 448–453 (2014) 123–127.

[45] S.S. Rath, N. Sinha, H. Sahoo, B. Das, B.K. Mishra, Molecular modeling studies of oleate adsorption on iron oxides, *Appl. Surf. Sci.* 295 (2014) 115–122.

[46] D. Sharma, M.I. Sabela, S. Kanchi, P.S. Mdluli, G. Singh, T.A. Stenström, K. Bisetty, Biosynthesis of ZnO nanoparticles using *Jacaranda mimosifolia* flowers extract: Synergistic antibacterial activity and molecular simulated facet specific adsorption studies, *J. Photochem. Photobiol. B* 162 (2016) 199–207.

CHAPTER 5: Tuning the morphological structure, light absorption, and photocatalytic activity of Bi_2WO_6 and Bi_2WO_6-BiOCl through cerium doping

5.1. Introduction

As one of the simplest members of the Aurivillius oxide family, Bi_2WO_6 is composed of perovskite-like $[WO_4]^{2-}$ layers sandwiched between bismuth oxide $[Bi_2O_2]^{2+}$ layers, favoring the efficient separation of photogenerated electron–hole pairs and improving the photocatalytic activity because of the formed internal electric fields between the slabs [1,2]. Recent studies have demonstrated that the photocatalytic performance of Bi_2WO_6 can be enhanced by compositing with other semiconductors, such as $BiVO_4$ [3], WO_3 [4], Fe_3O_4 [5], $ZnWO_4$ [6], and $CeVO_4$ [7].

Particularly, to improve its photocatalytic performance, Bi_2WO_6 was composited with BiO*X* (*X* = Cl, Br, and I), which are important V–VI–VII ternary semiconductor compounds that have a tetragonal matlockite structure, a layered structure characterized by $[Bi_2O_2]$ slabs interleaved by double slabs of halogen atoms [8]. For instance, a BiOCl–Bi_2WO_6 heterojunction with a chemically bonded interface was synthesized via a facile one-step solvothermal method and yielded a high photodegradation rate of rhodamine B under visible light irradiation due to the favorable band offsets across the Bi_I–O–Bi_{II} bonded interface, leading to efficient interfacial charge carrier transfer [9]. In comparison with the BiOBr–Bi_2WO_6 nanosheet composite, the BiOBr–Bi_2WO_6 mesoporous nanosheet composite prepared by using a facile hydrothermal synthetic route with a controlled fraction of $Ti(O^iPr)_4$ exhibited a much improved photocatalytic activity under visible light irradiation because of (i) the large specific surface area with hierarchical pore sizes and a highly exposed BiOBr (001) facet, (ii) the evidently enhanced charge separation efficiency, and (iii) high light harvesting efficiency [10]. The stable 30%Bi_2WO_6/BiOI heterojunction photocatalyst synthesized using a facile hydrothermal method based on the efficient chemical etching principle showed high visible-light-induced photocatalytic and antibacterial activities for the degradation of methylene blue and the killing of *P. aeruginosa*, *E. coli*, and *S. aureus* owing to the efficient separation of photogenerated electron–hole pairs on the formed *p*–*n* heterojunction [11].

In recent years, doping with lanthanide ions, such as La^{3+} [12], Sm^{3+}/Sm^{2+} [13], Eu^{3+} [14], Gd^{3+} [15], Ho^{3+} [16], Er^{3+} [17], and Yb^{3+} [16], has shown to be an efficient approach to improve the photocatalytic activity of Bi_2WO_6 because of their unique optical properties and 4f electron configuration.

As a common emerging water pollutant, salicylic acid (2-hydroxybenzoic acid) is widely used in the production of cosmetics, food, and pharmaceutical (a main precursor of aspirin) and dermatological products [18]. Due to its widespread use, salicylic acid has been consistently detected up to relatively high concentrations of 50 $\mu g \cdot L^{-1}$ in surface water [19] and 89.1 $\mu g \cdot L^{-1}$ in the effluents of municipal wastewater treatment plants [20]. As an example, aspirin degrades in an aqueous medium into several toxic intermediates causing environmental pollution, which ultimately affects human health [21,22]. However, microbiological and/or conventional secondary physicochemical treatments [23] cannot completely remove salicylic acid. Therefore, effective advanced oxidation processes are needed to ensure the total elimination of salicylic acid in water.

Very recently, the immobilized photocatalytic structures of self-organized and well-aligned TiO_2 nanotubular films fabricated by galvanostatic anodization demonstrated a slightly higher efficiency for the degradation of salicylic acid compared with that of TiO_2-P25 at alkaline to acidic pH values due to the easy removal of the formed intermediates from the highly porous surface [24]. Ma et al. [25] synthesized magnetically separable F-N co-doped TiO_2 using a facile sol-gel method grafted on magnetically activated carbon decorated with carbonized chitosan and found that the degradation of salicylic acid under visible light irradiation was strongly dependent on the molar ratio of F:Ti. A 3.0 L solar flow plant with a Pt/air-diffusion (anode/cathode) cell, a solar photoreactor and a photocatalytic photoreactor filled with TiO_2-coated glass spheres was utilized to couple solar photoelectro-Fenton (SPEF) and solar heterogeneous photocatalysts (SPC) for the efficient mineralization of salicylic acid [26].

The present study aims at tuning the morphological structure, light absorption, and photocatalytic activity of Bi_2WO_6 and Bi_2WO_6-BiOCl through cerium doping. The adsorption and photocatalytic activities of pure and Ce-doped Bi_2WO_6 and Bi_2WO_6-BiOCl powders were evaluated for the removal of salicylic acid, as an emerging water pollutant in the dark and

under visible light irradiation. It was found that the cerium doping can effectively improve the photocatalytic activity, and the use of Ce-doped Bi_2WO_6 and Bi_2WO_6-BiOCl powders can be extended to the degradation of other organic pollutants in water.

5.2. Experimental

5.2.1. Synthesis

Pure and cerium-doped Bi_2WO_6 and Bi_2WO_6-BiOCl powders were synthesized by a hydrothermal method. The experimental procedures were as follows. For pure and Ce-doped Bi_2WO_6, 2–x mmol of $Bi(NO_3)_3 \cdot 5H_2O$ (≥ 98.0%, Sigma-Aldrich), x mol of $CeCl_3 \cdot 7H_2O$ (x = 0, 0.5, 1, 2, 4, 6, 8 and 10 mol%) (99.9%, Sigma-Aldrich), and 2 mmol of $Na_2WO_4 \cdot 2H_2O$ (99%, Alfa Aesar) were dissolved in 10 mL of ethylene glycol (99.8%, Sigma-Aldrich) and 15 and 15 mL of deionized water. For pure and Ce-doped Bi_2WO_6-BiOCl, 2–x mmol of $Bi(NO_3)_3 \cdot 5H_2O$, x mol of $CeCl_3 \cdot 7H_2O$ (x = 0, 0.5, 1, 2, 4, 6, 8 and 10 mol%), and 2 mmol of $Na_2WO_4 \cdot 2H_2O$ were dissolved in 2 mL of dilute HCl and 18 and 20 mL of deionized water. After being well homogenized under vigorous magnetic stirring for 30 min, the pH of the suspension was adjusted to 9 by the dropwise addition of 28% aqueous ammonia solution (Merck), and the suspension was transferred into a Teflon-lined stainless steel autoclave with a filling capacity of 75% and maintained at 180°C for 12 h. The resultant precipitate was collected, washed with deionized water several times and dried at 100°C for 12 h.

5.2.2. Characterization

X-ray diffraction (XRD) patterns were acquired with a Siemens D5000 diffractometer using Cu Kα radiation (λ = 0.15418 nm) in the 2θ scan range from 10 to 70° and compared with entries from the ICDD-PDF-2 powder pattern database. The particle morphologies and sizes of the synthesized samples were examined using a ZEISS Supra 40 VP scanning electron microscope. The ultraviolet-visible (UV-vis) diffuse reflectance spectra were recorded on a Lambda 20 UV-vis spectrometer (PerkinElmer, Inc.) equipped with an integrating sphere, and $BaSO_4$ was used as a reference. The optical absorption spectra were converted from the UV-vis diffuse reflectance spectra using the Kubelka–Munk function, $F(R) = (1 - R)^2/2R = k/s$, where R is the absolute reflectance of the sampled layer, k is the molar absorption coefficient, and s is the scattering coefficient. A zeta potential analyzer (ZetaPALS, Brookhaven Instruments Corporation) was used to characterize the electrokinetic

potential of pure and Ce-doped Bi_2WO_6 and Bi_2WO_6-BiOCl particles in colloidal dispersions. For the zeta-potential measurements at a neutral pH adjusted by a NaOH aqueous solution, the suspension was prepared by dispersing the as-synthesized powders in deionized water under continuous magnetic stirring. The specific surface areas (S_{BET}) of the samples were determined by the Brunauer–Emmett–Teller (BET) method from the linear portion of the nitrogen gas adsorption isotherms measured at –196°C using an Autosorb-1A (Quantachrome Instruments). The surface chemical composition and elemental states were analyzed by X-ray photoelectron spectroscopy (JPS-9010MC, JEOL) using nonmonochromated Mg Kα radiation (1253.6 eV) with a 10 mA emission current and a 10 kV acceleration voltage. The XPS profiles were fitted using a Gaussian–Lorentzian function, and the peak positions were normalized by positioning the C 1s peak at 284.5 eV. The chemical compositions of the samples were analyzed by X-ray fluorescence (RIX2000, Rigaku).

5.2.3. Photocatalytic activity test

To study the effect of cerium doping, salicylic acid was selected as the probe molecule to evaluate the adsorption and photocatalytic activities of Ce-doped Bi_2WO_6 and Bi_2WO_6-BiOCl photocatalysts under visible light irradiation. The photodegradation of salicylic acid by the hydrothermally synthesized samples was performed in a 60 mL glass-tube reactor under simulated solar light using a 300 W Xe lamp (AM1.5G filter; 18.5 $mW \cdot cm^{-2}$). The photodegradation reaction temperature was maintained at 25°C by water flowing through the cooling jacket of the reactor. The initial concentration of salicylic acid in aqueous solution was 25 $mg \cdot L^{-1}$, and the photocatalyst sample content was 1.0 $g \cdot L^{-1}$. First, the photocatalyst sample was dispersed in a glass vial containing a 50 mL of salicylic acid in an aqueous solution, and the suspension was stirred in the dark for 2 h to ensure adsorption-desorption equilibrium prior to simulation with solar light irradiation. During the photodegradation reaction, 2 mL of the suspension was taken out at a predetermined time interval for subsequent analysis of the salicylic acid concentration. The concentration of salicylic acid was analyzed by a U-3010 UV-vis spectrophotometer (Hitachi) by measuring the change in the intensity of the absorption peaks of salicylic acid at 296 nm. The total organic carbon (TOC) content of the solution was analyzed using a total organic carbon analyzer (5050A, Shimadzu).

5.3. Results and Discussion

5.3.1. Characterization of the prepared samples

The crystal structures of the as-synthesized samples were characterized by powder X-ray diffraction. The XRD patterns of the samples doped with different contents of cerium ranging from 0 mol% to 10 mol% are shown in Figure 5.1 with the International Center for Diffraction Data Powder Diffraction File (ICDD PDF) data. As shown in Figure 5.1a, the diffraction lines in the XRD pattern of the sample hydrothermally synthesized using ethylene glycol as a solvent correspond to orthorhombic Bi_2WO_6 with a space group of $Pca2_1$ (ICDD PDF# 39–0256), confirming the phase purity of Bi_2WO_6. The diffraction lines in the XRD pattern of the sample hydrothermally synthesized using dilute HCl as a solvent are in good agreement with the orthorhombic phase of Bi_2WO_6 (ICDD PDF# 39–0256) and the tetragonal phase of BiOCl with a space group of $P4/nmm$ (ICDD PDF# 06–0249), indicating the co-existence of the Bi_2WO_6 and BiOCl phases in the sample (Figure 5.1b). Along with Bi_2WO_6, the BiOCl phase was also formed because of a rapid reaction of Bi^{3+} and the available Cl^- ions dissociated from HCl in the synthesis solution:

$$Bi^{3+}(aq) + Cl^-(aq) + H_2O(l) \rightarrow BiOCl(s) + 2H^+(aq).$$

Since the effective ionic radius of Ce^{3+} (r_{ion} = 1.01 Å for CN = 6) is very similar to that of Bi^{3+} (r_{ion} = 1.03 Å for CN = 6), there is no significant shift in the 2θ angle of the diffraction patterns, demonstrating that the Bi^{3+} ions were substitutionally replaced by the Ce^{3+} ions in the alternatively stacked $[Bi_2O_2]^{2+}$ layers of the Bi_2WO_6 and BiOCl crystal structures. Notably, an increase in the Ce content up to 10 mol% neither segregated the Ce-rich phases nor changed the preferential orientations, implying that all doped cerium ions were fully accommodated into the Bi_2WO_6 and BiOCl lattices. However, an increase in the Ce content up to 4 mol% gradually decreased the content of the Bi_2WO_6 phase in the sample, while the BiOCl phase became more predominant due to the increase in the concentration of the Cl^- ions in the synthesis solution highly saturated with cerium trichloride. From 6 mol% to 10 mol% Ce, the Bi_2WO_6 phase completely vanished, leaving behind BiOCl as a single phase. The diffraction lines resulting from the {111} plane of the Bi_2WO_6 and BiOCl crystals are obviously stronger compared to other diffraction lines, confirming the dominance of the {111} plane in the synthesized crystals. It is thought that the Ce^{2+} and Ce^{4+} ions were unlikely formed under the current synthesis conditions applied in this study. The XRD results suggest

that the selection of a solvent type (ethylene glycol or dilute HCl) and the content of cerium dopants are important for the synthesis of the phase-pure Ce-doped Bi_2WO_6 and Bi_2WO_6-BiOCl powders.

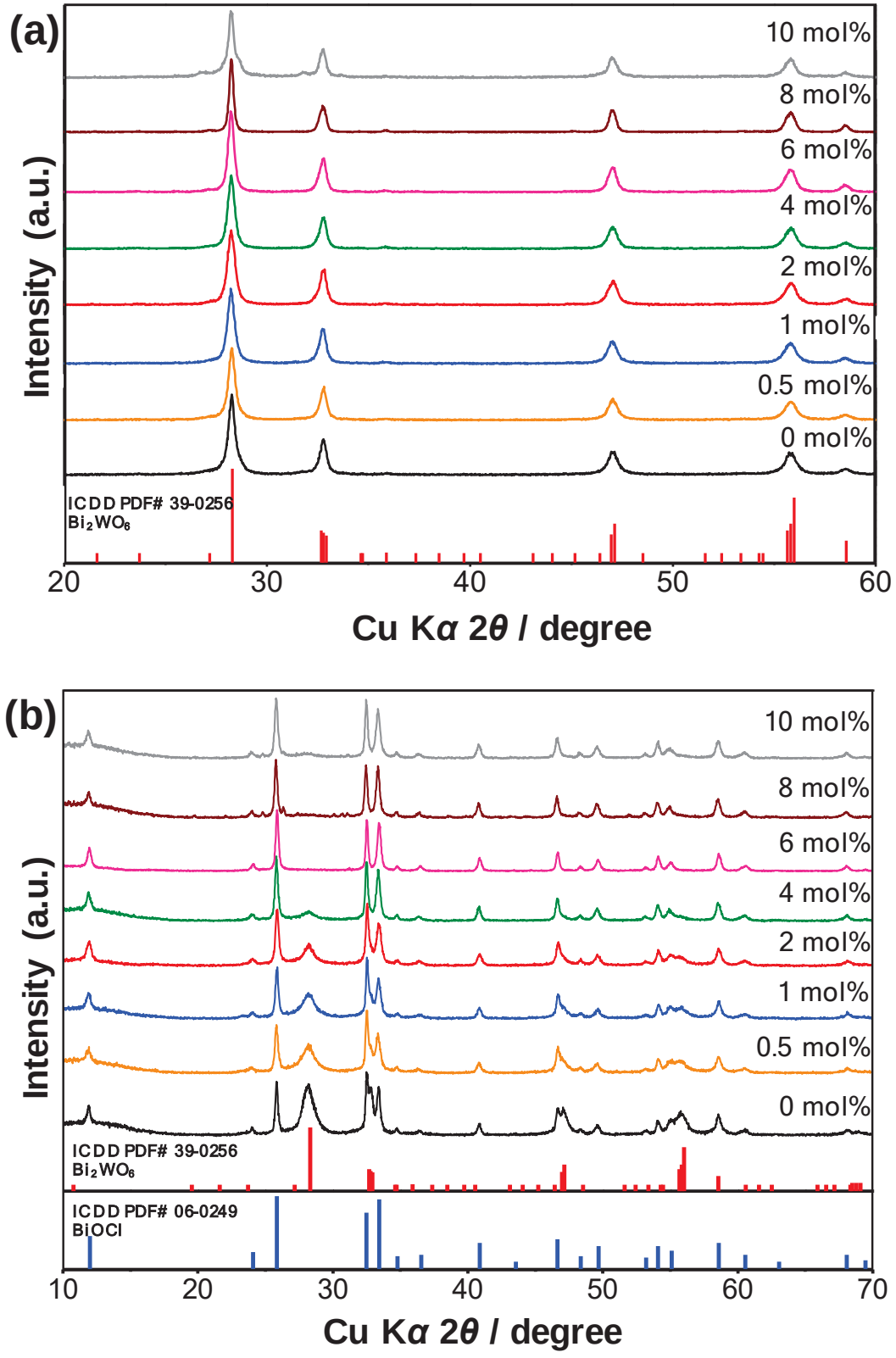

Figure 5.1. XRD patterns of (a) Bi_2WO_6 and (b) Bi_2WO_6-BiOCl powders doped with different contents of cerium ranging from 0 mol% to 10 mol%.

The morphology and microstructure of the as-synthesized samples were examined by scanning electron microscopy, and the results are represented in Figures 5.2 and 5.3. Figure 5.2 shows the typical SEM images of the non-doped and Ce-doped Bi_2WO_6 powders. As depicted in Figure 5.2a, non-doped Bi_2WO_6 powders exhibit hierarchical, not well-defined, structures with an average diameter of less than 3 μm. These hierarchical structures were assembled by a random aggregation of numerous nanosheets with a thickness of approximately 25 nm. Interestingly, with an increasing content of cerium dopant up to 6 mol%, these hierarchical structures gained their clear flower-like morphology constructed by parallelly and perpendicularly stacked nanosheets (Figures 5.2b-f). A further increase in the content of cerium dopant to 8 mol% led to the formation of acicular crystals on the surface of these flower-like hierarchical structures (Figure 5.2g), which were ultimately converted into the aggregated acicular nanocrystals at 10 mol% Ce (Figure 5.2h). Apparently, the thickness of the Bi_2WO_6 nanosheets was gradually reduced with increasing content of cerium dopant. Here, ethylene glycol was used as a solvent as well as a complexing agent forming a chain structure on the surface of the crystallites via either covalent or hydrogen bonding. During the hydrothermal reaction, Bi_2WO_6 nuclei were formed first and served as seeds for the growth of Bi_2WO_6 nanosheets in the supersaturated solution. Due to its high intrinsic anisotropic nature, Bi_2WO_6 grew into two-dimensional nanosheets. Further, the nanosheets with a high anisotropic surface energy were self-assembled readily into flower-like hierarchical structures through an ethylene glycol-induced Ostwald ripening [27,28]. For the non-doped Bi_2WO_6-BiOCl composite, irregularly shaped nanosheets with an average size of 350 nm, which did not form flower-like hierarchical structures, are shown in Figure 5.3a. When the cerium was doped, the randomly distributed nanosheets of the non-doped composite were gradually transformed into mostly parallel intersected nanoplates with scalloped edges due to acid etching [29], resulting in the flower-like hierarchical structures with the size of approximately 3 μm (Figures 5.3b-f), and the nanoplates became completely dominant in the range of 6-10 mol% Ce. Strikingly, at 8 and 10 mol% Ce, the distance between the stacked nanoplates was significantly shortened, and a greater number of enlarged nanoplates were parallelly stacked (compactly packed) to form spherical structures (Figures 5.3g and h). On one hand, the morphological transformation can be interpreted by the gradual dominance of the BiOCl

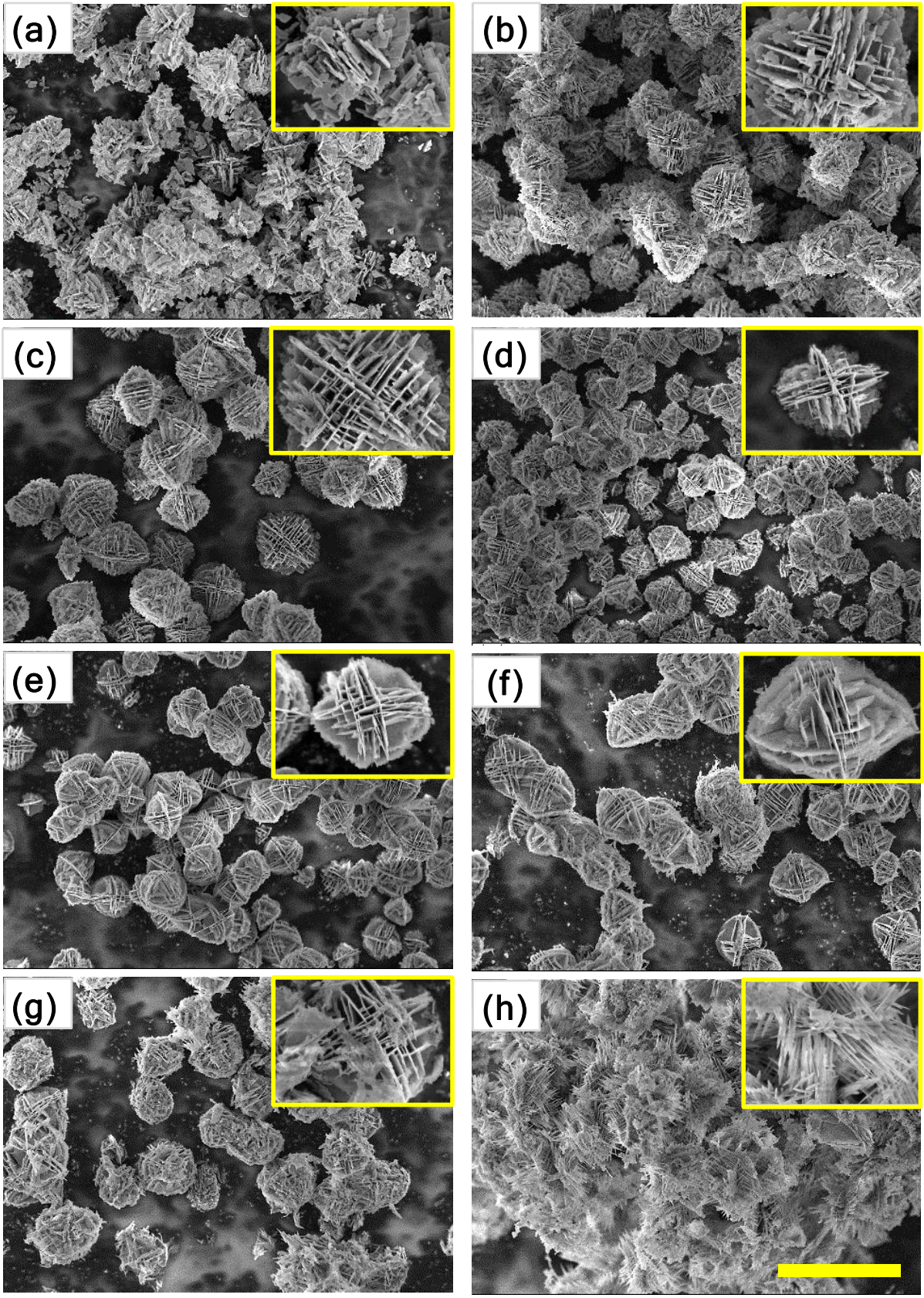

Figure 5.2. SEM images of Bi_2WO_6 powders doped with different contents of cerium: (a) 0 mol%, (b) 0.5 mol%, (c) 1 mol%, (d) 2 mol%, (e) 4 mol%, (f) 6 mol%, (g) 8 mol%, and (h) 10 mol%. The scale bar is 5 μm.

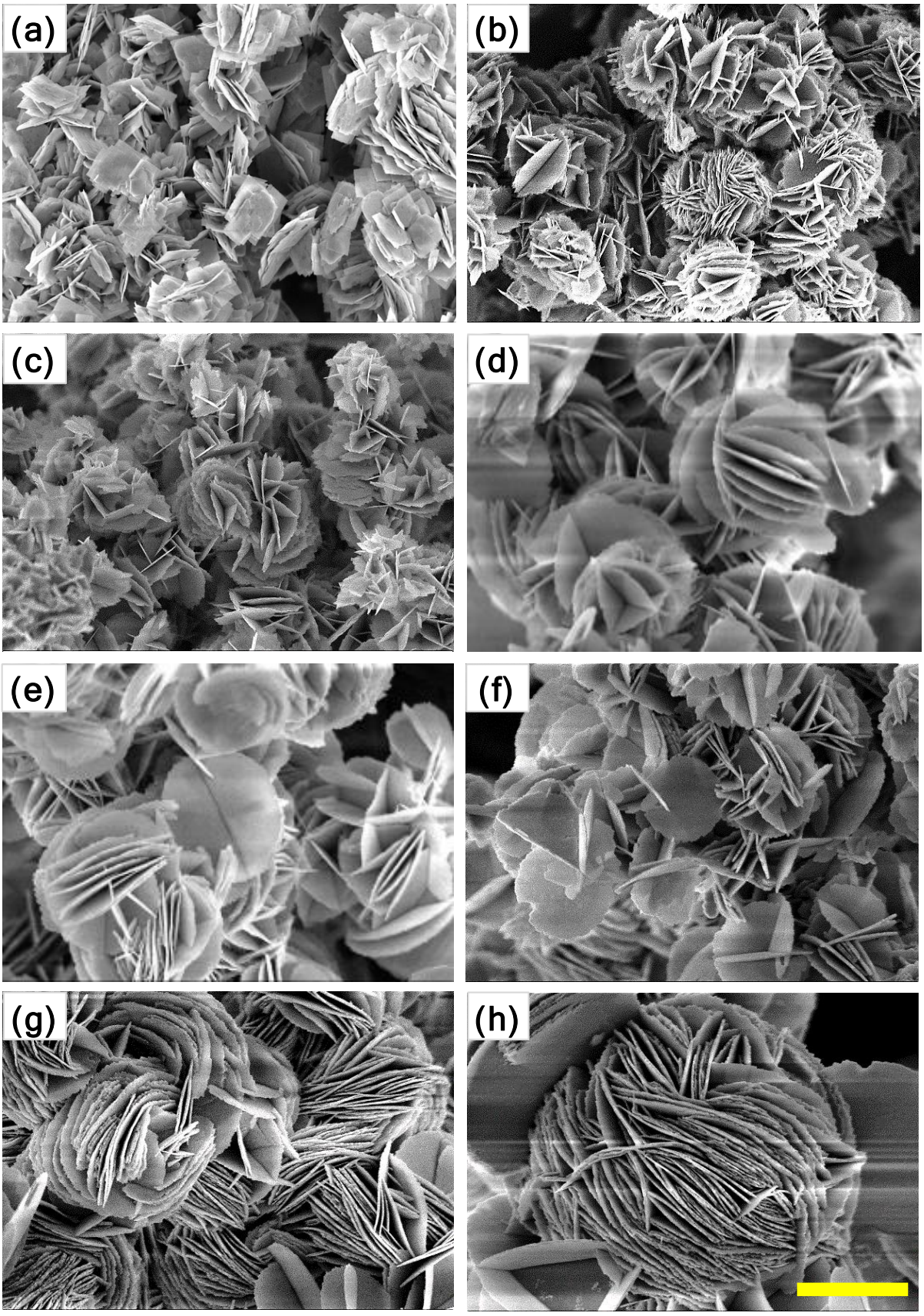

Figure 5.3. SEM images of Bi_2WO_6-BiOCl powders doped with different contents of cerium: (a) 0 mol%, (b) 0.5 mol%, (c) 1 mol%, (d) 2 mol%, (e) 4 mol%, (f) 6 mol%, (g) 8 mol%, and (h) 10 mol%. The scale bar is 1 μm.

phase over the Bi_2WO_6 phase in the composite. On the other hand, as most cerium ions were substitutionally introduced into BiOCl and Bi_2WO_6 without a noticeable lattice distortion, the selective adsorption of excessive Cl^- ions on specific crystal facets possibly governed the crystal growth, leading to the morphological variation with increasing concentration of cerium trichloride in the synthesis solution [30]. These flower-like hierarchical structures can absorb more photon energy due to multiple scattering, the photogenerated charge carriers can easily transfer to the surface/interface because of the nanoscale thickness of the nanosheets, and the mesopores of the synthesized samples can improve the transfer rate of the organic molecules, which contribute to the enhancement in the photocatalytic activity of the synthesized samples.

The surface chemical compositions and chemical states of the as-synthesized samples (non-doped and 2 mol% Ce-doped Bi_2WO_6 and Bi_2WO_6-BiOCl) were investigated by X-ray photoelectron spectroscopy (XPS), and the Bi 4f, W 4f, O 1s, Cl 2p, and Ce 3d XPS core-level spectra of the samples are shown in Figure 5.4. The XPS peaks centered at 164.6 and 159.3 eV can be assigned to the binding energies of Bi $4f_{5/2}$ and Bi $4f_{7/2}$, respectively, indicating that bismuth has an oxidation state of +3. The XPS peaks centered at 37.1 and 34.9 eV can be ascribed to the binding energies of W $4f_{5/2}$ and W $4f_{7/2}$, respectively, confirming that the tungsten has an oxidation state of +6. The O 1s binding energy of 530.8 eV can be attributed to the lattice oxygen in Bi_2WO_6 and BiOCl, and no other pronounced peaks characteristic of the chemisorbed or dissociated oxygen species are noted. In the XPS spectra of Cl 2p, the binding energies of Cl $2p_{1/2}$ and Cl $2p_{3/2}$ are observed at 199.4 and 197.8 eV, respectively, which is the characteristic of Cl^- in BiOCl. The Ce 3d XPS spectra can be deconvoluted into two pairs of spin-orbital bands: Ce^{3+} $3d_{3/2}$ and Ce^{3+} $3d_{5/2}$ at 906.7 and 888.6 eV, respectively and Ce^{4+} $3d_{3/2}$ and Ce^{4+} $3d_{5/2}$ at 903.1 and 885.3 eV, respectively [31]. To determine an exact content of cerium doped in the prepared photocatalysts, the X-ray fluorescence spectroscopy (XRF) analysis was performed. According to the XRF results, about 0.99, 2.01, 3.92, 5.93, 7.98, and 9.90% Ce were detected in the Bi_2WO_6 and Bi_2WO_6-BiOCl samples doped with 1, 2, 4, 6, 8, and 10 mol.% Ce, respectively. The obtained values are very close to the theoretical content of Ce, confirming the successful doping of cerium in the Bi_2WO_6 and Bi_2WO_6-BiOCl samples.

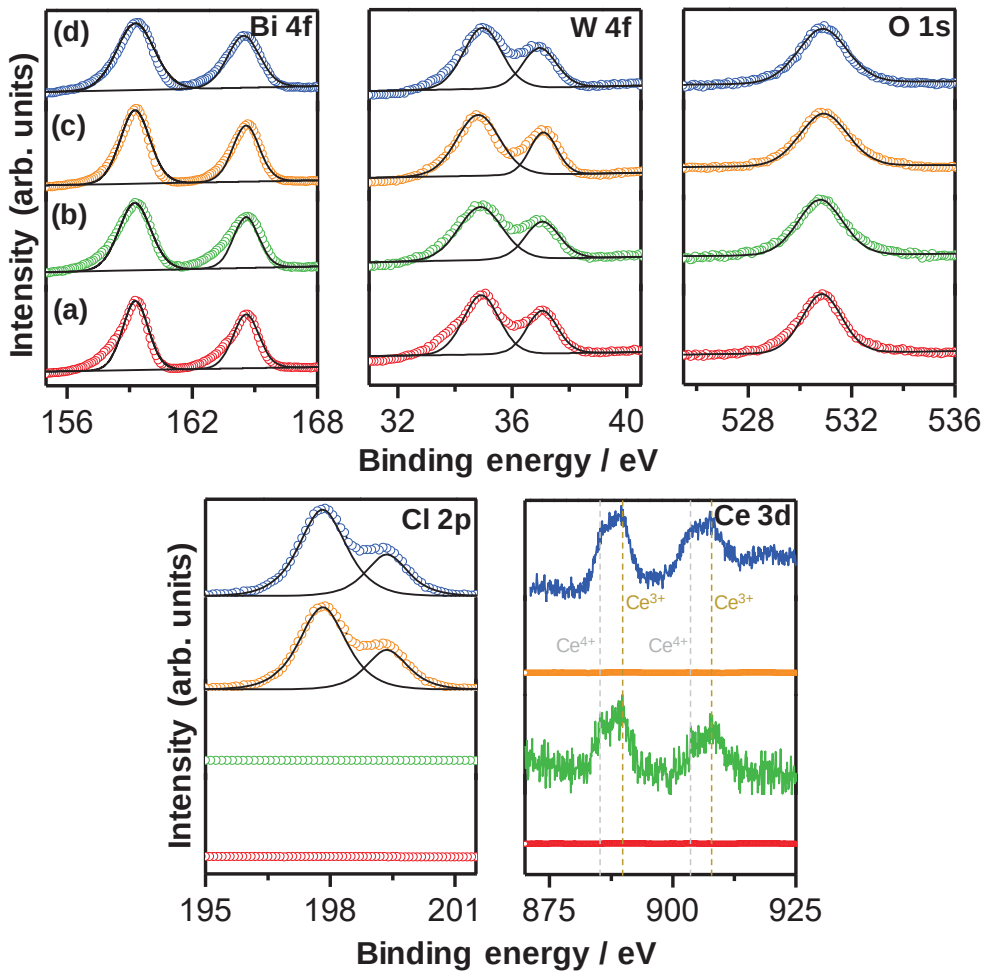

Figure 5.4. XPS core-level spectra of Bi 4f, W 4f, O 1s, Cl 2p, and Ce 3d of non-doped (a,c) and 2 mol% Ce-doped (b,d) Bi_2WO_6 and Bi_2WO_6-BiOCl powders.

The UV-vis diffuse reflectance spectra were measured to evaluate the light absorption properties of the as-synthesized samples. As shown in Figure 5.5, pure Bi_2WO_6 (Figure 5.5a, black line) displays a typical absorption edge at approximately 460 nm, whereas pure Bi_2WO_6-BiOCl (Figure 5.5b, black line) shows a slightly lower absorption edge at approximately 450 nm in the visible range owing to the incorporation of the BiOCl. For Ce-doped Bi_2WO_6, the absorption edge is significantly extended up to > 700 nm and the intensity of the background absorption is markedly increased with the increasing content of cerium dopant in Bi_2WO_6 from 0 to 10 mol%, which is possibly due to the formation of defects. Interestingly, the Ce-doped Bi_2WO_6-BiOCl samples indicated a smaller redshift (up to 600 nm with 10 mol% Ce) of the absorption band compared to that of the Ce-doped Bi_2WO_6 samples. This finding is because most cerium ions were incorporated into the BiOCl lattice rather than in the Bi_2WO_6 lattice. The redshift in the absorption spectra can be ascribed to the charge

transfer between the Bi_2WO_6 and BiOCl valence or conduction bands and the cerium ion 4f level. The corresponding band gap energies calculated from the Tauc plot of $(\alpha hv)^{1/2}$ versus photon energy (hv) for the Bi_2WO_6 and Bi_2WO_6-BiOCl samples with increasing cerium dopant content follow the order: 2.71 and 2.77 eV for 0 mol% Ce > 2.44 and 2.50 eV for 0.5 mol% Ce > 2.23 and 2.26 eV for 1 mol% Ce > 2.00 and 2.22 eV for 2 mol% Ce > 1.93 and 2.21 eV for 4 mol% Ce > 1.80 and 2.17 eV for 6 mol% Ce > 1.67 and 2.13 eV for 8 mol% Ce > 1.37 and 2.11 eV for 10 mol% Ce. This sequence implies that the addition of cerium plays an important role in changing the optical properties, utilizing the visible light of solar energy, and enhancing the photocatalytic activity of Bi_2WO_6 and Bi_2WO_6-BiOCl.

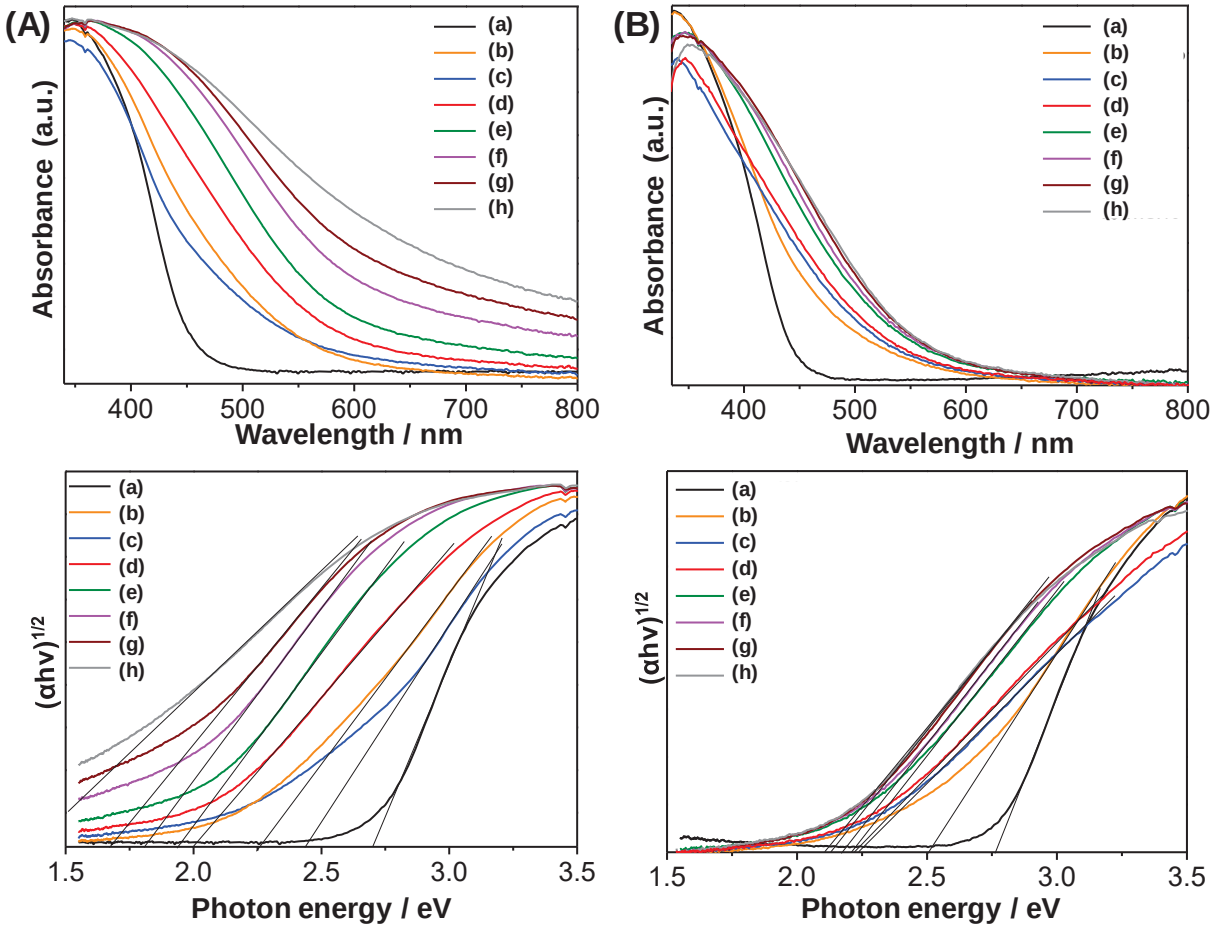

Figure 5.5. UV−vis diffuse reflectance spectra (*top*) and Tauc plots (*bottom*) of Bi_2WO_6 (A) and Bi_2WO_6-BiOCl (B) powders doped with different contents of cerium: (a) 0 mol%, (b) 0.5 mol%, (c) 1 mol%, (d) 2 mol%, (e) 4 mol%, (f) 6 mol%, (g) 8 mol%, and (h) 10 mol%.

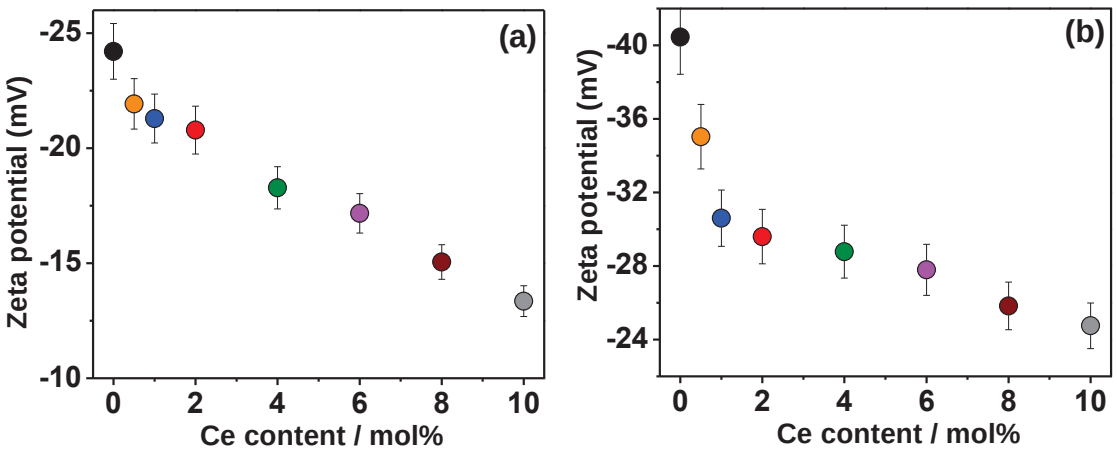

Figure 5.6. Zeta potential of (a) Bi_2WO_6 and (b) Bi_2WO_6-BiOCl powders at neutral pH as a function of cerium dopant content.

Figure 5.6 shows the zeta-potential values of non-doped and Ce-doped Bi_2WO_6 and Bi_2WO_6-BiOCl powders as a function of the cerium dopant content. As shown, both samples indicate no point of zero charge and exhibit negative zeta-potential values at the neutral pH of deionized water, indicating that the as-synthesized samples have negatively charged surfaces. The surface charge of the as-synthesized samples mainly result from the edge surfaces and structural charge sites. The edge surface charge comes from proton adsorption by the hydroxyl groups, whereas the structural charge sites have permanent negative charges. Compared with Bi_2WO_6, the Bi_2WO_6-BiOCl powders possess a greater negative charge due to the presence of Cl^- ions on the surface of BiOCl, creating negatively charged monolayers, which are eventually replaced partly by OH^- because of a surface hydration. Adjacent hydroxyl groups interact with the particle surface during the formation of a hydrated layer, which may result in hydrogen bonding between neighboring hydroxyl groups. In both cases, cerium doping may possibly reduce the negative charge values that provide a less favorable environment for the adsorption of negatively charged hydroxyl groups on the surfaces through electrostatic interactions.

5.3.2. Adsorption capacity and photocatalytic activity of the prepared samples

The adsorption capacity and photocatalytic activity of non-doped and Ce-doped Bi_2WO_6 and Bi_2WO_6-BiOCl samples were evaluated *via* the adsorption and photodegradation of salicylic acid in the dark and under visible light irradiation, respectively, and the results are

shown in Figure 5.7 and Table 5.1. The adsorption capacity of the synthesized samples for salicylic acid was directly proportional to the measured specific surface area. Specifically, the higher the specific surface area is, the greater the adsorption capacity is. With an increasing content of Ce dopants, the specific surface area and adsorption of salicylic acid gradually increase in the following order: 6.1 $m^2 \cdot g^{-1}$ and 7.2% (0 mol% Ce) < 6.7 $m^2 \cdot g^{-1}$ and 8.8% (0.5 mol%) < 7.3 $m^2 \cdot g^{-1}$ and 11.6% (1 mol%) < 9.4 $m^2 \cdot g^{-1}$ and 14.0% (2 mol%) < 11.6 $m^2 \cdot g^{-1}$ and 17.6% (4 mol%) < 14.2 $m^2 \cdot g^{-1}$ and 23.2% (6 mol%) < 15.8 $m^2 \cdot g^{-1}$ and 25.6% (8 mol%) < 18.3 $m^2 \cdot g^{-1}$ and 30.4% (10 mol%) for Bi_2WO_6 and 9.6 $m^2 \cdot g^{-1}$ and 11.6% (0 mol%) < 11.4 $m^2 \cdot g^{-1}$ and 14.0% (0.5 mol%) < 14.8 $m^2 \cdot g^{-1}$ and 21.6% (1 mol%) < 18.7 $m^2 \cdot g^{-1}$ and 27.2% (2 mol%) < 29.5 $m^2 \cdot g^{-1}$ and 34.0% (4 mol%) < 36.9 $m^2 \cdot g^{-1}$ and 35.6% (6 mol%) < 40.2 $m^2 \cdot g^{-1}$ and 39.2% (8 mol%) < 48.6 $m^2 \cdot g^{-1}$ and 43.6% (10 mol%) for Bi_2WO_6-BiOCl. In contrast, the photodegradation of salicylic acid over the synthesized samples did not follow this trend. The results indicate that cerium doping has not only tuned the morphological structure but also increased the specific surface area, improving the adsorption capacity of Bi_2WO_6 and Bi_2WO_6-BiOCl for salicylic acid.

Table 5.1. Adsorption and photodegradation of salicylic acid over the non-doped and Ce-doped Bi_2WO_6 and Bi_2WO_6-BiOCl.

Sample	S_{BET}	Salicylic acid adsorption in the dark		Salicylic acid photodegradation under visible light irradiation	
Ce-doped Bi_2WO_6	$m^2 \cdot g^{-1}$	μmol	%	% at 5 h	k, min^{-1}
0 mol%	6.1	23.2	7.2	60.8	-0.105
0.5 mol%	6.7	22.8	8.8	87.2	-0.233
1 mol%	7.3	22.1	11.6	91.6	-0.297
2 mol%	9.4	21.5	14.0	79.2	-0.159
4 mol%	11.6	20.6	17.6	76.4	-0.137
6 mol%	14.2	19.2	23.2	74.8	-0.095
8 mol%	15.8	18.6	25.6	71.2	-0.090
10 mol%	18.3	17.4	30.4	70.4	-0.147

Ce-doped Bi_2WO_6-BiOCl	$m^2 \cdot g^{-1}$	μmol	%	% at 5 h	k, min^{-1}
0 mol%	9.6	22.1	11.6	70.0	-0.224
0.5 mol%	11.4	21.5	14.0	79.2	-0.250
1 mol%	14.8	19.6	21.6	96.8	-0.360
2 mol%	18.7	18.2	27.2	72.8	-0.169
4 mol%	29.5	16.5	34.0	68.4	-0.136
6 mol%	36.9	16.1	35.6	66.0	-0.128
8 mol%	40.2	15.2	39.2	60.8	-0.092
10 mol%	48.6	14.1	43.6	53.2	-0.040

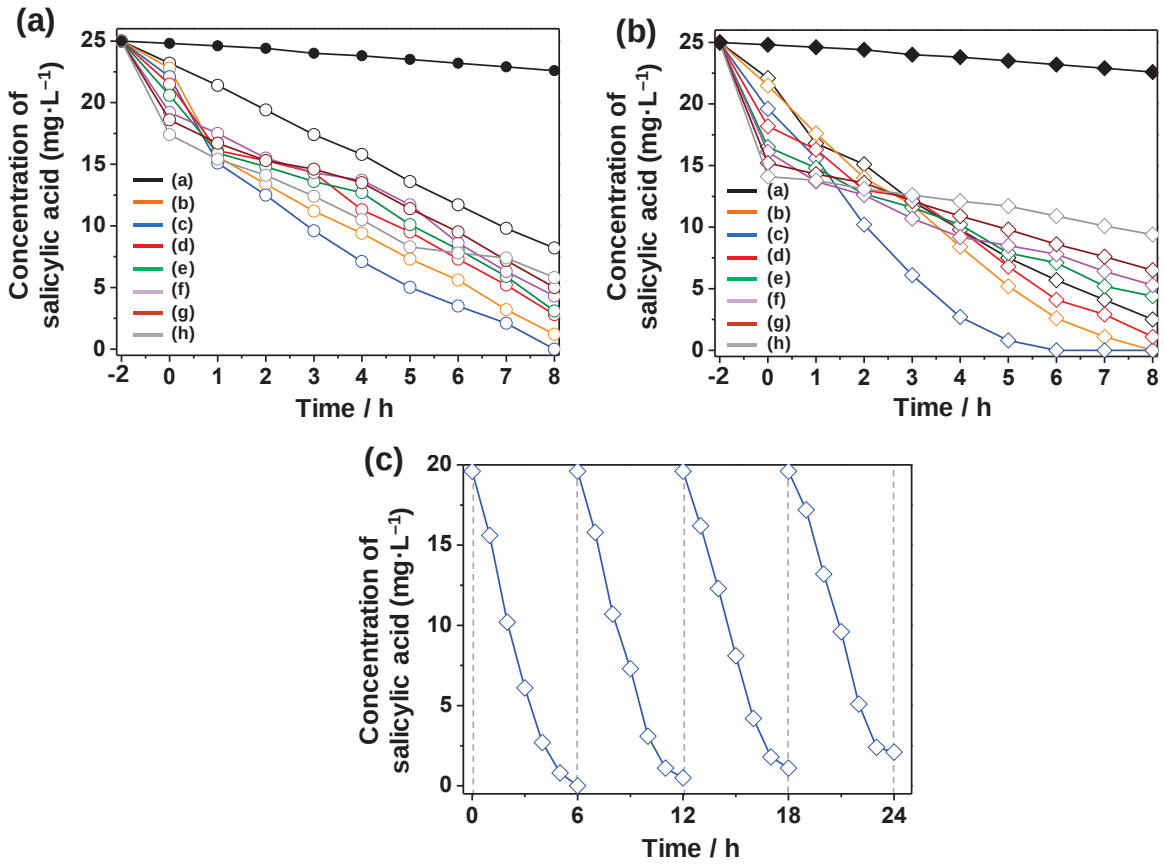

Figure 5.7. Adsorption and photocatalytic activity for the removal of salicylic acid of (a) Bi_2WO_6 and (b) Bi_2WO_6-BiOCl powders doped with different contents of cerium ranging from 0 mol% to 10 mol%. (c) Photocatalytic activity for the degradation of salicylic acid over the Bi_2WO_6-BiOCl powders doped with 1 mol% Ce for four cycles.

5.3.3. Molecular modeling of adsorption of salicylic acid molecules on the prepared samples

The adsorption affinities and preferential sites of salicylic acid molecules on non-doped and Ce-doped Bi_2WO_6, BiOCl, and Bi_2WO_6-BiOCl were computationally studied using molecular dynamics simulations [32]. The adsorption of salicylic acid molecules onto the surfaces is visually illustrated in Figures 5.8 and 5.9. The adsorption energies of the most stable configuration of a salicylic acid molecule and a water molecule over mineral surfaces were exothermic due to the strong mineral–adsorbate interaction (Figure 5.8). The simultaneous adsorption of the salicylic acid and water molecules on the Ce-doped Bi_2WO_6 mineral is stronger (more exothermic) than that on Bi_2WO_6 (Δ_{ads} = (E_{ads}(HSal+H_2O)-(E_{ads}(HSal)+E_{ads}(H_2O))$_{Bi2WO6}$-(E_{ads}(HSal+H_2O)-(E_{ads}(HSal)+E_{ads}(H_2O))$_{Ce\text{-}doped\ Bi2WO6}$ = 10 kcal·mol^{-1}). However, the Δ_{ads} value is less (0.25 kcal·mol^{-1}) for the Ce-doped BiOCl surface than the BiOCl surface. The obtained results can be explained via an approximation of the formation of different electronic structures of the adsorbed layer of water molecules that interact with the mineral surface through the H-bonds network and close contact. The adsorbed salicylic acid molecules can be stabilized by interaction with the layer of water molecules and direct interaction with the mineral surface. The salicylic acid molecules can interact with the surface atoms using the carboxyl ($O_{C=O}$, O_{COH}, H_{COOH}) and hydroxyl (O_{OH}, H_{OH}) groups.

Figure 5.9 shows the most stable molecular configurations with H bonds over the Bi_2WO_6, Ce-doped Bi_2WO_6, BiOCl, and Ce-doped BiOCl surfaces:

(i) *Salicylic acid adsorption model*. Over the Bi_2WO_6 and Ce-doped Bi_2WO_6 surfaces, salicylic acid molecules have an intramolecular H bond (O_{COH}… H_{COOH} – 2.354 Å) and prefer to connect to the surface oxygen atoms directly (H_{COOH}… O—Bi – 2.736 and 2.739 Å). The BiOCl surface contacts the salicylic acid molecules via H_{COOH}…Cl – 2.932 Å, whereas the Ce-doped BiOCl surface has no H bonds except a typical intramolecular H bond (O_{COH}… H_{COOH} – 2.322 Å).

(ii) *Water adsorption model*. The layered structure of the adsorbed water molecules differs for the Bi_2WO_6 and Ce-doped Bi_2WO_6 surfaces. Over the Bi_2WO_6 surface, the water molecules form a monolayer with intermolecular H bonds (O_{H2O}…H_{H2O} – 2.443-2.669 Å) and

interact with the surface (H_{H2O} …. O—W – 2.774-2.902 Å, H_{H2O} …. O—Bi – 2.851-2.983 Å). However, over the Ce-doped Bi_2WO_6 surface, the water molecules form separated agglomerates that are in contact with the surface (H_{H2O} …. O—W – 2.989-2.905 Å), whereas the H bond provides the possibility for the salicylic acid molecules to enter the surface directly. However, over the Bi_2WO_6 and Ce-doped Bi_2WO_6 surfaces, the salicylic acid molecules have no direct interaction with the surface and connect to the layer of water molecules by the intermolecular H bonding. The results from the zeta-potential analysis of the Bi_2WO_6 and Ce-doped Bi_2WO_6 particles confirm the formation of a layer of water molecules on the mineral surface. Over the BiOCl and Ce-doped BiOCl surfaces, the water molecules are chained by H bonds (O_{H2O}…H_{H2O} – 2.443-2.669 Å) without a strong interaction with the surface (close contacts H…Cl – 3.1 Å). The layer of water molecules over the Ce-doped BiOCl surface exhibits much closer contact H…Cl and some periodical order depending on the presence of Ce atoms.

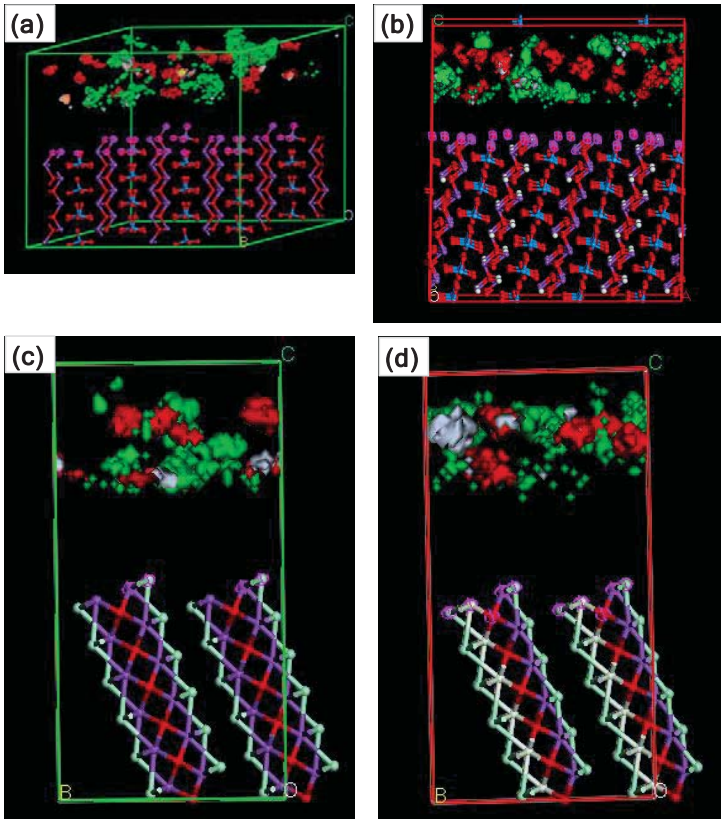

Figure 5.8. Visualization of adsorption of the salicylic acid and water molecules onto (1 1 1) cleavage surfaces of (a) Bi_2WO_6, (b) Ce-doped Bi_2WO_6, (c) BiOCl, and (d) Ce-doped BiOCl: bismuth, violet; tungsten, blue; oxygen, red; chlorine, light-green; and cerium, beige. Density isosurface: salicylic acid, red; water, green.

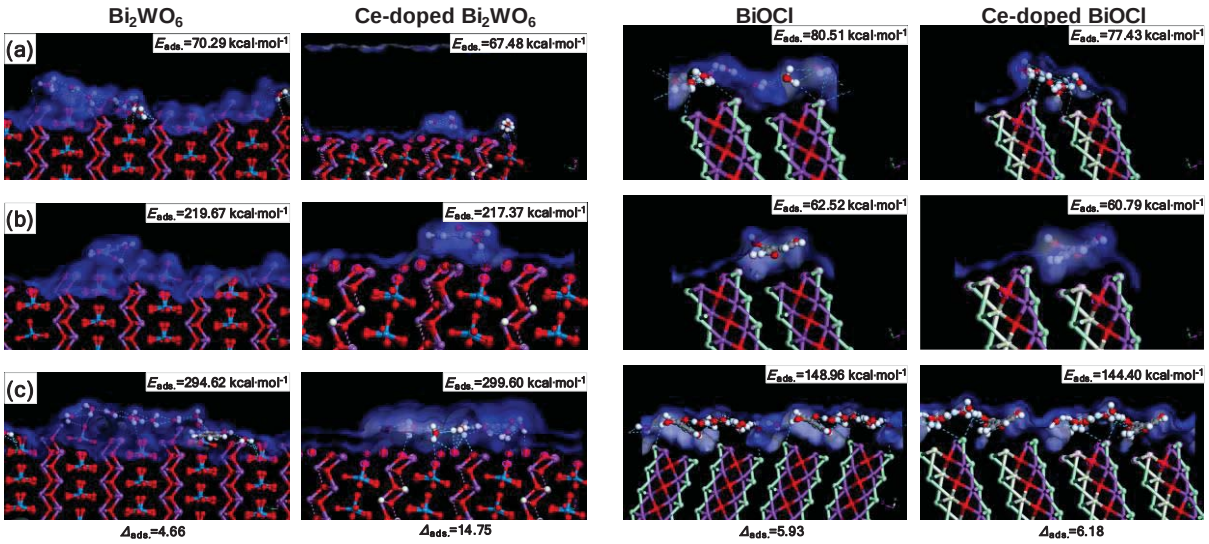

Figure 5.9. Structure model of adsorption of (a) water molecules, (b) salicylic acid molecules, and (c) water and salicylic acid molecules: bismuth, violet; tungsten blue; oxygen, red; chlorine, light-green; and cerium, beige. Isosurface: Connolly surface, blue.

(iii) *Salicylic acid and water adsorption model.* The salicylic acid molecules prefer to bind to the surface oxygen atoms indirectly through the water molecules that are already in contact with the Bi_2WO_6 (H_{H2O} …. O—W – 2.741-2.805 Å) and Ce-doped Bi_2WO_6 (H_{H2O} … O—Bi – 2.763, H_{H2O}… O—W – 2.835-2.954, and H_{H2O} … O—Ce – 2.854 Å). The BiOCl surface directly binds with the salicylic acid molecules via H bonding (H_{COOH}…Cl – 2.932 Å), the water molecules involved in the H-bond network with the salicylic acid molecules (O_{OH}…H_2O, $O_{C=O}$…H_2O, O_{COOH}… H_2O) and other water molecules. The Ce-doped BiOCl surface has demonstrated no direct bonding to the salicylic acid molecules, which involve the layer of water molecules located over the surface using close contacts Cl…H_2O – 3.133-3.148 Å. The field density shows separated spaces breaking near the randomly distributed Ce atoms (Figure 5.8).

The results indicate that the Ce-doped Bi_2WO_6 surface exhibits a better interaction with the salicylic acid and water molecules, resulting in higher photocatalytic activity, as predicted by the molecular dynamics calculations. Interestingly, the Ce-doped BiOCl surface possesses no pronounced impact on the adsorption of salicylic acid molecules, but the positive effect of the combination of the high specific surface area and electronic interaction between the

salicylic acid and layer of water molecules is observed for the Ce-doped Bi_2WO_6-BiOCl sample.

The photodegradation efficiency of salicylic acid over the synthesized samples was estimated based on the change in the intensity of absorption peaks of salicylic acid at 296 nm and the results of the total organic carbon (TOC) analysis. As shown in Figures 5.7a and b, the direct photolysis of salicylic acid performed for comparison under identical experimental conditions in the absence of photocatalysis was negligible, indicating that salicylic acid is stable under visible light irradiation. In both cases, the photodegradation efficiency of salicylic acid over the synthesized samples at 5 h gradually reaches the maximum (91.6% for Bi_2WO_6 and 96.8% for Bi_2WO_6-BiOCl) at 1 mol% Ce.

A further increment in the Ce content up to 10 mol% gradually decreased the photodegradation efficiency of salicylic acid over the Bi_2WO_6 and Bi_2WO_6-BiOCl samples. Excess Ce species possibly covered the active sites or acted as a recombination center, reducing the separation efficiency of the charge carriers. Therefore, 1 mol% was found to be the optimum concentration of Ce doping in Bi_2WO_6 and Bi_2WO_6-BiOCl, promoting the effective separation and transfer of photogenerated charge carriers, resulting in high photocatalytic performance. Compared to Bi_2WO_6, the Bi_2WO_6-BiOCl samples exhibited higher photocatalytic activity owing to the formation of a *p–n* heterojunction in the composite. The experimentally obtained data were fitted in the pseudo first-order kinetic equation $\ln(C/C_0) = -kt$, and the apparent rate constants of the photodegradation of salicylic acid are given in Table 5.1. Among the samples, the 1 mol% Ce-doped Bi_2WO_6-BiOCl sample showed the highest apparent rate constant (k = -0.360 min^{-1}), which is more than three times higher than that of non-doped Bi_2WO_6 (k = -0.105 min^{-1}), due to the synergistic effect of cerium doping and the formed *p–n* heterojunction. For future practical applications, it is important to investigate the reusability and stability of the synthesized materials during a photocatalytic reaction. In this context, the 1 mol% Ce-doped Bi_2WO_6-BiOCl sample was subjected to four successive photocatalytic experiments by adding a fresh aqueous solution containing salicylic acid in each run under visible light irradiation. As shown in Figure 5.7c, the photodegradation efficiency of salicylic acid over the sample slightly decreased due to the loss of photocatalyst particles during the separation after each cycle, suggesting that the synthesized composite has

good stability and can be consecutively used in water purification processes.

Based on the above results and previous reports, a possible mechanism for the enhanced photocatalytic activity of the Bi_2WO_6-BiOCl composite for the degradation of salicylic acid is schematically illustrated in Figure 5.10. When *p*-type BiOCl and *n*-type Bi_2WO_6 are in contact, a *p–n* heterojunction forms, resulting in the formation of an internal electric field at the interface of the *p–n* heterojunction after equilibrium. The formed heterojunction in turn accelerates the separation of photogenerated electron-hole pairs [33]. According to the calculated data reported previously [9], in the Bi_2WO_6-BiOCl heterojunction, the electrons in the conduction band of BiOCl transfer to the conduction band of Bi_2WO_6 because the conduction band of the latter is more positively positioned than that of the former. Simultaneously, additional electrons are excited to the conduction band of Bi_2WO_6 under visible light irradiation. The transferred and excited electrons can reduce O_2 to O_2^{-}• and transform into •OH. Meanwhile, the holes in the valence band of Bi_2WO_6 transfer to the valence band of BiOCl because the valence band of BiOCl is more negatively located than that of Bi_2WO_6 and oxidize H_2O and OH^- to •OH. Along with the holes, the generated •OH by both electrons and holes will be involved in the degradation of salicylic acid under visible light [32,34,35].

As the holes and electrons are separated in the valence band of BiOCl and the conduction band of Bi_2WO_6, respectively, the formed Bi_2WO_6-BiOCl heterojunction therefore possesses a lower recombination rate of photogenerated electrons and holes at the interface, contributing to the enhanced photocatalytic activity:

Ce-doped Bi_2WO_6-BiOCl + $h\nu$ → Ce-doped Bi_2WO_6-BiOCl ($e^- + h^+$) (1)

Ce-doped Bi_2WO_6-BiOCl (e_{CB}^-) + $O_{2(ads.)}$ → Ce-doped Bi_2WO_6-BiOCl + O_2^-•$_{(ads.)}$ (electron trapping by O_2 adsorption) (2)

$2^{\bullet}O^{2-} + 2e^- + 2H^+ \rightarrow 2H_2O_2$ (3)

$H_2O_2 + e^- + H^+ \rightarrow 2{\bullet}OH$ (4)

$H_2O + h^+ \rightarrow {\bullet}OH + H^+$ (5)

$(C_7H_6O_3)_{ads} + {\bullet}OH \rightarrow (C_7H_6O_3)_{ads}^+ \rightarrow (Intermediate)_{ads} \rightarrow CO_2 + H_2O$ + by-products (6)

$(C_7H_6O_3)_{ads} + h^+ \rightarrow (C_7H_6O_3)_{ads}^+ \rightarrow (Intermediate)_{ads} \rightarrow CO_2 + H_2O$ + by-products (7)

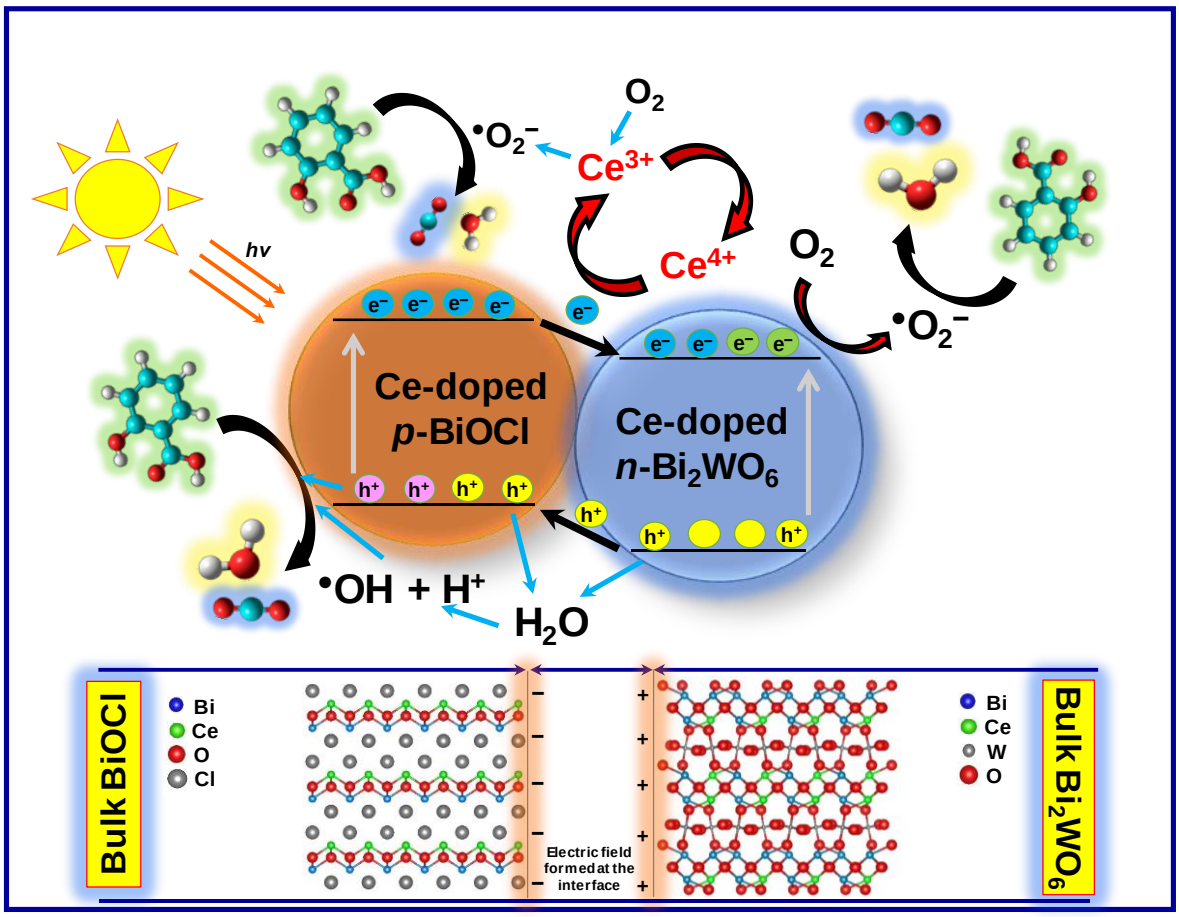

Figure 5.10. Schematic representation of the photodegradation mechanism of salicylic acid over the Bi_2WO_6-BiOCl powders doped with 1 mol% Ce under visible light irradiation.

Although the formation of the intermediates is complex and not particularly investigated in the present work, it is thought that the photodegradation of salicylic acid over the Bi_2WO_6 and Bi_2WO_6-BiOCl samples follows the most likely reaction pathway, resulting in the formation of 1,2-dihydroxybenzene, 2,3-dihydroxybenzoic acid, hydroquinone, benzoquinone, muconic acid, maleic acid, oxalic acid, malic acid, malonic acid, and acetic acid as intermediates, which explains the opening of the aromatic ring [36]. Previously, a high degree of mineralization of salicylic acid over TiO_2/SiO_2 fibers was achieved through the homogeneous photochemical oxidation by adding an adequate amount of H_2O_2 due to the formation of •OH radicals [37]. Arfanis et al. [24] reported that TiO_2 nanotubular films showed a negligible variation in their photocatalytic activity towards the photodegradation of salicylic acid in a wide pH range of aqueous solutions, making them suitable for applications under different conditions. Lang et al. [38] suggested that salicylic acid molecules can also act

as sensitizers for photochemical oxidation by absorbing photons at higher wavelengths, which contributes to the photocatalytic activity.

As the Bi_2WO_6 amount in the composite gradually decreases with increasing Ce content, a decrease in the photocatalytic activity is observed, demonstrating the pivotal role of the formed heterojunction. The improvement in the photocatalytic activity of the samples doped with an appropriate amount of cerium stems from (i) the presence of a Ce^{3+}/Ce^{4+} redox couple that can act as an electron scavenger and superoxide radicals (O_2^{-}•) producers, (ii) the formation of oxygen vacancies with the relatively high mobility of bulk oxygen species, and (iii) the different optical properties that result from the various electronic structures of Ce^{3+} with $4f^15d^0$ and Ce^{4+} with $4f^05d^0$. During the reaction, the photogenerated electrons are trapped by Ce^{4+}, and Ce^{4+} is reduced to Ce^{3+}, which can be oxidized back to Ce^{4+} by the adsorbed oxygen in the system. The adsorbed oxygen reacts with Ce^{3+} and e^- to produce O_2^{-}•. In addition to the efficient separation of electrons and holes, the Ce^{3+}/Ce^{4+} redox couple also promotes the generation of O_2^{-}• that can also contribute to the improvement of photocatalytic activity along with the •OH and holes [7,39,40]:

$$Ce^{4+} + e^- \rightarrow Ce^{3+} \text{ (electron trapping)} \quad (8)$$

$$Ce^{3+} + O_2 \rightarrow Ce^{4+} + O_2^{-}\bullet \text{ (electron transfer)} \quad (9)$$

$$(C_7H_6O_3)_{ads} + O_2^{-}\bullet \rightarrow (\text{intermediate})_{ads} \rightarrow CO_2 + H_2O. \quad (10)$$

The obtained results showed that the synthesized materials can be used for the purification of water contaminated with various pharmaceuticals and personal care products.

5.4. Conclusions

In summary, we have successfully synthesized non-doped and Ce-doped Bi_2WO_6 and Bi_2WO_6-BiOCl powders by a hydrothermal method. The Bi_2WO_6-BiOCl composite was formed when ethylene glycol was replaced by dilute HCl as a solvent in the hydrothermal system. The formation of flower-like morphologies was governed by a complexing agent (ethylene glycol) forming a chain-like structure on the crystallite surface and the selective adsorption of excessive Cl^- ions on the specific surface of crystallite, leading to a morphological variation. Cerium doping could extend the absorption edges of Bi_2WO_6 and Bi_2WO_6-BiOCl up to 460 and > 700 nm, respectively. According to the molecular dynamics calculation results, Ce doping enhances the interaction of the Bi_2WO_6 surface with the

salicylic acid molecules in Ce-doped Bi_2WO_6-BiOCl due to the improved interaction between the Bi_2WO_6 surface and the layer of water molecules through which the salicylic acid molecules are connected by hydrogen bonding. Among the samples, the 1 mol% Ce-doped Bi_2WO_6-BiOCl sample showed the highest apparent rate constant (k = -0.360 min^{-1}), which is more than three times higher than that of non-doped Bi_2WO_6 (k = -0.105 min^{-1}), due to the synergistic effect of cerium doping and the formed *p–n* heterojunction. More importantly, the synthesized composite possesses good photostability and can be reused during water treatment.

5.5. References

[1] N. Zhang, R. Ciriminna, M. Pagliaro, Y.-J. Xu, Nanochemistry-derived Bi_2WO_6 nanostructures: towards production of sustainable chemicals and fuels induced by visible light, *Chem. Soc. Rev.* 43 (2014) 5276–5287.

[2] G. Zhu, J. Liang, M. Hojamberdiev, S. Aldabe Bilmes, X. Wei, P. Liu, J. Zhou, Ethylenediamine (EDA)-assisted hydrothermal synthesis of nitrogen-doped Bi_2WO_6 powders, *Mater. Lett.* 122 (2014) 216–219.

[3] P. Ju, P. Wang, B. Li, H. Fan, S. Ai, D. Zhang, Y. Wang, A novel calcined Bi_2WO_6/$BiVO_4$ heterojunction photocatalyst with highly enhanced photocatalytic activity, *Chem. Eng. J.* 236 (2014) 430–437.

[4] Y. Peng, Q.-G. Chen, D. Wang, H.-Y. Zhou, A.-W. Xu, Synthesis of one-dimensional WO_3–Bi_2WO_6 heterojunctions with enhanced photocatalytic activity, *CrystEngComm* 17 (2015) 569–576.

[5] X. Xu, X. Shen, G. Zhu, L. Jing, X. Liu, K. Chen, Magnetically recoverable Bi_2WO_6–Fe_3O_4 composite photocatalysts: Fabrication and photocatalytic activity, *Chem. Eng. J.* 200–202 (2012) 521–531.

[6] M. Hojamberdiev, K.-i. Katsumata, K. Morita, S. Aldabe Bilmes, N. Matsushita, K. Okada, One-step hydrothermal synthesis and photocatalytic performance of $ZnWO_4$/Bi_2WO_6 composite photocatalyst for efficient degradation of acetaldehyde under UV light irradiation, *Appl. Catal. A* 457 (2013) 12–20.

[7] M. Hojamberdiev, Z.C. Kadirova, Y. Makinose, G. Zhu, S. Emin, N. Matsushita, M. Hasegawa, K. Okada, Involving $CeVO_4$ in improving the photocatalytic activity of a

Bi_2WO_6/allophane composite for the degradation of gaseous acetaldehyde under visible light, *Colloids Surf. A* 529 (2017) 600–612.

[8] L. Ye, Y. Su, X. Jin, H. Xie, C. Zhang, Recent advances in BiOX (X = Cl, Br and I) photocatalysts: synthesis, modification, facet effects and mechanisms, *Environ. Sci.: Nano* 1 (2014) 90–112.

[9] W. Yang, B. Ma, W. Wang, Y. Wen, D. Zeng, B. Shan, Enhanced photosensitized activity of a BiOCl–Bi_2WO_6 heterojunction by effective interfacial charge transfer, *Phys. Chem. Chem. Phys.* 15 (2013) 19387–19394.

[10] Y. Li, Y. Liu, J. Wang, E. Uchaker, Q. Zhang, S. Sun, Y. Huang, J. Li, G. Cao, Titanium alkoxide induced BiOBr–Bi_2WO_6 mesoporous nanosheet composites with much enhanced photocatalytic activity, *J. Mater. Chem. A* 1 (2013) 7949–7956.

[11] Y. Xiang, P. Ju, Y. Wang, Y. Sun, D. Zhang, J. Yu, Chemical etching preparation of the Bi_2WO_6/BiOI p–n heterojunction with enhanced photocatalytic antifouling activity under visible light irradiation, *Chem. Eng. J.* 288 (2016) 264–275.

[12] C. Wang, Q. Zhu, C. Gu, X. Luo, C. Yu, M. Wu, Photocatalytic degradation of two different types of dyes by synthesized La/Bi_2WO_6, *RSC Adv.* 6 (2016) 85852–85859.

[13] F. Wang, W. Li, S. Gu, H. Li, X. Wu, X. Liu, Samarium and Nitrogen Co-Doped Bi_2WO_6 Photocatalysts: Synergistic Effect of Sm^{3+}/Sm^{2+} Redox Centers and N-Doped Level for Enhancing Visible-Light Photocatalytic Activity, *Chem. Eur. J.* 22 (2016) 12859–12867.

[14] Y. Tian, L. Zhang, J. Zhang, A superior visible light-driven photocatalyst: Europium-doped bismuth tungstate hierarchical microspheres, *J. Alloys Compd.* 537 (2012) 24–28.

[15] N. Tian, Y. Zhang, H. Huang, Y. He, Y. Guo, Influences of Gd Substitution on the Crystal Structure and Visible Light-Driven Photocatalytic Performance of Bi_2WO_6, *J. Phys. Chem. C* 118 (2014) 15640–15648.

[16] H. Li, H. Hao, S. Jin, W. Guo, X. Hu, H. Hou, G. Zhang, S. Yan, W. Gao, G. Liu, Synthesis of Yb^{3+}/Ho^{3+} co-doped Bi_2WO_6 upconversion photocatalyst with highly improved visible light photocatalytic activity, *Catal. Commun.* 97 (2017) 60–64.

[17] M. Wang, Z. Qiao, M. Fang, Z. Huang, Y. Liu, X. Wu, C. Tang, H. Tang, H. Zhu, Synthesis of Er-doped Bi_2WO_6 and enhancement in photocatalytic activity induced by visible light, *RSC Adv.* 5 (2015) 94887–94894.

[18] N.K. Stamatis, I.K. Konstantinou, Occurrence and removal of emerging pharmaceutical, personal care compounds and caffeine tracer in municipal sewage treatment plant in Western Greece, *J. Environ. Sci. Health B* 48 (2013) 800–813.

[19] C.I. Kosma, D.A. Lambropoulou, T.A. Albanis, Investigation of PPCPs in wastewater treatment in Greece: occurrence removal and environmental risk assessment, *Sci. Total Environ.* 466–467 (2014) 421–438.

[20] E.N. Evgenidou, I.K. Konstantinou, D.A. Lambropoulou, Occurrence and removal of transformation products of PPCPs and illicit drugs in wastewaters: a review, *Sci. Total Environ.* 505 (2015) 905–926.

[21] D. Mukherjee, A.K. Ray, S. Barghi, Mechanism of Acetyl Salicylic Acid (Aspirin) Degradation under Solar Light in Presence of a TiO_2-Polymeric Film Photocatalyst, *Processes* 4 (2016) 1–9.

[22] Opinion of the scientific committee on cosmetic products and non-food products intended for consumers concerning salicylic acid (SCCNFP/0522/01, final), 4 June 2002. http://ec.europa.eu/health/ph_risk/committees/sccp/documents/out170_en.pdf

[23] I. Sirés, E. Brillas, Remediation of water pollution caused by pharmaceutical residues based on electrochemical separation and degradation technologies: a review, *Environ. Int.* 40 (2012) 212–229.

[24] M.K. Arfanis, P. Adamou, N.G. Moustakas, T.M. Triantis, A.G. Kontos, P. Falaras, Photocatalytic degradation of salicylic acid and caffeine emerging contaminants using titania nanotubes, *Chem. Eng. J.* 310 (2017) 525–536.

[25] R. Ma, X. Wang, J. Huang, J. Song, J. Zhang, X. Wang, Photocatalytic degradation of salicylic acid with magnetic activated carbon-supported F-N codoped TiO_2 under visible light, *Vacuum* 141 (2017) 157–165.

[26] B. Garza-Campos, E. Brillas, A. Hernández-Ramírez, A. El-Ghenymy, J.L. Guzmán-Mar, E.J. Ruiz-Ruiz, Salicylic acid degradation by advanced oxidation processes. Coupling of

solar photoelectro-Fenton and solar heterogeneous photocatalysis, *J. Hazard. Mater.* 319 (2016) 34–42.

[27] X. Wang, X. Wan, L. Chang, Solvothermal Synthesis of Bi_2WO_6 Hollow Microspheres Via Ostwald Ripening with Their Enhanced Photocatalytic Activity, *Catal. Lett.* 144 (2014) 1268–1277.

[28] Z. Cui, H. Yang, B. Wang, R. Li, X. Wang, Effect of Experimental Parameters on the Hydrothermal Synthesis of Bi_2WO_6 Nanostructures, *Nanoscale Res. Lett.* 11 (2016) 190 (9 pages).

[29] K. Xu, X. Fu, Z. Peng, Facile synthesis and photocatalytic activity of La-doped BiOCl hierarchical, flower-like nano-/micro-structures, *Mater. Res. Bull.* 98 (2018) 103–110.

[30] J. An, B. Tang, X. Zheng, J. Zhou, F. Dong, S. Xu, Y. Wang, B. Zhao, W. Xu, Sculpturing Effect of Chloride Ions in Shape Transformation from Triangular to Discal Silver Nanoplates, *J. Phys. Chem. C* 112 (2008) 15176–15182.

[31] M.S.P. Francisco, V.R. Mastelaro, P.A.P. Nascente, A.O. Florentino, Activity and Characterization by XPS, HR-TEM, Raman Spectroscopy, and BET Surface Area of CuO/CeO_2-TiO_2 Catalysts, *J. Phys. Chem. B* 105 (2001) 10515–10522.

[32] M. Hojamberdiev, Z.C. Kadirova, Y. Makinose, G. Zhu, N. Matsushita, J. Rodríguez, S. Aldabe Bilmes, M. Hasegawa, K. Okada, Influence of BiOI content on the photocatalytic activity of Bi_2WO_6/BiOI/allophane composites and molecular modeling studies of acetaldehyde adsorption, *J. Taiwan Inst. Chem. Eng.* 81 (2017) 258–264.

[33] Y. Chen, G. Zhu, M. Hojamberdiev, J. Gao, R. Zhu, C. Wang, X. Wei, P. Liu, Three-dimensional Ag_2O/Bi_5O_7I p–n heterojunction photocatalyst harnessing UV–Vis–NIR broad spectrum for photodegradation of organic pollutants, *J. Hazard. Mater.* 344 (2018) 42–54.

[34] S. Li, X. Bian, J. Gao, G. Zhu, M. Hojamberdiev, C. Wang, X. Wei, Effect of oxygen vacancy and surface plasmon resonance: A photocatalytic activity study on $Ag/Bi_4Ti_3O_{12}$ nanocomposites, *J. Mater. Sci.: Mater. Electron.* 28 (2017) 17896–17907.

[35] G. Zhu, Y. Liu, M. Hojamberdiev, J. Han, J. Rodríguez, S. Aldabe Bilmes, P. Liu, Thermodecomposition synthesis of porous β-$Bi_2O_3/Bi_2O_2CO_3$ heterostructured

photocatalysts with improved visible light photocatalytic activity, *New J. Chem.* 39 (2015) 9557–9568.

[36] D. Mukherjee, A.K. Ray, S. Barghi, Mechanism of Acetyl Salicylic Acid (Aspirin) Degradation under Solar Light in Presence of a TiO_2-Polymeric Film Photocatalyst, *Processes* 4 (2016) 13 (9 pages).

[37] C. Adán, J.M. Coronado, R. Bellod, J. Soria, H. Yamaoka, Photochemical and photocatalytic degradation of salicylic acid with hydrogen peroxide over TiO_2/SiO_2 fibres, *Appl. Catal. A* 303 (2006) 199–206.

[38] K. Lang, J. Brodilová, S. Luňák, Photochemical Hydroxylation of Salicylic Acid with Hydrogen Peroxide; Mechanistic Study of Substrate Sensitized Reaction, *Collect. Czech. Chem. Commun.* 61 (1996) 1729–1737.

[39] H. Huang, K. Liu, K. Chen, Y. Zhang, Y. Zhang, S. Wang, Ce and F Comodification on the Crystal Structure and Enhanced Photocatalytic Activity of Bi_2WO_6 Photocatalyst under Visible Light Irradiation, *J. Phys. Chem. C* 118 (2014) 14379–14387.

[40] M. Hojamberdiev, K.-i. Katsumata, N. Matsushita, K. Okada, Preparation of Bi_2WO_6– and BiOI–allophane composites for efficient photodegradation of gaseous acetaldehyde under visible light, *Appl. Clay Sci.* 101 (2014) 38–43.

CHAPTER 6: Reduced graphene oxide-modified Bi_2WO_6/BiOI composite for the effective photocatalytic removal of organic pollutants and molecular modeling of adsorption

6.1. Introduction

The release of harmful substances into the ecosystem, particularly water bodies and Earth's atmosphere, without first being treated has potential adverse impacts on human health and the environment. The importance of air and water pollution is also highlighted in the 2030 Agenda for Sustainable Development adopted at the United Nations Sustainable Development Summit on 25 September 2015 through several Sustainable Development Goals. In particular, some organic air and water pollutants are known to be resistant to environmental degradation through chemical, biological, and photolytic processes and can induce various serious diseases. Since the Honda-Fujishima effect was first reported in 1972, semiconductor-based photocatalysis has been regarded as one of the most green and economical processes for potential application in environmental remediation due to its use of abundant solar energy [1]. Initially, most studies were heavily concentrated on developing UV-light-responsive photocatalysts that absorb only UV light, which is present in a small amount in the solar spectrum. Over the past years, to efficiently utilize solar energy, much effort has been made towards the development of various visible-light-responsive photocatalysts, including oxide (Fe_2O_3 [2], $BiVO_4$ [3], doped-TiO_2 [4], etc.), mixed anion (oxynitrides [5], oxyhalides [6], etc.) and non-oxide (sulfides [7], nitrides [8], etc.) compounds.

Bismuth-containing photocatalysts (e.g., Bi_2O_3, Bi_2MO_6 (M = Cr, Mo, or W), $BiVO_4$, BiOX (X = Cl, Br or I), $BiPO_4$, $(BiO)_2CO_3$, and pentavalent bismuthates) have attracted much attention due to their appropriate band gap for visible-light absorption, high mobility of photogenerated charge carriers resulting from the well-dispersed Bi 6s orbital, layered structure, easily tailored morphology, and non-toxicity [9]. Among them, Bi_2WO_6, as one of the simplest members of the Aurivillius oxide family of layered perovskites, is structurally composed of alternating perovskite-like blocks (BO_6 octahedra) and fluorite-like Bi_2O_2 layers [10] and has an optical band gap of 2.80 eV. To enhance its photocatalytic performance for

the removal of organic pollutants, Bi_2WO_6 was coupled with other semiconductors [9,11,12], metals [13,14], or clays [15,16] or doped with Pt [17], Ce [18], or N [19].

Carbon-based materials are known to have unique electrical and electronic properties, high specific surface area, and mechanical strength and have been applied to improve the photocatalytic performance of various inorganic photocatalysts due to their ability to improve the adsorption of pollutants, increase the light absorption intensity, prolong the lifetime of electron-hole pairs, and extend the light absorption range. Xu and coworkers [20] found that TiO_2-graphene in essence has the same effect as composite materials of other TiO_2-carbon allotropes (carbon nanotubes, fullerenes, and activated carbon) on the enhancement of the photocatalytic activity of TiO_2. Katsumata et al. [21] reported that rutile-C_{60} exhibits much higher photocatalytic activity for the decolorization of methylene blue than anatase-C_{60} due to the effective transfer of photogenerated electrons from C_{60} to the rutile phase. WO_3 was composited with polymeric graphitic carbon nitride (*g*-C_3N_4) to improve its photocatalytic activity for the degradation of gaseous acetaldehyde under visible-light irradiation [22]. A carbon nanotube–TiO_2 Schottky barrier junction was demonstrated to be an effective way to increase the recombination time [23]. A remarkable 10-fold enhancement in the photoelectrochemical water splitting reaction over that of pure $BiVO_4$ was observed on a $BiVO_4$-reduced graphene oxide composite prepared using a single-step photocatalytic reaction [24].

To further improve the photocatalytic performance of the Bi_2WO_6/BiOI composite, it is necessary to hybridize it with a conjugated π-structured material with good electrical conductivity [25] to reduce the direct recombination of photogenerated charge carriers. Therefore, reduced graphene oxide was chosen in this study to modify the Bi_2WO_6/BiOI composite, and the effect of the content of reduced graphene oxide on the photocatalytic removal of colorless organic pollutants (acetaldehyde and chloramphenicol) from model contaminated air and water under visible-light irradiation was investigated. The possible mechanism for the enhanced photocatalytic activity of reduced graphene oxide/Bi_2WO_6/BiOI was also discussed in detail.

6.2. Experimental

6.2.1. Synthesis

$Bi(NO_3)_3 \cdot 5H_2O$ (99.9%), KI (99.5%), $KMnO_4$ (99.3%), $NaNO_3$ (98.0%), sulfuric acid (95%), ethylene glycol (99.0%), graphite (98+%), and aqueous ammonia (28%) were obtained from Wako Pure Chemical Industries, Ltd., and $Na_2WO_4 \cdot 2H_2O$ (99+%) was purchased from Strem Chemicals, Inc. All chemical reagents were of analytical grade and used as received without further purification. Deionized water (Millipore Milli-Q Plus purification system, 18.2 MΩ·cm) was used throughout the experiments.

Graphene oxide (GO) and Bi_2WO_6 (BW) powders were synthesized according to previously reported synthetic procedures [11,26]. The reduced graphene oxide/Bi_2WO_6/BiOI (rGO/BW/BI) composite was prepared by a hydrothermal method. First, 0.5 mmol of $Bi(NO_3)_3 \cdot 5H_2O$ was dissolved in 10 mL of ethylene glycol, and 0.5 mmol of KI was dissolved in 10 mL of deionized water. Both solutions were mixed together under vigorous stirring. Meanwhile, 0.5 mmol of the as-synthesized Bi_2WO_6 powder (0.3489 g) and a desired amount of GO powder (0.5, 1.0, 2.5, 5.0, or 10 wt% rGO) were separately dispersed in 10 mL of deionized water. Subsequently, the precursor solution of BiOI was mixed with the aqueous suspension of Bi_2WO_6 and GO powders under vigorous stirring at room temperature for 30 min. The pH of the suspension was adjusted to 7 by the dropwise addition of an aqueous ammonia solution. After vigorous stirring for another 30 min, the formed suspension was transferred into a 40 mL Teflon-lined stainless-steel autoclave, which was then sealed and maintained at 180°C for 12 h. After the hydrothermal synthesis, the composite powders were collected by centrifugation, washed with deionized water several times and dried at 80°C for 8 h. For comparison, BiOI, Bi_2WO_6/BiOI, rGO/Bi_2WO_6 (1 wt% rGO), and rGO/BiOI (1 wt% rGO) were also prepared by a hydrothermal method under identical synthetic conditions as those applied for the synthesis of the rGO/Bi_2WO_6/BiOI composite.

6.2.2. Characterization

The crystalline phases were identified by powder X-ray diffraction (XRD) using an RINT-2100 diffractometer (Rigaku) with monochromatic Cu Kα radiation (λ = 1.5405 Å) at 40 kV and 40 mA. The powder samples were scanned at a scanning rate of $2° \cdot min^{-1}$ over the 2θ range of 10–70°. The samples were also characterized by a T64000 Raman spectrometer (Horiba Jobin Yvon S.A.S.) with an Ar laser (514.5 nm) operated at 50 mW. The particle morphology and size were examined by using an S-4500 ultrahigh-resolution scanning

electron microscope (SEM, Hitachi) operated at an accelerating voltage of 15 kV. The elemental composition of the sample was analyzed by energy-dispersive X-ray spectroscopy (Hitachi) attached to the SEM. Transmission electron microscopy (TEM) observations were performed with an EM-002B high-resolution electron microscope (TOPCON) operated at an accelerating voltage of 200 kV in order to distinguish the crystal structures in the composite. The ultraviolet-visible (UV-vis) diffuse reflectance spectra of the samples were recorded on a Lambda 950 UV/VIS/NIR spectrophotometer (Perkin-Elmer), equipped with an integrating sphere, with $BaSO_4$ as the reference, over the wavelength range of 200–800 nm. The surface compositions and chemical states were analyzed by X-ray photoelectron spectroscopy (XPS, JPS-9010MC, JEOL) using non-monochromatic Mg Kα radiation (1253.6 eV). The specific surface area (S_{BET}) was calculated by the Brunauer-Emmett-Teller (BET) method from the linear portion of the nitrogen gas adsorption isotherm of a sample preheated at 120°C for 4 h under vacuum and measured at 77 K using an Autosorb-3B instrument (Quantachrome).

6.2.3. Adsorption and photocatalytic activity tests

The adsorption ability and photocatalytic activity of the prepared samples were evaluated towards the adsorption and photodegradation of colorless organic pollutants under visible-light irradiation. Acetaldehyde (AcH) and chloramphenicol (CAP) were chosen as the indoor air and water pollutants, respectively.

In the AcH test, the powder sample (50 mg) was placed in a 500 mL reaction vessel made of Pyrex® glass, and the lid, inlet, and outlet were firmly closed. Pure air (Taiyo Nippon Sanso Corp.) was blown through the reaction vessel to remove any air contaminants. Then, a certain amount of AcH was introduced into the reaction vessel using a 2 mL Pressure-Lok® glass syringe until the concentration of AcH reached 250 ppm. After reaching adsorption equilibrium in the dark for 12 h, the reaction vessel was placed under FL10 W white fluorescent daylight lamps (> 400 nm, Toshiba), which emitted visible light with an irradiance of ~8000 lux, as measured with an LX-101A light meter (Lutron Electronic Enterprise Co., Ltd.). To eliminate UV light, an SC42 cutoff filter (< 420 nm, Fujifilm) was used. The decrease in the AcH concentration and the increase in the CO_2 concentration were monitored during the photocatalytic reaction using a GC-2014 gas chromatograph (Shimadzu), equipped

with a 2 m Porapak-Q column, methanizer, and flame ionization detector. N_2 was used as the carrier gas.

In the CAP test, the powder sample (50 mg) was ultrasonically dispersed in a 50 mL aqueous solution containing 15 $mg \cdot L^{-1}$ $C_{15}H_{15}Cl_2N_2$ (Sigma Chemie GmbH) in a reaction vessel made of quartz. Prior to visible-light irradiation, the suspension was magnetically stirred in the dark for 1 h to ensure adsorption-desorption equilibrium. A 400 W halogen lamp with a 400 nm cutoff filter was used as the visible-light source. During the photocatalytic reaction, 2 mL of suspension was taken out at a given time interval and centrifuged for subsequent analysis of the CAP concentration using a U-3010 UV–vis spectrophotometer (Hitachi) by measuring the characteristic absorption peak of CAP at 278 nm in comparison to the reference sample (deionized water).

The precision and repeatability tests were measured under standard conditions with a photocatalyst dosage of 1 $g \cdot L^{-1}$, at pH = 7, and 20°C. Each photocatalytic activity test was done at least three times to guarantee the accuracy and repeatability of the photocatalyst, and the error bars represent standard deviation based on replicated experiments with data analysis by using Origin 8.0 software.

6.3. Results and Discussion

6.3.1. Characterization of the prepared samples

The X-ray diffraction (XRD) patterns of the rGO, rGO/Bi_2WO_6 (1 wt% rGO), rGO/BiOI (1 wt% rGO), Bi_2WO_6/BiOI, and BiOI samples are shown in Figure 6.1A. The XRD pattern shown in Figure 6.1A(a) presents two broad diffraction peaks centered at 2θ = 26.1° and 45.8°, respectively, which are related to the (002) and (100) crystal planes in reduced graphene oxide. No (001) diffraction peak, which is generally associated with the intercalation of oxygen-containing functional groups, belonging to graphene oxide at approximately 2θ = 12-16° was observed [27]. This indicates that graphene oxide was completely converted to reduced graphene oxide (sp^2 carbon) with poor ordering and without notable stacking due to the removal of oxygen-containing functional groups and the ring-opening of the epoxide during the reduction process [28]. The XRD pattern of rGO/Bi_2WO_6 in Figure 6.1A(b) also shows the broad diffraction peaks of rGO and diffraction peaks with lower intensity at 2θ = 28.3, 32.8, 47.0, and 55.8°, which can be assigned to the (113), (200), (026), and (313) crystal

planes of orthorhombic Bi_2WO_6 (ICDD PDF# 73-2020), respectively, indicating the lower crystallinity of the synthesized Bi_2WO_6 powders. In contrast, the broad diffraction peaks of rGO are not readily observed in the XRD pattern of rGO/BiOI (Figure 6.1A(c)). As shown, high-intensity diffraction peaks are observed at 2θ = 29.5, 31.6, 45.4, 51.2, and 55.1°, which are attributed to the (102), (110), (200), (114), and (212) crystal planes of tetragonal BiOI (ICDD PDF# 75-5209), respectively, implying that the BiOI powders have higher crystallinity than the Bi_2WO_6 powders when combined with rGO [19]. In Figure 6.1A(d), the diffraction peaks of Bi_2WO_6 and BiOI can be clearly seen in the XRD pattern of the Bi_2WO_6/BiOI sample, whereas the XRD pattern in Figure 6.1A(e) confirms the phase purity of the synthesized BiOI powders. Figure 6.1B shows the XRD patterns of the rGO/Bi_2WO_6/BiOI composites prepared with 0.5, 1.0, 2.5, 5.0, and 10 wt% rGO. The diffraction peaks in all the XRD patterns are readily assigned to the Bi_2WO_6 and BiOI phases. Although the amount of rGO was increased to up to 10 wt% in the composite, the two broad diffraction peaks of rGO are not observed due to the presence of the high-intensity diffraction peaks of Bi_2WO_6 and BiOI.

The Raman spectra (E_{Laser} = 514.5 nm) of rGO, rGO/Bi_2WO_6 (1 wt% rGO), rGO/BiOI (1 wt% rGO), Bi_2WO_6/BiOI, and BiOI are shown in Figure 6.2. In Figure 6.2A(a), the Raman spectrum of rGO exhibits typical intense *D* (defect band) and *G* (graphitic) bands at 1352 and 1601 cm^{-1}, respectively, confirming the formation of rGO. The *G* band is attributed to the high frequency of the $E_{2g}^{(2)}$ mode at the center of the Brillouin zone, evidencing the presence of sp^2-hybridized carbon atoms [29]. The *D* band is assigned to the A_{1g} breathing modes at the neighboring corners of the first Brillouin zone (sp^3 defects in the sp^2 lattice) [30]. The (I_D/I_G) ratio is estimated to be 0.98, suggesting a multilayered structure of rGO. However, this ratio slightly changes to 0.95 and 0.90 for rGO/Bi_2WO_6 and rGO/BiOI, respectively. The mode-assignable Raman peaks of Bi_2WO_6 and BiOI are not clearly observed in the Raman spectra of the rGO/Bi_2WO_6 and rGO/BiOI samples due to lower crystallinity of the Bi_2WO_6 powders and intense Raman peaks of rGO (Figure 6.2A(b) and (c)). In Figure 6.2A(d), the Raman peaks at 808 cm^{-1} and 710 cm^{-1} are assigned to the symmetric and asymmetric stretching modes of the WO_6 octahedra. The Raman peaks at 415, 304, 284, 232, 218, and 192 cm^{-1} (some of them cannot be seen) correspond to the bending modes of the WO_6 octahedra and

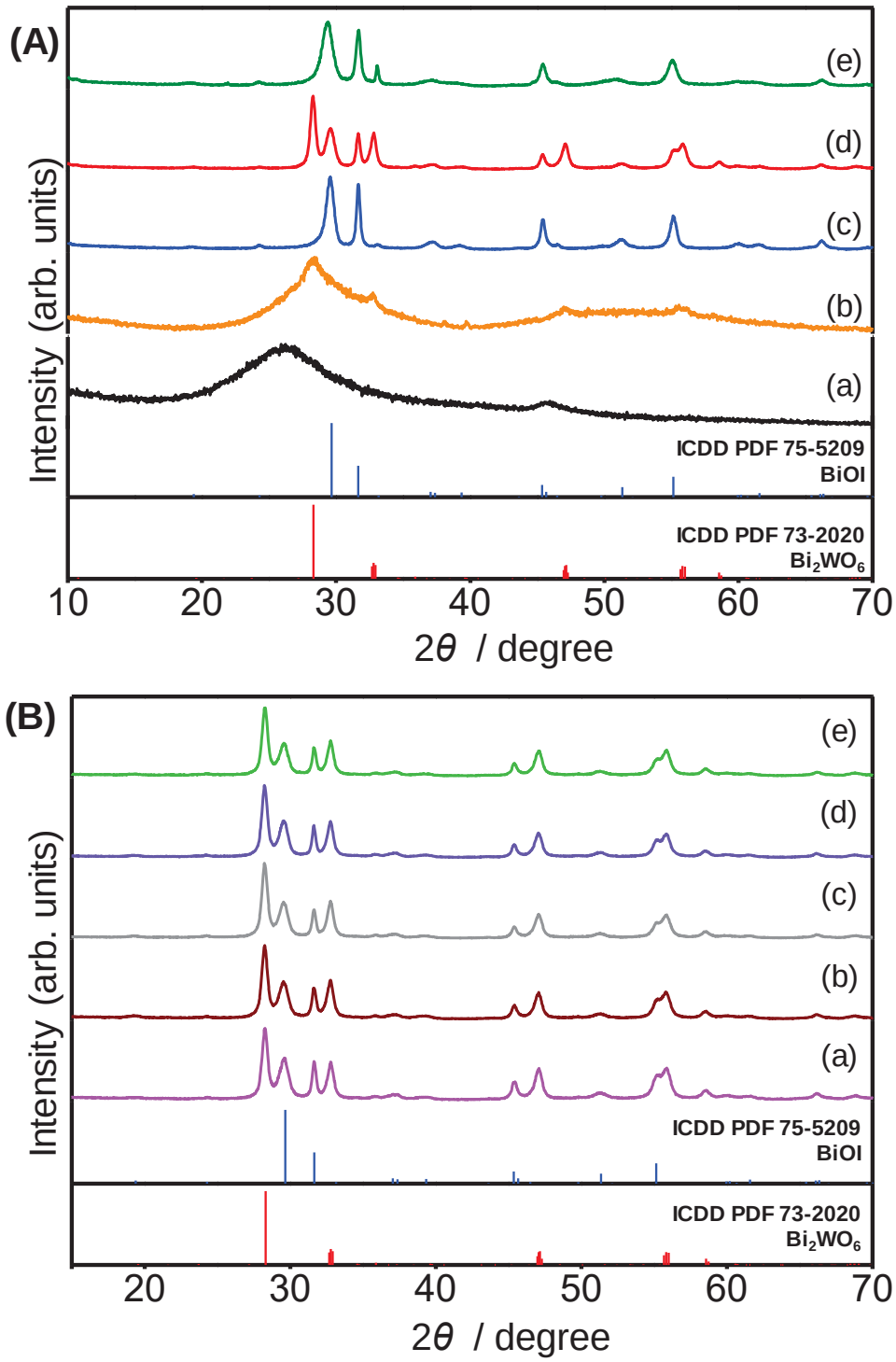

Figure 6.1. (A) XRD patterns of (a) rGO, (b) rGO/Bi_2WO_6 (1 wt% rGO), (c) rGO/BiOI (1 wt% rGO), (d) Bi_2WO_6/BiOI, and (e) BiOI. **(B)** XRD patterns of the rGO/Bi_2WO_6/BiOI composites prepared with (a) 0.5, (b) 1.0, (c) 2.5, (d) 5.0, and (e) 10 wt% rGO.

the stretching and bending modes of the BiO_6 polyhedra. In Figure 6.2A(e), the Raman peak at 145 cm^{-1} in the Raman spectrum of BiOI (not obvious) is related to the Bi–I stretching mode [9,16]. As shown in Figure 6.2B, the main features of the Raman peaks of rGO,

Bi_2WO_6, and BiOI are identical for all the rGO/Bi_2WO_6/BiOI composites prepared with 0.5, 1.0, 2.5, 5.0, and 10 wt% rGO. The main difference is observed in the intensity of the *D*/*G* bands. That is, with increasing amount of rGO, the intensity of the *D*/*G* band also increased. From the XRD and Raman spectroscopy results, it can be inferred that the rGO/Bi_2WO_6/BiOI composite can be easily prepared by the hydrothermal method.

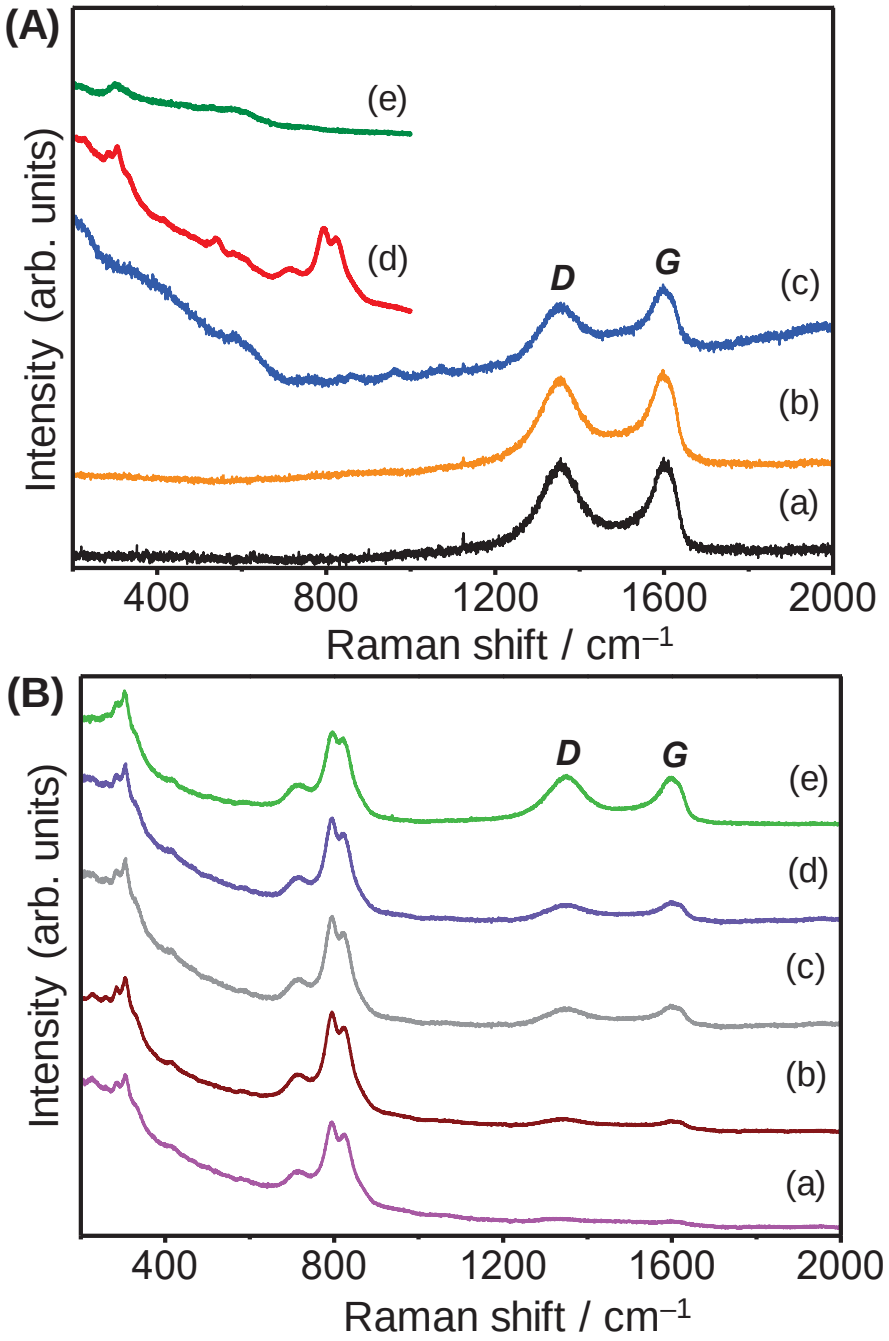

Figure 6.2. (A) Raman spectra of (a) rGO, (b) rGO/Bi_2WO_6 (1 wt% rGO), (c) rGO/BiOI (1 wt% rGO), (d) Bi_2WO_6/BiOI, and (e) BiOI. **(B)** Raman spectra of rGO/Bi_2WO_6/BiOI composites prepared with (a) 0.5, (b) 1.0, (c) 2.5, (d) 5.0, and (e) 10 wt% rGO.

The morphology of the prepared samples was examined by scanning electron microscopy, and the SEM images of rGO, rGO/Bi_2WO_6 (1 wt% rGO), rGO/BiOI (1 wt% rGO), Bi_2WO_6/BiOI, and BiOI are illustrated in Figure 6.3A. As shown in Figure 6.3A(a), rGO consists of randomly aggregated sheets and corrugations. Clearly, Bi_2WO_6 nanoparticles with lower crystallinity were deposited on the rGO surface (Figure 6.3A(b)). The well-defined hierarchical structures of BiOI were constructed by the self-assembly of thin nanosheets and appear as partly joined spherical particles with an average size of less than 1.5 μm on the rGO surface (Figures 6.3A(c) and (e)). Figure 6.3A(d) depicts that the spherical BiOI particles and Bi_2WO_6 nanoplates were concurrently loaded on the rGO surface. Figure 6.3B represents the SEM images of the rGO/Bi_2WO_6/BiOI composites prepared with 0.5, 1.0, 2.5, 5.0, and 10 wt% rGO. As shown, the large hierarchical structures of Bi_2WO_6 in undefined forms and spherical BiOI particles were randomly loaded on the rGO surface (Figure 6.4). With increasing amount of rGO, the size of the hierarchical structures of Bi_2WO_6 slightly increased. Apparently, some disassembled sheets of rGO, nanoplates of Bi_2WO_6 and more crumpled structures can also be seen on the rGO surface.

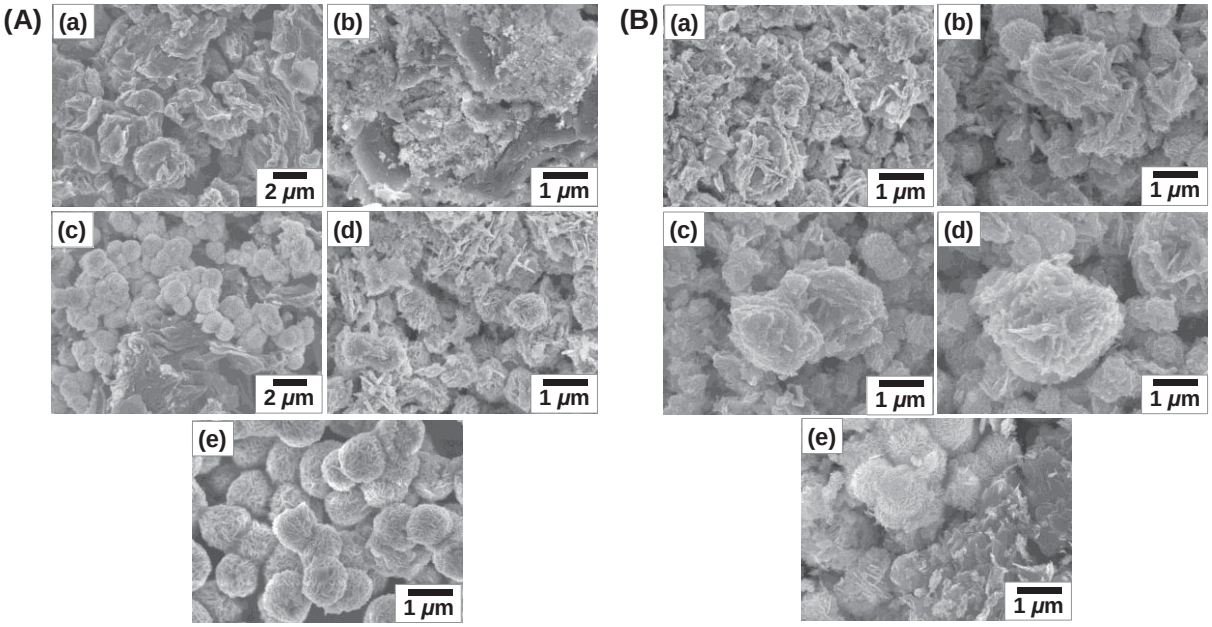

Figure 6.3. (A) SEM images of (a) rGO, (b) rGO/Bi_2WO_6 (1 wt% rGO), (c) rGO/BiOI (1 wt% rGO), (d) Bi_2WO_6/BiOI, and (e) BiOI. **(B)** SEM images of rGO/Bi_2WO_6/BiOI composites prepared with (a) 0.5, (b) 1.0, (c) 2.5, (d) 5.0, and (e) 10 wt% rGO.

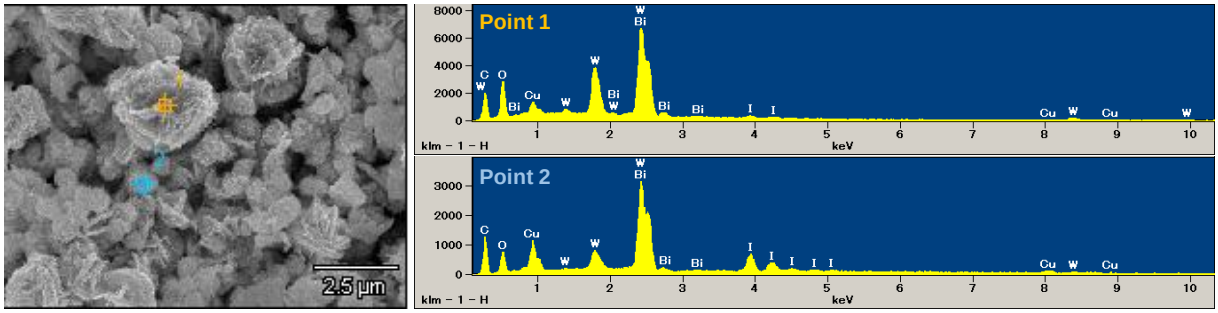

Figure 6.4. SEM image and EDX spectra of 5 wt% rGO/Bi_2WO_6/BiOI composite.

Figure 6.5 shows the TEM images, HRTEM images and SAED patterns of the rGO, rGO/Bi_2WO_6, rGO/BiOI, Bi_2WO_6/BiOI, and rGO/Bi_2WO_6/BiOI samples. The thin sheet-like structure of graphene and its entangled parts are observed in the TEM image of rGO in Figure 6.5a. However, determination of the number of layers of this sheet-like graphene is difficult. The SAED image shows a diffuse ring pattern, reflecting the amorphous nature of rGO. In Figure 6.5b, Bi_2WO_6 crystals with an average size of approximately 10 nm were embedded in the rGO sheets, whereas spherical BiOI particles with an average size of less than 1.5 μm were deposited on the rGO sheets (Figure 6.5c). Compared with the SAED image of rGO/BiOI, which clearly demonstrates the polycrystalline nature of the BiOI particles, the SAED image of rGO/Bi_2WO_6 indicates unclear diffuse ring patterns, revealing the lower crystallinity of the Bi_2WO_6 crystals. As seen in the TEM images in Figures 6.5d and e, a heterojunction was possibly formed in the Bi_2WO_6/BiOI and rGO/Bi_2WO_6/BiOI samples through the attachment of small particles of Bi_2WO_6 on the spherical particles of BiOI. Compared with Bi_2WO_6/BiOI, the Bi_2WO_6/BiOI heterojunction is located on the rGO sheets. Moreover, the Bi_2WO_6 crystals and BiOI particles were separately distributed on the rGO sheets (Figure 6.5e). The continuous ring-like patterns in their SAED images confirm their polycrystalline nature and correspond to orthorhombic Bi_2WO_6 and tetragonal BiOI. From the HRTEM images, it is evident that excellent interfacial contacts were created between the Bi_2WO_6 and BiOI crystals and the rGO sheets, promoting efficient electron transfer and enhancing the photocatalytic activity.

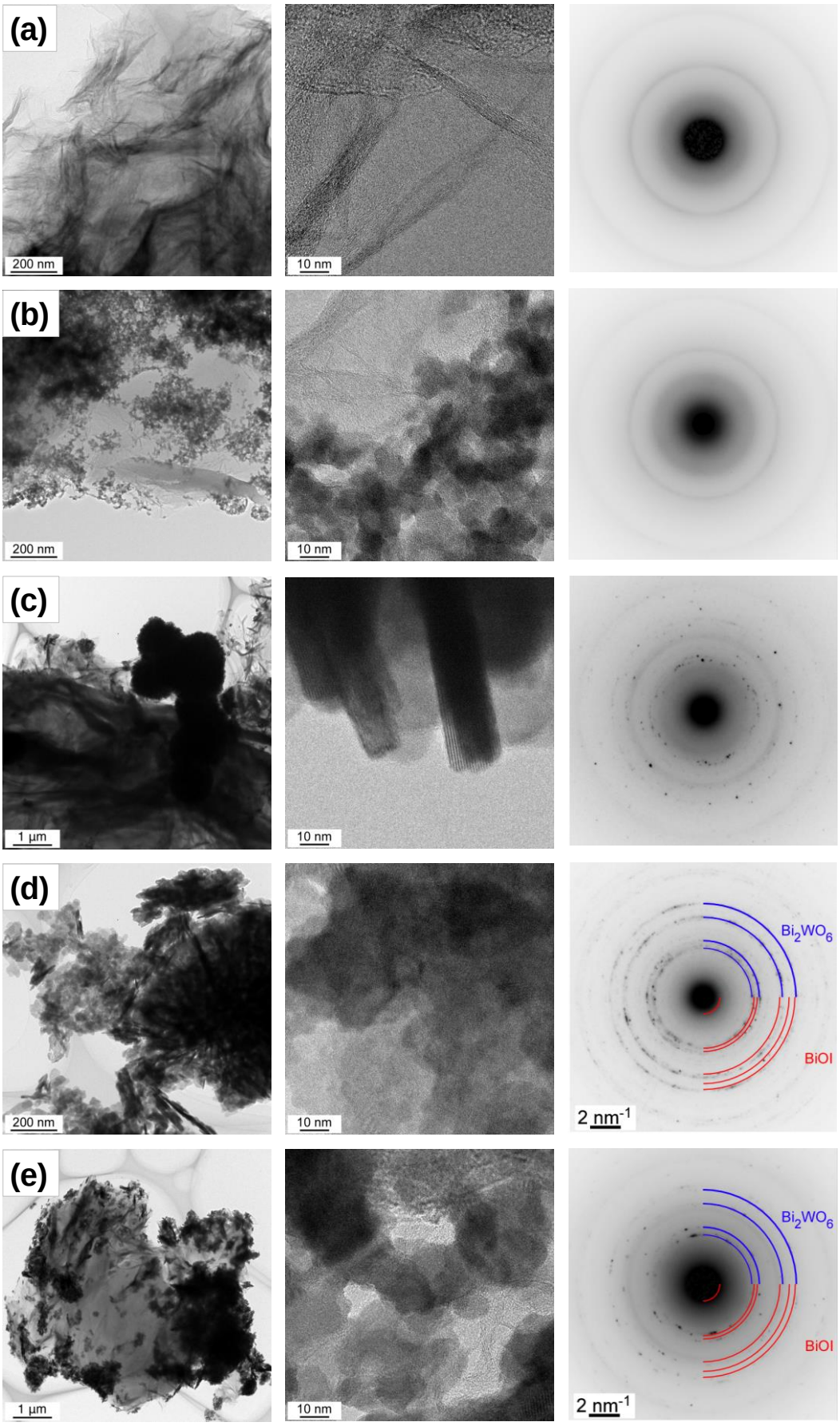

Figure 6.5. TEM (*left*) and HRTEM (*middle*) images and SAED patterns (*right*) of (a) rGO, (b) rGO/Bi_2WO_6, (c) rGO/BiOI, (d) Bi_2WO_6/BiOI, and (e) rGO/Bi_2WO_6/BiOI.

Ultraviolet-visible (UV-vis) spectroscopy is an effective optical characterization technique to understand the electronic structure of semiconductors. The UV-vis diffuse reflectance spectra of rGO, rGO/Bi_2WO_6 (1 wt% rGO), rGO/BiOI (1 wt% rGO), Bi_2WO_6/BiOI, and BiOI are shown in Figure 6.6a. As expected, the UV-vis diffuse reflectance spectrum of rGO exhibits the highest absorption intensity among the samples, without indicating a clear absorption edge. In contrast, the Bi_2WO_6/BiOI and BiOI powders have obvious absorption edges at approximately 665 nm in the visible-light region, corresponding to a band gap energy of 1.86 eV. The absorption edge of rGO/Bi_2WO_6 is observed at approximately 442 nm (the approximate band gap energy is 2.80 eV), whereas the absorption edge of rGO/BiOI is observed at approximately 665 nm (the approximate band gap energy is 1.86 eV). Despite having different absorption edges, both samples show a slight redshift towards higher wavelengths and higher absorption intensity in the visible-light region than their counterparts synthesized without rGO. This may be due to the interaction of Bi_2WO_6 and BiOI with rGO at the heterojunction. The colors of the rGO, rGO/Bi_2WO_6 (1 wt% rGO), rGO/BiOI (1 wt% rGO), Bi_2WO_6/BiOI, and BiOI powders are observed to be black, dark gray, brown, orange, and reddish-orange, respectively. Figure 6.6b shows the UV-vis diffuse reflectance spectra of the rGO/Bi_2WO_6/BiOI composites prepared with 0.5, 1.0, 2.5, 5.0, and 10 wt% rGO. Similarly, all the composites exhibit absorption edges at approximately 665 nm with a slight redshift towards higher wavelengths and higher absorption intensity beyond the absorption edges with increasing amount of rGO. As shown, the orange color of the prepared composite powders gradually darkens with increasing amount of rGO. The introduction of rGO in the Bi_2WO_6/BiOI composite enhanced the visible-light absorption owing to the chemical bonding of Bi_2WO_6 and BiOI with specific sites of rGO, suggesting that the prepared composites could exhibit improved photocatalytic activity.

Since the adsorption process plays an important role in improving the photodegradation efficiency of various organic pollutants, it is indispensable to analyze the porous properties of the prepared samples by N_2 physisorption measurement. Figure 6.7 shows the nitrogen gas adsorption-desorption isotherms of the samples, and their specific surface areas calculated by the Brunauer-Emmett-Teller method (S_{BET}) are listed in Table 6.1. In Figure 6.7A, the

nitrogen gas adsorption-desorption isotherm of rGO is of type IV, according to the IUPAC classification [31], with a type H_3 hysteresis loop, indicating the presence of slit-like pores formed by the aggregation of plate-like particles. This result is consistent with the SEM observations.

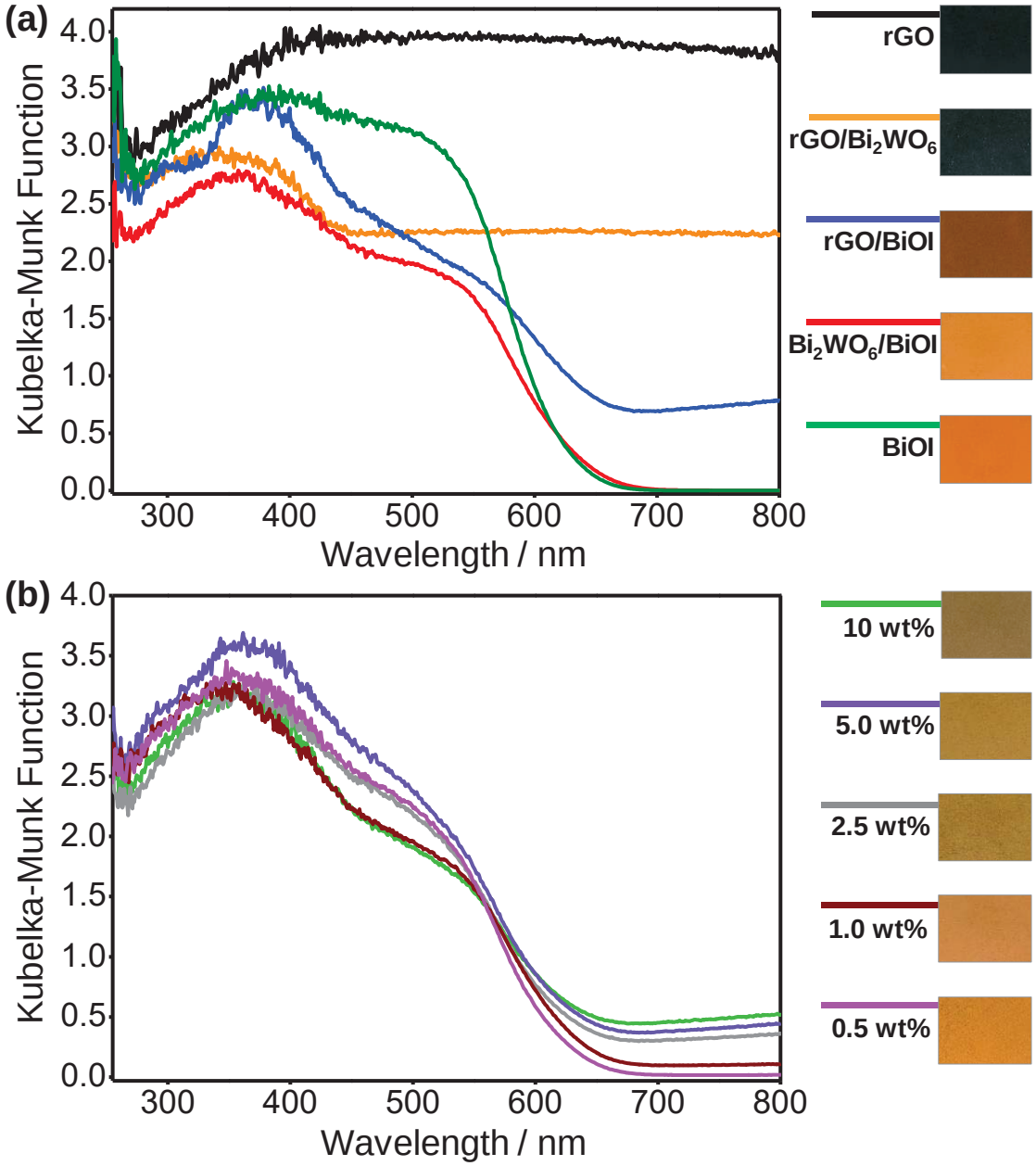

Figure 6.6. (a) UV-Vis diffuse reflectance spectra of rGO, rGO/Bi_2WO_6 (1 wt% rGO), rGO/BiOI (1 wt% rGO), Bi_2WO_6/BiOI, and BiOI. **(b)** UV-Vis diffuse reflectance spectra of rGO/Bi_2WO_6/BiOI composites prepared with 0.5, 1.0, 2.5, 5.0, and 10 wt% rGO.

Table 6.1. Adsorption and photodegradation of acetaldehyde and chloramphenicol over the prepared samples.

Sample	S_{BET} ($m^2 \cdot g^{-1}$)	Acetaldehyde (AcH)				Chloramphenicol (CAP)			
		Adsorption, %	Photgodeg-radation, %	Total, %	k_{app}, min^{-1}	Adsorption, %	Photgodeg-radation, %	Total, %	k_{app}, min^{-1}
rGO	40.2	10.89	6.44	17.33	-0.0001	23.33	4.67	28.00	-0.0001
1 wt% rGO/Bi_2WO_6	52.1	22.22	77.11	99.33	-0.0025	25.33	64.67	90.00	-0.0031
1 wt% rGO/BiOI	34.5	14.44	85.56	100.00	-0.0109	22.00	78.00	100.00	-0.0083
Bi_2WO_6/BiOI	27.7	13.33	86.67	100.00	-0.0069	17.33	82.60	99.93	-0.0069
BiOI	34.2	15.11	84.89	100.00	-0.0064	19.33	79.33	98.67	-0.0059
0.5 wt% rGO/Bi_2WO_6/BiOI	26.8	14.22	85.78	100.00	-0.0130	16.00	84.00	100.00	-0.0094
1 wt% rGO/Bi_2WO_6/BiOI	25.7	14.44	85.56	100.00	-0.0157	18.00	82.00	100.00	-0.0112
2.5 wt% rGO/Bi_2WO_6/BiOI	24.0	14.00	86.00	100.00	-0.0137	16.00	84.00	100.00	-0.0105
5 wt% rGO/Bi_2WO_6/BiOI	23.6	13.78	86.22	100.00	-0.0125	19.33	80.40	99.73	-0.0068
10 wt% rGO/Bi_2WO_6/BiOI	24.4	14.44	85.56	100.00	-0.0105	15.33	79.00	94.33	-0.0048

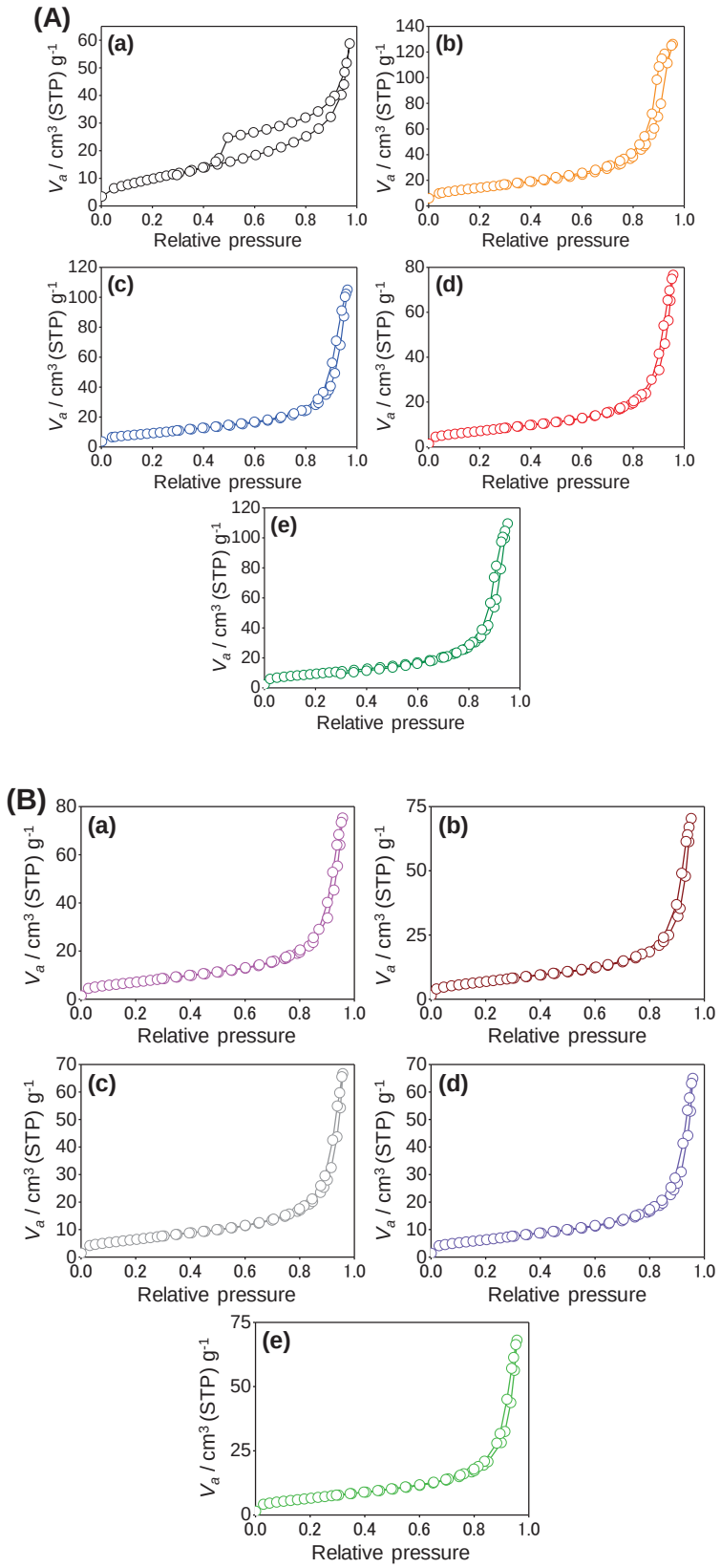

Figure 6.7. (A) Nitrogen gas adsorption-desorption isotherms of (a) rGO, (b) rGO/Bi_2WO_6 (1 wt% rGO), (c) rGO/BiOI (1 wt% rGO), (d) Bi_2WO_6/BiOI, and (e) BiOI. **(B)** Nitrogen gas adsorption-desorption isotherms of rGO/Bi_2WO_6/BiOI composites prepared with (a) 0.5, (b) 1.0, (c) 2.5, (d) 5.0, and (e) 10 wt% rGO.

Additionally, a steep increase beyond P/P_0 = 0.8 is noted due to capillary condensation in the mesopores. In contrast, the rGO/Bi_2WO_6 (1 wt% rGO), rGO/BiOI (1 wt% rGO), Bi_2WO_6/BiOI, and BiOI powders represent type II nitrogen gas adsorption-desorption isotherms in the IUPAC classification, manifesting the adsorption of nitrogen gas on a non-porous or macroporous adsorbent with strong adsorbate-adsorbent interactions. The calculated S_{BET} values of the rGO, 1 wt% rGO/Bi_2WO_6, 1 wt% rGO/BiOI, Bi_2WO_6/BiOI, and BiOI powders are 40.2, 52.1, 34.5, 27.7, and 34.2 $m^2 \cdot g^{-1}$, respectively. Among the samples, the 1 wt% rGO/Bi_2WO_6 sample shows the highest S_{BET} value (52.1 $m^2 \cdot g^{-1}$) because of the additional contribution of the Bi_2WO_6 nanocrystals. The change in the nitrogen gas adsorption-desorption isotherms of the rGO/Bi_2WO_6/BiOI composites upon increasing the amount of rGO shows a nearly identical tendency, attesting a type II isotherm for all composites (Figure 6.7B). Interestingly, nitrogen gas adsorption at low P/P_0 followed by reaching a well-defined adsorption saturation plateau (type I isotherm), corresponding to the microporous nature of the carbon species, was not observed despite an increase in the rGO amount. The estimated S_{BET} values of the composites range between 23.6 and 26.8 $m^2 \cdot g^{-1}$ and show no correlation with the rGO amount. The high specific surface area of the prepared composites is anticipated to expose more active sites and to favor the mass transport of organic molecules, thereby enhancing the photocatalytic activity.

The surface compositions and chemical states were analyzed by X-ray photoelectron spectroscopy (XPS). The Bi 4f, W 4f, O 1s, I 3d, and C 1s XPS core-level spectra of the 5 wt% rGO/Bi_2WO_6/BiOI composite are shown in Figure 6.8. In Figure 6.8a, the XPS peaks located at 163.5 and 158.1 eV can be ascribed to the binding energies of Bi $4f_{7/2}$ and Bi $4f_{5/2}$, respectively, confirming that bismuth has an oxidation state of +3. The binding energies of W $4f_{5/2}$ and W $4f_{7/2}$ are observed at 36.1 and 33.9 eV, respectively, indicating that tungsten has an oxidation state of +6 (Figure 6.8b) [32,33]. In Figure 6.8c, the O 1s XPS peak can be deconvoluted into five components. The two components centered at 530.2 and 531.3 eV are characteristic of oxygen bonded to bismuth in BiOI and Bi_2WO_6 and chemisorbed/intercalated or dissociated oxygen species, respectively [34,35]. The two components centered at 532.5 and 533.9 eV correspond to C─O (oxygen singly bonded to aliphatic carbon) and phenolic (oxygen singly bonded to aromatic carbon) groups, respectively [36]. A component indicating

C═O (oxygen doubly bonded to aromatic carbon) was not obvious at 531.08 eV. The I 3d XPS spectrum shows splitting peaks at binding energies of 630.6 and 619.5 eV (Figure 6.8d), which are assignable to I $3d_{3/2}$ and I $3d_{5/2}$ [37], respectively. The deconvoluted C 1s XPS spectrum reveals four different peaks centered at binding energies of 284.6, 285.2, 286.5, and 289.1 eV, corresponding to the carbon-carbon bond in aromatic rings (C═C/C─C), hydroxyl and epoxy groups (C─OH and C─O─C), carbonyl groups (>C═O), and carboxyl groups (HO─C═O), respectively [36]. The XPS results demonstrated the coexistence of Bi_2WO_6, BiOI, and rGO in the composite.

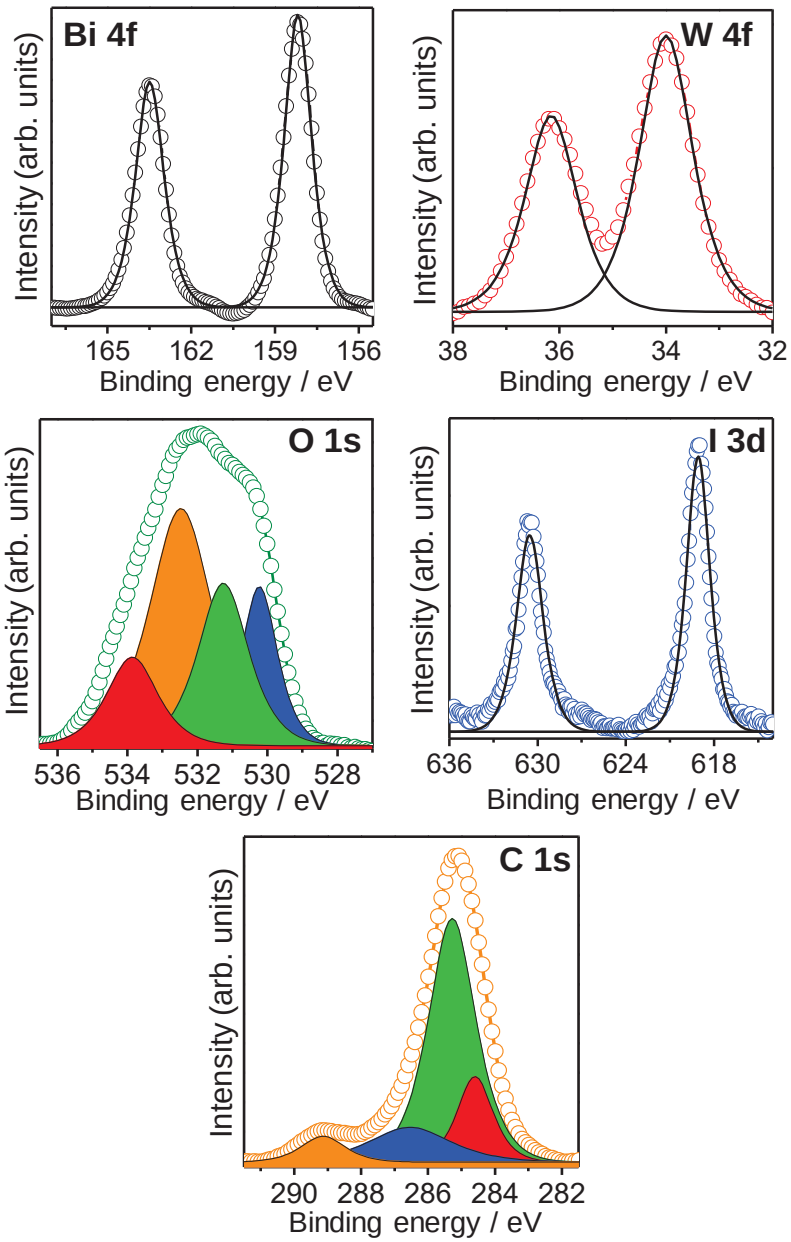

Figure 6.8. Bi 4f, W 4f, O 1s, I 3d, and C 1s XPS spectra of 5 wt% rGO/Bi_2WO_6/BiOI composite.

6.3.2. Adsorption capacity and photocatalytic activity of the prepared samples

To investigate the adsorption capacity and photocatalytic efficiency of the prepared samples, acetaldehyde (AcH) and chloramphenicol (CAP) were chosen to represent colorless indoor air and water organic pollutants, respectively. The blank tests conducted without a photocatalyst in the dark and under visible-light irradiation showed no significant change in the concentrations of AcH and CAP, confirming their stability, especially under visible-light irradiation. As shown in Figure 6.9, with photocatalyst, the concentrations of AcH and CAP gradually decreased during adsorption in the dark and photodegradation under visible-light irradiation. A 12 h adsorption process increased the removal of AcH from 10.89% to 22.22%, while a 15.33-25.33% removal of CAP was achieved in the 1 h adsorption process, depending on the specific surface areas of the prepared samples (Table 6.1). Namely, the 1 wt% rGO/Bi_2WO_6 sample showed the highest adsorption capacity for both AcH (22.22%) and CAP (25.33%) among the samples because of its largest specific surface area. Interestingly, a rise in the amount of rGO does not show a pronounced effect on the adsorption capacity. Upon visible-light irradiation, the decrease in the concentrations of AcH and CAP continues, and the photodegradation efficiencies of AcH and CAP reach 100% for the 1 wt% rGO/Bi_2WO_6/BiOI sample as early as 2 h and 4 h, respectively.

Since it enables the determination of the photocatalytic activity independent of the adsorption period in the dark as well as the remaining concentrations of AcH and CAP in the reactor, the apparent photodegradation rate constant, as a basic kinetic parameter, was applied to compare the photocatalytic activities of the prepared samples. Therefore, the apparent first-order kinetic equation $\ln(C/C_0) = -k_{app} \cdot t$ was used to fit the experimental data, where k_{app} is the apparent photodegradation rate constant, C is the concentration of AcH or CAP at t, and C_0 is the initial concentration of AcH or CAP at $t = 0$, which is equal to the equilibrium concentration after adsorption in the dark [38]. The calculated rate constants of the prepared samples are given in Table 6.1. Clearly, the rGO/Bi_2WO_6/BiOI composites showed higher k_{app} values than rGO, BiOI, Bi_2WO_6/BiOI, rGO/Bi_2WO_6 (1 wt% rGO), and rGO/BiOI (1 wt% rGO) due to the synergistic effects of the formed *p-n* heterojunction and the presence of rGO. In comparison to that of Bi_2WO_6/BiOI (k_{app} = -0.0069 min^{-1} for AcH and CAP), k_{app} was drastically increased with the introduction of up to 1 wt% rGO in the composite (k_{app} = -

0.0157 min^{-1} for AcH and k_{app} = -0.0112 min^{-1} for AcH). A further increase in the amount of rGO gradually reduced the k_{app} value of the composite. Such negative impact from overloading rGO is generally attributed to the blocking of light absorption and promotion of the recombination of photogenerated electrons and holes [39]. As the k_{app} values of the prepared rGO/Bi_2WO_6/BiOI composites significantly differ despite their similar specific surface areas, such variance in their k_{app} values can be explained by the enhanced interfacial charge transfer achieved by the incorporation of an appropriate amount of the rGO rather than the negligible contribution of the specific surface area.

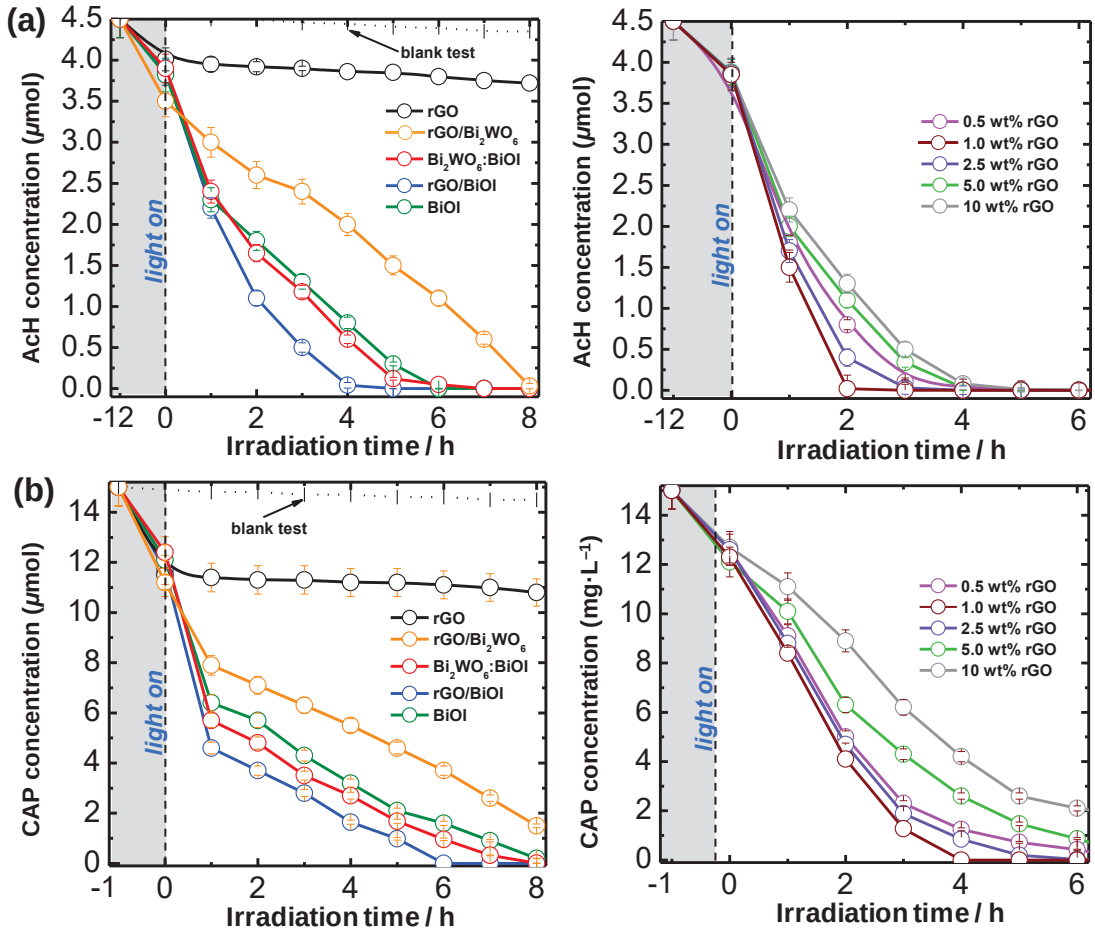

Figure 6.9. Adsorption and photocatalytic activity for the removal of (a) gaseous acetaldehyde and (b) chloramphenicol in aqueous solution of the prepared samples under visible light irradiation.

To elucidate the improvement of the photocatalytic activity of the Bi_2WO_6/BiOI composite for the photodegradation of AcH and CAP upon introducing rGO, plausible mechanisms are further discussed here. Here, the synergistic effects of the formed *p-n*

heterojunction and the presence of rGO are considered. As described in our previous work [9], a *p*-*n* heterojunction is formed upon contact between *n*-type Bi_2WO_6 and *p*-type BiOI, promoting the diffusion of electrons from Bi_2WO_6 to BiOI until the Fermi levels of Bi_2WO_6 and BiOI are equalized. Therefore, the conduction band edge of BiOI becomes higher than that of Bi_2WO_6, while the valence band edge of Bi_2WO_6 is positioned lower than that of BiOI. This creates an internal electric field at the interface of the *p*-*n* heterojunction at equilibrium. During the photocatalytic reaction, electrons in the valence band move to the conduction band, and electrons from the conduction band of BiOI migrate to the more positively located conduction band of Bi_2WO_6, while holes in the valence band of Bi_2WO_6 transfer to the valence band of BiOI. Electrons in the conduction band react with oxygen to produce $O_2^{\bullet-}$, which attacks the AcH and CAP molecules. Holes in the valence band either directly react with the AcH and CAP molecules and/or react with H_2O on the surface of the composite to produce •OH and other active species that are also involved in the photodegradation reaction. As a result, such an accelerated separation process of photogenerated electrons and holes reduces the recombination rate and improves the photocatalytic efficiency. Possibly, the photodegradation of AcH leads to the formation of the final products, CO_2 and H_2O, whereas the photodegradation of CAP includes the generation of NO_3^-, Cl^-, NH_4^+, CO_2, and H_2O as final products at different stages [40,41]. The transformation pathways of AcH and CAP, like other organic pollutants, by photocatalytic oxidation are complex, producing various intermediate products, and the present study is not aimed to identify the formed intermediates and transformation pathways. However, based on available data, plausible mechanisms for the degradation of AcH and CAP over the prepared photocatalyst composite are suggested here:

$$rGO/Bi_2WO_6/BiOI + h\nu \rightarrow rGO/Bi_2WO_6/BiOI\ (e^{CB}- + h^{VB+}) \quad (1)$$

$$H_2O \rightarrow H^+ + OH^- \quad (2)$$

$$e^{CB} + O_2 \rightarrow O_2^{\bullet-} \quad (3)$$

$$O_2^{\bullet-} + H^+\ aq. \rightarrow HO_2^{\bullet} \quad (4)$$

$$HO_2^{\bullet} + HO_2^{\bullet} \leftrightarrow H_2O_2 + O_2 \quad (5)$$

$$h^{VB+} + OH^-\ aq. \rightarrow OH^{\bullet-} \quad (6)$$

$$AcH + (O_2^{\bullet-}, HO_2^{\bullet}, H_2O_2, OH^{\bullet-}) \rightarrow CO_2 + H_2O \quad (7)$$

$$CAP + (O_2^{\bullet-}, HO_2^{\bullet}, H_2O_2, OH^{\bullet-}) \rightarrow \text{Degr. products} \rightarrow NO_3^-, Cl^-, NH_4^+, CO_2, \text{and } H_2O \quad (8)$$

As shown in Figure 6.9, rGO does not have any significant photocatalytic activity towards the degradation of AcH and CAP; however, it can provide a large number of active sites for the degradation reaction of organic molecules. The photoelectrons in the conduction bands of Bi_2WO_6 and BiOI move to the rGO surface, facilitating fast and long-range interfacial charge transfer with the π–π graphitic carbon network [42]. The synergistic effects of rGO in adsorbing the AcH and CAP molecules and capturing photoinduced electrons significantly improved the photodegradation efficiency. As rGO is known to be a *p*-type semiconductor due to the large electronegativity of oxygen atoms compared with that of carbon atoms [43], an additional *p*-*n* heterojunction is constructed when rGO and *n*-type Bi_2WO_6 come in contact, contributing to the overall improvement in the photodegradation efficiency. Clearly, the rGO/Bi_2WO_6/BiOI composite demonstrated a much higher photodegradation rate constant towards the degradation of AcH and CAP than its Bi_2WO_6/BiOI counterpart.

According to the S_{BET} values, all samples showed similar adsorption behavior for AcH in the range of 13-15% except the rGO/Bi_2WO_6 sample, which exhibited the highest adsorption in the dark (22%) but unexpectedly the lowest photodegradation activity due to its lower crystallinity. At the same time, the addition of Bi_2WO_6 to the rGO/BiOI composite greatly improved the photocatalytic activity. Although the rGO sample has the lowest AcH adsorption (11%), rGO and its composites have the highest CAP adsorption in aqueous solution (22-25%) compared with the samples prepared without rGO (16-19%). To explain this observation, molecular modeling of the electronic structures and adsorption process was applied.

6.3.3. Molecular modeling of adsorption of acetaldehyde and chloramphenicol molecules on the prepared samples

The adsorption affinities of the AcH molecules in the gas phase and the CAP molecules in aqueous solution to the modeled rGO, BiOI (102) and Bi_2WO_6 (113) surfaces were studied using a layer building tool that allows the generation of layered structures and interfaces (Figure 6.10). The most efficient interactions occurring between the sorbate molecules and the BiOI and Bi_2WO_6 minerals in the presence of rGO were studied.

To determine the most stable electronic configuration of the rGO surface and the AcH or CAP molecules on the surface, we used the Forcite and Adsorption Locator modules in Accelrys Materials Studio [44]. The BiOI and Bi_2WO_6 structures were modeled using experimental data and the crystallographic structural database [45,46] The predominant planes were taken as the more exposed surfaces from the XRD and HR-TEM data. The AcH and CAP+water molecules showed negative adsorption energies, implying more exothermic adsorption and a stronger mineral–adsorbate interaction. The adsorption energy (E_{ads}) is equal to the energy, in kcal·mol^{-1}, released (or required) when the relaxed sorbent molecules (AcH or CAP+water) are adsorbed on the surfaces of rGO, BiOI and Bi_2WO_6 or between the two surfaces of BiOI and rGO/BiOI, Bi_2WO_6 and rGO/Bi_2WO_6, and BiOI and Bi_2WO_6. The interactions in the rGO/Bi_2WO_6/BiOI sample were evaluated based on the data calculated for the rGO/BiOI, rGO/Bi_2WO_6, BiOI/Bi_2WO_6 and rGO samples.

The obtained results revealed that the interaction (E_{ads}) between the AcH molecules and the BiOI, Bi_2WO_6, and rGO surfaces decreases in the order of rGO (-7.88 kcal·mol^{-1}) > BiOI (-7.48 kcal·mol^{-1}) > Bi_2WO_6 (-6.22 kcal·mol^{-1}), and the interaction (E_{ads}) between the CAP+water molecules with the BiOI, Bi_2WO_6, and rGO surfaces decreases in the order of BiOI (-91.91 kcal·mol^{-1}) > rGO (-89.14 kcal·mol^{-1}) > Bi_2WO_6 (-74.08 kcal·mol^{-1}). Thus, the BiOI and rGO surfaces have higher adsorption affinities than the Bi_2WO_6 surface, and the adsorption efficiency of the Bi_2WO_6 composites is consequently improved.

The data calculated for the layered structure unit cell containing rGO between two layers of the Bi_2WO_6 or BiOI surfaces are shown in Figure 6.10 and can be summarized as follows.

Bi_2WO_6 and rGO/Bi_2WO_6 surfaces. The addition of rGO slightly influenced the affinity to the sorbate ($\Delta_{AcH} = E_{ads}(rGO/Bi_2WO_6) - E_{ads}(Bi_2WO_6) = -7.9 - (-6.22) = -1.68$ and $\Delta_{CAP+water} = -80.61 - (-74.08) = -6.53$ kcal·mol^{-1}). Figure 6.10 shows an approximately equal distribution of the sorbate field density along the Bi_2WO_6 and rGO/Bi_2WO_6 surfaces. However, the calculated values of $\sum E_{ads}(rGO) + E_{ads}(Bi_2WO_6)$ are two times higher than the values of $E_{ads}(rGO/Bi_2WO_6)$, indicating no pronounced adsorption after the introduction of rGO.

AcH: $\sum E_{ads}(rGO) + E_{ads}(Bi_2WO_6) = -14.1$ kcal·mol^{-1}

CAD+water: $\sum E_{ads}(rGO) + E_{ads}(Bi_2WO_6) = -163.22$ kcal·mol^{-1}

BiOI and rGO/BiOI surfaces. In contrast, the addition of rGO strongly increased the affinity to the sorbate (Δ_{AcH} = E_{ads}(rGO/BiOI) - E_{ads}(BiOI) = -19.93 - (-7.48) = -12.45 and $\Delta_{CAP+water}$ = -183.58 - (-91.91) = -91.67 kcal·mol^{-1}). The calculated values of $\sum E_{ads}$(rGO) + E_{ads}(BiOI) are similar to the values of E_{ads}(rGO/BiOI) for the AcH and CAP molecules, which show a stronger affinity to the rGO/BiOI surface than the BiOI surface.

AcH: $\sum E_{ads}$(rGO) + E_{ads}(BiOI) = -15.36 kcal·mol^{-1}

CAP + water: $\sum E_{ads}$(rGO) + E_{ads}(BiOI) = -181.05 kcal·mol^{-1}

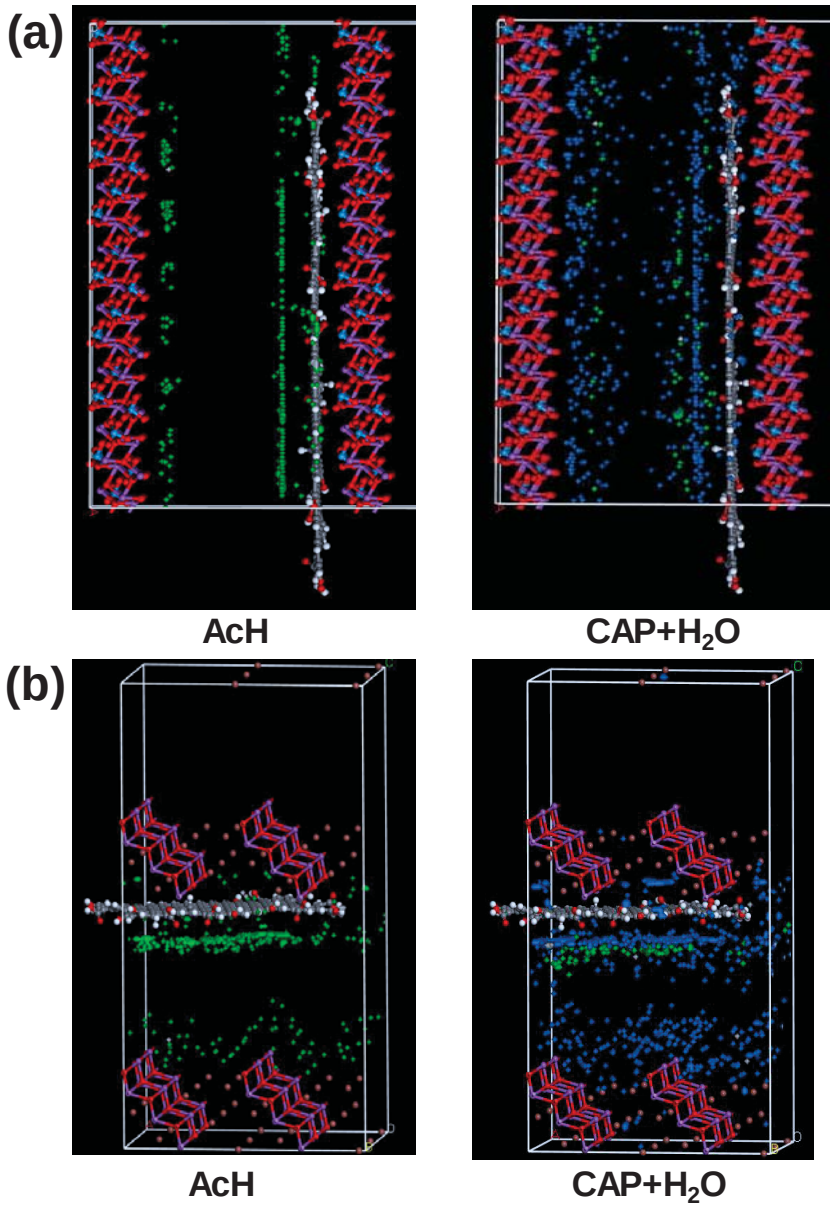

Figure 6.10. Visualization of adsorption of sorbate molecules onto surfaces of (a) rGO/Bi_2WO_6 and (b) rGO/BiOI: bismuth, violet; tungsten blue; oxygens, red; iodine, brown. Isosurface: acetaldehyde and chloramphenicol, green; water, blue.

Figure 6.10 confirms the concentration of the sorbate field density along the rGO-BiOI surfaces.

BiOI and Bi_2WO_6 surfaces. The similar E_{ads} values of the AcH molecules in the BiOI/Bi_2WO_6 (-6.18 kcal·mol^{-1}), Bi_2WO_6 (-6.22 kcal·mol^{-1}), and rGO/Bi_2WO_6 (-7.9 kcal·mol^{-1}) samples and similar E_{ads} values of the CAP+water molecules in the BiOI/Bi_2WO_6 (-74.42 kcal·mol^{-1}), Bi_2WO_6 (-74.07 kcal·mol^{-1}), and rGO/Bi_2WO_6 (-80.61 kcal·mol^{-1}) samples confirm the preferential adsorption of AcH molecules on the Bi_2WO_6 surface. However, adsorption on the rGO/Bi_2WO_6 and rGO/BiOI surfaces is slightly better than that on the BiOI and Bi_2WO_6 surfaces.

rGO/BiOI and rGO/Bi_2WO_6 surfaces. The evaluation of the interactions in the rGO/Bi_2WO_6/BiOI sample was made using two different approximations as follows:

AcH adsorption:

E_{ads}^{*}(rGO/Bi_2WO_6/BiOI) = E_{ads}(rGO/BiOI) + E_{ads}(rGO/Bi_2WO_6) = -27.83 kcal·mol^{-1}

E_{ads}^{**}(rGO/Bi_2WO_6/BiOI) = 2 E_{ads}(rGO) + 2 E_{ads}(Bi_2WO_6/BiOI) = -28.12 kcal·mol^{-1}

CAP+water adsorption:

E_{ads}^{*}(rGO/Bi_2WO_6/BiOI) = E_{ads}(rGO/BiOI) + E_{ads}(rGO/Bi_2WO_6) = -264.19 kcal·mol^{-1}

E_{ads}^{**}(rGO/Bi_2WO_6/BiOI) = 2 E_{ads}(rGO) + 2 E_{ads}(Bi_2WO_6/BiOI) = -327.12 kcal·mol^{-1}

Comparison of the values obtained from the two different approximations shows good correlation (Δ(AcH) = E_{ads}^{*} - E_{ads}^{**} = 0.3 kcal·mol^{-1}) and (Δ(CAP+water) = E_{ads}^{*} - E_{ads}^{**} = 62 kcal·mol^{-1}).

The molecular modeling studies of the Bi_2WO_6, BiOI, and rGO samples show that rGO and BiOI significantly increase the adsorption and concentration of the sorbates over the rGO/BiOI surface in the rGO/Bi_2WO_6/BiOI and rGO/BiOI composites and consequently improve the photocatalytic activity. The role of rGO in the rGO/Bi_2WO_6 and rGO/Bi_2WO_6/BiOI composites is mainly determined by the S_{BET} factor instead of the electronic structure or sorbate affinity because the AcH and CAP molecules have similar affinity to the rGO and Bi_2WO_6 surfaces.

6.4. Conclusions

In summary, we successfully improved the photocatalytic activity of the Bi_2WO_6/BiOI composite by modifying it with rGO in varying content. The results from XRD, SEM, EDS,

TEM, UV-Vis, and N_2 gas adsorption measurements confirmed the formation of the rGO/Bi_2WO_6/BiOI composite. In comparison with the Bi_2WO_6/BiOI composite, the rGO/Bi_2WO_6/BiOI composite with 1 wt% rGO exhibited a remarkable improvement in the photocatalytic activity for the degradation of AcH and CAP molecules. Improvement in the adsorption of AcH and CAP molecules, easy capture of photoinduced electrons, and formation of an additional *p*-*n* heterojunction with *n*-type Bi_2WO_6 should be responsible for the improved photocatalytic activity. The results obtained from molecular modeling studies revealed that rGO and BiOI can significantly increase the adsorption of AcH and CAP+water molecules over the rGO/BiOI surface in the rGO/Bi_2WO_6/BiOI and rGO/BiOI composites and improve the photocatalytic activity over that of Bi_2WO_6. The prepared rGO/Bi_2WO_6/BiOI composite can be used in environmental remediation processes.

6.5. References

[1] A. Fujishima, K. Honda, Electrochemical Photolysis of Water at a Semiconductor Electrode, *Nature* 238 (1972) 37–38.

[2] Z.C. Kadirova, M. Hojamberdiev, K. Katsumata, T. Isobe, N. Matsushita, A. Nakajima, K. Sharipov, K. Okada, Preparation of iron oxide-impregnated spherical granular activated carbon-carbon composite and its photocatalytic removal of methylene blue in the presence of oxalic acid, *J. Environ. Sci. Health A* 49 (2014) 763–769.

[3] M. Hojamberdiev, G. Zhu, Z.C. Kadirova, J. Han, J. Liang, J. Zhou, X. Wei, P. Liu, Morphology-controlled growth of $BiVO_4$ crystals by hydrothermal method assisted with ethylene glycol and ethylenediamine and their photocatalytic activity, *Mater. Chem. Phys.* 165 (2015) 188–195.

[4] M. Hojamberdiev, G. Zhu, P. Sujaridworakun, S. Jinawath, P. Liu, J.-P. Zhou, Visible-light-driven N–F-codoped TiO_2 powders derived from different ammonium oxofluorotitanate precursors, *Powder Technol.* 218 (2012) 140–148.

[5] B. Czech, M. Hojamberdiev, UVA- and visible-light-driven photocatalytic activity of three-layer perovskite Dion-Jacobson phase $CsBa_2M_3O_{10}$ (*M* = Ta, Nb) and oxynitride crystals in the removal of caffeine from model wastewater, *J. Photochem. Photobiol. A* 324 (2016) 70–80.

[6] C. Tan, G. Zhu, M. Hojamberdiev, K. Okada, J. Liang, X. Luo, P. Liu, Y. Liu, Co_3O_4 nanoparticles-loaded BiOCl nanoplates with the dominant {001} facets: efficient photodegradation of organic dyes under visible light, *Appl. Catal. B* 152–153 (2014) 425–436.

[7] R. Doong, C. Chen, R.A. Maithreepala, S. Chang, The influence of pH and cadmium sulfide on the photocatalytic degradation of 2-chlorophenol in titanium dioxide suspensions, *Water Res.* 35 (2001) 2873–2880.

[8] Y. Wang, X. Wang, M. Antonietti, Polymeric graphitic carbon nitride as a heterogeneous organocatalyst: From photochemistry to multipurpose catalysis to sustainable chemistry, *Angew. Chem. Int. Ed.* 51 (2012) 68–89.

[9] M. Hojamberdiev, Z.C. Kadirova, Y. Makinose, G. Zhu, N. Matsushita, J. Rodríguez, S. Aldabe Bilmes, M. Hasegawa, K. Okada, Influence of BiOI content on the photocatalytic activity of Bi_2WO_6/BiOI/allophane composites and molecular modeling studies of acetaldehyde adsorption, *J. Taiwan Inst. Chem. Eng.* 81 (2017) 258–264.

[10] B. Aurivillius, The structure of Bi_2NbO_5F and isomorphous compounds, *Ark Kemi* 5 (1952) 39–47.

[11] M. Hojamberdiev, Z.C. Kadirova, Y. Makinose, G. Zhu, S. Emin, N. Matsushita, M. Hasegawa, K. Okada, Involving $CeVO_4$ in improving the photocatalytic activity of a Bi_2WO_6/allophane composite for the degradation of gaseous acetaldehyde under visible light, *Colloids Surf. A* 529 (2017) 600–612.

[12] M. Hojamberdiev, K. Katsumata, K. Morita, S. Aldabe Bilmes, N. Matsushita, K. Okada, One-step hydrothermal synthesis and photocatalytic performance of $ZnWO_4$/Bi_2WO_6 composite photocatalysts for efficient degradation of acetaldehyde under UV light irradiation, *Appl. Catal. A* 457 (2013) 12–20.

[13] X. Hu, J. Tian, Y. Xue, Y. Li, H. Cui, Bi_2WO_6 nanosheets decorated with Au nanorods for enhanced near-infrared photocatalytic properties based on surface plasmon resonance effects and wide-range near-infrared light harvesting, *ChemCatChem* 9 (2017) 1511–1516.

[14] Z. Li, L. Zhu, W. Wu, S. Wang, L. Qian, Highly efficient photocatalysis toward tetracycline under simulated solar-light by Ag^{+}-CDs-Bi_2WO_6: Synergistic effects of silver ions and carbon dots, *Appl. Catal. B* 192 (2016) 277–285.

[15] Y. Guo, G. Zhang, H. Gan, Synthesis, characterization and visible light photocatalytic properties of Bi_2WO_6/rectorite composites, *J. Colloid Interface Sci.* 369 (2012) 323–329.

[16] M. Hojamberdiev, K. Katsumata, N. Matsushita, K. Okada, Preparation of Bi_2WO_6– and BiOI–allophane composites for efficient photodegradation of gaseous acetaldehyde under visible light, *Appl. Clay Sci.* 101 (2014) 38–43.

[17] M.-A. Lavergne, C. Chanéac, D. Portehault, S. Cassaignon, O. Durupthy, Optimized design of Pt-doped Bi_2WO_6 nanoparticle synthesis for enhanced photocatalytic properties, *Eur. J. Inorg. Chem.* 2016 (2016) 2159–2165.

[18] M. Hojamberdiev, Z. Kadirova, E. Zahedi, D. Onna, M.C. Marchi, G. Zhu, N. Matsushita, M. Hasegawa, S.A. Bilmes, K. Okada, Tuning the morphological structure, light absorption, and photocatalytic activity of Bi_2WO_6 and Bi_2WO_6-BiOCl through cerium doping, *Arab. J. Chem.* (2018) DOI: 10.1016/j.arabjc.2018.07.014

[19] G. Zhu, J. Liang, M. Hojamberdiev, S.A. Bilmes, X. Wei, P. Liu, J. Zhou, Ethylenediamine (EDA)-assisted hydrothermal synthesis of nitrogen-doped Bi_2WO_6 powders, *Mater. Lett.* 122 (2014) 216–219.

[20] Y. Zhang, Z. Tang, X. Fu, Y. Xu, TiO_2-graphene nanocomposites for gas-phase photocatalytic degradation of volatile aromatic pollutant: Is TiO_2-graphene truly different from other TiO_2-carbon composite materials? *ACS Nano* 4 (2010) 7303–7314.

[21] K. Katsumata, N. Matsushita, K. Okada, Preparation of TiO_2-fullerene composites and their photocatalytic activity under visible light, *Int. J. Photoener.* 2012 (2012) 9 pages. DOI: 10.1155/2012/256096.

[22] K. Katsumata, R. Motoyoshi, N. Matsushita, K. Okada, Preparation of graphitic carbon nitride (g-C_3N_4)/WO_3 composites and enhanced visible-light-driven photodegradation of acetaldehyde gas, *J. Hazard. Mater.* 260 (2013) 475–482.

[23] K. Woan, G. Pyrgiotakis, W. Sigmund, Photocatalytic carbon-nanotube–TiO_2 composites, *Adv. Mater.* 21 (2009) 2233–2239.

[24] Y.H. Ng, A. Iwase, A. Kudo, R. Amal, Reducing graphene oxide on a visible-light $BiVO_4$ photocatalyst for an enhanced photoelectrochemical water splitting, *J. Phys. Chem. Lett.* 1 (2010) 2607–2612.

[25] L. Zhang, Y. Zhu, A review of controllable synthesis and enhancement of performances of bismuth tungstate visible-light-driven photocatalysts, *Catal. Sci. Technol.* 2 (2012) 694–706.

[26] W.S. Hummers Jr., R.E. Offeman, Preparation of Graphitic Oxide, *J. Am. Chem. Soc.* 80 (1958) 1339–1339.

[27] B. Gupta, N. Kumar, K. Panda, V. Kanan, S. Joshi, I. Visoly-Fisher, Role of oxygen functional groups in reduced graphene oxide for lubrication, *Sci. Rep.* 7 (2017) 45030.

[28] Z. Fan, K. Wang, T. Wei, J. Yan, L. Song, B. Shao, An environmentally friendly and efficient route for the reduction of graphene oxide by aluminum powder, *Carbon* 48 (2010) 1670–1692.

[29] J.B. Wu, M.L. Lin, X. Cong, H.N. Liu, P.H. Tan, Raman spectroscopy of graphene-based materials and its applications in related devices, *Chem. Soc. Rev.* 47 (2018) 1822–1873.

[30] A.C. Ferrari, Raman spectroscopy of graphene and graphite: Disorder, electron–phonon coupling, doping and nonadiabatic effects, *Solid State Commun.* 143 (2007) 47–57.

[31] M. Thommes, K. Kaneko, A.V. Neimark, J.P. Olivier, F. Rodriguez-Reinoso, J. Rouquerol, K.S.W. Sing, Physisorption of gases, with special reference to the evaluation of surface area and pore size distribution (IUPAC Technical Report), *Pure Appl. Chem.* 87 (2015) 1051–1069.

[32] R. Tang, H. Su, Y. Sun, X. Zhang, L. Li, C. Liu, B. Wang, S. Zeng, D. Sun, Facile fabrication of Bi_2WO_6/Ag_2S heterostructure with enhanced visible-light-driven photocatalytic performances, *Nanoscale Res. Lett.* 11 (2016) 126–138.

[33] K. Kawashima, M. Hojamberdiev, H. Wagata, E. Zahedi, K. Yubuta, K. Domen, K. Teshima, Two-step synthesis and visible-light-driven photocatalytic water oxidation activity of AW(O,N)$_3$ (A = Sr, La, Pr, Nd and Eu) perovskites, *J. Catal.* 344 (2016) 29–37.

[34] J. Di, J. Xia, M. Ji, B. Wang, S. Yin, H. Xu, Z. Chen, H. Li, Carbon quantum dots induced ultrasmall BiOI nanosheets with assembled hollow structures for broad spectrum photocatalytic activity and mechanism insight, *Langmuir* 32 (2016) 2075–2084.

[35] M. Hojamberdiev, M.F. Bekheet, J.N. Hart, J.J.M. Vequizo, A. Yamakata, K. Yubuta, A. Gurlo, M. Hasegawa, K. Domen, K. Teshima, Elucidating the impact of *A*-site cation change on photocatalytic H_2 and O_2 evolution activities of perovskite-type *Ln*$TaON_2$ (*Ln* = La and Pr), *Phys. Chem. Chem. Phys.* 19 (2017) 22210–22220.

[36] A. Ganguly, S. Sharma, P. Papakonstantinou, J. Hamilton, Probing the thermal deoxygenation of graphene oxide using high-resolution in situ X-ray-based spectroscopies, *J. Phys. Chem. C* 115 (2011) 17009–17019.

[37] Y. Liu, G. Zhu, J. Gao, R. Zhu, M. Hojamberdiev, C. Wang, X. Wei, P. Liu, A novel synergy of Er^{3+}/Fe^{3+} co-doped porous Bi_5O_7I microspheres with enhanced photocatalytic activity under visible-light irradiation, *Appl. Catal. B* 205 (2017) 421–432.

[38] Z.C. Kadirova, M. Hojamberdiev, K.-I. Katsumata, T. Isobe, N. Matsushita, A. Nakajima, K. Okada, Fe_2O_3-loaded activated carbon fiber/polymer materials and their photocatalytic activity for methylene blue mineralization by combined heterogeneous-homogeneous photocatalytic processes, *Appl. Surf. Sci.* 402 (2017) 444–455.

[39] Y.-C. Chen, K.-i. Katsumata, Y.-H. Chiu, K. Okada, N. Matsushita, Y.-J. Hsu, ZnO–graphene composites as practical photocatalysts for gaseous acetaldehyde degradation and electrolytic water oxidation, *Appl. Catal. A* 490 (2015) 1–9.

[40] B. Gao, S. Dong, J. Liu, L. Liu, Q. Feng, N. Tan, T. Liu, L. Bo, L. Wang, Identification of intermediates and transformation pathways derived from photocatalytic degradation of five antibiotics on $ZnIn_2S_4$, *Chem. Eng. J.* 304 (2016) 826–840.

[41] Y. Zhang, Y. Shao, N. Gao, Y. Gao, W. Chu, S. Li, Y. Wang, S. Xu, Kinetics and by-products formation of chloramphenicol (CAP) using chlorination and photocatalytic oxidation, *Chem. Eng. J.* 333 (2018) 85–91.

[42] P. Huo, C. Liu, D. Wu, J. Guan, J. Li, H. Wang, Q. Tang, X. Li, Y. Yan, S. Yuan, Fabricated Ag/Ag_2S/reduced graphene oxide composite photocatalysts for enhancing visible light photocatalytic and antibacterial activity, *J. Ind. Eng. Chem.* 57 (2018) 125–133.

[43] X. Li, R. Shen, S. Ma, X. Chen, J. Xie, Graphene-based heterojunction photocatalysts, *Appl. Surf. Sci.* 430 (2018) 53–107.

[44] R.L.C. Akkermans, N.A. Spenley, S.H. Robertson, Monte Carlo methods in materials studio, *Mol. Sim.* 39 (2013) 1153–1164.

[45] cif file of BIOI. R.W.G. Wyckoff, *Crystal Structures* 1 (1963) 294–296.

[46] cif file of Bi_2WO_6. 23584-ICSD.

CHAPTER 7: Conclusions

7.1. General conclusions

Air and water pollution has been one of the challenging environmental issues in modern society. Since the Honda-Fujishima effect was first reported in 1972, a semiconductor-based photocatalysis has been regarded as one of the most green and economical processes for potential application in environmental remediation. Bismuth-based semiconductors are regarded as a promising group of advanced photocatalytic materials due to their suitable band gap for visible light response, an increased mobility of photo-generated charge carriers because of well-dispersed Bi 6s orbital, non-toxicity, and easy tailoring of their morphologies. To utilize its full potential in environmental remediation, the present study was carried out to enhance the photocatalytic performance of layered Bi_2WO_6, one of the simplest members of the Aurivillius oxide family of layered perovskites, through cerium doping and compositing it with other semiconductors, such as $ZnWO_4$, BiOI, $CeVO_4$, and reduced graphene oxide.

CHAPTER 1 introduces past achievements, the state of the art, and future perspectives in heterogeneous photocatalysis and its application in environmental remediation, particularly in photocatalytic air and water purification. The layered compounds, bismuth-based photocatalysts, and composite photocatalysts and their application in environmental remediation are discussed. The scheme of research and objectives of the present work are presented.

CHAPTER 2 describes the influence of pH and Bi_2WO_6 content on the formation of the $ZnWO_4/Bi_2WO_6$ composite photocatalyst synthesized by a one-step hydrothermal method and the effect of Bi_2WO_6 content on the performance for the photocatalytic degradation of gaseous acetaldehyde under UV light irradiation. An increase in the Bi_2WO_6 content of the $ZnWO_4/Bi_2WO_6$ composite photocatalyst led to a monotonic shift of the absorption edge from about 355 nm to longer wavelength up to about 450 nm and an enhancement of photocatalytic activity for the conversion of acetaldehyde into CO_2 under UV light irradiation in comparison to individual $ZnWO_4$ and Bi_2WO_6. The enhanced photocatalytic activity of $ZnWO_4/Bi_2WO_6$ composite photocatalyst is attributed to the *n*-*n* isotype junctions formed between the two semiconductors and to the improved charge separation and transfer.

CHAPTER 3 emphasizes the involvement of $CeVO_4$ in improving the photocatalytic activity of a Bi_2WO_6/allophane composite for the degradation of gaseous acetaldehyde under visible light irradiation. The Bi_2WO_6/$CeVO_4$/allophane composites (BW/CV/A) with different amounts of $CeVO_4$ nanocrystals were prepared by mechanical mixing and hydrothermal synthesis. The adsorption capacity for acetaldehyde was strongly dependent on the $CeVO_4$ content in the prepared composites. The hydrothermally synthesized BW1/CV1/A (Bi_2WO_6:$CeVO_4$ = 1:1 mass ratio) composite photocatalyst exhibited higher photocatalytic activity than the mechanically mixed BW1/CV1/A composite. The enhanced photocatalytic activity of BW1/CV1/A is related to the extended light absorption, unique structure that improved the transport of the reactant and the final product molecules, and the effective separation of photogenerated electron-hole pairs.

CHAPTER 4 presents the effect of different Bi_2WO_6:BiOI molar ratios on the adsorption capacity and photocatalytic activity of the Bi_2WO_6/BiOI/allophane (BW/BI/A) composites prepared by mechanical mixing and hydrothermal synthesis. The overall morphology of the composite photocatalyst was changed with increasing the BiOI content. The BW/BI/A composites exhibited absorption edges in the wavelength range of 640–650 nm. The specific surface area, adsorption capacity, and photocatalytic activity of the BW/BI/A composite gradually decreased as the BiOI content increased. The BW/0.5BI/A composite exhibited high adsorption capacity, excellent photocatalytic performance and stability owing to its large specific surface area, greater number of easily accessible active sites, facilitated diffusion of reactants, multiple scattering of incident light, and *p–n* heterojunction.

CHAPTER 5 underlines the important role of cerium doping on tuning the morphological structure, light absorption, and photocatalytic activity of Bi_2WO_6 and Bi_2WO_6-BiOCl synthesized by a hydrothermal method using ethylene glycol and dilute HCl as solvent, respectively. The formation of flower-like morphologies was governed by ethylene glycol forming a chain-like structure on the crystallite surface and the selective adsorption of excessive Cl^- ions on the specific surface of crystallite, leading to a morphological variation. Cerium doping extended the absorption edges of Bi_2WO_6 and Bi_2WO_6-BiOCl up to 460 and > 700 nm, respectively. The results from molecular dynamics calculation confirmed that cerium doping could enhance the interaction of the Bi_2WO_6 surface with the salicylic acid molecules

in Ce-doped Bi_2WO_6-BiOCl. The 1 mol% Ce-doped Bi_2WO_6-BiOCl composite photocatalyst showed the highest apparent rate constant (k = -0.360 min^{-1}), which is more than three times higher than that of non-doped Bi_2WO_6 (k = -0.105 min^{-1}), due to the synergistic effect of cerium doping and the formed *p–n* heterojunction.

CHAPTER 6 highlights the modification of the Bi_2WO_6/BiOI composite with reduced graphene oxide in a varying content for enhancing the photocatalytic performance towards the degradation of colorless organic pollutants: acetaldehyde and chloramphenicol under visible light irradiation. The 1 wt% rGO/Bi_2WO_6/BiOI composite exhibited a remarkable improvement in the photocatalytic activity for the degradation of acetaldehyde and chloramphenicol molecules due to the improved adsorption, efficient separation and transfer of photogenerated electrons, and the formation of an additional *p-n* heterojunction. The results from molecular dynamics calculation revealed that rGO and BiOI can significantly increase the adsorption of organic molecules over the rGO/BiOI surface in the rGO/Bi_2WO_6/BiOI.

7.2. Application of results

With the rapid pace of industrialization and urbanization, the number of organic pollutants in air and water has been significantly increased, leading to the complication in their removal processes. Therefore, novel methods are required to remove these emerging organic pollutants in air and water. Heterogeneous photocatalysis has proven to be effective in complete mineralization of these organic pollutants under light irradiation. We have successfully improved the photocatalytic performance for degradation of various organic pollutants existing in either a gas phase or a liquid phase of layered Bi_2WO_6 through cerium doping and compositing with other semiconductors, such as $ZnWO_4$, BiOI, $CeVO_4$, and reduced graphene oxide. The developed samples can be easily synthesized by hydrothermal method and reused because of their good stability during the photocatalytic reaction. The photocatalytic reactor can be scaled up using these prepared composite photocatalysts by taking into account the most important factors and applied for environmental remediation applications, including removal of harmful organic compounds, pesticides, herbicides, pharmaceuticals, microorganisms (bacteria, viruses), and gasses, in the future.

.

7.3. Future prospective

The research area of Bi_2WO_6-based photocatalysts is much younger than that of TiO_2, and it is progressing successfully. The development of TiO_2 photocatalysts from fundamental studies to practical application gives a strong motivation to further advance the research area of Bi_2WO_6-based photocatalysts. In this study, Bi_2WO_6, one of the simplest members of the Aurivillius oxide family of layered perovskites, was synthesized by cerium doping and compositing it with $ZnWO_4$, BiOI, $CeVO_4$, and reduced graphene oxide to develop efficient and stable photocatalytic materials for environmental remediation. In the future, the following topics can be of great interest to expand this research area:

- Photocatalytic activity for the removal of various pharmaceuticals from contaminated water and antibacterial/antivirus activity of the developed photocatalytic materials can be evaluated to extend the application area of the developed materials.
- Photocatalytic reactor can be scaled up using these developed photocatalytic materials by controlling various parameters for environmental remediation application, and the photocatalytic activity for the removal of pesticides, herbicides, etc. can be tested.
- Codoping and fabrication of nanostructures with high specific surface area of Bi_2WO_6 and synthesis of solid solution can be carried out to further enhance the photocatalytic performance for solar water splitting and removal of organic pollutants in liquid and gas phases.
- Visible light absorption of Bi_2WO_6 can be extended to longer wavelengths by loading visible-light-active transition/noble metal complexes on the surface of Bi_2WO_6 and compositing it with various transition metal oxynitrides or oxyhalides.

List of publications:

1. **Mirabbos Hojamberdiev**, Ken-ichi Katsumata, Koji Morita, Sara Aldabe Bilmes, Nobuhiro Matsushita, Kiyoshi Okada, One-step hydrothermal synthesis and photocatalytic performance of $ZnWO_4/Bi_2WO_6$ composite photocatalysts for efficient degradation of acetaldehyde under UV light irradiation, *Applied Catalysis A: General* 457 (2013) 12–20.
2. **Mirabbos Hojamberdiev**, Ken-ichi Katsumata, Nobuhiro Matsushita, Kiyoshi Okada, Preparation of Bi_2WO_6– and BiOI–allophane composites for efficient photodegradation of gaseous acetaldehyde under visible light, *Applied Clay Science* 101 (2014) 38–43.
3. **Mirabbos Hojamberdiev**, Zuhra C. Kadirova, Yuki Makinose, Gangqiang Zhu, Saim Emin, Nobuhiro Matsushita, Masashi Hasegawa, Kiyoshi Okada, Involving $CeVO_4$ in improving the photocatalytic activity of a Bi_2WO_6/allophane composite for the degradation of gaseous acetaldehyde under visible light, *Colloids and Surfaces A* 529 (2017) 600–612.
4. **Mirabbos Hojamberdiev**, Zukhra C. Kadirova, Yuki Makinose, Gangqiang Zhu, Nobuhiro Matsushita, Juan Rodríguez, Sara Aldabe Bilmes, Masashi Hasegawa, Kiyoshi Okada, Influence of BiOI content on the photocatalytic activity of Bi_2WO_6/BiOI/allophane composites and molecular modeling studies of acetaldehyde adsorption, *Journal of the Taiwan Institute of Chemical Engineers* 81 (2017) 258–264.
5. **Mirabbos Hojamberdiev**, Zukhra C. Kadirova, Renato Vitalino Gonçalves, Kunio Yubuta, Nobuhiro Matsushita, Katsuya Teshima, Masashi Hasegawa, Kiyoshi Okada, Reduced graphene oxide-modified Bi_2WO_6/BiOI composite for the effective photocatalytic removal of organic pollutants and molecular modeling of adsorption, *Journal of Molecular Liquids* 268 (2018) 715–727.
6. **Mirabbos Hojamberdiev**, Zuhra Kadirova, Ehsan Zahedi, Diego Onna, María Claudia Marchi, Gangqiang Zhu, Nobuhiro Matsushita, Masashi Hasegawa, Sara Aldabe Bilmes, Kiyoshi Okada, Tuning the morphological structure, light absorption, and photocatalytic activity of Bi_2WO_6 and Bi_2WO_6-BiOCl through cerium doping, *Arabian Journal of Chemistry* (2018) in press. DOI: 10.1016/j.arabjc.2018.07.014

Conference presentations:

1. **Mirabbos Hojamberdiev**, Ken-ichi Katsumata, Nobuhiro Matsushita, Kiyoshi Okada, Bi_2WO_6/BiOI and Bi_2WO_6/Allophane/BiOI composite photocatalysts and their photocatalytic activity, *25th Fall Meeting of the Ceramic Society of Japan*, 19-21 September, 2012, Nagoya, Japan.
2. **Mirabbos Hojamberdiev**, Ken-ichi Katsumata, Yuki Makinose, Nobuhiro Matsushita, Kiyoshi Okada, Visible light-responsive Bi_2WO_6/Allophane and BiOI/Allophane composite photocatalysts: Hydrothermal synthesis, characterization and photocatalytic performances, *4th Annual International Workshop on Advanced Materials*, 23-26 February, 2013, Ras Al Khaimah, United Arab Emirates.
3. **Mirabbos Hojamberdiev**, Ken-ichi Katsumata, Nobuhiro Matsushita, Kiyoshi Okada, One-step hydrothermal synthesis and photocatalytic performance of $ZnWO_4/Bi_2WO_6$ composite photocatalyst, *Annual Meeting of the Ceramic Society of Japan*, 17-19 March, 2013, Tokyo, Japan.
4. **Mirabbos Hojamberdiev**, Yuki Makinose, Ken-ichi Katsumata, Toshihiro Isobe, Nobuhiro Matsushita, Kiyoshi Okada, Hydrothermal synthesis and visible-light-driven photocatalytic activity of allophane–wakefieldite-(Ce) composite, *International Conference on Advanced Materials Science and Technology (ICAMST 2013)*, 17-18 September, 2013, Yogyakarta, Indonesia.
5. **Mirabbos Hojamberdiev**, Ehsan Zahedi, Zukhra C. Kadirova, Masashi Hasegawa, Sara Aldabe Bilmes, Nobuhiro Matsushita, Tuning the Morphological Structure, Light Absorption, and Photocatalytic Activity of Bi_2WO_6 and Bi_2WO_6-BiOCl Through Cerium Doping, *7th International Conference on Nanostructures (ICNS7)*, 27 February-01 March 2018, Tehran, Iran.
6. **Mirabbos Hojamberdiev**, Gangqiang Zhu, Zukhra Kadirova, Masashi Hasegawa, Nobuhiro Matsushita, Bismuth-Based Visible-Light-Active Photocatalytic Nanomaterials for Environmental Remediation, *6th International Conference on Nanomaterials and Advanced Energy Storage Systems (INESS-2018)*, 8-10 August 2018, Astana, Kazakhstan.
7. **Mirabbos Hojamberdiev**, Two-dimensional photocatalytic materials for environmental application, *International Conference on Nano-Structured Materials & Devices (ICNSMD-2018)*, 17-20 December 2018, New Delhi, India.

Acknowledgements

First of all, I would like to express my sincere appreciation and deep gratitude to my supervisor Prof. Nobuhiro Matsushita for his invaluable supervision and constant support. His deep knowledge, continuous guidance, understanding and encouraging have been important to successfully complete this work.

I am much beholden to Prof. Kiyoshi Okada and Prof. Akira Nakajima for their fruitful discussions, stimulating suggestions and helpful and constructive comments. I would also like to extend my special thanks to Dr. Ken-ichi Katsumata and Dr. Toshihiro Isobe for their administrative and technical support.

I am delighted to extend my cordial acknowledgements to the previous and present members of OKADA-NAKAJIMA Lab, OKADA-MATSUSHITA Lab, and YANO-MATSUSHITA Lab at Tokyo Institute of Technology for their immense support and wonderful friendship.

I am indebted to my host Japanese family, Prof. Satoshi Kimura, Mrs. Tomoko Kimura and Mr. Atsushi Kimura, for giving me a unique opportunity to experience real Japanese life and culture for the first time during my Tokyo Tech UNESCO International Research Course for the Environment.

I am much obliged to my previous and present colleagues who directly and indirectly assisted in characterizing and evaluating the developed samples. I thank my parents and siblings for their continuous support.

Finally, I wish to thank my beloved wife, Ms. Kozue Kawata, for her kind understanding, courageous support, everlasting love, unlimited patience, and taking care of our son, little Enzo, during the course of this research work.